Helicene-porphyrin conjugates : exciton coupling and chiral-Induced spin selectivity

Paola Matozzo

To cite this version:

Paola Matozzo. Helicene-porphyrin conjugates : exciton coupling and chiral-Induced spin selectivity. Chemical Sciences. Université de Rennes, 2023. English. NNT : 2023URENS108 . tel-04842254

HAL Id: tel-04842254
https://theses.hal.science/tel-04842254v1

Submitted on 17 Dec 2024

COLLEGE DOCTORAL BRETAGNE
SCIENCES DE LA MATIERE DES MOLECULES ET MATERIAUX

Université de Rennes

THESE DE DOCTORAT DE

L'UNIVERSITE DE RENNES

ECOLE DOCTORALE N° 638
Sciences de la Matière, des Molécules et Matériaux
Spécialité : *chimie moléculaire et macromoléculaire*

Par
Paola MATOZZO

« Helicene-Porphyrin Conjugates: Exciton Coupling and Chiral-Induced Spin Selectivity effect »

Thèse présentée et soutenue à Rennes, le 23 Octobre 2023
Unité de recherche : UMR CNRS 6226 / Organométalliques : matériaux et catalyse (OMC)

Rapporteurs avant soutenance :

Jennifer WYTKO	Chargée de recherche CNRS, Université de Strasbourg
Neso SOJIC	Professeur, Ecole Nationale Supérieure de Chimie et de Physique, Bordeaux

Composition du Jury :

Président :	Bernard BOITREL	Directeur de recherche CNRS, Université de Rennes
Examinateurs :	Gennaro PESCITELLI	Professeur, Université de Pise
Rapporteurs :	Jennifer WYTKO	Chargée de recherche CNRS, Université de Strasbourg
	Neso SOJIC	Professeur, Ecole Nationale Supérieure de Chimie et de Physique, Bordeaux
Dir. de thèse :	Jeanne CRASSOUS	Directrice de recherche CNRS, Université de Rennes

Acknowledgements

I have been thinking about writing this part of the manuscript since the beginning of this "journey" and the time has come eventually.

First of all, I am grateful to Dr. Jeanne Crassous for giving me the chance to participate in this Marie Curie Ph.D. scholarship in her research team: I felt truly privileged to be part of such a highly reputed group and prestigious project, surrounded by outstanding scientists, to have the chance to exchange and work with them (I will not forget the nights in the lab at Weizmann in Israel) and to show during important conferences around Europe (and not only) the results I achieved.

I would like to thank the members of the jury, Dr. Jennifer Wytko, Prof. Neso Sojic, Dr. Bernard Boitrel and Prof. Gennaro Pescitelli, for accepting this invitation and for evaluating my work of these three years.

Huge thank to Natalia: I should have realized way before how much important is to have someone like you next to me. Thank you for always having an answer and the will to find one to help me, for all the discussions and the shared opinions.

I would like to thank the whole PMM group, starting from Dr. Ludovic Favereau and Dr. Pierre-Antoine Bouit, who take care of all of us, to all the students and postdocs. Thanks to the "old generation", Etienne, Kais (for the shared work and the suggestions), Victor (for the open-hearted conversations), Nicolas, Chok (favorite labmate ever), Tito (thank you for your scientific help and for our chatting in the office), Thiti, Emilien, Don Carl, and to the "new ones": Mathias (and his kindness), Maxime (and his tarot), Nastya (for our exchange of daily hopeless looks), Alexandre, Louis, Maxime R., Catherine, Yan Yan, Sebastian and Deb (thanks a lot for putting up with all my silly jokes and for your wise advice about life). Thanks to Patty for all the laughs, the unforgettable sentences, and for being always sincere.
I must thank my "third brother" Stefano, who has always been there to take care of me (and who has made me worried about him so often…): talking with you has really changed my day many times; and of course thanks to Giorgia, not only for her motivational phrases and chemistry suggestions, but in particular for the good vibes and the real support she gave me.

I would like to thank as well the HEL4CHIROLED group and the other Ph.D. students. Some special words to the Italian Training Network (as Prof. Di Bari said) + Oliver: recently, somebody told me that what we will truly remember in our life is the people we have met. I couldn't have imagined that beyond the scientific exchanges, the chemistry advice, and the complaints (of course), I would find true friends.

It is important to thank as well all our scientific collaborators. First, I would like to thank Dr. Nicolas Vanthuyne for the HPLC separations on chiral phase, to our theoretical collaborators, Prof. Jochen Autschbach, Dr. Laura Abella, and Dr. Pierpaolo Morgante, whose calculations helped in better understanding all the experimental results obtained, and to Dr. Bruno Fabre for his commitment to the work on the Si surfaces. Special thanks to Prof. Ron Naaman who accepted to host me in his laboratories and to his postdocs (Dr. Kakali Santra and Dr. Anil Kumar) who are still working on my

compounds to provide new interesting results; thanks to JASCO Europe and Paolo Albertini who hosted me and gave a so extensive training on the chiroptical measurements.

Thank you to my Italian community in Rennes who was my second family during these three years and who made me feel at home when I felt so far from everyone, and thanks to my real family (my parents and my brothers) who has always supported all my decisions and choices even though I know they don't agree with many of them…

To conclude, I thank my beloved friends, in particular, Luana and Annette and our timeless friendship, they know everything I have come through during this adventure and they never let me alone despite all the kilometers; and Charles, who saw the worst part of me and managed to turn it into something good by staying by my side.

Table of contents

Abbreviations **1**

General introduction **2**

References **4**

Chapter 1. Introduction to helicenes: chiroptical properties and Chiral-Induced Spin Selectivity **5**

I. Introduction **6**

- I.1. Introduction to chirality 6
  - I.2.1. Synthetic methods 9
  - I.2.2. Racemization barrier and configurational stability 12
  - I.2.3. Examples of resolution 12
  - I.2.4. Examples of asymmetric synthesis 13

II. Chiroptical properties **15**

- II.1. Optical rotation 15
- II.2. Electronic Circular Dichroism ECD 16
- II.3. Circularly Polarized Luminescence CPL 22

III. Chiral-induced spin selectivity effect **25**

- III.1. Theoretical background 25
- III.2. Measuring the spin selectivity: methods and experimental studies 27
  - III.2.1. Photoemission 27
  - III.2.2. Magnetoresistance 29
  - III.2.3. Conductive-probe atomic force microscopy (cp-AFM) 30
  - III.2.4. Spin-dependent electrochemistry (SDE) 31
- III.3. CISS effect in helicenes 35
- III.4. Future perspectives and applications 39

References **40**

Chapter 2. Helicene-porphyrin conjugates: synthesis and Exciton Coupling chirality **45**

I. Context and target molecules **46**

- I.1. Porphyrins: structure and spectroscopic properties 46
- I.2. Conformations of the porphyrin macrocycle 48
- I.3. Chiral porphyrins and Exciton Coupling chirality 52
  - I.3.1. Bis-porphyrins formed via achiral linkages 54
  - I.3.2. Rigid systems 56
  - I.3.3. Bis-porphyrins containing chiral linkages 57
  - I.3.4. Helicene-porphyrin conjugates. 60

I.4. Application in spintronics 61
I.5. Targeted molecules: helicene-porphyrin conjugates 64
II. Synthesis for the helicene-bis-porphyrin derivatives implying a spacer 65
II.1. Synthetis for H6Pr1-3 series 64
II.2. Synthetis for H6Pr1-3 series 64
III. Optical and chiroptical properties of the spacer-bearing derivatives 69
III.1. UV-vis and ECD spectra of the H6Pr1 series 69
III.1.1. Calculated UV-vis spectra 70
III.1.2. Calculated circular dichroism (CD) 73
III.2. Total luminescence and CPL of the H6Pr1 series 75
III.3. UV-vis and ECD spectra of PrZnPhH6 76
III.4. Total luminescence and circularly polarized luminescence of PrZnPhH6 77
IV. Conclusions 78
V. Experimental procedures 79
References 85
Chapter 3. Helicene-porphyrin conjugates: influence of the spacer on EC chirality 89
I. Context and target molecules 90
II. Synthesis for the porphyrin-helicene derivatives with no spacer 91
II.1. Synthetic procedure for MPrH6 series 91
II.2. Synthetic procedure for MPrOMeH6 series 92
III. Optical and chiroptical properties of the derivatives with no spacer 95
III.1. UV-vis and ECD spectra of MPrH6 95
III.2. Total luminescence and circularly polarized luminescence of MPrH6 98
III.3. UV-vis and ECD spectra of MPrOMeH6 series 100
III.4. Total luminescence and circularly polarized luminescence of PrOMeH6 103
III.5. Comparisons among the different Zn derivatives 104
IV. CISS effect measurements: mc-AFM 107
V. Conclusion 110
VI. Experimental procedures 112
References 118
Chapter 4. Synthesis of helicene derivatives for surface grafting and Spin Dependent Electrochemistry 119
I. Context and target molecules 120

I.1. The principle of spin-dependent electrochemistry 120
I.2. Chiral helical polymers 121
I.3. Self-assembled monolayers 124
I.4. Targeted molecules 126
II. Synthesis of helicenic ligands 127
III. Optical and chiroptical characterizations 130
IV. Cyclic voltammetry 131
IV.1. Electrochemistry in solution 131
IV.2. Spin Dependent Electrochemistry 132
V. Conclusions 135
VI. Perspectives 135
VII. Experimental part 139
References 146
Conclusions and perspectives 146

Abbreviations

[α] Specific rotation
Ar Aromatic
AFM Atomic Force Microscopy
B_{CPL} Circularly polarized luminescence brightness
BINAP 2,2’-Bis(diphenylphosphino)-1,1’ binaphthyle
BNP 1,1′-Binaphthyl
cat. Catalytic
CD Circular dichroism
CE Cotton effect
CIP Cahn-Ingold-Prelog
CISS Chiral-induced spin selectivity
COD 1,5-Cyclooctadiene
COSY Correlation spectroscopy
cp-AFM Conductive-probe atomic force microscopy
CPL Circularly polarized luminescence
CT Charge transfer
DMSO Dimethylsulfoxide
DPP Diketopyrrolopyrrole
EC Exciton Coupling
ECD Electronic circular dichroism
ee Enantiomeric excess
eq. Equivalent
FMO Frontier Molecular Orbital
ESI Electrospray ionization
g_{abs} Dissymmetry factor in CD
g_{lum} Dissymmetry factor in CPL
HOMO Highest occupied molecular orbital
HPLC High performance liquid chromatography
HR-MS High resolution mass spectroscopy
LUMO Lowest unoccupied molecular orbital
MALDI Matrix assisted laser desorption ionization
MCH Methylcyclohexane
mc(p)-AFM Magnetic conductive (probe) Atomic Force Microscopy
MO Molecular orbital
***n*-BuLi** *n*-Butyllithium
NMR Nuclear magnetic resonance
OLED Organic light-emitting diode
PAH Polyaromatic hydrocarbon
Pc Phtalocyanine
PDT Photodynamic therapy
QUINAP *R/S*-1-(2-Diphenylphosphino-1-naohthyl)isoquinoline
rt Room temperature
rac Racemic
S0 ground state
S1 Excited state
SAM Self-assembled monolayer
SDE Spin Dependent Electrochemistry
SOC Spin-orbit coupling
TAPA (*R*)-2-(2,4,5,7-Tetranitro-9-fluorenylideneaminooxy)propanoic acid
TD-DFT Time dependent density functional theory
TFA Trifluoroacetic acid
THF Tetrahydrofuran
UV-Vis Ultraviolet-visible
ϕ Quantum yield
δ Chemical shift
ε Molar exctinction coefficient
λ Wavelength

General introduction

Helicenes are the archetypes of helical molecules composed by *n ortho*-fused aromatic or heteroaromatic rings whose helical structure leads to an inherent chirality and intriguing properties. In fact, these molecules strongly interact with circularly polarized light giving rise to remarkable chiroptical responses such as high optical rotation values, intense electronic circular dichroism, and circularly polarized luminescence.

Hence, helicenes were examined as chiral sensors and switches, chiral ligands in asymmetric catalysis and as circularly polarized emitters in devices or in supramolecular assemblies, among others [1].

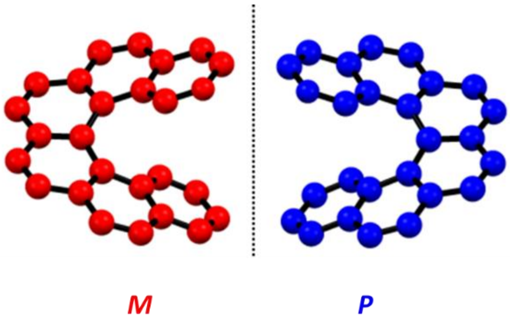

Figure 1. Ball and stick representation of the two enantiomers of helicene.

In the last decades, a new fascinating property related to chiral molecules was disclosed: it was demonstrated that electron transmission through chiral molecules is spin dependent. According to this concept, the electrons injected through a chiral material should have their spin selected in a preferred direction. This is called the Chiral-Induced Spin Selectivity effect (CISS) and it opens the door to new spintronics applications for this type of compounds [2].

After the first report in 2016 by Lacour's group about helicene showing spin polarization, our group contributed to the field by observing CISS effects in supramolecular self-assemblies of helicenes obtained from carbo[6]helicene bearing different aggregating units [3, 4].

In this context, we designed novel helicene derivatives with the aim of exploring the spin filtering ability of this chiral platform through different techniques, such as the magnetic conductive atomic force microscopy (mc-AFM) and the Spin Dependent Electrochemistry (SDE). The work was carried out in collaboration with the group of prof. Ron Naaman at Weizmann Institute of Science in Israel within the HEL4CHIROLED project (from the European Union's Horizon 2020 Research and Innovation Programme under the Marie Sklodowska-Curie grant agreement No 859752).

After a quick introduction to chirality and the helical motif, the first chapter will be dedicated to various methods of helicene synthesis and to the illustration of their chiroptical behavior. A particular focus will be put on the Exciton Coupling (EC) chirality [5] and then on the definition of the CISS effect, the measurement techniques and some straightforward examples in the literature.

In the second chapter, the synthesis and the chiroptical properties of the first helicene bis-porphyrin conjugates (**H6Pr** series) will be described. By introducing porphyrin substituents into helicenic scaffolds we confirmed the presence and effectiveness of EC chirality in helicenes, as previously reported by our group and supported by a computational analysis [6]. In fact the concept of EC chirality can be introduced into helicenes to produce chiral molecules with strong chiroptical properties, such as huge electronic circular dichroism (ECD) and strong circularly polarized luminescence (CPL) emission, as a result of placing achiral strongly polar groups within a helical environment. Moreover, it may be powerful to enhance CISS effects because it enables the engineering of both magnetic and electric dipolar transition moments. Finally, Suzuki couplings instead of Sonogashira ones are described to generate **PrZnPhH6** bearing ethynyl-phenyl spacers with improved synthetic yields. The π-conjugation and distance between porphyrin units is shown to impact the overall chiroptical responses.

This investigation on the Exciton Coupling phenomenon, in particular on the role of the distance between the chromophores and the conjugation, will be pursued in the third chapter, where different families of helicene-porphyrin derivatives will be explored (**MPrH6** and **MPrOMeH6**). On the basis of the results obtained, a promising candidate, namely **ZnPrH6**, was selected for the CISS effect measurements: the preliminary data by mc-AFM will thus be presented.

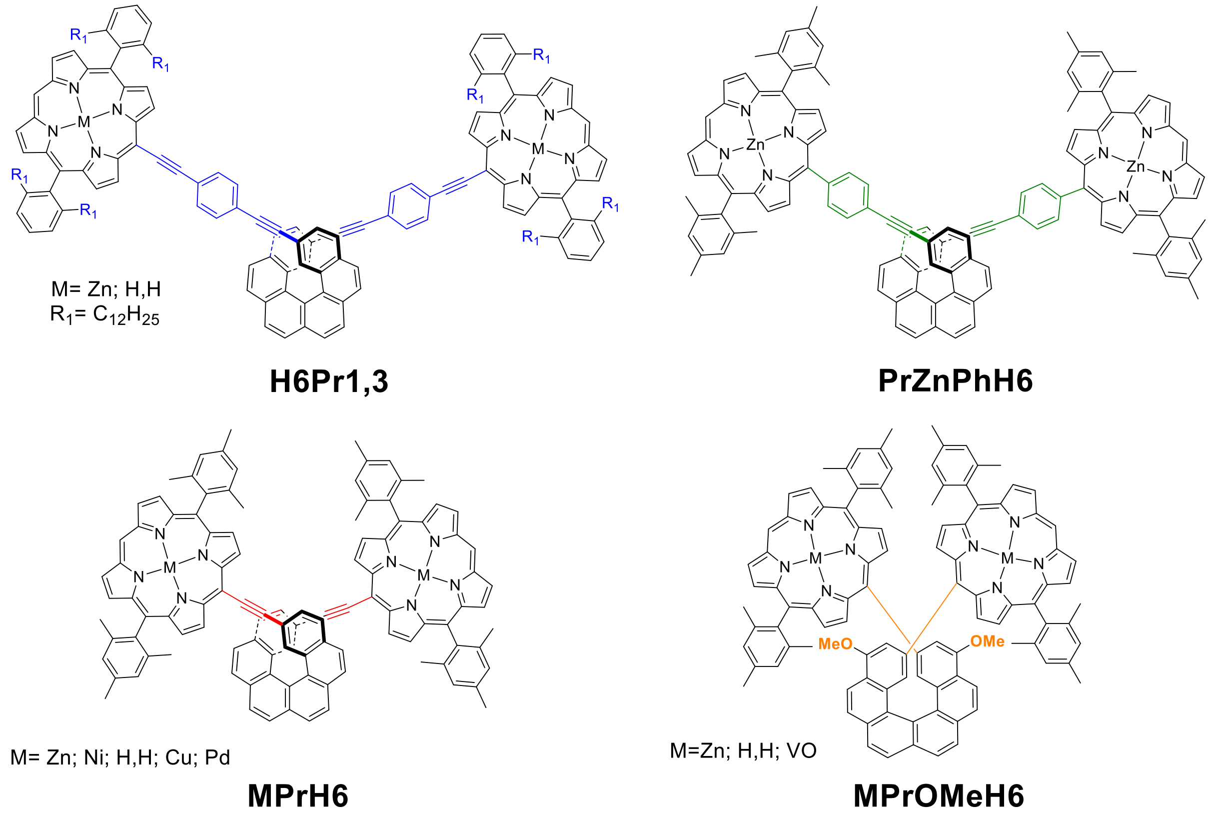

Figure 2. Helicene-porphyrin conjugates presented in this work

In the last chapter, we will explore another technique to measure the spin filtering capacity of helicene, such as the Spin Dependent Electrochemistry, on different surfaces. With this purpose, the helicenic unit was decorated with a redox moiety and a grafting group in order to achieve a proper orientation on the surface and explore how the electron transfer reaction depends on the chirality and affects the electrochemical current.

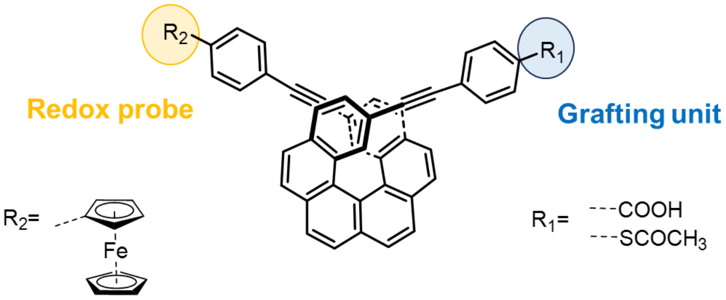

Figure 3. Schematic representation of helicene derivatives for electrochemistry.

References

[1] J. Crassous, I. G. Stara and I. Stary (Eds), Helicenes: Synthesis, Properties and Applications, Wiley, 2022.

[2] R. Naaman and D. H. Waldeck, *J. . Phys. Chem. Lett.,* vol. 3, p. 2178–2187, 2012.

[3] R. Rodríguez, C. Naranjo, A. Kumar, K. Dhbaibi, P. Matozzo, F. Camerel, N. Vanthuyne, R. Gómez, R. Naaman, L. Sánchez and J. Crassous, *Chem. Eur. J.,* 2023, accepted, doi: 10.1002/chem.202302254.

[4] R. Rodríguez, C. Naranjo, A. Kumar, P. Matozzo, T. K. Das, Q. Zhu, N. Vanthuyne, R. Gómez, R. Naaman, L. Sánchez and J. Crassous, *J. Am. Chem. Soc.,* vol. 144, pp. 7709–7719, 2022.

[5] N. Berova, L. D. Bari et G. Pescitelli, *Chem. Soc. Rev.,* vol. 36, pp. 914–931, 2007.

[6] a) K. Dhbaibi, L. Favereau, M. Srebro-Hooper, M. Jean, N. Vanthuyne, F. Zinna, B. Jamoussi, L. D. Bari, J. Autschbach and J. Crassous, *Chem. Sci.,* vol. 9, pp. 735-742, 2018. b) K. Dhbaibi, P. Matozzo, L. Abella, M. Jean, N. Vanthuyne, J. Autschbach, L. Favereau and J. Crassous, *Chem. Commun.,* vol. 57, pp. 10743–10746, 2021.

Chapter 1

Introduction to helicenes: chiroptical properties and Chiral-Induced Spin Selectivity

I. Introduction

I.1. Introduction to chirality

Chirality (from the Greek, “kheir” which means hand) is the property that refers to objects that are non-superimposable with their image given by a plane mirror. Chirality is present at every scale of the universe, from the smallest (for example elementary particles, or amino acids such as cysteine in **Figure 1**) to the biggest (the spiral galaxies) [1, 2].

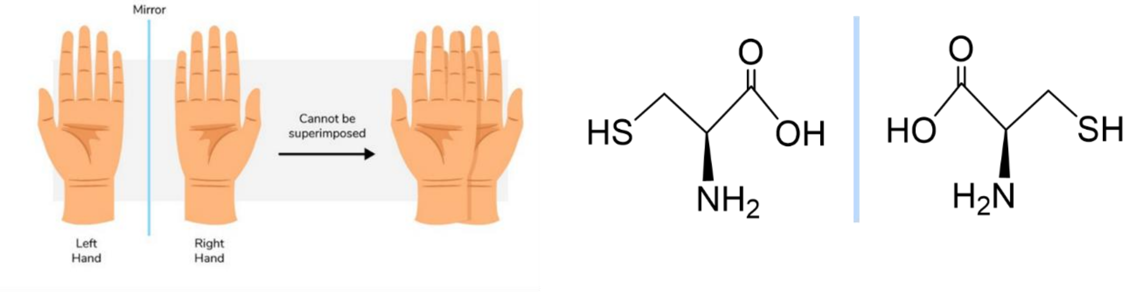

Figure 1. Most common example of chirality, human hands, and amino acid structure.

In chemistry, a molecule is chiral if it lacks any improper axis of rotation (S_n). Molecules that share the same structure are referred to as isomers. When they also exhibit distinct spatial arrangements, we can define them as stereoisomers. Among stereoisomers, those that are mirror images of each other are known as enantiomers, while those that lack mirror-image symmetry are categorized as diastereoisomers.

The concept of chirality in a molecule arises from the presence of certain elements of chirality, such as central, axial, planar, and helical configurations (**Figure 2**).

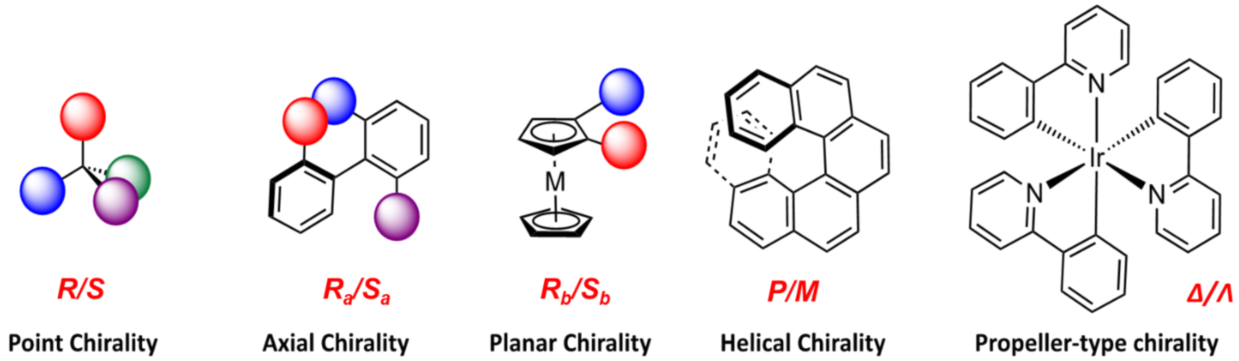

Figure 2. Different types of chirality (taken from ref [2]).

One common form of chirality, the so-called central or point chirality, often arises from sp^3 carbon atoms that hold four distinct substituents.

Point chirality is perhaps the most identified form and is widespread in biologically active compounds like amino acids, sugars, steroids, and terpenes. Namely, biological receptors exhibit stereosensitivity, so that enantiomers of a chiral molecule can induce different biological responses. For instance, one enantiomer of a chiral drug might yield the desired pharmaceutical effect, while the other could be inactive or even harmful, as illustrated by the Thalidomide case [3].

To distinguish between the two enantiomers, a set of notations called stereodescriptors has been established. For central chirality, the *R*/*S* notation is used, following the priority rules outlined by Cahn-Ingold-Prelog (CIP).

Furthermore, there are molecules with axial chirality, that arises from an axis with a locked configuration: sterically congested substituted biaryl systems are an example of this family and they are described using R_a/S_a descriptors. Planar chirality is observed in molecules with non-coplanar dissymmetric planes, denoted by $R_p/\underline{S}_p$ descriptors.

Helical chirality manifests in molecules with inherent helical shapes like helicenes, as well as in propeller-shaped molecules like octahedral metal complexes (designated by Δ/Λ stereodescriptors). The category of helicenic molecules will be explored throughout this manuscript.

I.2. Introduction to helicenes

Helicenes are polycyclic aromatic compounds composed of *n* aromatic or heteroaromatic rings assembled in an *ortho*-fused manner (**Figure 3**) which give them an inherent helical shape.

According to IUPAC nomenclature, the term carbo[n]helicene is used to denote a helical molecule formed of n ortho-fused benzene rings. The prefix penta-, hexa-, hepta-, and so on, can also be used to specify the number of fused benzenes (for example hexahelicene). When a heteroatom is incorporated into the helical backbone, the general term hetero[n]helicene is used, where 'hetero' refers to 'aza', 'bora', 'oxa', 'phospha', 'thia'.

When the number of rings *n* is ≥ 5, because of the steric hindrance of the terminal rings, helicenes can bend in opposite directions and have a C_2-symmetric axis (when non-substituted), which is perpendicular to the helical axis. This enables them to be chiral, even though they have no asymmetric carbons or other chiral centers: on the basis of the helicity rule proposed by Cahn, Ingold, and Prelog in 1966, a left-handed helix, thus with an anticlockwise screw sense, is designated “minus” and denoted by *M* whereas a right handed one, with a clockwise screw sense, is designated “plus” *P*.

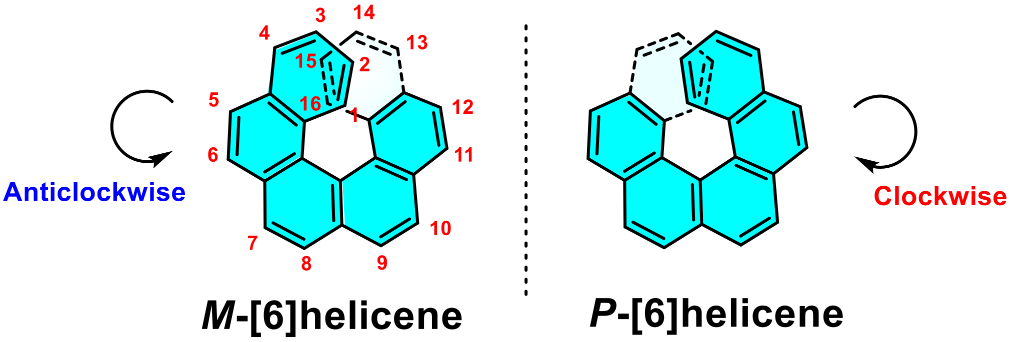

Figure 3. Ortho-fused aromatic rings structures and representation of the two enantiomers of carbo[6]helicene.

As the number of fused rings increases, the helicene spirals up along the helical axis to form a cylindrical structure with a constant pitch (in both the inner and the outer helices). The interplanar angle (or the dihedral angle) of the two terminal rings depends on the helicenes length and on the substituents. For example, the interplanar angles of carbohelicenes (**Figure 4**) increase as the helicenes are elongated from [4]helicene (26.7°) to [6]helicene (58.5°) but decrease with further elongation [4]. Moreover, if the terminal rings are linked by a short alkyl chain, the angle also tends to be reduced [5].

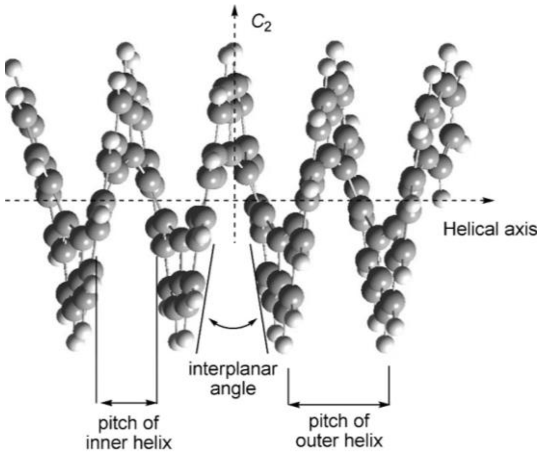

Figure 4. Ball and stick model of helicene [10]: the pitches and angle are illustrated.

From a historical point of view, despite the denomination was introduced later by Newman and Lednicer *et al.* in 1956, the first two helicenes 1,1-dinaphto-2,2-imin **A1** and 1,1-dinaphto-2,2-ortho-diazin **A2**, could date back to 1903, when Meisenheimer and Witte studied the reduction of 2-nitronaphthalene [6]. Then, in 1955, Newman and co-workers were the first to report the synthesis of carbo[6]helicene **A3** and its resolution [7] [8].

After this pioneering work, another significant achievement was made in 1967 by Martin and co-workers, who demonstrated the use of photocyclization for the preparation of the first carbo[7]helicene **A4** and more generally, its usefulness in helicenes synthesis (**Figure 5**) [9].

These pivotal studies helped open the door to a new interest over helicenes, their chiroptical properties and their applications as helically chiral objects in chemistry. Numerous investigations were carried out to obtain more and more sophisticated helicenic structures that illustrated their use in various fields of applications including asymmetric catalysis, as luminescent materials or as sensors. Many reviews about helicene chemistry, their synthesis and applications have been published since then [10, 11, 12, 13, 14, 15, 16] .

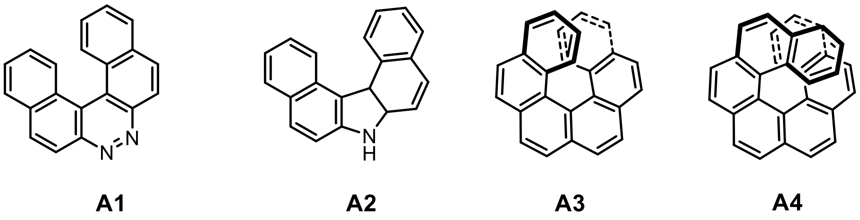

Figure 5. The first examples of [n]helicenes reported in the literature.

I.2.1. Synthetic methods

There are many different methods that were reported to prepare helicenes or heterohelicenes since the very early reports. Among them, the most common and developed ones are the Mallory photocyclization of stilbenic precursors or the metal-catalyzed [2+2+2] cyclotrimerization reactions starting from triynes precursors.

In 1967, Martin and co-workers reported the first photoinduced synthesis of heptahelicene. Since then, photocyclization has become one of the most important methods for the synthesis of many helicene homologues (from [5]- to [14]helicene) and derivatives, because the stilbene-type precursors are easily prepared by Wittig olefination and the helicenes can be obtained in relatively few steps. The Mallory photocyclization method allows the preparation of polyaromatic hydrocarbons (PAHs) starting from a stilbene precursor by UV irradiation in the presence of an oxidant, usually I_2 [17].

The mechanism is described in **Scheme 1** and it is the strategy applied by our group for the preparation of helicene. The first step is a light-induced *trans* to *cis* isomerization of the starting stilbene followed by the electrocyclization affording a dihydrophenanthrene. The latter is further oxidized affording the targeted phenanthrene. As the oxidation by I_2 produced HI as a by-product, the presence of dioxygen in the medium is necessary to regenerate the starting oxidant by oxidizing the HI produced in order to reduce the possibilities of undesirable side reactions. These reaction conditions are called catalytic in I_2 as it is regenerated during the reaction. It just requires an initial bubbling of air before starting the irradiation. Anyway, in some cases, the iodine must be introduced in stoichiometric conditions under inert conditions and in the presence of an external acid quencher like propylene oxide or THF to trap the quantity of HI produced [18, 19]. For instance, Katz et al. developed a synthetic strategy using an excess of propylene oxide plus a stoichiometric amount of iodine in an inert atmosphere, which not only enhanced the yields greatly compared with the traditional catalytic conditions for the photocyclization of stilbenes but also prevented photoreductive or photo-oxidative side reactions of the double bonds [20]. In the frame of helicene synthesis, stilbenic precursors are usually synthesized using a Wittig reaction from a phosphonium salt and any substituted benzaldehyde.

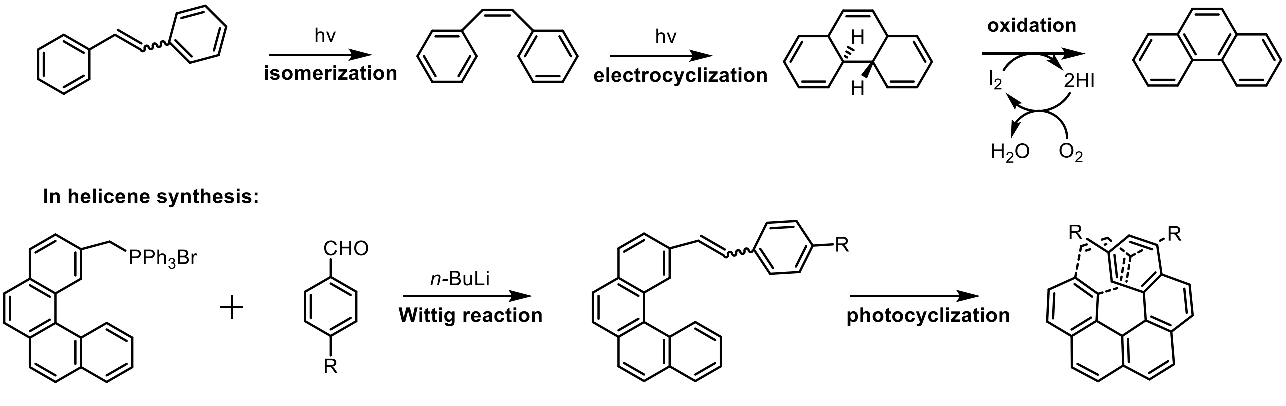

A5

Scheme 1. Mechanism of Mallory photocyclization and application to helicenes synthesis.

Despite its versatility, the facile access to the precursors and the shortening of syntheses, photocyclization methods display some limitations: the photoreaction can take place at either the 2- or the 3-position of the precursor, for example, resulting in isomers which are sometimes difficult to separate and some functional groups like acetyl, amine or nitro groups, are not tolerated in the reaction [21, 22].

Moreover, to avoid the formation of side products like those of the [2+2] intermolecular cycloaddition, highly dilute conditions are required. Thus, some important improvements, for example the continuous flow reactor strategy, have been developed, allowing a proper scale-up of this reaction [23].

Alternative non-photochemical methodologies for the synthesis of helicenes were also investigated. A thermal Diels–Alder reaction of aromatic (bis)vinylethers with *p*-benzoquinone in excess to afford helicenes with terminal quinone moieties was widely explored by Katz and coworkers and followed by Carreño and Urbano [24, 25, 26].

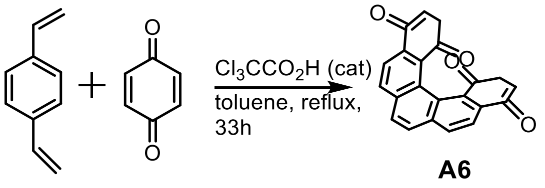

Scheme 2. Example of Diels-Adler type reaction for obtaining helicene embedded with quinones.

More recently, the most complex helicene architectures were obtained by using multiple intramolecular oxidative aromatic coupling (a Scholl reaction or related processes) to form highly laterally extended or condensed multipole helicenes [27, 28, 29, 30].

The range of the non-photochemical synthetic methods for the preparation of helicenes includes as well reactions like the Friedel–Crafts-type cyclization of 1,1-difluoro-1-alkenes [31], or the nucleophilic aromatic substitution reactions employed by Lacour's group to achieve cationic helicene derivatives (**Scheme 3**) [32].

Nucleophic aromatic substitution

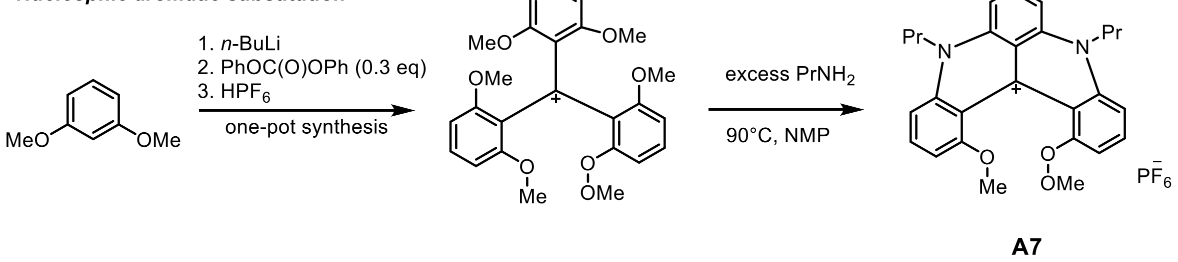

Friedel-Crafts-type cyclization

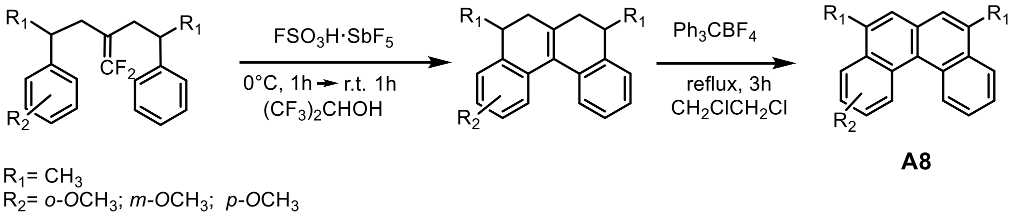

Scheme 3. Synthetic strategy used by Lacour's group starting for triangulenium salts and Friedel-Crafts type cyclizaton followed by aromatization.

One of the most powerful non-photochemical pathway for the preparation of helicenes is the [2+2+2] cycloisomerization, due to moderate to high yields, good functional group tolerance, and the ability to prepare longer helicenes [33].
The methodology was introduced to the synthesis of helicenes by Stara, Starý et al. in 1998 [34] and it takes advantage of the previous fundamental achievements of Vollhardt [35] who discovered the considerable synthetic potential of transition-metal-catalyzed [2 + 2 + 2] alkyne cycloisomerization.
In contrast to other synthetic methodologies for the preparation of helicenes, the intra/intermolecular [2 + 2 + 2] cycloisomerization of π-electron systems leads to the closure of three cycles of the helicene backbone in a single synthetic operation. Since a multiple cyclization of this type is also feasible, the helicene backbone can grow rapidly.

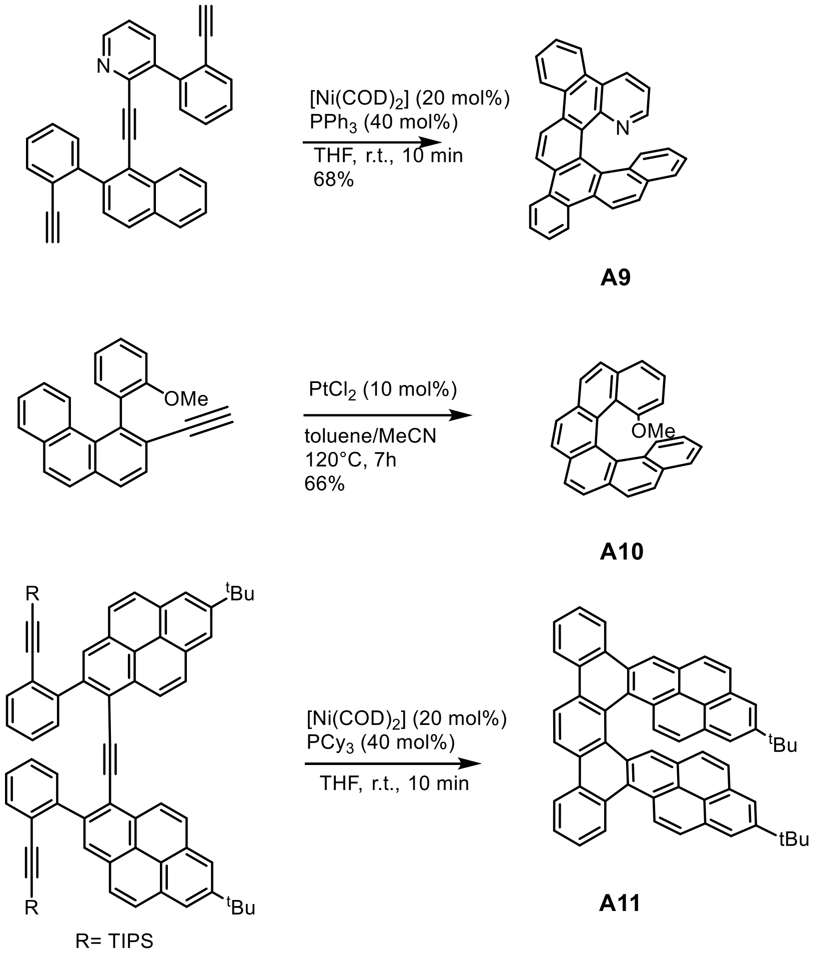

Scheme 4. Examples of cycloisomerization reactions in helicene chemistry

After this discovery, they exploited the approach to synthesize and functionalize tetrahydrohelicenes and helicenes with 64-72% yields and more complex structures like chiral nanographenes. It is the case of the cycloisomerization of dipyrenyl-derived triynes, where the pyrene units were incorporated into [7]helicene (**A11** in **Scheme 4**) or oxa[7]helicene scaffolds [36]. However, the main disadvantage of this method is that triynes require long linear syntheses.

I.2.2. Racemization barrier and configurational stability

The configurational stability of an enantiopure helicene is significantly influenced by its structural characteristics, including the number of rings and substituents. It is imperative that helicenes do not undergo racemization, especially if designed as chiral entities for those applications, such as enantioselective catalysis or spintronic devices or as chiral luminescent materials.

Hence, investigating the racemization tendency of synthesized helicenes is significant.

In the case of carbo[4]helicene, its lack of configurational stability arises from the minimal steric hindrance between its terminal rings. As a result, unless substituted at inner positions like in **A7**, isolating either the *P* or *M* enantiomer is not feasible, as they rapidly interconvert through helix inversion, even at lower temperatures. In contrast, longer [n]helicenes (where n ≥ 5) exhibit enhanced steric hindrance, enabling the isolation of either the *P* or *M* helix even at room temperature.

The earliest observation of racemization was made by Newman and colleagues concerning carbo[6]helicene **A3.** During melting point measurements, they noted partial racemization after heating the enantiopure sample at 250°C [8].

After this study, Martin and Merchant examined the racemization barrier of carbo[7]helicene **A4**, calculating it as ΔG_{rac} = 37 kcal/mol at 205°C and 36.2 kcal/mol at room temperature. These calculations suggest that the racemization process is largely negligible at room temperature [37].

Various investigations conducted on the racemization of different types of helicenes ascertain that longer helicenes generally exhibit higher racemization barriers. Furthermore, the presence of substituents strategically placed to hinder the inversion, such as positions 1 or 14 within a [5]helicene, effectively increases the racemization barrier. Notably, the increase in barrier strength is not linearly proportional to the number of rings *n* in the helicene structure: it is worth stressing that the racemization barrier for 1-methyl[5]helicene exceeds that of [6]helicene, highlighting the pivotal role of steric hindrance in preventing helix inversion (**Table 1**).

Table 1. Values of the experimental Gibbs energy of racemization at the indicated temperature (in Kelvin).

Compound	ΔG_{rac} (kcal/mol) (T in K) [38]
[5]helicene	24.1 (300)
[6]helicene	36.2 (300)
[7]helicene	41.7 (300)
1-methyl-[5]helicene	38.6 (473)
1-methyl-[6]helicene	43.8 (542)

I.2.3. Examples of resolution

When a helicene is configurationally stable, it is possible to isolate its *P* and its *M* enantiomers. In early research, recrystallization in the presence of a chiral reagent and crystal picking were the principal methods employed for the resolution of helicene. The first resolution was realized by Newman *et al.* on the carbo[6]helicene using a chiral resolving agent, *R*- or *S*-2-(2,4,5,7-tetranitro-9-fluorenylideneaminooxy)-propanoic acid (**TAPA**) that can form charge transfer complexes by π-π interactions with the [6]helicene thus affording diastereomeric pairs separable by selective crystallization (**Figure 6**) [8].

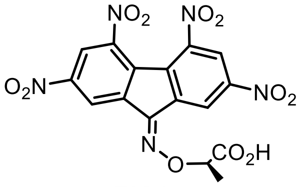

TAPA

Figure 6. Structure of the TAPA derivatizing agent.

A second approach consists in the use of a chiral auxiliary that reacts on the helicene skeleton to afford a pair of diastereoisomers readily separable by conventional silica gel chromatography.

Subsequent removal of the auxiliary produces the two enantiopure isolated *P* and *M* helicenes. A straightforward example of this methodology was published in 2005 by Lacour's group who used (+)-(R_S)-methyl-*p*-tolylsulfoxide as a chiral resolving agent for the preparation of enantiopure [4]heterohelicenium **A7**. It should be noted that, despite being a [4]helicene, it is configurationally stable due to the two methoxy groups located inside the helix (**Scheme 5**) [39].

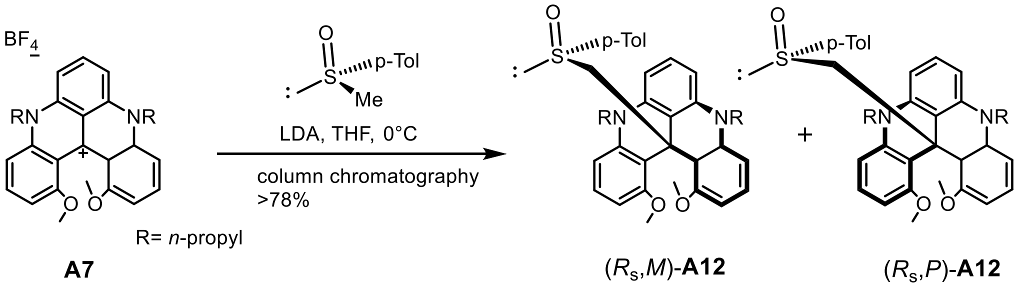

Scheme 5. Example of resolution of a helicene employing a chiral auxiliary adopted by Lacour.

Finally, a third approach requires the use of semi-preparative HPLC with a chiral stationary phase to separate the two enantiomers of a configurationally stable helicene.

This method is based on the selective affinity of one enantiomer over the other for the stationary phase which results in different retention times on the column. Elution would then afford the isolated enantiopure helicenes. The first report of this method was made by Klemm and Reed who used a TAPA impregnated stationary phase for the partial resolution of the carbo[5]helicene [44].

This method is usually chosen by our group to obtain enantioenriched helicenes, in collaboration with Dr. Nicolas Vanthuyne (Chirosciences, Aix-Marseille University).

I.2.4. Examples of asymmetric synthesis

The asymmetric synthesis of helicenes was reported as early as 1970s, when Kagan, Celvin, and co-workers used circularly polarized light to induce the helicity, where the reaction produced helicenes with a low specific rotation value [40, 41, 42].

Since then, chemists have been trying to find practical methods for the direct synthesis of optically pure helicenes. The first enantioselective synthesis was reported in 1999 by two papers. Starý, Stará, and co-workers described a route to asymmetric synthesis of helicene via a Ni-mediated [2+2+2] cycloisomerization of triynes with up to 48% ee [43] while Carreño, Urbano, and co-workers used an enantiopure (S_S)-tolylsulfinylquinone as a traceless auxiliary for the synthesis of **A6** by Diels-Alder reaction. After the reaction and pyrolytic removal of the sulfoxide group, the *M* enantiomer was obtained in 80% *ee* (**Scheme 6**) [44].

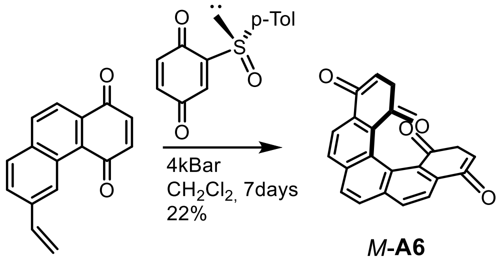

Scheme 6. Enantioselective synthesis of a helicene-bisquinone using a chiral sulfoxide.

Similarly, enantioselective methods to synthesize optically active helicenes using cycloisomerization of alkyne-substituted biaryls were also developed notably by Alcarazo and co-workers who reported recently the use of TADDOL-based chiral gold(I)phosphonite catalyst for the synthesis of non-racemic [6]helicenes with high enantioselectivity, together with Stary, Stara *et al.* who used ([Ni(COD)$_2$]/*R*$_a$-QUINAP) (**Scheme 7**) [45, 46, 33].

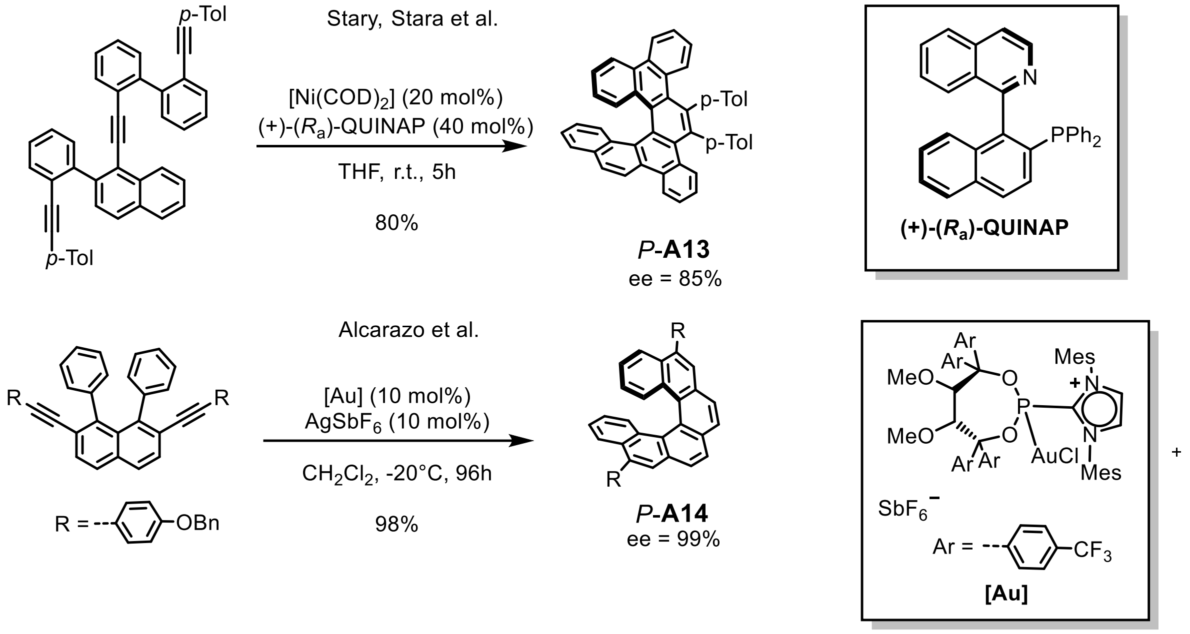

Scheme 7. Examples of asymmetric cycloisomerization reactions leading to enantiopure helicenes.

Moreover Collins *et al.* achieved the preparation of the [7]helicene through olefin metathesis in 80% *ee* using a chiral derivative of the known Grubbs 2nd generation ruthenium(II) catalyst [47].

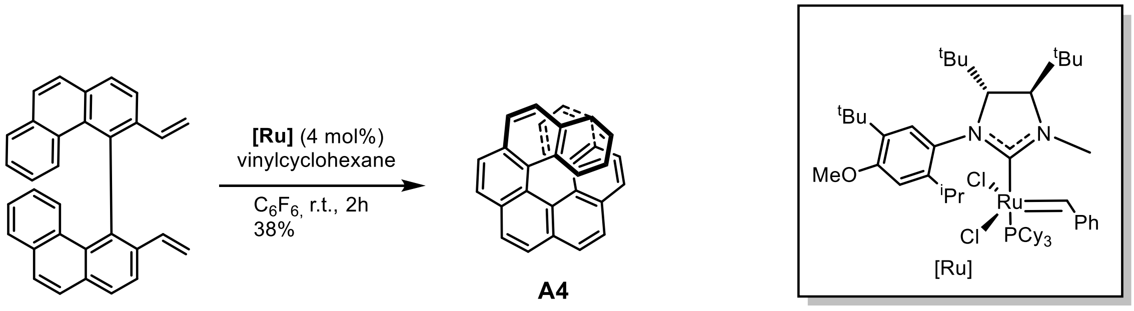

Scheme 8. Olefin metathesis using a Ru catalyst used by Collins et al.

II. Chiroptical properties

II.1. Optical rotation

Chiral objects interact with polarized light [1]. When a beam of planarly polarized light travels through a chiral sample, it will exit with its plane of polarization that has rotated with an angle α called the optical rotation due to circular birefringence. By convention, if an observer views the light coming in its eye with the plane of polarization that has turned in a clockwise sense, then α is positive and the chiral object is dextrorotatory. In contrary, the plane of polarization has turned in an anticlockwise sense, α is negative and the compound is levorotatory.

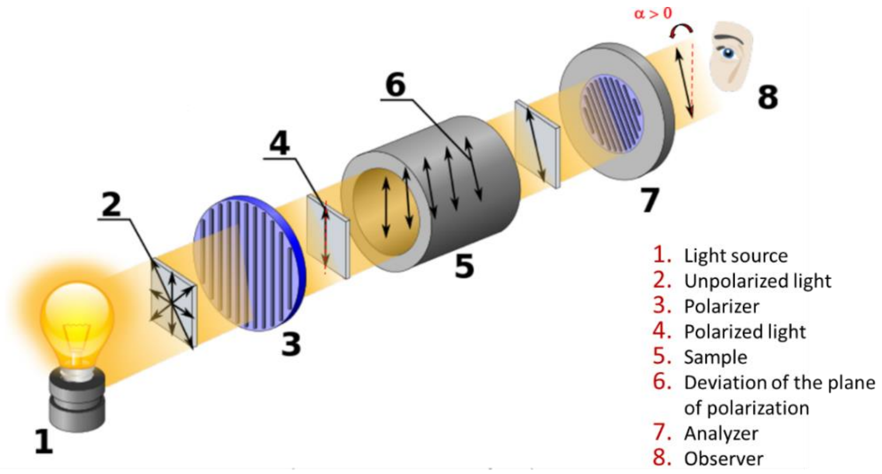

Figure 7. Schematic illustration of a polarimeter.

The measurement of α is conducted using a polarimeter and a light beam with a fixed wavelength, frequently the sodium D line (with λ = 589 nm). The specific rotation $[\alpha]_D^T$ of a chiral substance is then determined employing the expression below, at a given temperature (T), and wavelength (denoted as D, representing 589 nm):

$$[\alpha]_D^T = \frac{\alpha}{c \times l}$$

Here, α stands for the measured optical rotation in degrees, c represents the concentration in g/cm³, l indicates the path length of the cell used for measurement in decimetres (dm).
Additionally, the molar rotation $[\varphi]_D^T$ is defined in relation to specific rotation:

$$[\varphi]_D^T = [\alpha]_D^T \times \frac{MW}{100}$$

MW is the molecular weight of the chiral molecule in grams per mole (g/mol).
Since $[\varphi]_D^T$ is not dependent on the mass of the compounds, this property facilitates the comparison of optical activities between molecules possessing varying molecular weights.

Due to their inherent helical shape, helicenes have high specific (expressed in 10^{-1} deg.cm^2.g^{-1}) and high molar rotations (expressed in 10^{-3} deg.cm^2.mol^{-1}). **Table 2** provides some values measured for some representative helicenes, in comparison to tartaric acid.

Table 2. Values of specific rotation (with molar concentration in parenthesis) and molar rotations of selected [n]helicenes.

Compound	**$[\alpha]_D^{25}$(solvent, concentration) (10^{-1} deg.cm^2.g^{-1})**	**$[\varphi]_D^{25}$ (10^{-1} deg.cm^2.g^{-1})**	**Molecular Weight (g.mol^{-1})**
P-[6]helicene	+3640 ($CHCl_3$, not precised)	+11900	328
P-[6]helicene	+ 5900 ($CHCl_3$, 6.0×10^{-2} M)	+22300	378
P-[6]helicene	+7170 ($CHCl_3$, 4.3×10^{-2} M)	+30600	428
P-[6]helicene	+8100 ($CHCl_3$, 6.1×10^{-2} M)	+38700	478
(+)-tartaric acid	+14 (H_2O, 3.6×10^{-2} M)	+22	148

The association of a specific configuration- *R/S* for instance- with a physical label, allowing the distinction of the two enantiomers, defines the absolute configuration.
[configuration] + [physical label] = [absolute configuration]
The physical label can have different natures. The most common usage involves using the sign of the optical rotation, described above [48].

II.2. Electronic Circular Dichroism ECD

Circular dichroism, or simply CD, can be defined as the difference between the absorption of left and right circularly polarized lights [49]. CD represents one of the most powerful techniques for stereochemical analysis: it is sensitive to the absolute configuration as well as to conformational features, which are often completely hidden in the ordinary absorption spectrum.

Following this definition, it can be expressed as:

$$CD = \Delta A = A_L - A_R$$

Where A_L and A_R are the absorptions of left and right circularly polarized light, respectively. For historical reasons, the output of CD instruments is usually measured as ellipticity θ (in mdeg), related to CD through θ(mdeg) = 33000 CD.

In analogy to the Beer-Lambert law, it can be defined also as a molar quantity:

$$\Delta\varepsilon = \varepsilon_L - \varepsilon_R = \frac{\Delta A}{c \times l}$$

Where ε_L and ε_R denote the molar extinction coefficients for left and right circularly polarized light, respectively, *c* the concentration of the sample and *l* the pathway. This definition of the circular dichroism points out that CD can be measured only at the absorption bands. As non-polarized absorptions, Δε depends on λ and the CD spectrum of the considered chiral compound can be obtained by plotting the former against the wavelength in a graph. Two pure enantiomers should display mirror-image spectra

Additionally, the magnitude of the circular dichroism can be evaluated through the absorptive dissymmetry factor (or anisotropy factor) g_{abs}, calculated from the ratio of the circular dichroism of the compound over its molar absorptivity (related to its absorption of unpolarized light) at the wavelength λ:

$$g_{abs} = \frac{\Delta\varepsilon_{(\lambda)}}{\varepsilon_{(\lambda)}}$$

For each electronic transition one can define an electric $\vec{\mu}$ and a magnetic $\vec{m}$ transition dipole, which are correlated to the electron density redistribution taking place during the transition. Very often, when it is not vanishing for symmetry reasons, the electric dipole term is very much larger than the magnetic dipole. So that for unpolarized allowed and forbidden electric-dipole transitions can be distinguished.

In the context of chiroptical spectroscopy, both transition dipole moments play a critical role. The simplest chiral electronic displacement which can give rise to CD is along a helical path, which implies a simultaneous translation and rotation of charge, that is a transition with $\vec{\mu} \neq 0$ and $\vec{m} \neq 0$ and for which the two vectors are not orthogonal. Hence, the intensity of the CD band is proportional to the scalar product of these two dipole moments, defined as rotational strength:

$$R_{ij} = \overrightarrow{\mu_{ij}} \cdot \overrightarrow{m_{ij}}$$

where i and j are the initial and final states, respectively.

Evaluation of R_{ij} and its sign is the basis for non-empirical interpretation of CD spectra and configurational assignments.

Like for the optical rotation, helicenes show an intense activity in electronic circular dichroism. Historically, the first CD spectra of a helicene was measured by Newman *et al.* for the carbo[6]helicene [50]. The spectrum displays two characteristic structured bands of opposite signs (**Figure 8**): a negative one at about 250 nm (for the *P*, Δε= - 200 to -100 $M^{-1}cm^{-1}$) and a positive one around 330 nm (for the ***P***, Δε= +100 to +200 $M^{-1}cm^{-1}$) with the *M* enantiomer having the mirror-image spectra. However, the longer the [*n*]helicene is, the more red-shifted the bands, thanks to the extension of the conjugation [51].

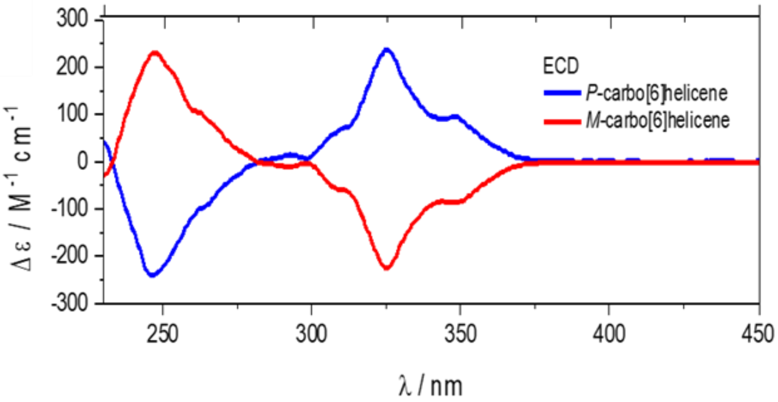

Figure 84. CD spectrum of carbo[6]helicene.

- **Exciton Coupling chirality**

With the aim of elucidating some results that will be presented throughout this manuscript, it is worth to illustrate a specific phenomenon related to the circular dichroism, that is the Exciton Coupling.

When two (or more) chromophores are in close special proximity and have a proper (chiral) mutual orientation, the interactions between their transition dipoles is responsible for large rotational strengths. Among various possibilities of mixing between electric- and magnetic-dipole allowed transitions, the most significant case arises when chromophores with strong electric-dipole allowed transitions like π-π* transitions couple with each other.

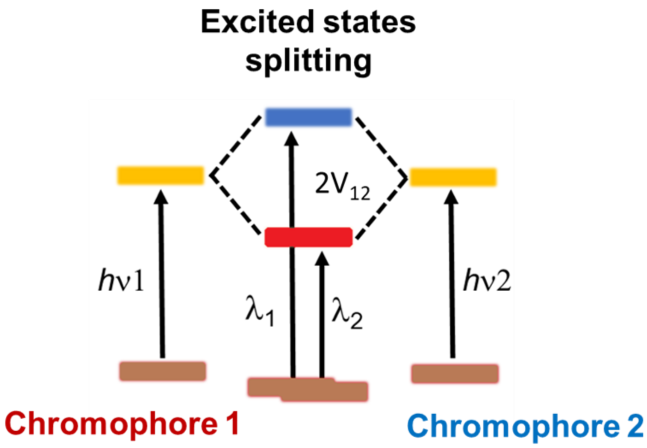

Figure 9. Splitting of the excited states of two degenerate exciton-coupled chromophores linked by a chiral spacer. Adapted from [54].

As a consequence of the coupling between two chromophores, the two otherwise degenerate excited states split into two levels separated by a quantity called Davydov splitting, while the ground state remains unsplit. The potential V_{12} for the interaction between electric transition dipoles can be defined as

$$V_{12} = \frac{\mu_1\mu_2}{r_{12}}\,[(\overrightarrow{e_1}\cdot\overrightarrow{e_2}) - 3(\overrightarrow{e_1}\cdot\overrightarrow{e_{12}})(\overrightarrow{e_2}\cdot\overrightarrow{e_{12}})]$$

Where μ_1 and μ_2 and r_{12} are the intensities and mutual distance of the two transition dipoles, while $\vec{e}$ are the corresponding unit vectors.

This splitting of excited states gives rise to a particular bisignate circular dichroism couplet, centerd around the wavelength transition of the isolated chromophore (**Figure 10**).

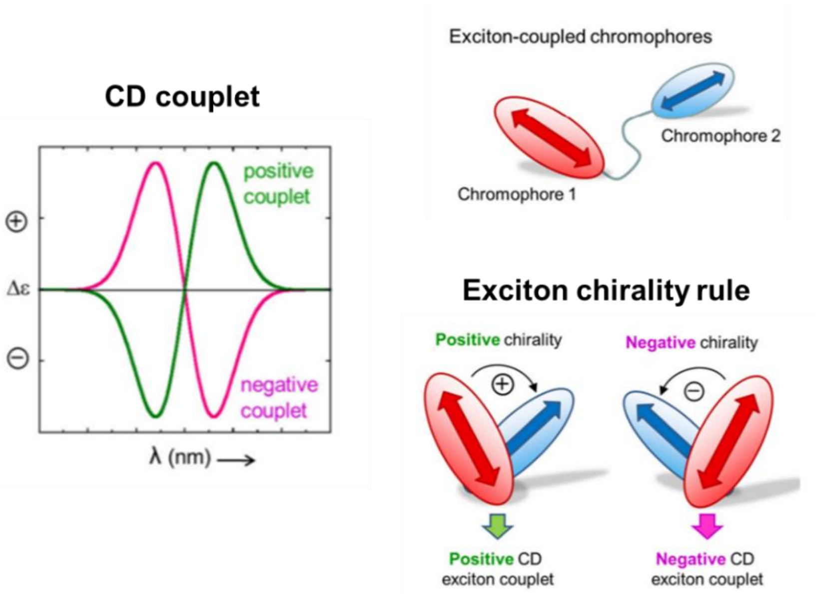

Figure 10. Exciton chirality rule represented through the transition dipole moments.

If the two coupling transitions are the same, such as for two identical chromophores, exciton coupling is said to be degenerate and the couplet crossover point occurs in correspondence of the chromophore UV maxima. Otherwise, for energetically separated transitions, one will observe two separated CD bands, each of which corresponds to one UV maximum [52]; in this case, nondegenerate exciton coupling occurs, as shown by Nakanishi and Weisler through different polyols bearing anthroate and cinnamate units: their interaction gives rise to two Cotton effects at two different wavelengths[53].

The CD couplet intensity is directly proportional to the dipole strength and inversely proportional to the square of the interchromophoric distance. Indeed, strongly absorbing chromophores in close special proximity and close in energy are expected to give rise to very intense CD couplets.

The sign of exciton chirality reflects the mutual arrangement of the transition dipole moments and it can be evaluated in the following way. If the long axes of the two interacting chromophores have a clockwise screw sense, the CD shows a positive first Cotton effect at longer wavelength; if they have a counterclockwise screw sense, a negative first Cotton effect at longer wavelength and a positive second Cotton effect at shorter wavelength are observed[54].

It is called the *Exciton Chirality rule*. A positive couplet signifies that the two transition dipole moments define a positive chirality, corresponding to clockwise rotation to move from the dipole in the front to that in the back and *vice versa*. A negative couplet signifies that the two transition dipole moments describe a negative chirality. Therefore, the chirality defined by the transition dipole moments is a consequence of both the absolute configuration of the molecule and the molecular conformation. Therefore the Exciton Chirality method is considered to be a suitable tool for the assignment of the absolute configuration of natural products and other compounds, as widely explored in the literature since several decades [55].

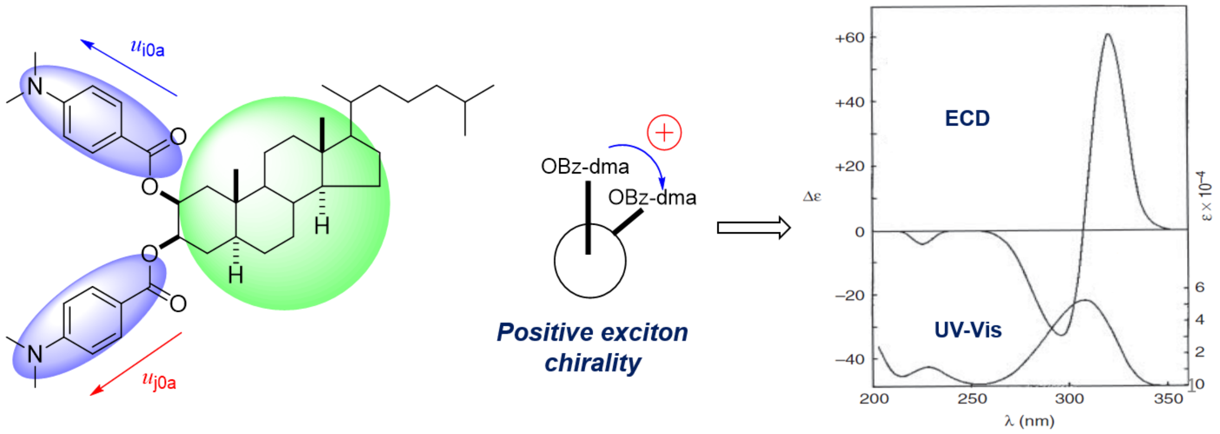

Figure 11. Bis(p-dimethylaminobenzoate) used as example for the Exciton Chirality rule.

Figure 11 shows the UV and CD spectra of bis(*p*-dimethylaminobenzoate), which has an intense π-$\pi*$ transition (λ_{max} 307 nm, ε 54300) polarized along the long axis of the chromophore. Qualitatively, the Newman projection allows the determination of the type of helicity between the two axes formed by the chromophores present, thereby providing an idea about the type of chirality (positive or negative) based on the direction of rotation of the electric transitions. In this specific case, we have a clockwise rotation so a positive chirality.

The CD spectrum shows a first positive and a second negative Cotton effect, that is consistent with the previous consideration and a positive chirality.

Our group investigated in depth the role of helicenes in exciton coupling and the influence on the chiroptical properties of the system. In 2017, the synthesis and chiroptical properties of π-conjugated diketopyrrolopyrrole (DPP)-helicene derivatives were reported, highlighting the role of helicenes for efficient exciton coupling between achiral organic DPP dyes [56].

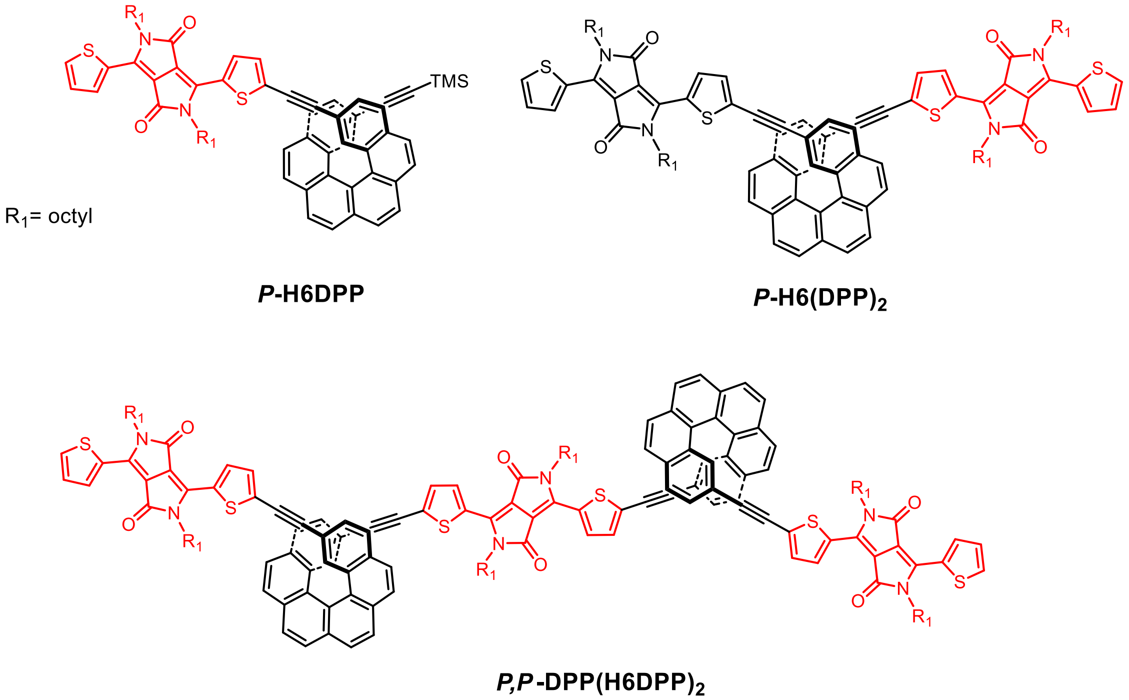

***P*-H6DPP**

***P*-H6(DPP)$_2$**

***P,P*-DPP(H6DPP)$_2$**

Figure 12.. Structure of DPP-helicene conjugates.

The functionalization of helicene with one or two DPP units via an alkyne bridge induced a significant modification of its CD spectrum. For instance, the compound *P*-**H6DPP** exhibits a broad positive band ranging from 320 nm to 440 nm ($\Delta\varepsilon$ = +88 M^{-1} cm^{-1} at 400 nm) (**Figure 13**). Additionally, a very weak signal can be detected at 580 nm with $\Delta\varepsilon$ = +5 M^{-1} cm^{-1}. In the ECD spectrum of *P*-**H6(DPP)₂**, a remarkable similarity can be observed compared to the compound *P*-**H6DPP**, with a slight red shift in the lower part of the spectrum below 500 nm.

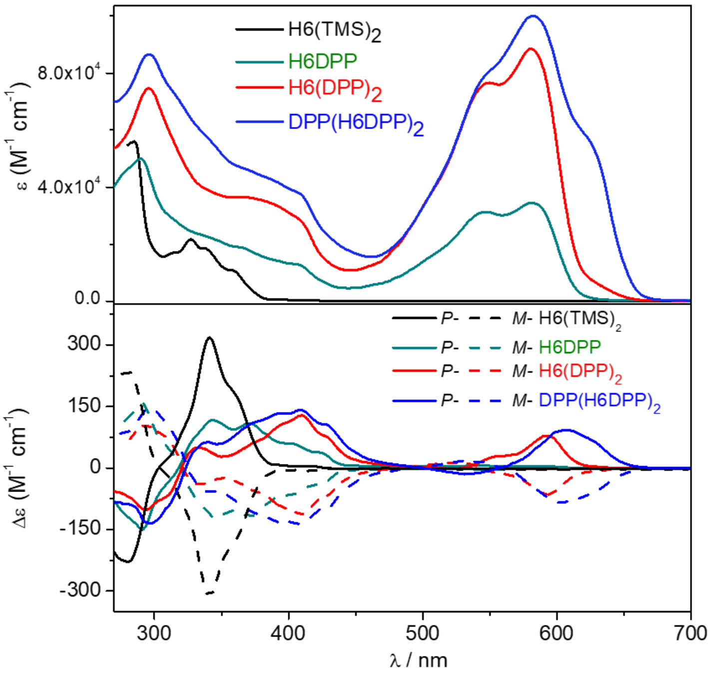

Figure 53. Absorption (top) and ECD (bottom) spectra of the four derivatives. The EC couplet is centred around 550 nm.

Furthermore, the dissymmetry factor is six times larger in the case of *P*-**H6(DPP)₂** (g_{abs} = $\Delta\varepsilon/\varepsilon$ = +9.0 × 10^{-4}) compared to the simple *P*-**H6DPP** (g_{abs} = $\Delta\varepsilon/\varepsilon$ = +1.5 × 10^{-4}). The presence of a weak negative band at 540 nm ($\Delta\varepsilon$ = -2 M^{-1} cm^{-1}) for the compound **H6(DPP)₂**, the amplification of its CD response in the visible region (> 500 nm), and the weak electronic communication between the DPP units at the helix end have allowed us to propose the hypothesis of excitonic coupling between the π-π* transitions of the DPP-alkyne, that was confirmed by computational investigations. TD-DFT analysis on a truncated system (with *n*-octyl groups replaced by methyl) with a structural optimizations for different rotamers (BP/SV(P)), assigned the lowest-energy (ca. 580 nm) strong band for **H6DPP** and **H6(DPP)₂** to an almost pure (95%) HOMO-to-LUMO π-to-π* transition within DPP.

The calculated **H6(DPP)₂** CD spectrum (**Figure 14**) at low energy is caused by an intense pair of excitations with opposite rotatory strengths at ca. 560 (+) and 545 nm (-). The MO pair contributions to the first excitation are 51% HOMO to-LUMO and 44% HOMO-1-to-LUMO+1 and these orbitals of **H6(DPP)₂** are essentially linear combinations of the DPP substituents' FMOs. They are DPP-centered but also delocalized over the alkynyl bridge and conjugated with the adjacent rings of the helicene. Nevertheless, the DPP-centered π-orbitals are weakly interacting with each other through the helicene, as indicated by a small (0.03 to 0.04 eV) energy splitting between HOMO-1 and HOMO, and between LUMO and LUMO+1, respectively. The large rotatory strengths and the opposite signs of the first two excitations have the same characteristics as an exciton CD couplet.

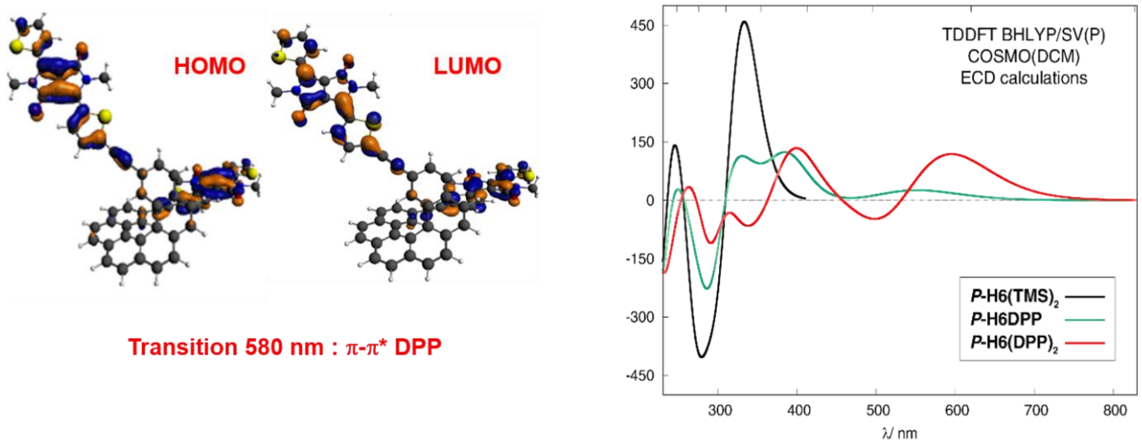

Figure 14. Isosurfaces of frontier MOs for ***H6(DPP)₂*** *(left) and ECD simulated spectra of H6TMS, the mono and disubstituted derivatives*

II.3. Circularly Polarized Luminescence CPL

Circularly polarized luminescence (CPL) spectroscopy measures the intensity difference ($\Delta I = I_L - I_R$) between the left and right circularly polarized spontaneous emission from an intrinsically chiral fluorophore or a fluorophore in a chiral environment. It can be defined as an emission analogue of CD [49, 57].

Plotting the difference in intensity between left (I_L) and right (I_R) circularly polarized luminescence against the wavelength λ gives the CPL spectrum of an enantiomer. Like in ECD, both enantiomers should have mirror-image spectra.

To quantify and evaluate the degree of dissymmetry of CPL of a chiral moiety, the luminescence dissymmetry factor, g_{lum} is calculated as:

$$g_{lum} = 2 \times \frac{I_L - I_R}{I_L + I_R}$$

By definition, the dissymmetry factor is comprised between -2 and +2. In absolute values, a chiral emitter with a dissymmetry factor of 2 or -2 is purely left- or right-circularly polarized luminescent while an emitter with a dissymmetry factor of 0 does not exhibit polarized luminescence. For a given electronic transition, it is theoretically possible to express the g-factor in terms of the rotational strength, R (related to the sign and intensity of the circularly polarized luminescence response associated with this transition), and the dipole strength, D (linked to the total luminescence intensity). The g-factor, in this context, can be defined as follows:

$$g_{lum} \sim \frac{4R}{D}$$

The rotational and dipole strengths of each transition can also be expressed in terms of their magnetic and electric dipole moments, m and μ, giving rise to a new expression:

$$g_{lum} \sim 4\frac{\mu \times m}{|\mu^2 + m^2|}\cos\theta$$

where θ is the angle between the electric and magnetic dipole moments of the considered transition.

Given that magnetic dipole moments are generally much smaller than electric moments (by a factor of ~1000), for transitions allowed according to Laporte's rules ($\Delta l = 1$, transitions commonly found in the majority of organic molecules), one can simplify by approximating the denominator to $|\mu|$.

$$g_{lum} \sim 4\frac{m}{|\mu|}\cos\theta$$

Thus, this value will increase for electronically forbidden but magnetically allowed transitions. This is the case of the Laporte-forbidden f–f transition of lanthanide complexes, which display the highest g_{lum} values [58]. Usually, for organic or organometallic chiral emitters, the g_{lum} is between 10^{-4} and 10^{-2}.

The g_{lum} factor of helicenic derivatives is in the range of organic molecules, precisely around 10^{-4}-10^{-2}. The introduction of heteroatoms, along with assembled and aggregated structures can be a way to achieve high photophysical performances and relatively high g_{lum} factor.

For instance, the functionalization of helicene with chromophores is an efficient tool to increase the chiroptical properties and the CPL response by exploiting the exciton coupling between them.

This is the case of the helicene-diketopyrrolopyrrole systems studied by our group and mentioned in the previous sector. Hence, after the characterization by CD spectroscopy, CPL spectra for each enantiomer of **H6DPP**, **H6(DPP)$_2$** and **DPP(H6DPP)$_2$** were recorded and displayed mirror-image signals corresponding to the emission wavelength of the chromophore, around 600 nm (**Figure 15**). The obtained reliable signals allowed us to determine g_{lum} factors ranging from 1.0×10^{-4} *P*-**H6DPP** to 9.0×10^{-4} for the more conjugated derivative *P*-**DPP(H6DPP)$_2$**. These values follow the same trend as those observed in the ECD spectra with g_{abs}.

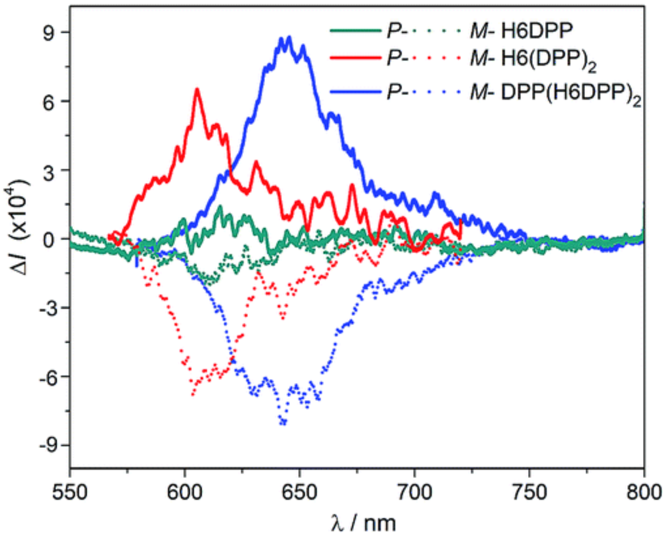

Figure 15. CPL spectra of the series H6DPP.

Table 3. gabs and glum values for the helicene-DPP conjugates.

Compound	g_{abs}	g_{lum}
H6DPP	± 1.5×10^{-4}	± 1×10^{-4}
H6(DPP)$_2$	± 9×10^{-4}	± 6×10^{-4}
DPP(H6DPP)$_2$	± 1.3×10^{-4}	± 9×10^{-4}

This similarity strongly suggests that both ground and emitting excited states have a similar chiral geometry, thus a coupling between the DPP-ethynyl units also in the excited state.

Another exhaustive example reported by our group is represented by extended π-helical push–pull helicene-based emitters (**Figure 16**) [59].

First, a comparison was performed between the carbo[6]helicene and the 2,15-bis-ethynyl derivative. The analysis for the relevant electric and magnetic transition dipole moments for the S1 to S0 emission showed a much higher g_{lum} factor for the bis-ethynyl helicene, owing to an angle of 109.5° between the two transition dipole moments. Moreover, a helicene-mediated exciton coupling involving the ethynyl substituents was present in the emission and contributed to the high CPL intensity. These first findings led to the functionalization of ethynyl groups with electron donor/acceptor units, with the aim of further enhancing the chiroptical response.

These compounds displayed strong ECD and CPL, with g_{lum} values of up to 3×10^{-2}.

Thus, a careful investigation by experimental and computational studies attributed to these push-pull helicene systems an optimized mutual orientation of the electric and magnetic dipoles in the excited state which facilitates an intense exciton coupling process mediated by the [6]helicene.

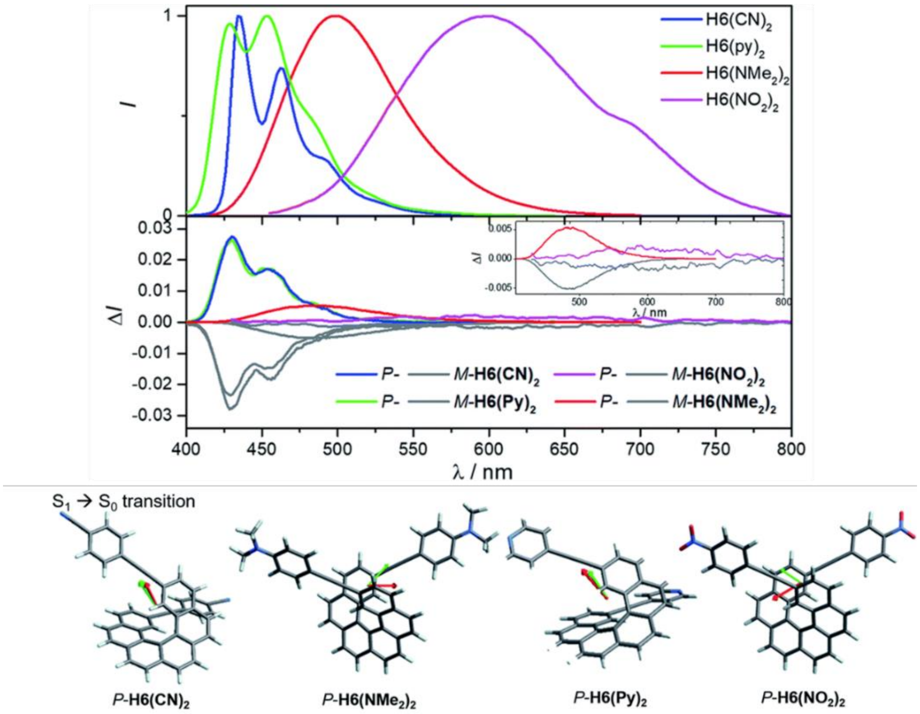

*Figure 16. Normalized luminescence and CPL spectra of P-**H6(CN)$_2$** (blue), P-**H6(Py)$_2$** (green), P-**H6(NMe$_2$)$_2$** (red) and P-**H6(NO$_2$)$_2$** (violet), and their M enantiomers (grey) in CH_2Cl_2 at 298 K; electric (green) and magnetic (red) transition dipole moment vectors.*

It is worth pointing out that to measure accurately measuring a CPL spectrum, both the total luminescence intensity and the intensity difference between left and right circularly polarized emission should be reasonably large, which is a essential difference between CPL and CD spectroscopy. Some additional difficulties in obtaining reliable and reproducible CPL may arise from various instrumental and experimental limitations: the instrumental setup, implying the alignment of light beam against polarizer/depolarizer, the photoelastic modulator, and monochromators should be properly calibrated and adjusted. Moreover, when the emission is too close in wavelength to the absorption (and CD) the observed CPL needs be corrected, because part of the emitted radiation may be reabsorbed by the chiral analyte; photoselection processes may also occur [60].

III. Chiral-induced spin selectivity effect

III.1. Theoretical background

In 1999 Naaman, Waldeck and their collaborators first demonstrated a direct link between chirality and spin [61]. After this work, several experiments showed that the transmission of electrons through chiral molecules is influenced by the orientation of their spins. This phenomenon, known as the Chiral-Induced Spin Selectivity (CISS) effect, presents several challenges but also promising opportunities for spintronic devices.

In the CISS effect, the chirality of the molecules is crucial for spin selectivity to occur. As an electron moves along a chiral molecule, it experiences the molecule's electrostatic potential, that, for a chiral molecule, is chiral per definition (**Figure 17**). The lack of inversion symmetry and the perpendicular electric field component create an "effective magnetic field" aligned with the electron's propagation axis. This magnetic field confines the electron's motion within the diameter of the helical molecule, similar to cyclotron motion which implies a Lorentz force. Mathematically, this magnetic field is represented as:

$$\vec{B} = \frac{\vec{v}}{c^2} \times \overrightarrow{E_{helix}}$$

in which $\vec{v}$ is the velocity of the moving electron, c is the speed of light, and $\overrightarrow{E_{helix}}$ chiral is the electric field acting on the electron while it moves through the chiral molecule. This electric field arises from the electrons and nuclei that constitute the chiral molecule. Because the electron has a magnetic dipole associated with its spin, the two spin states, that are degenerate when no magnetic field exists, are now split. Since chiral molecules has a three-dimensional nature, a component of the magnetic field lies parallel (or antiparallel) to the electron’s velocity direction. Thus the spin direction tends to be parallel or anti-parallel to the velocity and only one spin direction is stabilized, according to the handedness of the chiral molecule.

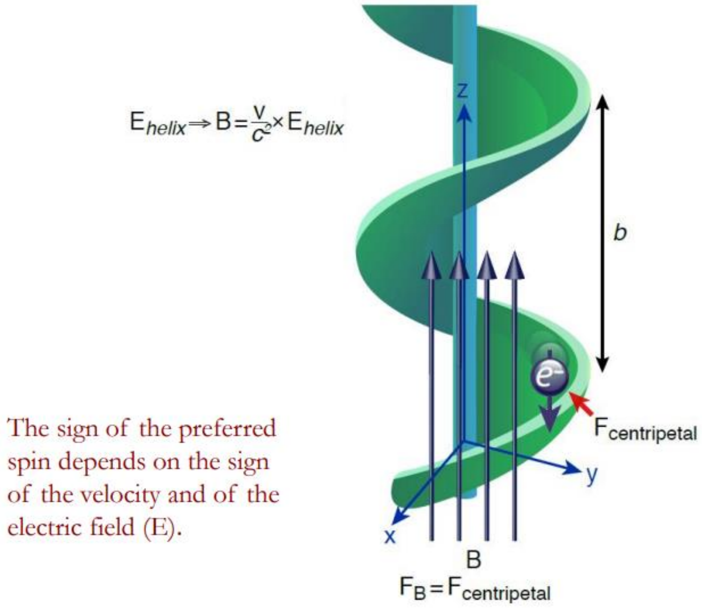

*Figure 17. Schematic description of the electron transmission through a chiral potential of pitch p. The electron is depicted as a sphere, and the arrow indicates its spin. The electron moves within the potential, while a constant force, (**F**centripetal), acts on it in the direction perpendicular to its velocity. This force is like a Lorentz force **F** that results from a magnetic field, **B**, applied along the axis of the molecule. Reproduced from [66].*

Numerous experimental demonstrations of the CISS effect exist, but a unified theoretical description is still lacking [62, 63, 64].

Despite their numerous differences, these studies share similar physical assumptions. In particular, they show that a chiral potential causes a significant coupling between a particle's linear momentum and its spin and it has an important implication for the efficiency of charge transport and the sense of the molecular helix.

To quantify the magnitude of the spin-orbit coupling, the magnetic field acting on the electron propagating along the helical potential axis is considered using the model of cyclotron motion:

$$|B_{eff}| = \frac{mv}{qr}$$

where m, v, and q are the electron's mass, velocity, and charge, respectively, and r is the radius of the helical path of the electron.

If we take the charge $q = 1.6 \times 10^{-19}$ C, the mass m as the rest mass of a free electron ($m = 9 \times 10^{-31}$ kg), take $v = 6 \times 10^5$ m/s, and use r = 0.5 nm, we find that the SOC is given by:

$$H_{SOC} = \frac{g\mu_B}{2}|B_{eff}| = \frac{g\mu_B mv}{2qr} = 390\ meV$$

where μ_B is the Bohr magneton, and g is the g factor for an electron.

By considering these values, this simplified picture yields an H_{SOC} that is large enough to explain the CISS effect [65].

Moreover, the coupling of the electron's linear momentum and its spin has an important implication for the efficiency of charge transport, that is the electron backscattering is suppressed.

Naaman and Waldeck described this phenomenon in a 2012 review as follows:
"the freely propagating electron has four states associated with its motion, which we can denote as |+,+⟩, |−,−⟩, |+,−⟩, and |−,+⟩, where the first variable relates to the direction of motion and the second to the direction of the spin. For an electron moving in the positive (+) direction through a left-handed helix, its up spin (+) is stabilized relative to its down spin (−); that is, |+,+⟩ is the ground state, and the state |+,−⟩ lies at higher energy. Thus, one state is stabilized by the spin−orbit energy, and the other is destabilized by the same energy, so that the difference between the states is twice the value of HSO. Furthermore, the |+,+⟩ state is degenerate with the state |−,−⟩, which corresponds to the electron moving in the opposite direction with the opposite spin. The state |+,−⟩ lying at higher energy is degenerate with the state |−,+⟩. For an electron to be elastically backscattered within a helical molecule, it has to change its state from |+,+⟩ to |−,−⟩, which requires a change in spin as well as momentum, thereby making it unlikely" [66].
This feature makes electron transfer for chiral molecules more efficient than for an achiral one and implies that CISS may be important for understanding electron transfer in biological molecules.

III.2. Measuring the spin selectivity: methods and experimental studies

We can describe the principal methods that can be used to measure spin-selectivity through molecules by dividing them into electron transmission (photoemission), electron transport (mc(p)-AFM and magnetoresistance) methods and electrochemical techniques.

III.2.1. Photoemission

The CISS effect was discovered for photoelectrons transmitted through self-assembled monolayers (SAMs) of chiral molecules [67]. More specifically the first results were obtained from low-energy photoelectron transmission (LEPET) spectroscopy studies of films comprised of amino acids deposited on a polycrystalline gold substrate [61]. The films consisted of either L- or D-stearoyl lysine, and FTIR studies demonstrated that the film's order and geometry were independent of the molecular enantiomer.

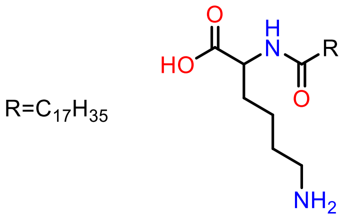

Figure 18. Racemic structure of n-steroyl lysine.

In this LEPET experiment, circularly polarized light was used to eject spin-polarized photoelectrons from the underlying Au substrate and the quantum yield and kinetic energy distribution of the photoelectrons was measured for different molecular assemblies. It was found that the quantum yield of photoelectrons depended on the relative polarization of the light and the chirality of the molecules in the film. For example, right-handed circularly polarized light showed a higher quantum yield of photoelectrons through an L-stearoyl lysine assembly than that through an *R*-stearoyl lysine assembly, even though the film thickness and order were the same. The effect amounts to about a 5−7% difference in the transmission efficiency between the two spins for a given handedness of the monolayer. Following this first study, several other LEPET studies on SAMs of chiral molecules were conducted including SAMs of polyalanine and SAMs of double-stranded DNA [68, 69].

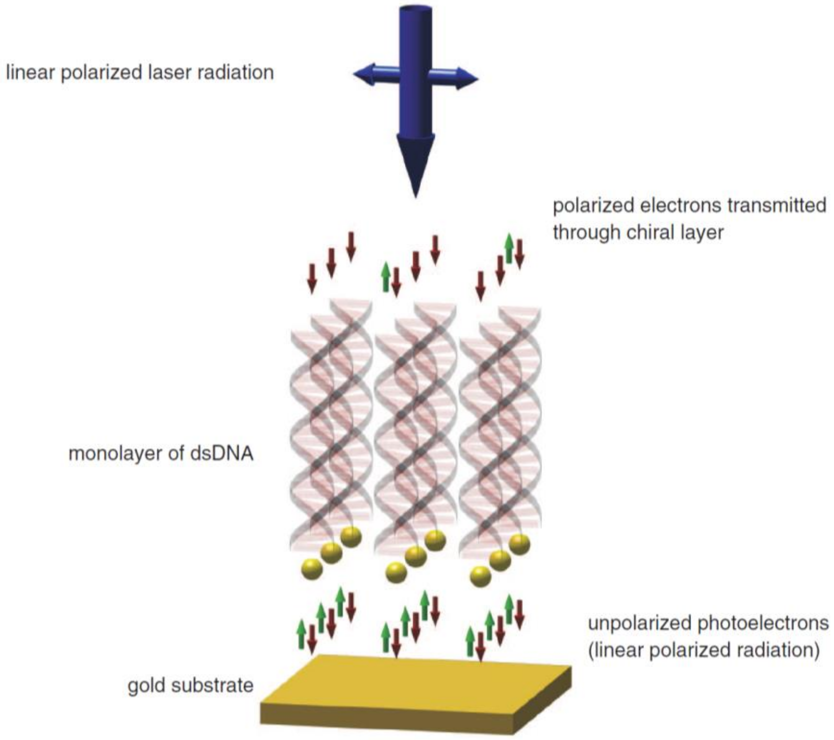

Figure 196. Schematic representation of the photoelectron transmission experiment. Reproduced from [69].

All of these studies confirmed the dependence of the electron transmission yield on the chirality of the molecules and the handedness of the light that was used to eject photoelectrons from the underlying gold substrate.

Another method for measuring spin selectivity in photoelectron transmission is the use of a Mott polarimeter (**Figure 20**) [76]. When the electrons are scattered from gold, which has a large SOC, the resulting angular distribution of the electrons depends on their initial spin as well as their angle of incidence. In the specific experiments aimed at measuring the CISS effect, either a SAM of chiral molecules or a film containing chiral molecules is deposited on a metal substrate, then the photoelectrons are ejected from the substrate by a laser pulse (the photons have enough energy to eject photoelectrons from the substrate but are not energetic enough to ionize the molecules). The photoelectrons are accelerated and guided by an electrostatic lens that changes the electron trajectory by 90◦ and does not change the spin orientation. In this way, an initial longitudinal spin polarization is converted into a transverse one for analysis. These high-energy electrons strike a polarizing element and are scattered at large angles; the spin-orbit interaction causes a left-right spatial scattering asymmetry that reflects the electron distribution of spin orientations. Hence, by having two detectors positioned on opposite sides (above and below) of the surface normal, one can determine the relative magnitudes of the two spin polarizations.

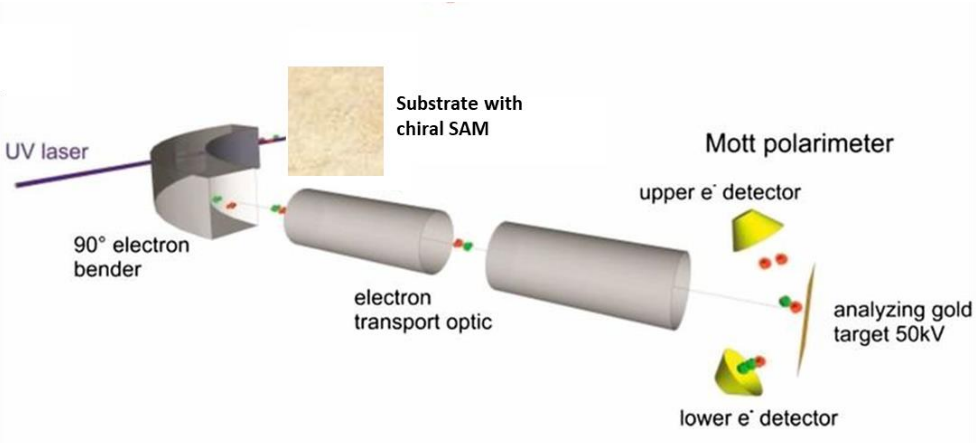

Figure 20. Schematic representation of a Mott polarimeter (modified from ref [71]).

III.2.2. Magnetoresistance

For electron transport the electron spin orientation is quantized relative to the electron's direction of propagation through the molecular structure, and any spin polarization or spin selectivity relates to the spin direction oriented parallel or antiparallel to the propagation direction.

Among the methods used for monitoring CISS effect in electron transport, some of them have been adapted from techniques used in solid-state physics.

As example, magnetoresistance measurement setups have been modified for this purpose (**Figure 21**).

Magnetoresistance is the change in the electrical resistance of a material subjected to an externally-applied magnetic field.

The common device consists of a nonmagnetic film(s) deposited between two ferromagnetic electrodes and the measurement of electrical current through the device as a function of an external magnetic field. In the CISS-based setups a chiral monolayer can be deposited between the two ferromagnetic electrodes [72] or only one magnetic electrode can be used as analyser of the spin conducted by the chiral layer. The magnetoresistance is defined as:

$$MR = \frac{R_H - R_{H=0}}{R_H} \times 100$$

where R_H is the measured infield resistance and $R_{H=0}$ is the zero-field resistance [73].

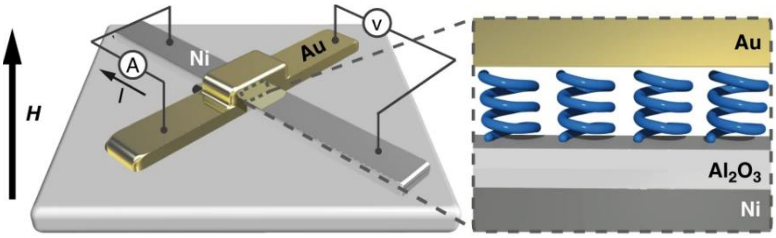

Figure 21. Schematics of an MR device, where H is the magnetic field [74].

III.2.3. Conductive-probe atomic force microscopy (cp-AFM)

Spin-dependent conduction through single molecules has been probed by the conductive-probe atomic force microscopy (cp-AFM) method [75]. **Figure 22** shows a schematic illustration for the measurement. The setup is similar to that typically used to measure conduction with no spin specification, but in this case, the substrate, on which the molecules are adsorbed, is made from a ferromagnetic material (mostly nickel) and an external magnetic field is applied.

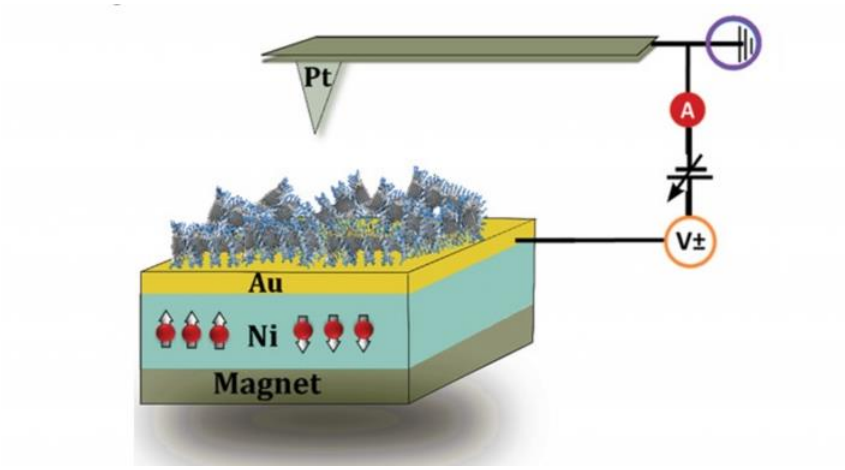

Figure 22. Illustration of a conductive probe AFM setup: the ferromagnetic layer is coated with a gold substrate covered by chiral molecules. The magnet is below this ferromagnetic layer. Adapted from [80].

A conductive AFM tip, operating in contact mode, is used to measure the current versus voltage curves, and it is done for different magnetizations (UP and DOWN) of the ferromagnetic substrate. Magnetization of the substrate breaks the degeneracy of the valence electrons and creates two overlapping conduction bands, one corresponding to electrons whose spins are aligned with the magnetic field (the so-called majority spins) and the other corresponding to spins aligned against the magnetic field.

By averaging the I−V curves obtained from different measurements, it was shown that the molecule's conductance depends on the magnetic field direction. When electrons are ejected out of the magnetized metallic substrate, they are mostly majority electrons (they are aligned with the magnetization direction) and if their spin orientation is consistent with the favoured spin orientation for transmission through the chiral molecule, the current for this magnetic field direction will be higher than the current measured under the situation where the substrate is magnetized in the opposite direction. Note that when the chiral molecule is deposited on a non-magnetic substrate, it is possible to use a magnetic tip and measure SP values by performing magnetic conductive probe AFM (mcp-AFM) measurements. The term cp-AFM is used for AFM using a conductive tip.

The extent of spin polarization from mc(p)-AFM studies is expressed as the ratio of currents with the two different configurations of the magnet (up and down) at a particular voltage $[(I_{up}/I_{down})_V]$ or as percentage of spin polarization $\{[(I_{up} - I_{down})/(I_{up} + I_{down})] \times 100\}$. It is important to appreciate that the dependence of the current on the voltage applied is in the nonlinear regime and hence the measurement is sensitive to the spin selectivity of the conduction.

Several experiments have been conducted using this technique. Among them, an illustrative example is represented by the work of Mishra and collaborators [76], using chiral polymer of poly(phenylacetylene) with a thiol group(-SH) as terminal unit to form a self-assembled monolayer (SAM) on the gold coated substrates (**Figure 23**). The aim is to obtain a specific configuration, where the adsorbed polymer is nearly perpendicular to the substrate plane. Therefore the spin polarization is measured for electrons transferred along the main axis of the polymer, probing the polymer backbone itself as a spin filter.

The SAMs of the polymers were absorbed on a ferromagnetic substrate (Ni coated with Au), an electric potential is varied between the substrate and the grounded Pt tip of the AFM and the current through the SAM is measured as a function of the potential of the magnetic substrate magnetized in the UP or DOWN directions.

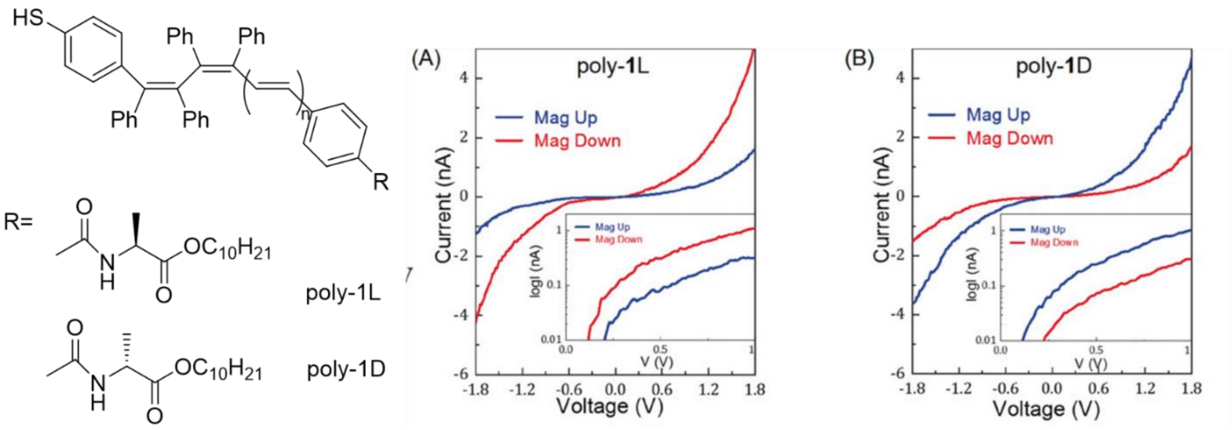

*Figure 23. Structure of the polyphenyl acetylene molecules and the average of the I-V curves for poly-**1**L (A) and poly-**1**D (B).*

The absolute spin polarization was about 50%. It is clear that a different threshold for charge injection is found for the two spins and the spin injected at lower potential depends on the handedness of the polymers. For the poly-1L (**Figure 24A**), the lower spin corresponds to the magnet pointing up.

III.2.4. Spin-dependent electrochemistry (SDE)

Spin-selective electrochemical studies have recently been performed[77]. In this case, a ferromagnetic electrode is used and a monolayer or film of chiral molecules is adsorbed on it. The redox couple can be either present in the solution or attached to the chiral film. In the case of spin-dependent cyclic voltammetry, a very thin film (or a SAM) of chiral molecules is deposited on a magnetic substrate. Thus the current through the adsorbate is monitored as a function of the applied voltage for two different magnetizations of the supporting substrate, which is controlled by applying an external magnetic field using a permanent magnet. The faradaic current through the layer is measured when the ferromagnetic substrate is magnetized so that its magnetic moment is pointing toward the adsorbed film (UP) or away from it (DOWN). In this experimental design, the difference in the current transmitted indicates the spin-selective electron transmission. In principle, the spin polarization, SP, can be obtained from the asymmetry in the current. More insights on this technique are given in **Chapter 4**.

It is worth highlighting two important observations coming from these experiments: the spin polarization is dependent on the length of the chiral film and on the optical activity.

In 2020 Naaman, Saligardi and co-workers carried out an exhaustive work by combining several methods in order to compare the length-dependent spin polarization in double-stranded DNA (dsDNA) oligonucleotides and oligopeptides. More specifically, different lengths of dsDNA oligonucleotides (20, 30, 40, 50 base pairs) and L-oligopeptides containing L-alanine, were attached to a thin gold film-coated Ni electrode via thiol groups and analyzed by conductive-probe AFM (cp-AFM), spin-dependent electrochemistry (SDE), and spin-dependent charge polarization (SDCP) [78]. The voltage was applied between the Pt tip, which was at ground potential, and the magnetic substrate. For both systems, the polarization is amost linearly dependent on the length of the molecules, using the same tip and applied force (**Figure 24**).

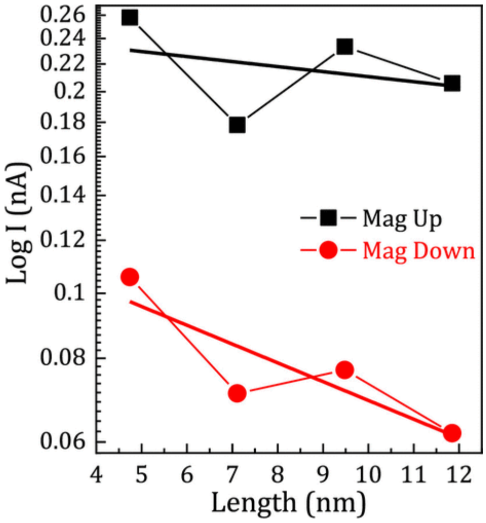

Figure 247. Length dependence for the dsDNA of the current measured for ds-DNA using cp-AFM, for magnet UP (black) and DOWN (red).

The favored spin is transmitted more efficiently as a function of length than the unfavored spin. These results support the notion that due to the coupling between the electron's linear momentum and its spin, the backscattering of the favored spin is reduced. Interestingly, the CD spectra of the molecules displayed a linear relationship between the peak intensities and the sample molecular lengths.

This latter fundamental observation was attested for the first time in 2017 by Waldeck and collaborators on quantum dots capped with D and L-cysteine but it is particularly evident for supramolecular systems [79].

This is the case of the nanofibers with a supramolecular helicity illustrated by Meijer and Namaan in 2020 [80]. These π-conjugated molecular materials were prepared using coronene bis-imide **(S)CBI** and tetra-amidated porphyrin cores appended with either chiral or achiral alkoxyphenyl groups. The supramolecular nanofibers were formed in solution phase and transferred to a gold-coated nickel surface (Au/Ni), which is magnetized with its magnetization perpendicular to the surface with the north pole pointing either up or down for the classical cp-AFM. The surprising difference, in spite the very similar structures, between the 3,4,5-trialkoxyphenyl (*S*)-**CBI-1** derivative with about 50% of spin polarization and the 3,5-dialkoxyphenyl-substituted (*S*)-**CBI-3** (**Figure 25**), showing 90%, led to a different investigation on the optical activity of the systems.

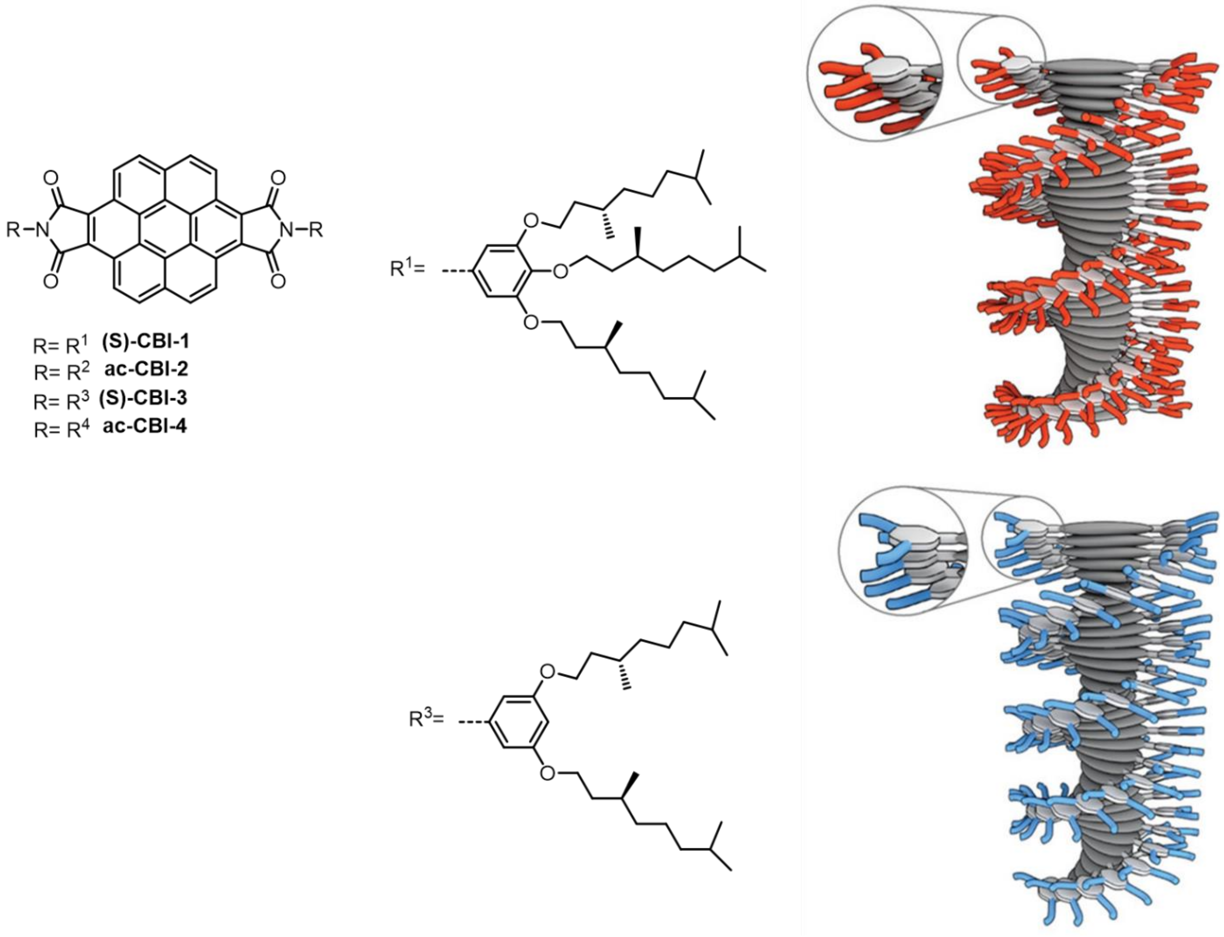

*Figure 25. The chemical structure of the CBI series involved in the comparative study. Schematic representation of the self-assembled nanofibers of P-helicity formed by (S)-**CBI-1** and (S)-**CBI-3** [80].*

Sergeant-and-soldier experiments were performed with the molecule exhibiting higher SP and the analogous achiral derivative using circular dichroism spectroscopy (**Figure 26a**). The molar circular dichroism coefficient (Δε) showed a nonlinear dependence on the fraction of chiral systems in the solution, confirming the chiral amplification in the system. Strikingly, this chiral amplification was also expressed in the spin polarization of electron transport measured via cp-AFM studies, giving the same trend observed in the CD studies **(Figure 26b**).

Thus, they confirmed the strong correlation between the molecular structure of the materials, their chiral supramolecular assembly with the related optical activity and consequently the spin polarization efficiency. The effect of temperature on the helicity inversion was both expressed in the inversion of the CD response and in the CISS effect (**Figures 26c-f**).

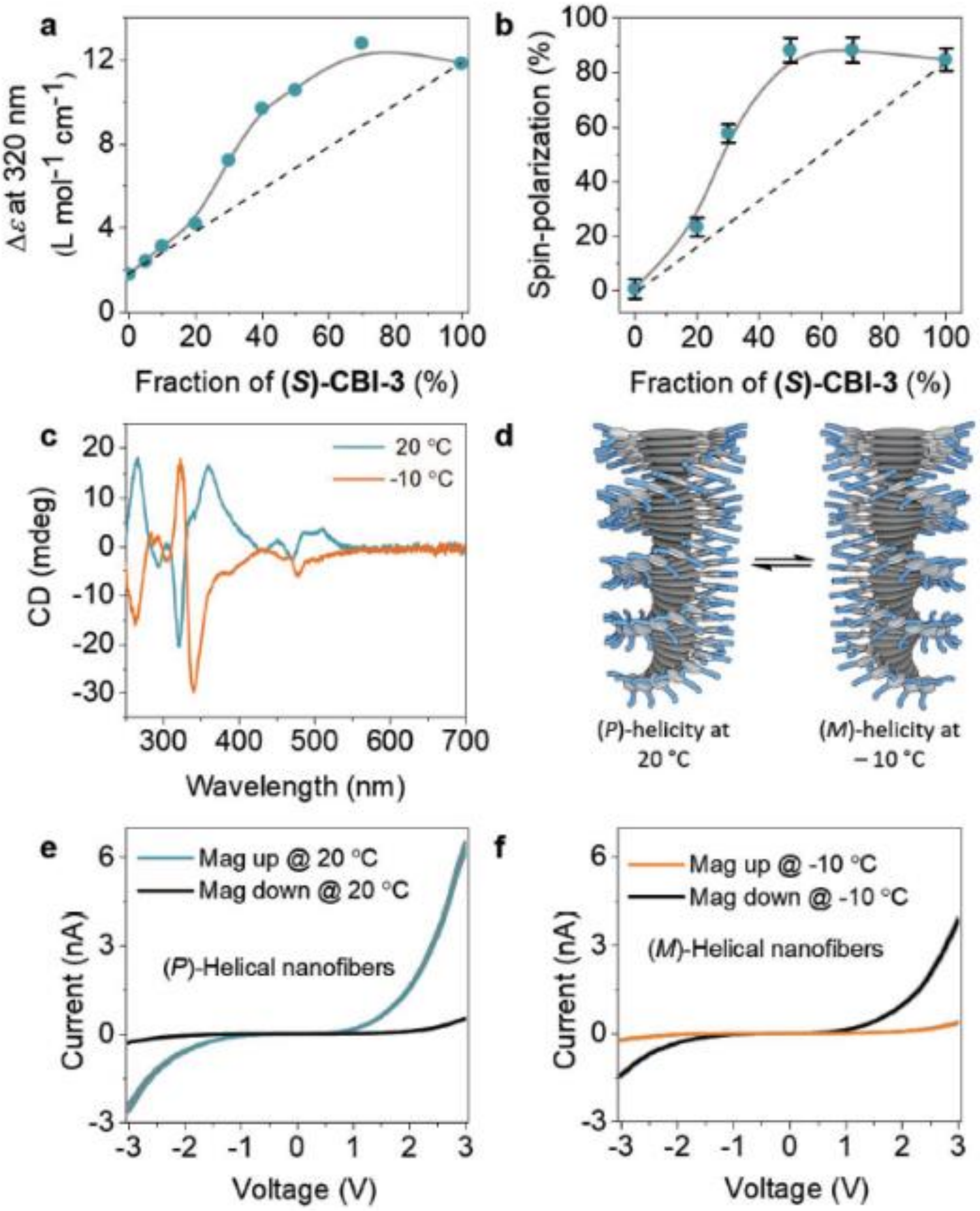

*Figure 26. a) Evolution of the molar circular dichroism (Δε) as a function of fraction of sergeant ((S)-**CBI-3**) in a sergeant and solider experiment involving (S)-**CBI-3** and ac-**CBI-4**; b) Spin polarization at +3 V measured using mc-AFM-based I–V curves at different fractions of (S)-**CBI-3** in nanofibers made from a mixture of (S)-**CBI-3** and ac-**CBI-4**; c) Temperature-dependent CD spectra of (S)-**CBI-3** ($c = 50 \times 10^{-6}$ m in MCH). d) Schematic illustrating the change in helicity of supramolecular nanofibers upon changing the temperature from +20 to −10 °C. e,f) The averaged I–V curves of (S)-**CBI-3** when drop cast on a Au/Ni substrate at +20 and −10 °C.*

The CISS effect was observed in biological systems such as DNA and aminoacids, in supramolecular assemblies and metal-organic frameworks but remarkable results were also achieved for hybrid perovskites and other inorganic systems [81]. The organic ligands and inorganic frameworks provide the sources of chirality and SOC, respectively, and by changing the layers and chemical composition of inorganic metal halides (for example from Pb to the less toxic Sn), the optical and spin selective electronic properties can be adjusted [82, 83].

III.3. CISS effect in helicenes

In 2016, Lacour and Naaman observed CISS effects in self-assembled monolayers (SAMs) of enantiopure cationic [4]helicene derivatives (**A7** derivatives, **Figure 27**) using two different experimental techniques [84].

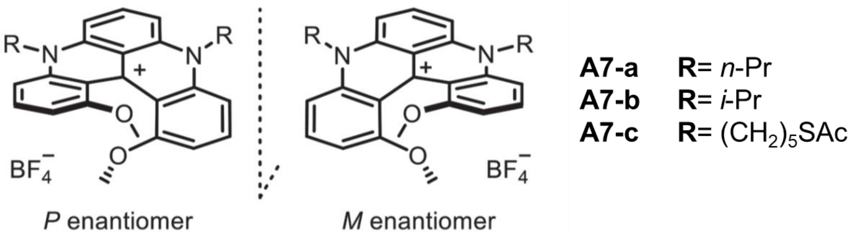

Figure 27. Structures of the helicenic systems studied by Lacour in 2016.

Firstly, the SP was measured by magnetic conductive probe atomic force microscopy (mcp-AFM) on cationic helicenes self-assembled on an HOPG substrate and using a magnetic (Fe-coated Si) tip yielded SP values of 43-49% (**Figure 28**).

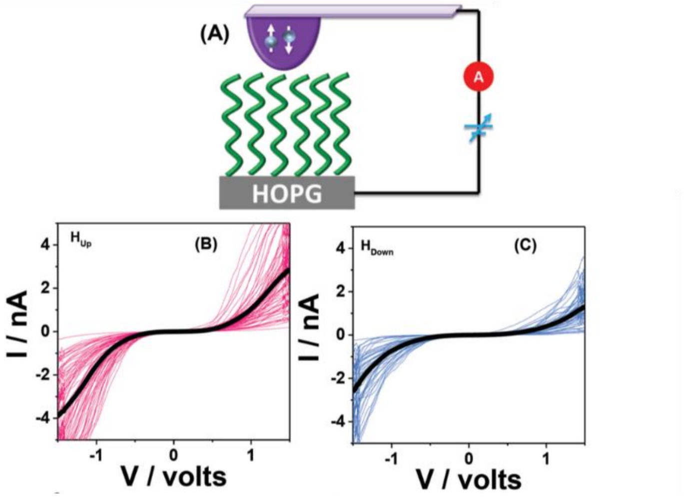

*Figure 28. A) Schematic representation of mCP-AFM measurements performed using Fe (magnetic) tip. (B) and (C) represent I- V curves obtained from various M – **A7-a** helicene junctions when tip is magnetized in UP and DOWN orientations, respectively. Reproduced from [84].*

Secondly, magnetoresistance (MR) measurements were conducted on a SAM formed of thiolated cationic helicenes **A7-c** deposited onto a gold surface that acted as the bottom electrode on which a thin layer of Al_2O_3 was deposited on the top of the helicene film, followed by Ni deposition, so that the Ni acted as the top contact.

More recently, in 2022, the same two techniques were used by our group to observe CISS effects in supramolecular self-assemblies of helicenes obtained from carbo[6]helicene bearing efficient aggregating amide units (**Figures 29**) [85]. The supramolecular assemblies were obtained starting from configurationally stable 2,15-(**H6-a**) and 4,13-bis-ethynyl-carbo[6]helicene (**H6-b**) decorated with two peripheral N-(2-(4-ethynylbenzamido)ethyl)-3,4,5-tridodecyloxybenzamides to favor efficiently the supramolecular interaction by the operation of a fourfold H-bonding array between the amides.

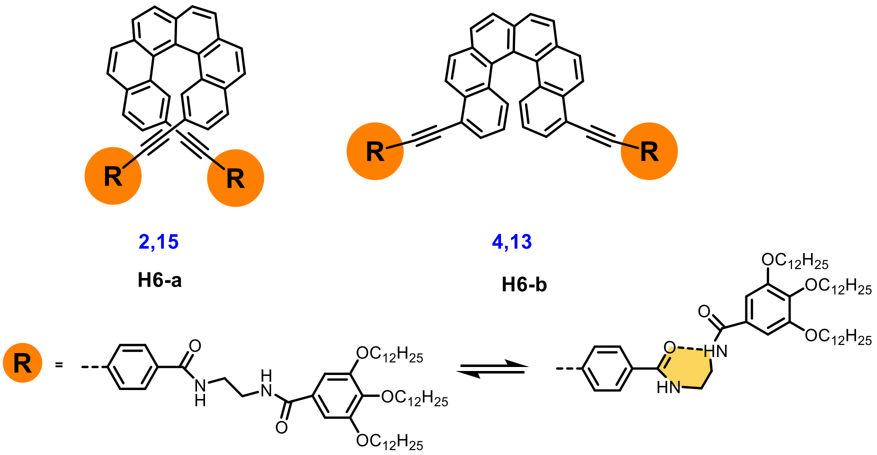

Figure 29. Schematic structures of the derivatives with the amide group.

The supramolecular organization and the chiroptical properties were investigated and displayed interesting differences. [6]Helicene **H6-a** forms globular nanoparticles and [6]helicene **H6-b** shows the presence of well-defined fibrillar aggregates with helical character.

Therefore, mc-AFM measurements were performed on these self-organized layers deposited onto a gold/nickel magnetic surface using a nonmagnetic tip and applying an up- or down-magnetic field (**Figure 31**): these systems revealed particularly high SP values of 60-80% depending on the assembling helical systems. These values are the highest to date in helicene-based systems.

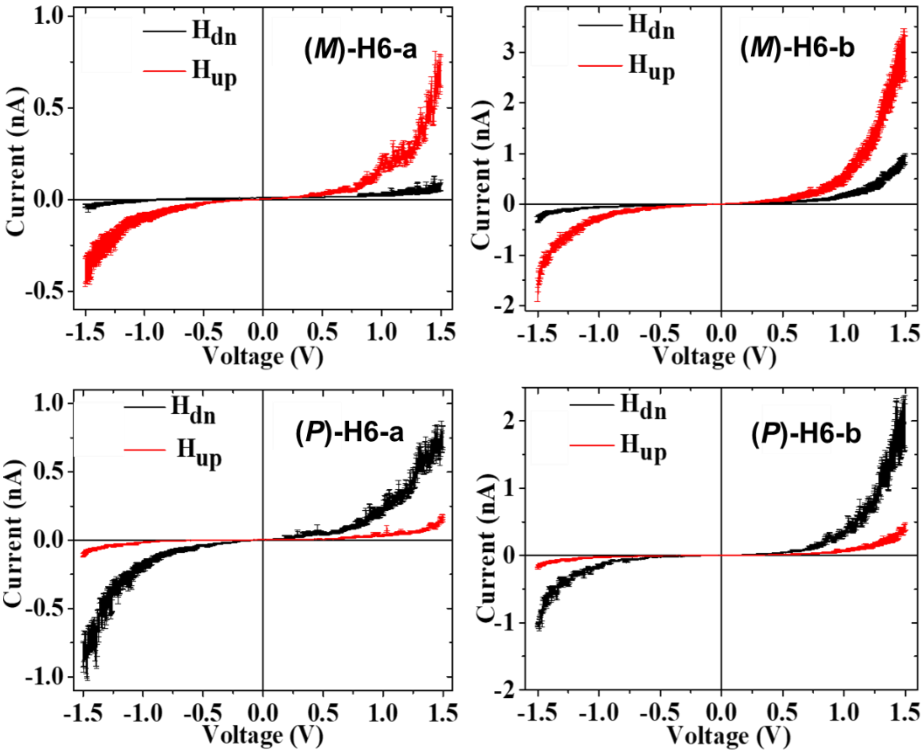

*Figure 8. Averaged current versus voltage (I–V) curves recorded for **H6-a** (left side) and **H6-b** (right side). Reproduced from [85].*

As depicted in the current-voltage curve (**Figure 31**), the sign of the SP is directly related to the stereochemistry of the helical scaffold. Therefore, for the *M* enantiomer, the magnetic field UP systematically induces high current transport while the downfield magnet gives low current. Furthermore, the strong SP value is directly related to the strong circular dichroism measured in helicene derivatives. Magnetoresistance measurements in these helicene assemblies showed modest MR values of 0.4-0.8% at 1 T with again interesting enhancement upon increasing the temperature.

Very recently, remarkable results using these two techniques were obtained by Mannini and co-workers using thioacetyl derivative of thio[4]helicene **HelSAc** [86].

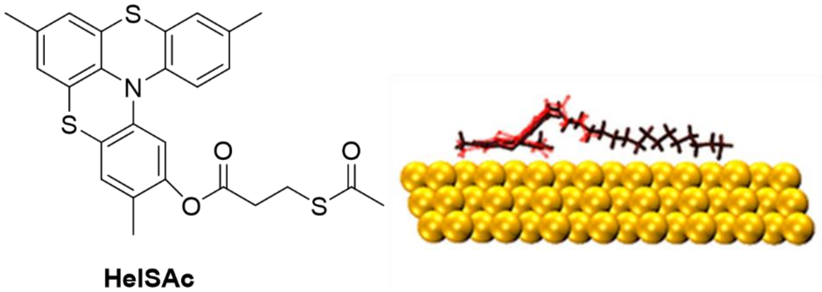

HelSAc

*Figure 9. Structure of **HelSAc** and optimized structure of (P)-**HelSAc** on Au(111) calculated by DFT from a side view. Reproduced from [86].*

The spin-selective transport properties were studied by assembling a molecular-based spintronic device, such as vertical spin valve, constituted by a helicene monolayer on gold and by measuring the magnetoresistance varying magnetic field and temperature. The monolayer was achieved by chemisorption on the gold substrate thanks to the spontaneous deprotection of the thioacetyl group in a dichloromethane solution at room temperature. The inversion of the signal according to the handedness of the helicene was observed, confirming the active role played by molecules in the spin filtering process. Moreover, magnetic conductive-atomic force microscopy (mc-AFM) was employed to measure the SP, showing a value of 60%. Interestingly, this system exhibits a relevant difference in current conduction inside a ±0.3 V range, while for other helicenes it is usually observed at ±1.5-2 V. This current conduction allows high spin polarization at very low potentials.

Another method to account for CISS effect in helicenes is to measure the polarization of electrons scattered through a surface-oriented monolayer. This was applied in 2018 by Ernst and Zacharias to a monolayer of carbo[7]helicenes vacuum-deposited onto a Cu(332) surface [87]. The transmission through *M*- or *P*-[7]helicene yielded longitudinal spin polarization SP_z = 6-8% after transmission of initially balanced left- and right-handed spin polarized electrons of a Mott Polarimeter. Theoretical calculations confirmed the semiclassical picture of electronic transport along a helical pathway under the influence of SOC induced by the electrostatic molecular potential. The spin polarization was also found to be surface-dependent. Indeed, while changing copper to silver then gold substrates which are heavier metals and thus display stronger spin-orbit coupling (SOC), stronger spin polarization was observed for silver and gold. Thus, the total difference in spin polarization induced by the *M*- and *P*-enantiomers was 11.7, 15.9, and 15.7% overall for Cu(332), Ag(110), and Au(111), respectively.

In 2016, Guo and coworkers calculated a SP_Z values up to 25% for the spin-polarized electron transport through molecular junction formed with carbohelicenes with three full helical turns [88]. In 2019, Mujica, Casanova and coworkers computationally explored the relative magnitude of both CISS and intersystem crossing (ISC) in photoexcited helical oligothiophenes and found that they are related to the strength of SOC associated with either the excited singlet-triplet transition or electron transport through the helix. Depending on the time scale, both mechanisms are connected to photo-induced electron transfer, which was assumed to take place through an initial one-photon singlet-singlet excitation process followed by singlet-triplet mixing, which provides the pathway for subsequent spin polarization. As expected the longer helicenes and sulphur heavy atoms were found to promote ISC but a clear influence on the CISS in the excited state still needs to be demonstrated[89].

The CISS effect was suggested to be efficient in spin-dependent electron transfer processes at liquid/solid interfaces, for instance, the electrocatalytic oxygen evolution reaction (OER) [90]. Indeed the CISS process affects the spin of the electrons at the catalyst surface, consequently influencing the reaction pathway and enhancing the oxygen evolution. In 2022, Avarvari, Lingenfelder and coworkers evaluated the chiral molecular functionalization on the oxygen evolution at 2D hybrid chiral/achiral molecule-transition metal oxide electrode, prepared from NiOx and NiFeOx deposited with hetero-helicenes, namely thiadiazole-[7]helicene and bis(thiadiazole)-[8]helicene (**Figure 33**). They showed that the OER was boosted by up to 130% compared to state-of-the-art 2D metal oxide based catalysts. They suggested that the process occurs via a spin-polarization mechanism [91].

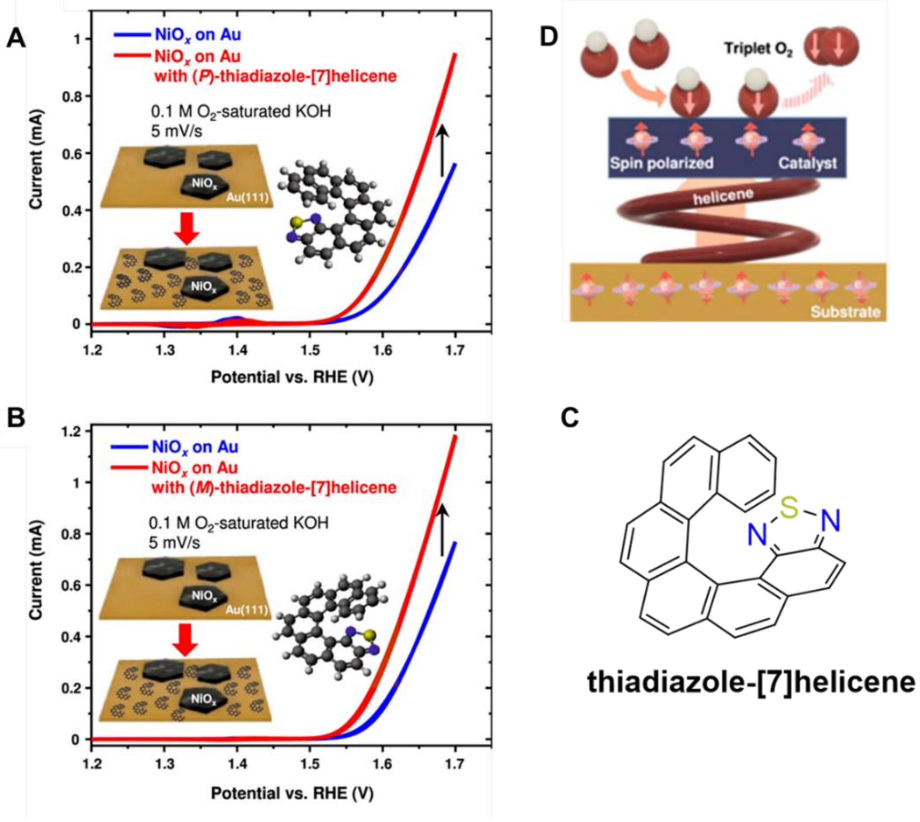

Figure 10. Panel (A) and (B): Helicene enantiomer functionalization effect on the OER activity; (C): structure of the mono thiadiazole derivative; (D): schematic illustration of the chiral effect of helicene on OER. Reproduced from [91].

III.4. Future perspectives and applications

Current research still needs to focus and clarify the fundamental mechanism of CISS phenomenon and how it depends on molecular parameters. These clarifications require the detailed study of various chiral systems so that the spin polarization through them can be compared and related to their structures. Indeed, this investigation will provide insights on the role of the CISS effect in biological electron transfer processes that occur through chiral systems and why nature might use spin-selective electron transfer.

From a less speculative point of view, the CISS effect provides a way to create spin-polarized electrons without use of a magnet and opens new possibilities for spintronics, in which most devices are currently constructed from magnetic materials.

Magnetic memory devices based on this effect have been already demonstrated [92]. In this study, the CISS effect was used in combination with spin-transfer torque memory (STT-RAM) to demonstrate a spin memory technology without the use of magnets. Indeed the magnet is replaced by a chiral SAM of α-helix L-polyalanine (AHPA-L) acting as spin filter that defines the spin polarization of the electrical current.

Moreover, the inclusion of a chiral perovskite layer, acting as spin filter, in a light-emitting diode LED device generate a "spin-polarized LED" without needing a magnetic field or extremely low temperatures[93]. In spin-LEDs the orientation and intensity of circularly polarized electroluminescence (CP-EL) is controlled by the spin polarization of the injected carriers. By using a hole injection layer composed of chiral 2D peroskite of *R*-/*S*-methylbenzyl ammonium lead iodide [(*R*/*S*-MBA)$_2$PbI$_4$], a 2.6% efficiency of the spin device was achieved at room temperature and without applying a magnetic field or using a ferromagnetic contact, with a spin-polarized current of up to 80%.

Despite the need of an extensive theoretical explanation and several aspects to be solved, the CISS effect has become a very promising driving force in spintronics, giving remarkable contributions in different fields, from optics to biology.

References

[1] E. L. Eliel and S. H. Wilen, Stereochemistry of Organic Compounds, New York: Wiley, 1994.

[2] J. R. Brandt, F. Salerno and M. J. Fuchter, *Nat. Rev. Chem,* vol. 1, 2017.

[3] N. Vargesson, *Birth Defects Res C Embryo,* vol. 105, pp. 140–156, 2015.

[4] W. H. Laarhoven and W. J. C. Prinsen, Topics in Current Chemistry, vol. 125, Springer-Verlag, Berlin, 1984.

[5] M. Joly, N. Defay, R. H. Martin, J. P. Declerq, G. Germain, B. Soubrierpayen and M. Vanmeerssche, *Helv. Chim. Acta,* vol. 60, pp. 537–560, 1977.

[6] J. Meisenheimer and B. D. K. Witte, *Chem. Ges. ,* vol. 36, pp. 4153–4164, 1903.

[7] M. S. Newman, W. B. Lutz and D. Lednicer, *J. Am. Chem. Soc.,* vol. 77, pp. 3420–3421, 1955.

[8] M. S. Newman and D. Lednicer, *J. Am. Chem. Soc.,* vol. 78, pp. 4765–4770, 1956.

[9] M. Flammang-Barbieux, J. Nasielski and R. H. Martin, *Tetrahedron Lett.,* vol. 8, pp. 743–744, 1967.

[10] Y. Shen and C.-F. Chen, *Chem. Rev.,* vol. 112, pp. 1463–1535, 2012.

[11] M. Gingras, *Chem. Soc. Rev,* vol. 42, pp. 1051-1095, 2013.

[12] M. Gingras, G. Felix and R. Peresutti, *Chem. Soc. Rev.,* vol. 42, pp. 1007–1050, 2013.

[13] N. Saleh, C. Shen and J. Crassous, *Chem. Sci.,* vol. 5, pp. 3680–3694, 2014.

[14] K. Dhbaibi, L. Favereau and J. Crassous, *Chem. Rev.,* vol. 119, pp. 8846–8953, 2019.

[15] E. S. Gauthier, R. Rodriguez and J. Crassous, *Angew. Chem. Int. Ed.,* vol. 59, pp. 22840–22856, 2020.

[16] J. Crassous, I. G. Stará and I. Starý (Eds), Helicenes: Synthesis, Properties and Applications, Wiley, 2022.

[17] C. S. Wood and F. B. Mallory, *J. Org. Chem.,* vol. 29, pp. 3373–3377, 1964.

[18] L. Liu, B. Yang, T. J. Kat and M. K. P. , *J. Org. Chem.,* vol. 56, pp. 3769–3775, 1991.

[19] H. R. Talele, A. R. Chaudhary, P. R. Patel and A. V. Bedekar, *ARKIVOC,* vol. 201, pp. 15–37, 2011.

[20] L. B. Liu, B. W. Yang, T. J. Katz and M. K. Poindexter, *J. Org. Chem.,* vol. 56, pp. 3769–3775, 1991.

[21] F. B. Mallory, C. S. Wood and J. T. Gordon, *J. Am. Chem. Soc.,* vol. 86, pp. 3094–3102, 1964.

[22] K. B. Jorgensen, *Molecules,* vol. 15, pp. 4334–4358, 2010.

[23] Q. Lefebvre, M. Jentsch and M. Rueping, *Beilstein J. Org. Chem.,* vol. 9, pp. 1883–1890, 2013.

[24] N. D. Willmore, L. B. Liu and T. J. Katz, *Angew. Chem. Int. Ed.,* vol. 31, pp. 1093−1095, 1992.

[25] K. E. S. Phillips, T. J. Katz, S. Jockusch, A. J. Lovinger and N. J. Turro, *J. Am. Chem. Soc.,* vol. 123, pp. 11899−11907, 2001.

[26] A. Urbano and M. C. E. Carreño, *Org. Biomol. Chem. ,* vol. 11, pp. 699−708, 2013.

[27] P. J. Evans, J. Ouyang, L. Favereau, J. Crassous, I. Fernandez, J. Perles and N. Martín, *Angew. Chem., Int. Ed,* vol. 57, pp. 6774−6779, 2018.

[28] C. M. Cruz, S. Castro-Fernandez, E. Maçôas, J. M. Cuerva and A. G. Campaña, *Angew. Chem., Int. Ed,* vol. 57, pp. 14782−14786, 2018.

[29] Y. Zhu, Z. Xia, Z. Cai, Z. Yuan, N. Jiang, T. Li, Y. Wang, X. Guo, Z. Li, S. Ma, D. Zhong, Y. Li and J. Wang, *J. Am. Chem. Soc.,* vol. 140, pp. 4222-4226, 2018.

[30] K. Kato, Y. Segawa, L. T. Scott and K. Itami, *Angew. Chem., Int. Ed.,* vol. 57, pp. 1337−1341, 2018.

[31] J. Ichikawa, M. Yokota, T. Kudo and S. Umezaki, *Angew. Chem., Int. Ed.,* vol. 47, pp. 4870−4873, 2008.

[32] J. Bosson, J. Gouin and J. Lacour, *Chem. Soc. Rev. ,* vol. 43, pp. 2824−2840, 2014.

[33] I. G. Stará and I. Starý, *Acc. Chem. Res.,* vol. 53, vol 11, pp. 144–158, 2020.

[34] I. G. Stará, I. Starý , A. Kollarovic´ , F. Teplý , D. Saman and M. Tichy, *J. Org. Chem. ,* vol. 63, pp. 4046−4050, 1998.

[35] K. P. C. Vollhardt, *Angew. Chem., Int. Ed.,* vol. 23, pp. 539−556, 1984.

[36] M. Buchta, J. Rybáček, A. Jančařík, A. A. Kudale, M. Buděšínský, J. V. Chocholoušová, J. Vacek, L. Bednárová, I. Císařová, G. J. Bodwell, I. Starý and I. G. Stará, *Chemistry - A European Journal,* vol. 24, pp. 8910−8917, 2015.

[37] R. H. Martin and M.-J. Marchant, *Tetrahedron Lett.,* vol. 13, pp. 3707–3708, 1972.

[38] C.-F. Chen and Y. Shen, Helicene Chemistry from synthesis to applications, Springer, Berlin, 2017.

[39] B. Laleu, P. Mobian, C. Herse, B. W. Laursen, G. Hopfgartner, G. Bernardinelli and J. Lacour, *Angew. Chem. Int. Ed.,* vol. 44, pp. 1879–1883, 2005.

[40] H. Kagan, A. Moradpou, J. Nicoud, G. Balavoin, R. Martin and J. Cosyn, *Tetrahedron Lett,* vol. 27, pp. 2479–2482, 1971.

[41] A. Moradpou, J. Nicoud, G. Balavoin, H. Kagan and G. Tsoucari, *J. Am. Chem. Soc.,* vol. 93, pp. 2353-2354, 1971.

[42] W. Bernstei, M. Calvin and O. Buchardt, *J. Am. Chem. Soc.,* vol. 94, pp. 494–498, 1972.

[43] I. Stara, I. Stary, A. Kollarovic, F. Teply, S. Vyskocil and D. Saman, *Tetrahedron Lett,* vol. 40, pp. 1993–1996, 1999.

[44] M. C. Carreno, R. Hernandez-Sanchez, J. Mahugo et A. Urbano, *J. Org. Chem.,* vol. 64, pp. 1387–1390, 1999.

[45] E. Gonzalez-Fernandez, L. D. M. Nicholls, L. D. Schaaf, C. Fares, C. W. Lehmann and M. Alcarazo, *J. Am.Chem. Soc.,* vol. 139, pp. 1428–1431, 2017.

[46] L. D. M. Nicholls, M. Marx, T. Hartung, E. Gonzalez-Fernandez, C. Golz and M. Alcarazo, *ACS Catal.,* vol. 8, pp. 6079–6085, 2018.

[47] A. Grandbois and S. K. Collins, *Chem. Eur. J.,* vol. 14, pp. 9323–9329, 2008.

[48] A. Collet, J. Crassous, J.-P. Dutasta and L. Guy, Molécules Chirales: Stéréochimie et Propriétés, EDP. sciences, Éd., 2006.

[49] N. Berova, P. L. Polavarapu, K. Nakanishi and R. W. Woody, Comprehensive Chiroptical Spectroscopy: Instrumentation, Methodologies, and Theoretical Simulations, Wiley, 2011.

[50] M. S. Newman, R. S. Darlak and L. L. Tsai, *J. Am. Chem. Soc.,* vol. 89, pp. 6191–6193, 1967.

[51] Y. Nakai, T. Mori and Y. Inoue, *J. Phys. Chem. A,* vol. 115, pp. 7372–7385, 2012.

[52] N. Harada and K. Nakanishi, Circular Dichroic Spectroscopy - Exciton Coupling in Organic Stereochemistry., University Science Books, 1983.

[53] W. T. Wiesler and K. Nakanishi, *J. Am. Chem. Soc.,* vol. 112, pp. 5574–5583, 1990.

[54] N. Berova, L. D. Bari and G. Pescitelli, *Chem. Soc. Rev.,* vol. 36, pp. 914–931, 2007.

[55] G. Pescitelli, *Chirality,* vol. 34, pp. 333–363, 2022.

[56] K. Dhbaibi, L. Favereau, M. Srebro-Hooper, M. Jean, N. Vanthuyne, F. Zinna, B. Jamoussi, L. D. Bari, J. Autschbach and J. Crassous , *Chem. Sci.,* vol. 9, pp. 735–742, 2018.

[57] J. P. Riehl and F. S. Richardson, *Chem. Rev.,* vol. 86, no. 1, pp. 1–15, 1986.

[58] F. Zinna and L. D. Bari, *Chirality,* vol. 27, no. 1, pp. 1-13, 2015.

[59] K. Dhbaibi, L. Abella, S. Meunier-Della-Gatta, T. Roisnel, N. Vanthuyne, B. Jamoussi, G. Pieters, B. Racine, E. Quesnel, J. Autschbach, J. Crassous and L. Favereau, *Chem. Sci.,* vol. 12, pp. 5522–5533, 2021.

[60] G. Longhi, E. Castiglioni, J. Koshoubu, G. Mazzeo and S. Abbate, *Chirality,* vol. 28, pp. 696–707, 2016.

[61] K. Ray, S. Ananthavel, D. Waldeck and R. Naaman, *Science,* vol. 283, pp. 814–816, 1999.

[62] R. Gutierrez, E. Dıaz, R. Naaman and G. Cuniberti, *Phys. Rev. B,* vol. 85, pp. 1-4, 2012.

[63] E. Medina, F. Lopez, R. M.A and V. Mujica, *Europhys. Lett.,* vol. 99, 2021.

[64] J. Gersten, K. Kaasbjerg and A. Nitzan, *J. Chem. Phys.,* vol. 139, pp. 1-21, 2013.

[65] R. Naaman and D. H. Waldeck, *Annual Review of Physical Chemistry,* vol. 66, pp. 263–281, 2015.

[66] R. Naaman and D. H. Waldeck, *J. Phys. Chem. Lett.,* vol. 3 , p. 2178–2187, 2012.

[67] P. V. Möllers, B. Göhler and H. Zacharias, *Isr. J. Chem.*, vol. 62, pp. 1-15, 2022.

[68] I. Carmeli, V. Skakalova, R. Naaman and Z. Vager, *Angew. Chem., Int. Ed.,* vol. 41, pp. 761–764, 2002.

[69] S. G. Ray, S. S. Daube, G. Leitus, Z. Vager and R. Naaman, *Phys. Rev. Lett.,* vol. 96, 2006.

[70] B. Goheler, V. Hamelbeck, T. Markus, M. Kettner, G. Hanne, Z. Vager, R. Naaman and H. Zacharias, *Science,* vol. 331, pp. 894–897, 2011.

[71] D. Mishra, T. Z. Markus, R. Naaman, M. Kettner, B. Göhler, H. Zacharias, N. Friedman, M. Sheves and C. Fontanesi, *PNAS,* vol. 110, pp. 14872–14876, 2013.

[72] S. Ravi, P. Sowmiya and A. Karthikeyan, *Spin,* vol. 3, 2013.

[73] S. Mishra, A. K. Mondal, E. Smolinsky, R. Naaman, K. Maeda, T. Nishimura, T. Taniguchi, T. Yoshida, K. Takayama and E. Yashima, *Angew. Chem.,* vol. 132, pp. 14779–14784, 2020.

[74] M. Suda, Y. Thathong, V. Promarak, H. Kojima, M. Nakamura, T. Shiraogawa, M. Ehara and H. M. Yamamoto, *Nat Commun,* vol. 10, 2455, pp. 1-7, 2019.

[75] Z. Xie, T. Markus, S. Cohen, Z. Vager, R. Gutierrez and R. Naaman, *Nano Lett.,* vol. 11, pp. 4652–4655, 2011.

[76] S. Mishra, A. K. Mondal, E. Z. B. Smolinsky, R. Naaman, K. Maeda, T. Nishimura, T. Taniguchi, T. Yoshida, K. Takayama and E. Yashima, *Angew. Chem. Int. Ed.,* vol. 132, pp. 14779–14784, 2020.

[77] C. Fontanesi, *Curr. Opin. Electrochem.*, vol. 7, pp. 36–41, 2018.

[78] S. Mishra, A. K. Mondal, S. Pal, T. K. Das, E. Z. B. Smolinsky, G. Siligardi and R. Naaman, *J. Phys. Chem. C,* vol. 124, pp. 10776–10782, 2020.

[79] B. P. Bloom, B. M. Graff, S. Ghosh, D. N. Beratan and D. H. Waldeck, *J. Am. Chem. Soc.,* vol. 139, pp. 9038−9043, 2017.

[80] C. Kulkarni, A. K. Mondal, T. K. Das, G. Grinbom, F. Tassinari, M. F. J. Mabesoone, E. W. Meijer and R. Naaman, *Adv. Mater.,* vol. 32, 2020.

[81] Y. Xua and W. Mi, *Mater. Horiz.,* vol. 10, pp. 1924-1955, 2023.

[82] H. P. Lu, C. X. Xiao, R. Y. Song, T. Y. Li, A. E. Maughan, A. Levin, R. Brunecky, J. J. Berry, D. B. Mitzi, V. Blum and M. C. Beard, *J. Am. Chem. Soc.,* vol. 142, pp. 13030–13040, 2020.

[83] Y. Lu, Q. Wang, R. Y. Chen, L. L. Qiao, F. X. Zhou, X. Yang, D. Wang, H. Cao, W. L. He, F. Pan, Z. Yang and C. Song, *Adv. Funct. Mater.,* vol. 31, 2021.

[84] V. Kiran, S. P. Mathew, S. R. Cohen and I. H. Delgado, *Adv. Mater.,* vol. 28, pp. 1957–1962, 2016.

[85] R. Rodríguez, C. Naranjo, A. Kumar, P. Matozzo, T. K. Das, Q. Zhu, N. Vanthuyne, R. Gómez, R. Naaman, L. Sánchez and J. Crassous, *J. Am. Chem. Soc,* vol. 144, pp. 7709–7719, 2022.

[86] N. Giaconi, L. Poggini, M. Lupi, M. Briganti, A. Kumar, T. K. Das, A. L. Sorrentino, C. Viglianisi, S. Menichetti, R. Naaman, R. Sessoli and M. Mannini, *ACS Nano,* vol. 17, pp. 15189–15198, 2023.

[87] M. Kettner, V. V. Maslyuk, D. Nürenberg and J. Seibel, *J. Phys. Chem. Lett.,* vol. 9, pp. 2025–2030, 2018.

[88] T.-R. Pan, A.-M. Guo and Q.-F. Sun, *Phys. Rev. B: Condens. Matter Mater. Phys.,* vol. 94, 2016.

[89] J. M. Matxain, J. M. Ugalde, V. Mujica, S. I. Allec, B. M. Wong and D. Casanova, *ChemPhotoChem,* vol. 3, pp. 770-777, 2019.

[90] W. Mtangi, F. Tassinari, K. Vankayala, A. V. Jentzsch, B. Adelizzi, A. R. A. Palmans, C. Fontanesi, E. W. Meijer and R. Naaman, *J. Am. Chem. Soc.,* vol. 139, pp. 2794–2798, 2017.

[91] Y. Liang, K. Banjac, K. Martin, N. Z. S. Lee, N. Vanthuyne, F. A. Garcés-Pineda, J. R. Galán-Mascarós, X. Hu, N. Avarvari and M. Lingenfelder, *Nat. Comm.,* vol. 13, 3356, pp. 1-9, 2022.

[92] O. B. Dor, S. Yochelis, S. Mathew, N. R. and Y. Paltiel, *Nat. Comm.,* vol. 4, 2256, 2013.

[93] Y. Z. L. Young-Hoon Kim # 1, X. Pan, C. Xiao, E. A. Gaulding, S. P. Harvey, J. J. Berry, Z. V. Vardeny, J. M. Luther and M. C. Beard, *Science,* vol. 371, pp. 1129-1133, 2021.

[94] N. Saleh, C. Shen and J. Crassous, *Chem. Sci.,* vol. 5, pp. 3680–3694, 2014.

[95] Q. Lefebvre, M. Jentsch and M. Rueping, *Beilstein J. Org. Chem.,* vol. 9, pp. 1883–1890, 2013.

Chapter 2

Helicene-porphyrin conjugates: synthesis and Exciton Coupling chirality

I. Context and target molecules

As we have already discussed in the introduction, there is a connection between the optical activity and the chiral-induced spin selectivity effect (CISS); indeed, a qualitative correlation was found between the magnitude of circular dichroism (CD) spectra and the sign and magnitude of the spin polarization resulting from the CISS effect [1]. Thus, a suitable strategy to increase the spin filter ability of a system is to tune and enhance the chiroptical properties and the CD response.

Our group successfully demonstrated a novel approach of chemical engineering to further improve chiroptical responses of helicenes. The functionalization of an achiral three-dimensional helical core with a chromophore, gives rise to an exciton coupling effect (see **Chapter 1** for more details). For example, the synthesis and chiroptical properties of π-conjugated diketopyrrolopyrrole–helicene derivatives have been reported. These compounds show intense electronic circular dichroism in the visible region along with near-IR circularly polarized luminescence[2] as a result of the exciton coupling between the achiral dyes.
Following this approach, we decided to tune the chiroptical activity of [6]helicene by using a different well-studied chromophores, such as porphyrins.
Porphyrins and porphyrin derivatives are important functional molecules and a class of organic chromophores. They have been employed in various applications in material science due to their characteristics and versatile functions, such as dye for dye-sensitizer solar cells (DSSCs)[3], molecular wires and electronic component[4] but they are as well widely utilized in biomedical fields, as biosensors, in bioimaging, in cancer therapy, and especially in photodynamic therapy (PDT)[5].
In this chapter, I will present the first results we achieved by functionalizing carbo[6]helicene with this chromophore.

I.1. Porphyrins: structure and spectroscopic properties

Porphyrins are aromatic macrocycles composed of four pyrroles separated by methine bridges. Despite having 22 π electrons, only 18 contribute to their aromaticity. The remaining four electrons have a particular reactivity similar to those of a C=C bond.
Porphyrins and their derivatives are widespread in natural systems and perform vital functions such as oxygen transport and photosynthetic processes[6, 7].

According to the nomenclature proposed by the IUPAC organization, a porphyrin possesses 8 β-pyrrolic positions and 4 *meso* positions (**Figure 1**). The arrangement of the four pyrroles defines an internal coordination site of L_2X_2 type, which exhibits a high affinity for metal ions. When a metal ion is present within the macrocyclic cavity, the term "metalloporphyrin" is used.
In contrast, the term "free base porphyrin" is used to describe the ligand itself.

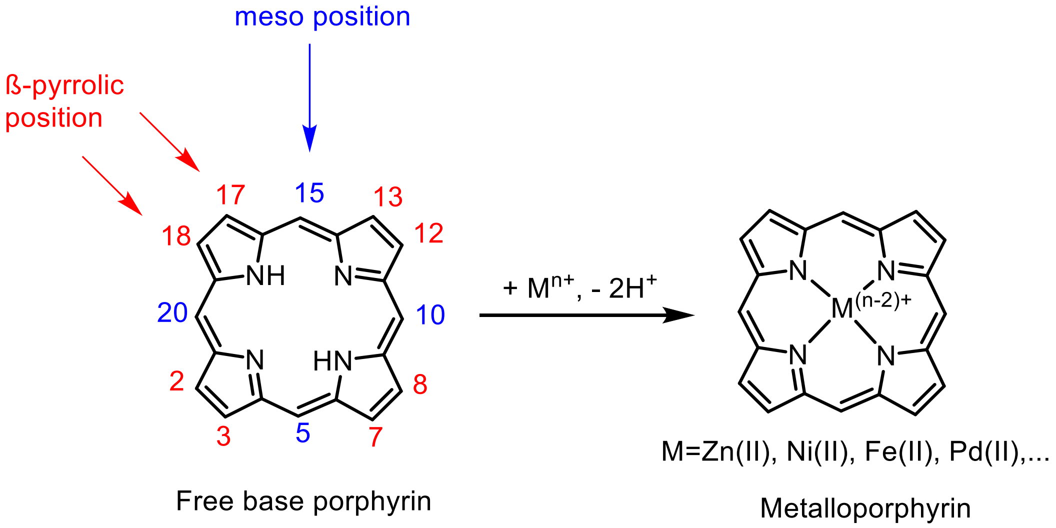

Figure 1. Porphyrin structure and nomenclature.Presentation of the β-pyrrolic and meso positions.

With twelve possible functionalization sites and an internal coordination site, porphyrins are aromatic surfaces that can show a wide variety of structures, and their properties can be easily modulated through internal and peripheral functionalization.

Due to the 18 π electrons, porphyrins are macrocycles with extended aromaticity, and their absorption occurs in the visible range. Thanks to their extremely high molar extinction coefficients, porphyrins and their derivatives are among the most intense natural pigments, giving colour to blood (hemoglobin) or plants (chlorophylls).

The electronic absorption spectra of porphyrins exhibit a characteristic pattern with π-π* transitions grouped into two distinct types:

- The "Soret or B band", located between 380 and 450 nm, corresponds to a transition between the ground state and the second excited state (S0-S2). This transition is allowed by the selection rules and shows very high molar extinction coefficients ($\varepsilon > 10^5$ $M^{-1}\cdot cm^{-1}$). A shoulder sometimes appears on the high-energy side of the B band, attributed to one mode of vibrational excitation B(1-0).
- The so-called "Q bands", they are located between 500 and 750 nm and they can be two or four depending on whether it is a free base porphyrin or a metalloporphyrin. These bands correspond to the S0-S1 transitions with molar extinction coefficients on the order of $\varepsilon = 10^3 - 10^4$ $M^{-1}\cdot cm^{-1}$.

In 1963, Gouterman proposed his "four orbital model" to interpret the shape of the obtained spectra. This model takes into account the energy levels of HOMO-1 (a_{2u}), HOMO (a_{1u}), LUMO and LUMO+1 ($e_g(x)$ and $e_g(y)$) in **Figure 2**, which are responsible for the different observed electronic transitions. When transitioning from a metalloporphyrin to a free base porphyrin, the loss of symmetry (from D_{4h} to D_{2h}) results in the lifting of degeneracy of the energy levels, leading to the appearance of two to four Q bands and in a shift in the wavelengths[8].

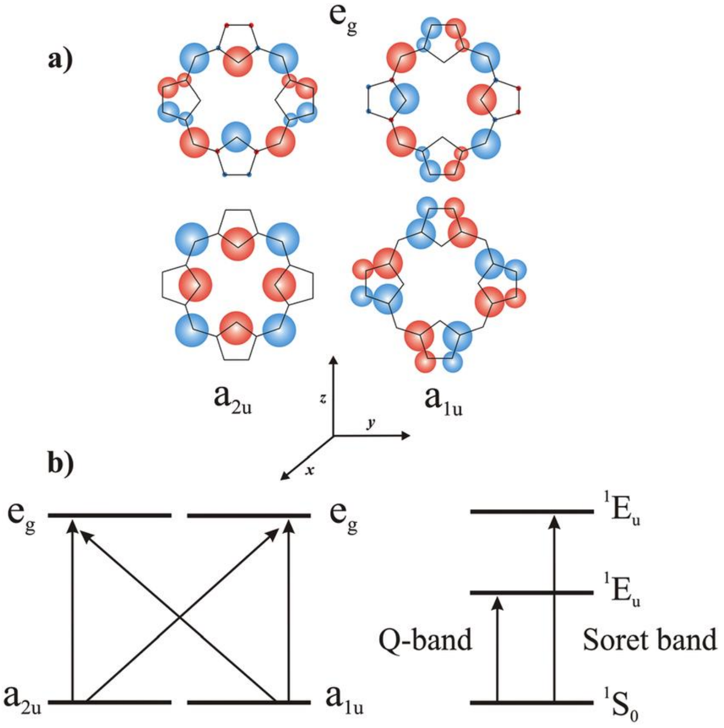

Figure 211. a) Gouterman's four orbital model and (b) energy levels showing the transitions of a porphyrin system. Picture reproduced from [7].

I.2. Conformations of the porphyrin macrocycle

Despite the aromaticity of the macrocycle, the shape of porphyrin molecules is not always symmetrical and invariant as originally imagined. Porphyrins can undergo deformations depending on the substituents present and the nature (size, coordination geometry, etc.) of the central metal ion (**Figure 3**).

In 1987, W.R. Scheidt classified the most frequently adopted conformations of porphyrins into four families: "saddle" (resembling a horse saddle), "ruffled" (undulated), "domed" (dome-shaped), and "waved" (wavy) [9].

a) Saddle, $B_{2u}(1)$ b) Ruffle, $B_{1u}(1)$

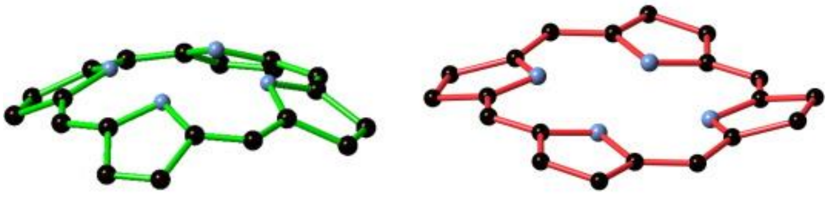

c) Dome, $A_{2u}(1)$ d) Wave, $E_{gx}(1)$ or $E_{gy}(1)$

Figure 3. The four principal modes of porphyrin 24-atom out-of-plane deformation. Picture reproduced from [8]

While certain porphyrins possess a mostly regular structure, deviations from the core pattern can occur due to various factors such as steric effects, bonding interactions, and electronic effects. These deviations are induced when the metal center requires a coordination environment that is either smaller or larger than what the planar macrocycle can provide. In such cases, the macrocycle undergoes distortion to accommodate the preferred coordination arrangement.

To achieve significant deviations from planarity in porphyrins, several strategies are employed. These include core modification, peripheral and electronic manipulation, and redox reactions. These strategies enable the synthesis of nonplanar porphyrins with altered chemical reactivity, electrochemistry, and (photo)physical properties.

- ***SADDLE CONFORMATION***

The saddle shape, characterized by the tilting of pyrrole units in an up-down-up-down manner, is commonly observed in porphyrins where the four N atoms are protonated (diacid porphyrins) and dodecasubstituted porphyrins. This conformation was initially identified and structurally characterized in "H4" porphyrin di-cation, obtained by acidification of the core [10]. In the "H4 diacid" shape, like **H4TPP**, the pyrrole units tilt away from each other instead of towards a shared center, as seen in metal complexes or free base porphyrins (**Figure 4**).

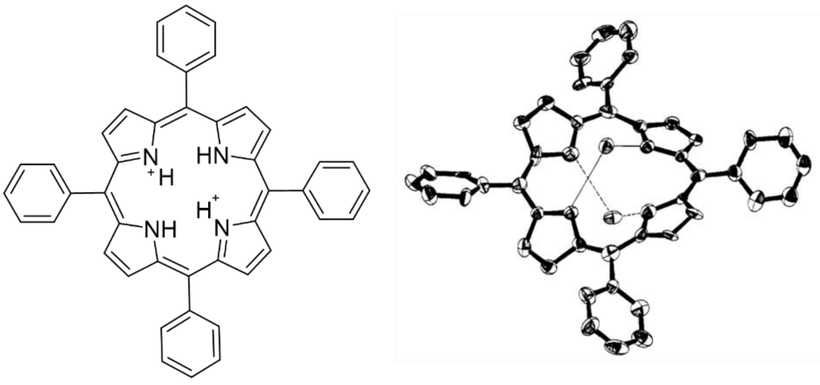

H4TPP

Figure 4. Porphyrin diacid structure and ball and stick model for it saddled conformation. Adapted from ref [9]

Similarly, nonplanarity in porphyrins has traditionally been induced by steric conflicts, particularly in highly substituted porphyrins. This is the case of dodecasubstituted porphyrins, which introduce significant degrees of nonplanarity due to the steric effects.

Thus, porphyrins that exhibit both core and peripheral patterns, such as dodecasubstituted porphyrin diacids or *N*-substituted derivatives, tend to adopt a saddle structure and are among the most distorted porphyrin structures.

- ***RUFFLED CONFORMATION***

The distortion of this conformation implies an out-of-plane movement typically accompanied by an overall contraction. Traditionally, the ruffling distortion has been observed in correlation with the coordination of Ni(II) metal ion in the core. The small size of Ni(II) forces the pyrrole units to come closer to one another, inducing the ruffling effect [11] (**Figure 5**).

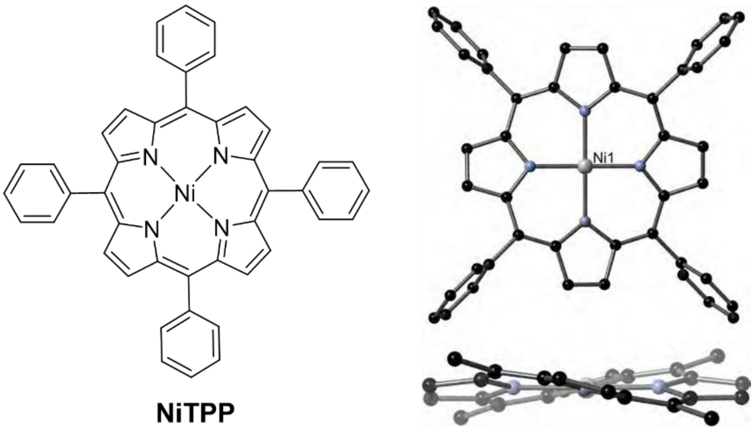

Figure 5. NiTPP and the top and side view of its crystal structure. The Images are generated from CCDC No. 1,320,805 CSD code ZZZUUC01

Analogously, peripheral modifications can also induce significant ruffled distortions, along with the formation of exocyclic C-C double bonds.

- ***DOMED CONFORMATION***

A dome conformation involves the concerted out-of-plane movement of all four pyrrole units. In its simplest representation, the pyrrole units rotate towards the same face, causing the nitrogen atoms to be positioned above the plane of the molecule. This dome-like formation is observed in porphyrins coordinated with lanthanoid and similar metal centers that have a large ionic radius and a tendency for higher coordination numbers [12].

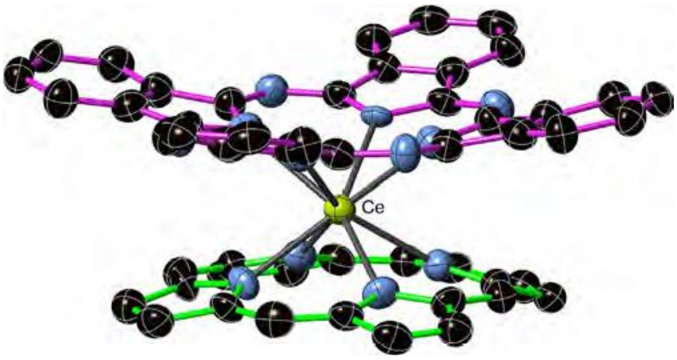

Figure 6. A typical lanthanoid octaethylporphyrin-naphthalocyanine sandwich complex. Reproduced from [11].

Compounds where a single porphyrin chelates each metal center exhibit less distortion compared to those forming a bis-tetradentate structure.

- ***WAVED CONFORMATION***

The wave distortion modes in porphyrins are initiated by the interaction of an individual pyrrole unit or two adjacent pyrrole units with a metal complex, while the other two do not interact with the metal. As a result, the macrocycle undergoes deformation along one of the two equivalent wave-shaped modes or a combination of these modes.

Peripheral deformation strategies, such as substitution at the 2,3,12,13-position of the porphyrin core with different and sterically demanding groups, are usually not effective in promoting a wave-shaped conformation in porphyrins, except for a few highly distorted examples. On the other hand, core modification strategies, such as the formation of bis-chelates, have proven to be effective, although only a limited number of examples have been reported [13, 14, 15].

Taking into account that the peripheral substitution is significative in the determination of the geometry, if one focuses on the differences among the metals in the same porphyrin ligand, simple synthetic Zn(II) porphyrins, such as (5,10,15,20-tetraphenyl porphyrinato)zinc(II), are highly symmetrical and approximately planar, as observed from crystal structure analysis [16], while the same ligand for Cu(II) and Ni (II) complexes predominantly adopt the ruffled out-of-plane geometry, as previously mentioned.

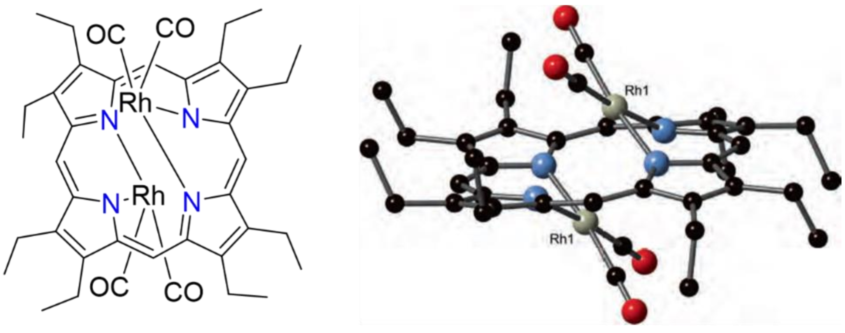

RhP(CO)$_4$

Figure 7. Bis chelating porphyrin with waved conformation. Reproduced from [12].

I.3. Chiral porphyrins and Exciton Coupling chirality

The majority of the numerous examples of chiral porphyrins described in the literature are chiral either due to the presence of a stereogenic center on one of their substituents, or to the distortion from planarity by the combination of multiple distortional modes by both peripheral and core substitutions [17, 18, 19].

Due to the large number of chiral porphyrin derivatives, only those examples containing bis-porphyrin units that give rise to an Exciton Coupling signature, which is the final aim of the design of our molecules, will be discussed.

It is known that the magnitude of a CD exciton couplet is directly proportional to the square of the extinction coefficients of the coupled chromophores and inversely proportional to the square of the distance between them [20] (see **Chapter 1**). This means that strong absorption results in highly intense CD signals.

Tetraphenylporphyrin derivatives are ideal chromophores for studying CD exciton couplets due to several advantages: (I) their spectra are mainly characterized by intense and narrow Soret bands around 410 nm, minimizing the possibility of overlap with other bands; (II) they exhibit strong molar absorption coefficients typically exceeding 5×10^5 M^{-1} cm^{-1}; (III) the strong absorption allows for through-space coupling over long distances; and (IV) they can be structurally modified in a versatile manner.

Over a period of approximately 10 years, Nakanishi and Berova and their co-workers initiated the method for determining the absolute configurations of amino-alcohols, amino-acids, α-hydroxy acids, secondary and primary monoamines, and α-chiral carboxylic acids by using flexible chain-linked zinc and magnesium bis-porphyrins (tweezers) [21, 22, 23, 24].

In a 1995 paper, they introduced porphyrins to the exciton-coupled method for conformational studies: in fact, this chromophore further enhances the sensitivity of the exciton-coupled CD method by almost 10-fold, due to the high value of its molar extinction coefficient and extend the applicability of the method thanks to the more red-shifted absorption. The 5-(p-carboxyphenyl)-10,15,20-triphenylporphin was prepared to react with glycols and 3-amino-17-hydroxysteroids to obtain the corresponding bisesters and amide esters respectively [25].

The transfer of the chirality of the guests to the bis-chromophoric host was detected in the CD spectrum by the presence of a bisignate EC curve, due to the helical arrangement of the two porphyrins (**Figure 8**).

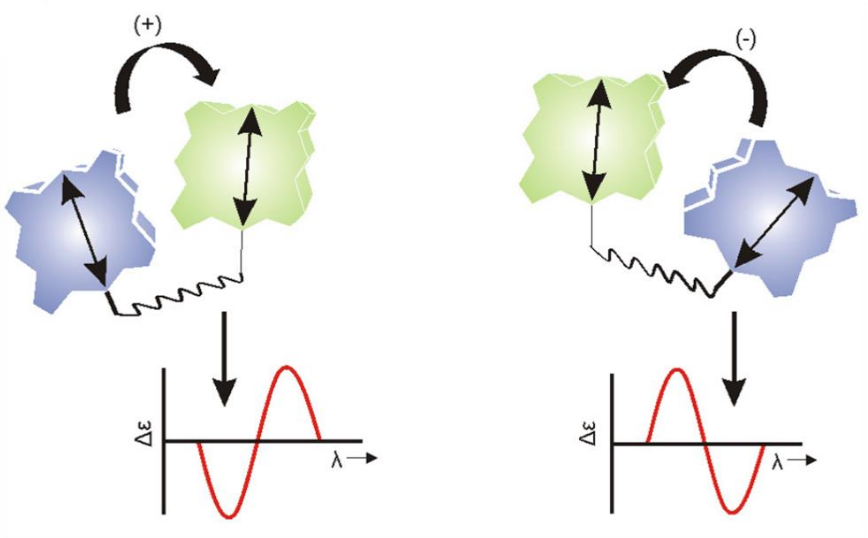

Figure 8. Schematic representation of the sense of the porphyrin twist and the expected CD spectrum; for clarity the bound chiral guest has been omitted. Reproduced from ref [19].

This transfer is a result of the helical arrangement of the two porphyrins. The chiral direction of the twist formed by the two porphyrins is determined by the stereogenic center of the substrate. Therefore, the observed sign of the CD curve is directly related to the helicity of the complex, and can be attributed to the chirality of the substrate. Consequently, this nonempirical assignment based on CD analysis provides characteristic information about the chirality of the system.

Berova and co-workers described three model categories of the spatial arrangement of these systems (**Figure 9**): class I, compounds with porphyrin rings with largely unrestricted rotation (about one or more preferential axes); class II, compounds with two porphyrin rings with fixed spatial orientation; and class III, compounds with porphyrins undergoing π-π stacking that are the more challenging one for computational studies [26].

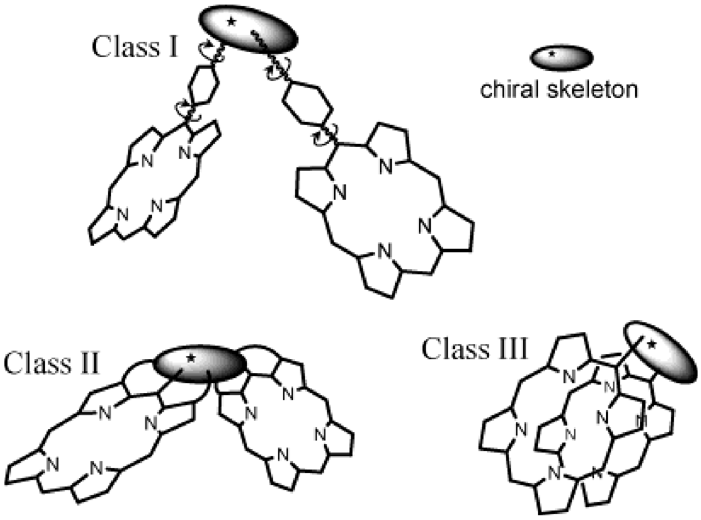

Figure 9. Schematic representation of the three classes of bis-porphyrin indicated by Berova and co-workers. Reproduced from [26].

Herein few examples of bis-porphyrins systems linked by diverse moieties will be illustrated.

I.3.1. Bis-porphyrins formed via achiral linkages

Bis-porphyrins containing achiral linkages are considered to be among the most useful chromophores for using exciton coupling (EC) circular dichroism spectroscopy to determine the absolute configuration of chiral substrates. In the free base form, they lack chirality and are therefore CD-silent. Upon mixing with a chiral guest, such as amino, hydroxyl, or carboxyl compounds, the host undergoes ditopic coordination, which is stereo-controlled by the chiral guest.

The two chromophores become mutually twisted and adopt a single preferred sense of chirality because they incorporate the guest in the binding pocket. Therefore, the obtained complex displays a very intense exciton split CD band within the Soret band region, which can be readily analyzed to determine absolute configuration of the guest molecule.

Different types of linkers have been reported, such as ether chains (**Figure 10A**), or a flexible ethane bridge linked at the *meso*-carbon positions (**Figure 10B**).

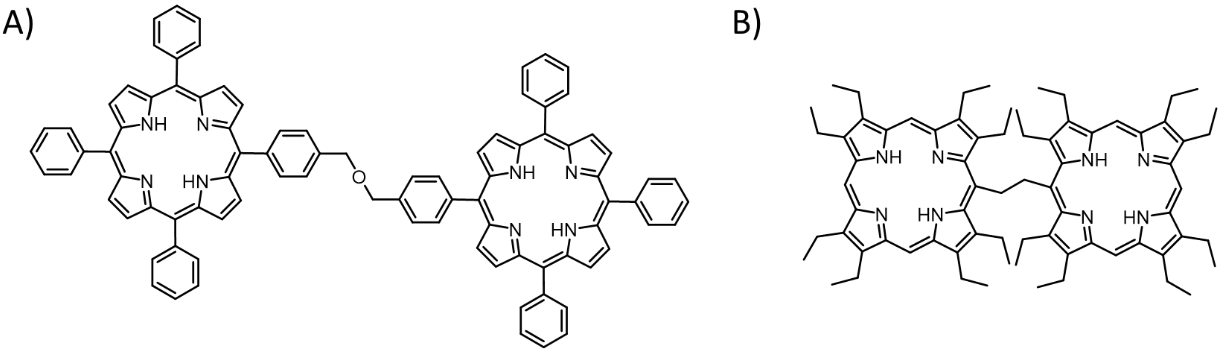

P1 **P2**

Figure 10. Schematic structures of ether (A) and ethane linked porphyrins (B).

The structure of the chiral guest plays a crucial role in the induction of the chirality. Indeed, Inoue, Borovkov, and co-workers reported the use of the Zn(II) metalloporphyrin from **Figure 11** to determine the absolute configuration of chiral substrates, in particular amines: *S*-enantiomers induced positive chirality, since a right-handed screw is formed, while *R*-enantiomers result in the formation of a left-handed screw due to negative chirality [27, 28].

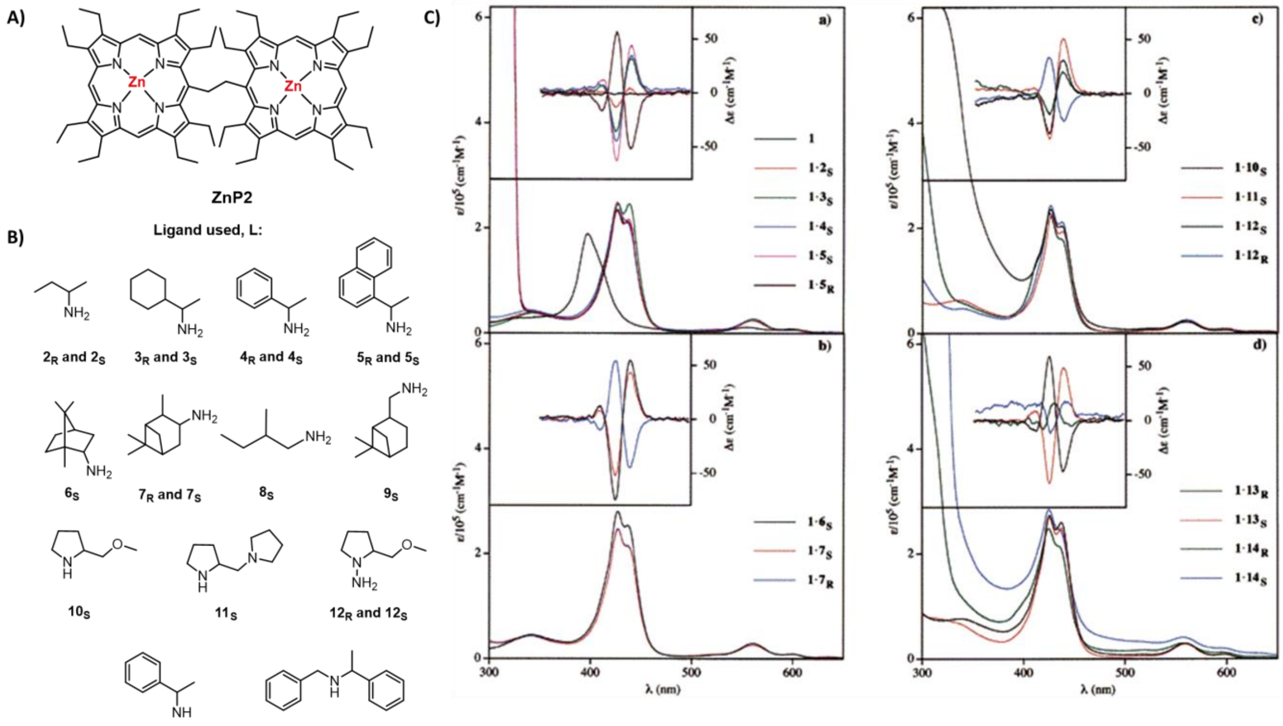

*Figure 11. From ref [28]: A) structure of the porphyrin system used; B) structure of the chiral amines; C) UV−vis and CD (inset) spectra of **ZnP2** in CH_2Cl_2 at 292 K without ligands (left) and in the presence of different chiral amines (right).*

Additionally, they could discriminate between different organic substrates, and showed that amines have larger affinities than alcohols, while primary amines bind more strongly than secondary amines; while aromatic ligands bind more weakly than aliphatic ligands, but larger aromatic rings have larger binding strengths. Moreover, the presence of large side substituents on the amines results in an intensification of the CD signals.

They concluded that for this type of system the chirality induction is strictly related to the structure of the optically active guest molecule: it particularly depends on the absolute configuration of the guest, the bulkiness in terms of sterics at the chiral center, the nature of the binding group and the binding site’s position with respect to the asymmetric carbon atom.

Another factor influencing the chirality of this host−guest system is the ligand stoichiometry. In fact, the amount of excess ligand has a significant impact on the transfer of the chirality information from the guest molecule to the achiral host [29]. This is the case for the complexation of this system with diphenylethylenediamine (*R,R*-DPEA). At low molar excess, the coordination results in a 1:1 tweezer complex with right-handed chirality, while the addition of a large excess of *R,R*-DPEA resulting in significant changes in the CD and absorption spectra, since there is a stepwise shift in the equilibrium toward 1:2 complex formation. This structure undertake a left-handed twist that minimizes steric hindrance that results from the interaction between the porphyrin ethyl group, and the bulkiest substituent of *R,R*-DPEA.

I.3.2. Rigid systems

Yoshida and Osuka reported the first example of a chiral *meso–meso*-linked bis-porphyrin resolved by chiral HPLC (**Figure 12**) [30].

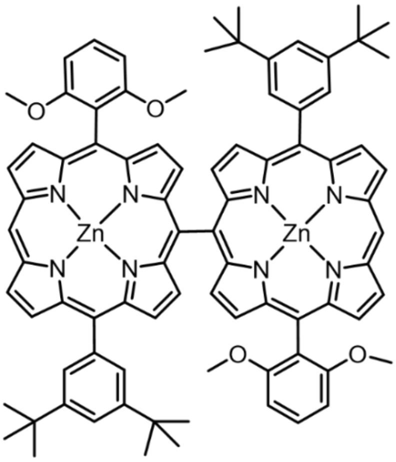

P3

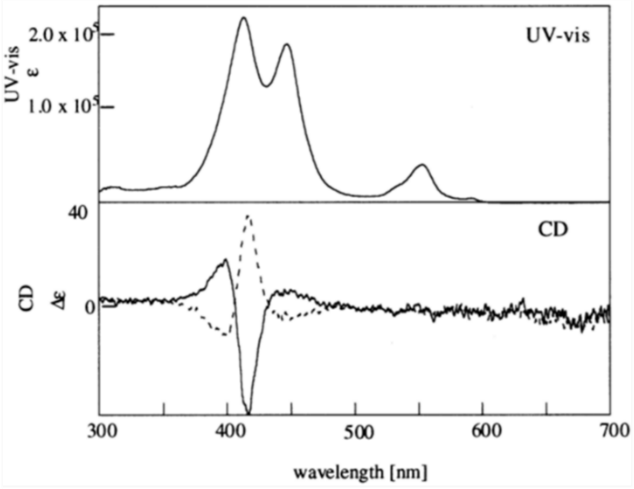

Figure 12. First example of chiral meso-meso linked porphyrins (left) and its UV-Vis and ECD spectra (right).

In this chromophore bearing different aryl groups the optical activity originated from the high rotational barrier around the *meso–meso* bond. The Soret bands of the enantiomers displayed oppositely signed Cotton effects and the presence of a stronger Cotton effect near 413 nm was assigned to the interaction of the transition dipole moments that lie perpendicular to the long-axis of the molecule.

Shortly after this, several *meso–meso*-linked systems were reported, which were strapped by dioxymethylene groups of varying length (**Figure 13**) [31].

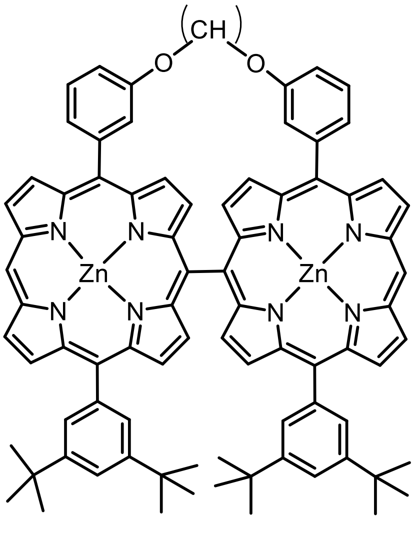

n= 10, 8, 6, 5, 4, 3, 2

P4

Figure 13. Schematic structure of the other meso-meso porphyrins strapped by dioxymethylene groups.

At shorter strap lengths, a gradual decrease was observed in the dihedral angle formed by the porphyrins and there is an increasing distortion. Opposite Cotton effects were observed in the Soret band region as expected.

Bringmann and co-workers reported the synthesis of *meso*-arylated β−β linked molecules, both as the metal-free ligand and with Ni(II), Cu(II), Zn(II), and Pd(II) as the central metals [32, 33]. The X-ray data revealed that the two Ni moieties had ruffled conformations, while the two Zn derivatives had nearly planar structures. When CD spectra were measured for the bis-Znporphyrin, the *P*-enantiomer exhibited a +/-/+ sequence, corresponding to the split Soret bands. This matches the CD pattern observed for the *meso*−*meso* linked porphyrins very closely (**Figure 14**).

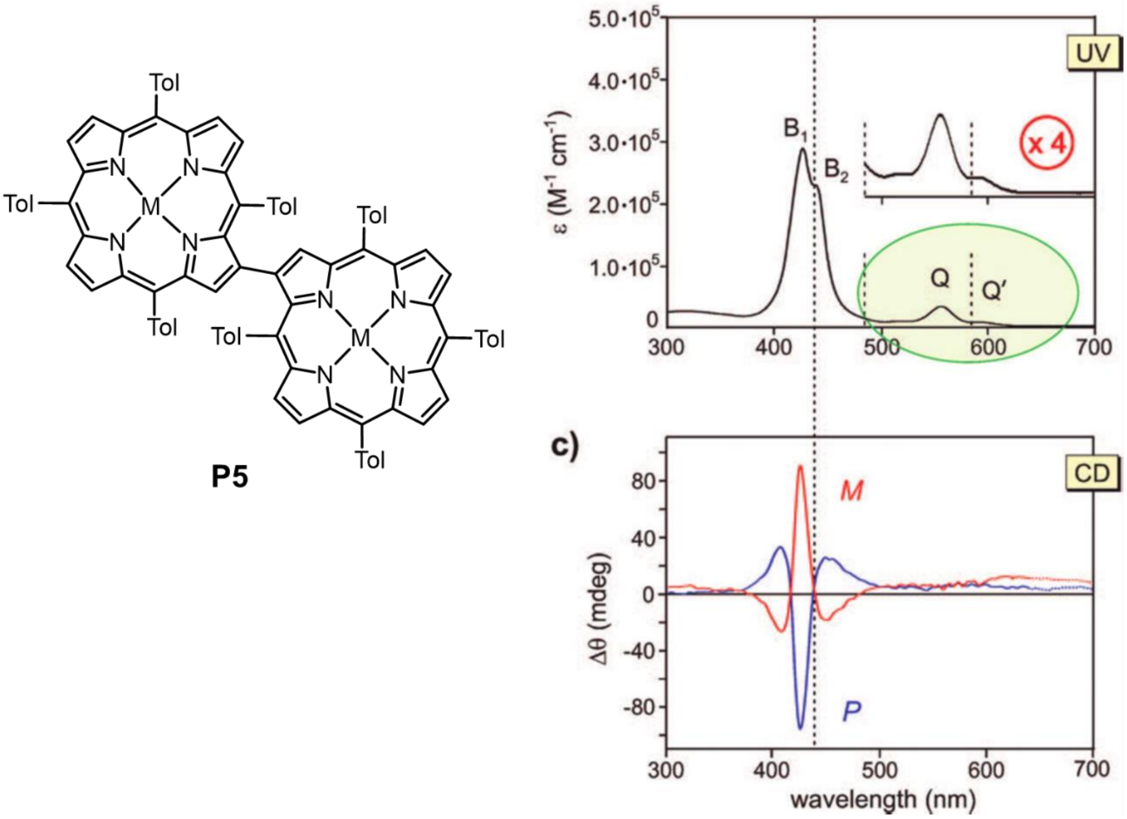
P5

Figure 14. Representation of the β−β linked compounds where M= Zn, Ni, Pd, Cu (left) and adsorption and ECD spectra of the Zn derivative. Adapted from [32].

I.3.3. Bis-porphyrins containing chiral linkages

These systems are chiral themselves because of a chiral linker between the two chromophores. Among the different chiral units, chiral 1,1′-binaphthyl (BNP) derivatives have been extensively used for different applications such as asymmetric catalysis and chiral molecular recognition [34].

Kimura and co-workers reported the synthesis and CD spectroscopy of bis-porphyrins **P6** with (S_a)- and (R_a)-BNP-linker moieties (**Figure 15**) [35].

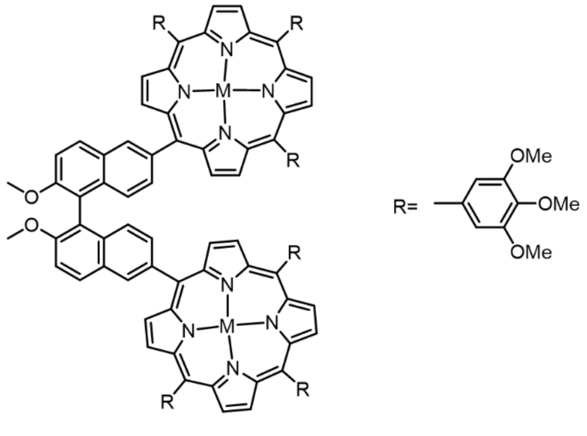

P6

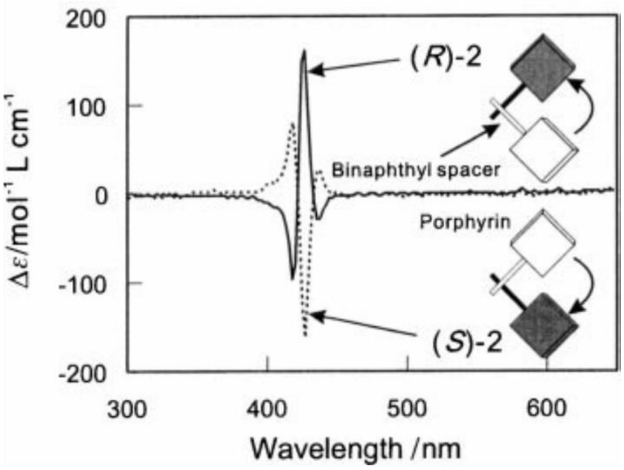

Figure 15. Kimura's porphyrin systems with chiral 1,1'-binaphthyl linker with the CD spectrum of the free base derivative. Adapted from ref [34].

In the Soret band region, the metal-free derivative displayed bisignate CD bands. In the CD spectrum of the R_a-enantiomer, a positive sign is observed at 427 nm, where the Soret absorption band lies, along with a negative sign at higher energy. Notably, when a central Fe(II) was added to form a metal complex, the intensity of the bisignate CD signal decreased to almost zero, with a positive CD signal observed in the Soret region for the *R*-enantiomer.

This implies that the CD signal in this region was the result of CD intensity induced by the coupling interaction between the BNP unit and the porphyrin chromophore.

Another example of BNP-linked bis-porphyrin was reported by Ema and co-workers (**Figure 16**). In this case, the substitution of the two BNP moieties forces the two porphyrin rings to form a chiral macrocyclic cavity which can interact with guest molecules. Nevertheless, the chiroptical properties of this system have not been investigated [36].

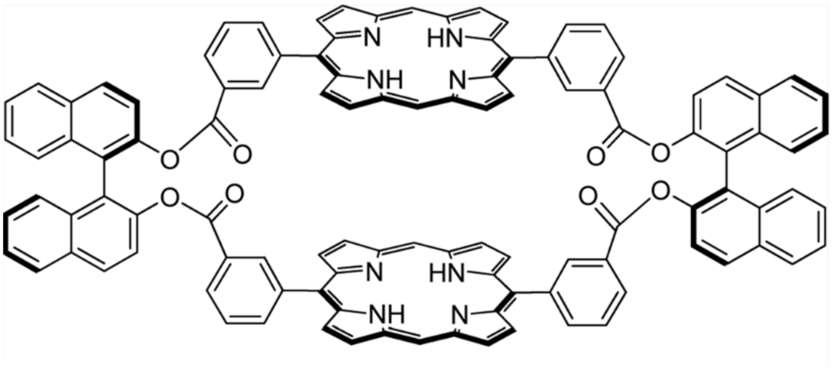

***R*-P7**

Figure 16. BNP-linked porphyrins by Ema and collaborators.

Two porphyrins can be introduced onto the terminal naphthalene units of 1,1'-position-linked optically active naphthalene dimers and oligomers (**Figure 17**). The largest example of this kind of system containing an octamer of binaphthyl consisting of 16 naphthalene units linking two TPP groups was reported by Tsubaki [37]. By examining X-ray data for several oligomers, together with calculations, it was concluded that, on average, the adjacent naphthalene moieties formed dihedral angles ranging from 74.7 to 113°, with an average of 90.0°.

Moreover, the intensity of the CD band can be assumed to be inversely proportional to the square of the interchromophoric distance. Since the naphthalene moieties are linked in a linear manner and the distance between the porphyrin rings can easily be estimated, this system represented an ideal model to explore the relationship between chirality and CD intensity.

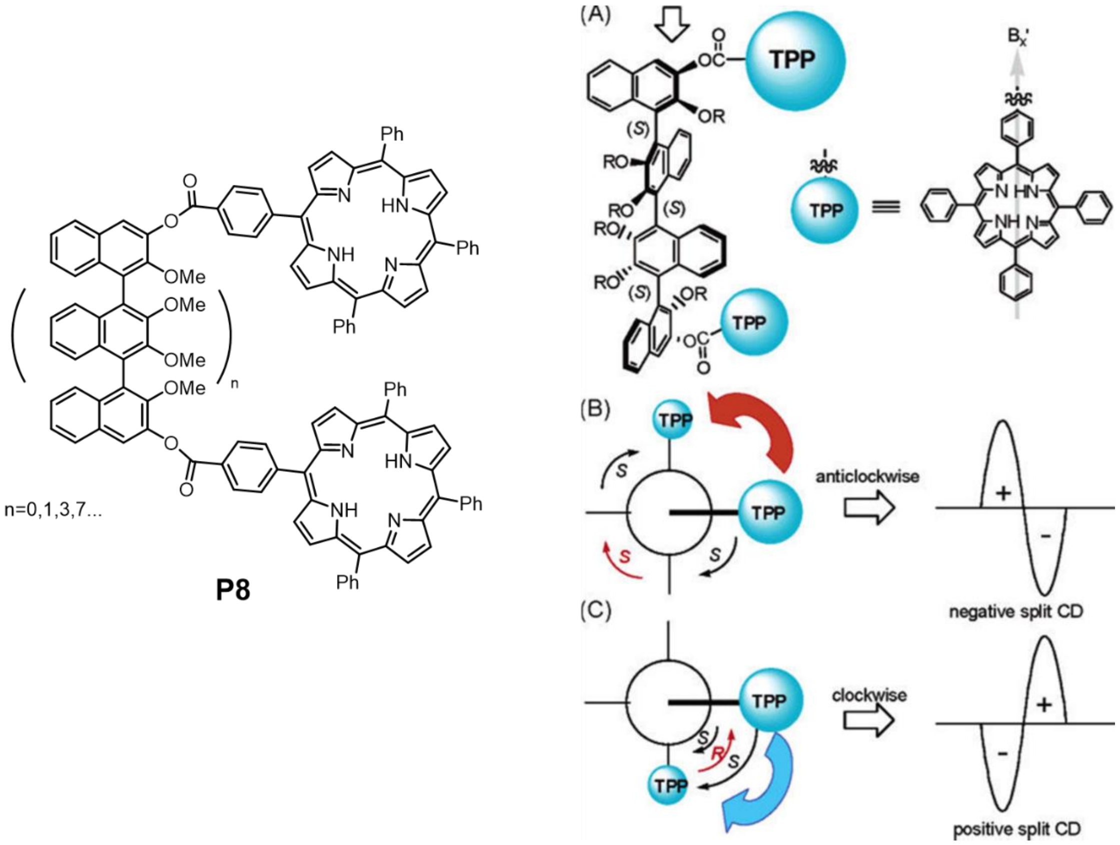
P8

Figure 17. Example of naphthalene-porphyrins oligomers (left). Schematic representation for the determination of the Absolute Configuration of Oligonaphthalenes illustrated by Tsubaki [37].

Since various functional biomolecules such as hemes, chlorophylls, and vitamin B12 contain porphyrins and related compounds within their active sites, the importance of biologically related units linked with this chromophore is increasing. These kinds of systems are useful as models for alternatively functionalized natural biomolecules which may have promising properties for application as chiral molecular receptors [38, 39, 40, 41, 42].

Chiral groups with higher flexibility can be utilized as spacers for various applications such as asymmetric catalysis and chirality sensing. The increased flexibility of the host, in terms of conformational freedom, enables it to effectively bind a broad range of chiral molecules. As an example, Sakai and co-workers introduced a porphyrin system that incorporates a chiral benzoate bridge, expanding the versatility of the host for these applications (**Figure 18**).

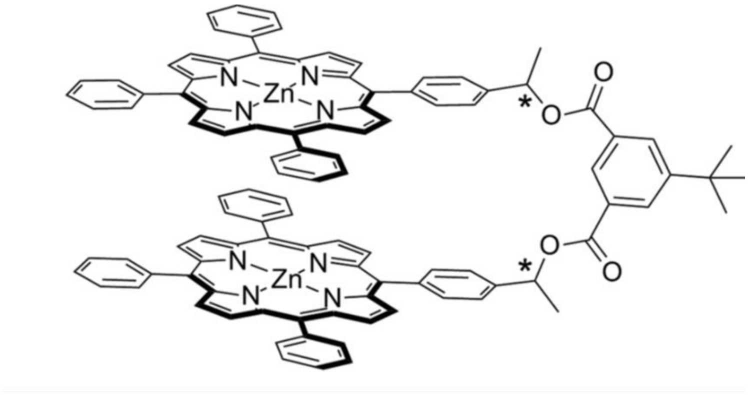

P9

Figure 18. Sakai's bis porphyrins system with chiral benzoate [41].

In the Soret band region, this strapped complex displayed oppositely signed Cotton effects of low intensity. Upon interaction with diamines, the CD signals were considerably increased, since the exciton coupling between the two porphyrin rings was enhanced [43].

I.3.4. Helicene-porphyrin conjugates.

Diverse helicene-porphyrinoids systems have been already reported in the literature, but none of these examples involves bis-porphyrin systems giving a clear EC response. For instance, T. J. Katz described the synthesis of phthalocyanines **Pc** fused with four enantiopure [7]helicenes **P10** through pyrazine functions ($|\Delta\varepsilon| = 120\ M^{-1}\ cm^{-1}$ at 423 nm and $|\Delta\varepsilon| = 19\ M^{-1}\ cm^{-1}$ at 481 nm for the Cu derivatives)[44] (**Figure 19**), while several years later, the group of B. K. Mandal prepared similar compounds, containing [5]helicenes and without the presence of pyrazine rings[45]. More recently, in 2021, P. Ravat extended this family of molecules by describing the design, stereospecific synthesis and self-assembly process of a [7]helicene-Zn phtalocyanine ($|\Delta\varepsilon| = 458\ M^{-1}mol^{-1}$ at 370 nm)[46]. These new compounds are named helicenocyanines and benzohelicenocyanines (**Figure 19**).

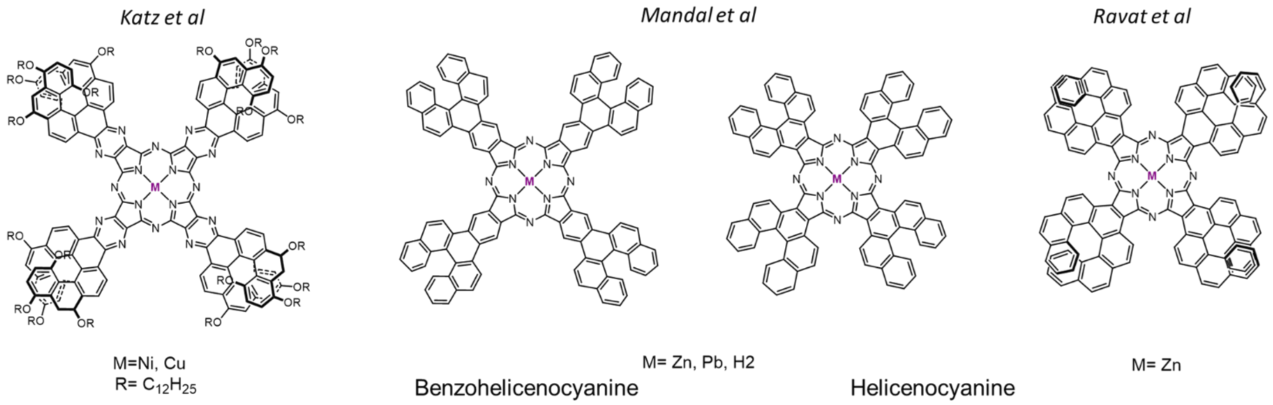

P10 **P11** **P12** **P13**

Figure 1912. Phtalocyanines reported by the group of T. J. Katz and helicenocyanines and benzohelicenocyanines described by B. K. Mandal and P. Ravat [44, 45, 46].

In 2018, the group led by A. Osuka successfully fused the macrocycle of a porphyrin with [n]helicenes (n = 4-6), where the presence of helicene made the chromophore chiral and induced chiroptical properties in the porphyrin. In the CD spectrum for the [6]helicene derivative **P16** displayed a Soret-like band ($\Delta\varepsilon = |140|$ M^{-1} cm^{-1} at 491 nm) whose intensity was comparable to that of the helicene signal ($\Delta\varepsilon = |98|$ M^{-1} cm^{-1} at 316 nm) [47] (**Figure 20**).

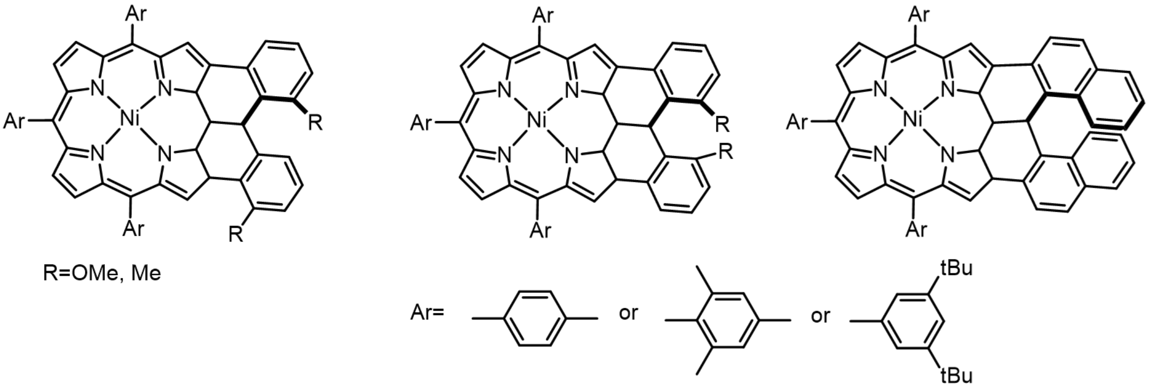

P14 **P15** **P16**

Figure 20. Helicene-porphyrin conjugate described by Osuka[47]

In the same year, the group led by L. Latos-Grażyński described the synthesis of carbaporphyrins incorporating [5]azahelicene motifs within the macrocycle [48].

More recently, in 2022, the group of Ruppert reported the synthesis of enantiopure helicene-fused and helicene-substituted porphyrins and their chiroptical properties [49], as depicted in **Figure 21**. Both compounds were separated by chiral HPLC and the presence of the helicene gave a symmetrical ECD response for the two enantiomers. Interestingly the fused-helicene derivatives displayed a red-shift (around 100 nm for the Soret band and the Q band) over the entire UV-visible area of the electronic spectrum.

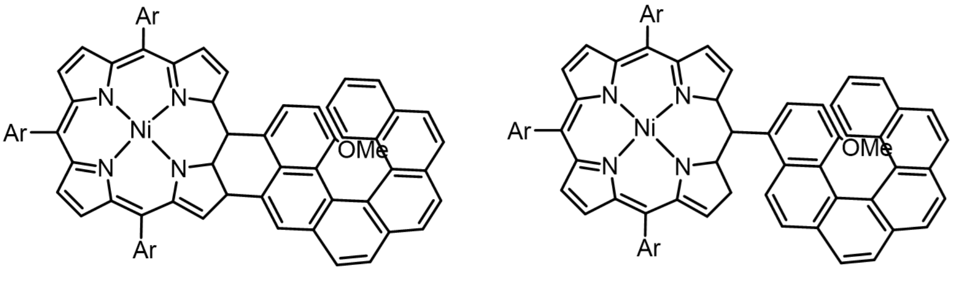

P17 **P18**

Figure 21. Helicene-fused porphyrin designed by Ruppert's group [49].

I.4. Application in spintronics

It is worth to point out that the choice of porphyrins as chromophores is not only related to the strong absorption and epsilon values, that are suitable for the EC, but also to those properties connected to the spintronic requests, such as the polarizabilities and the long spin relaxation time[50, 51, 52].

Naaman, Therien and co-workers combined, in 2019, a chiral molecule, which acts as spin filter, with a porphyrinic system as a non-chiral molecular wire that effectively maintains the spin polarization. The chiral helical unit they selected is (L-proline)$_8$ **Pro8**, which was used to obtain a self-assembled monolayer (SAM), as well as the same peptide conjugated to (porphinato)zinc or *meso*-to-*meso* ethyne-bridged (porphinato)zinc structures **PZn$_n$** with different lengths (**Figure 22**). These SAMs were examined by magnetic conducting atomic force microscopy (mc-AFM), spin-dependent electrochemistry, and spin Hall devices capable of measuring the spin polarizability that accompanies charge polarization.

The derivatives bearing the porphyrin wires exhibit higher Hall voltages than the simple **Pro8** and the charge polarization-induced spin polarization increases dramatically as the conjugation length of the achiral **PZn$_n$** component increases. Similarly, mC-AFM data show that the spin selectivity increases with the increasing **Pro8PZn1–3** length scale, highlighting that the difference between the effective barriers for the conduction of the two spin states of the electrons is amplified with augmented **PZn$_n$** polarizability [53].

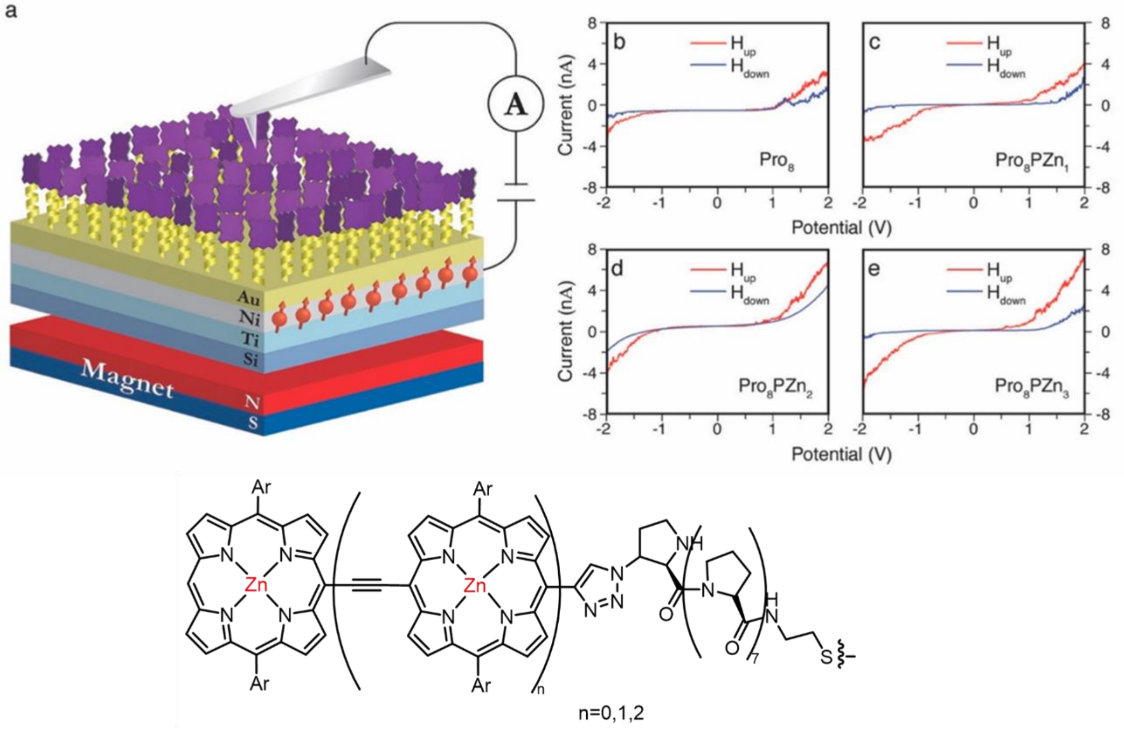

Pro$_8$Zn$_n$

Figure 22. a) Schematic representation of the mc-AFM setup together with the I-V curves; b) the structure of Pro8PZn$_n$. Adapted from ref [53].

The same authors published the synthesis and spin filtering properties of chiral porphyrin wires obtained from similar *meso*-to-*meso* ethyne-bridged multi[(porphinato)Zn oligomers coordinated to a chiral binaphthyl type binucleating ligand (**Figure 23**) [54].

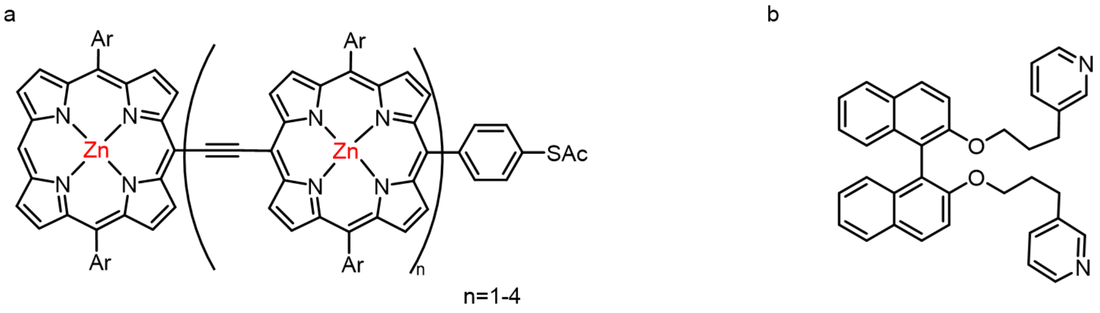

PZn$_n$SAc **B$_{R/S}$**

Figure 23. Structure of the meso-to-meso ethyne-bridged multi[(porphinato)Zn oligomers and of the racemic ligand.

The coordination to the chiral ligand engenders twisted chiral structures which express differential absorption of left- and right-handed circularly polarized light. While the ligands display symmetric CD signals that depend on their absolute chirality, the typical Cotton effect is absent for the porphyrin oligomers. In fact, the addition of the ligand generates a chiral interplanar torsional twist of adjacent planar porphyrin macrocycles.

The circular dichroism spectra of these systems highlight visible (Vis)–near-infrared (NIR) signals that intensify with increasing conjugation length (**Figure 24**).

The utility of **PZn$_4$SAc** and **PZn$_4$SAc-B$_{R/S}$** wires to generate and transmit spin-polarized currents was evaluated using magnetic-conductive atomic force microscopy (mc-AFM): SAMs of the achiral and chiral coordinated wires were grown on the typical Ni/Au substrate and a Pt-coated AFM tip was used to measure the spin current passing through the monolayers for the different magnetic field directions applied (UP or DOWN). The I-V curves showed that for the simple porphyrin oligomer no difference was evident when the direction of the magnetic field was changed, while the two derivatives bearing a different enantiomer as chiral ligand displayed an antisymmetric response. The spin polarization value was found about 32%.

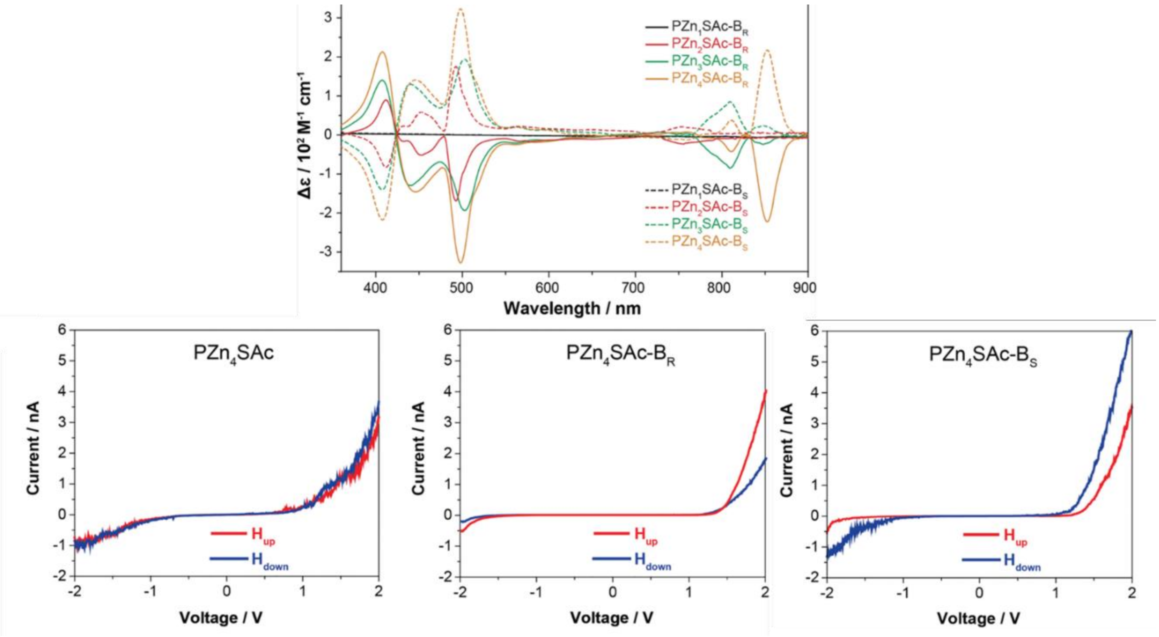

*Figure 24. ECD spectra of the different length derivatives (top) and I-V curves from mc-AFM for the racemic **PZn$_4$SAc** and the two enantiomers. Reproduced from ref [54].*

I.5. Targeted molecules: helicene-porphyrin conjugates

In this context, based on this knowledge and on the results obtained by our group in functionalizing carbo[6]helicene with DPP, we have designed novel bis-porphyrin derivatives using carbo[6]helicene as a chiral linker, to explore and rationalize the role of the helical π-conjugation in the EC phenomenon with the aim of enhancing the chiroptical activity.

We have prepared four distinct families of helicene-porphyrin derivatives by varying the spacing and conjugation between the chiral unit and the chromophore (**Figure 25**). The objective was to investigate the impact of these modifications on the chiroptical properties, particularly the ECD response through the EC chirality, and to exploit the enhancement of the chiral activity for CISS effect applications.

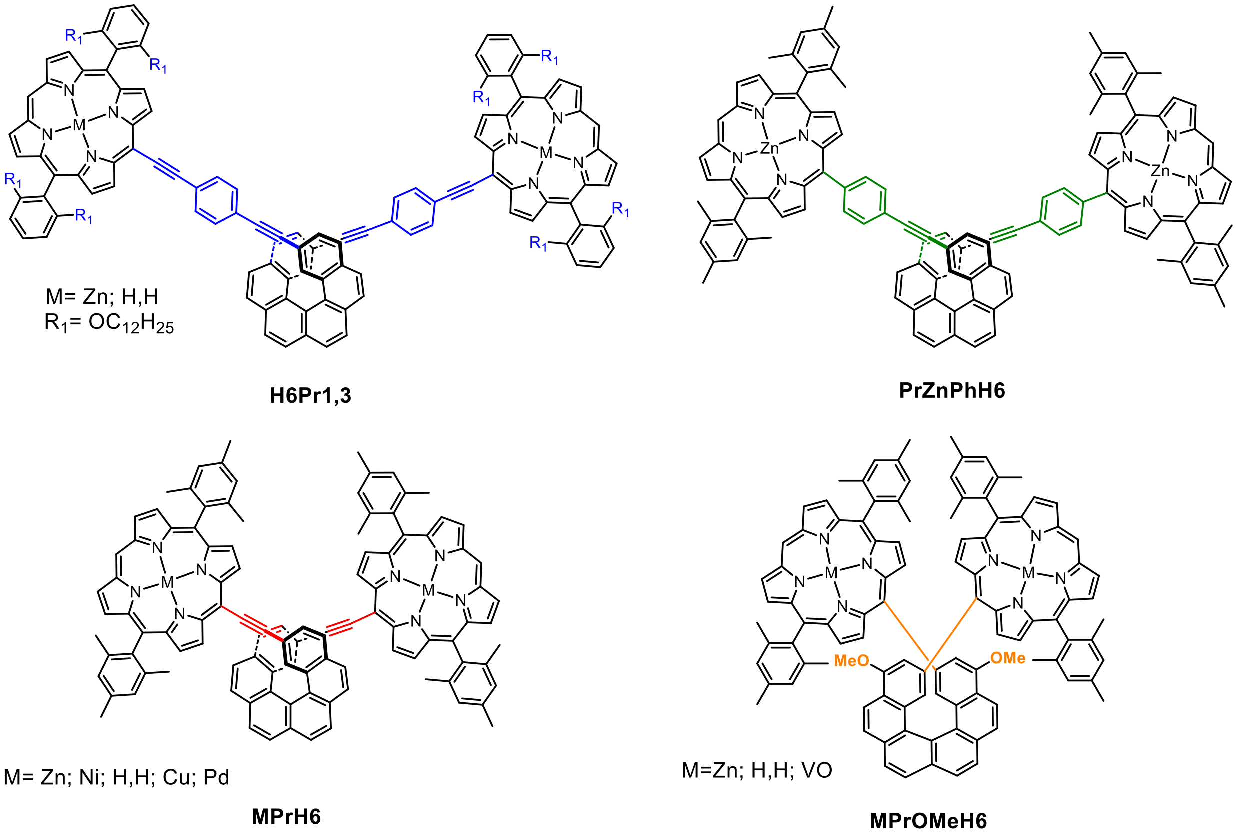

H6Pr1,3

PrZnPhH6

MPrH6

MPrOMeH6

Figure 25. Structures of the four different target systems

In this chapter we will focus on the derivatives bearing ethynyl-phenyl spacers between the helicene moiety and the chromophores such as **H6Pr** and **PrZnPhH6**.

The first system **H6Pr1**,**3** was designed starting from 2,15-bis-ethynyl carbo[6]helicene and 5,15-(di-2,6-dodecyloxyphenyl)porphyrin as precursors in order to confirm the role of the helicenic scaffold in the EC phenomenon and to explore the synergetic effect of helicenes and porphyrins in obtaining improved chiroptical properties. The achievement of a strong EC bisignature at the Soret band in the ECD spectrum, along with a CPL response, led to the rationalization of novel structures by using a less sterically hindered porphyrin, such as 5,15-(dimesityl)porphyrin, and by varying the linker between the chiral moiety and the chromophore. The variation of the spacer will be detailed in **Chapter 3**.

In a first step, by modifying the synthetic strategy, **PrZnPhH6** was prepared. The choice of a simple phenyl unit instead of phenyl-ethynyl in the spacer gave rise to a similar but less intense chiroptical activity.

II. Synthesis for the helicene-bis-porphyrin derivatives implying a spacer

II.1. Synthesis of H6Pr1-3 series

We have designed two different families of helicene-bis-porphyrin derivatives by varying the distance and the conjugation between the chiral moiety and the chromophore through a spacer, with the aim of investigating the influence on the chiroptical response. Each compound was synthesized in the two enantiomeric forms *P* and *M*, starting from the corresponding enantiopure helicene unit.

The first system has a 1,4-bis-(ethynyl)-phenyl conjugated spacer between the helicene building block and the porphyrin units. The strategy used involves two Sonogashira coupling reactions and it was carried out in collaboration with Dr. Kais Dhbaibi.
Indeed, the spacer was directly added to the 2,15-bis-ethynyl carbo[6]helicene (Chapter 1, Scheme1), via a first coupling with the ((4-iodophenyl)ethynyl)trimethylsilane, under classical conditions, followed by a deprotection of the triple bond, affording the 2,15-bis(4-ethynyl-phenyl-ethynyl)-carbo[6]helicene **H6PhH**. This product reacted with the previously prepared Zn brominated derivative of the 5,15-(di-2,6-dodecyloxyphenyl)porphyrin **PrZnBr^{OAlk}**, as shown in **Scheme 1**.

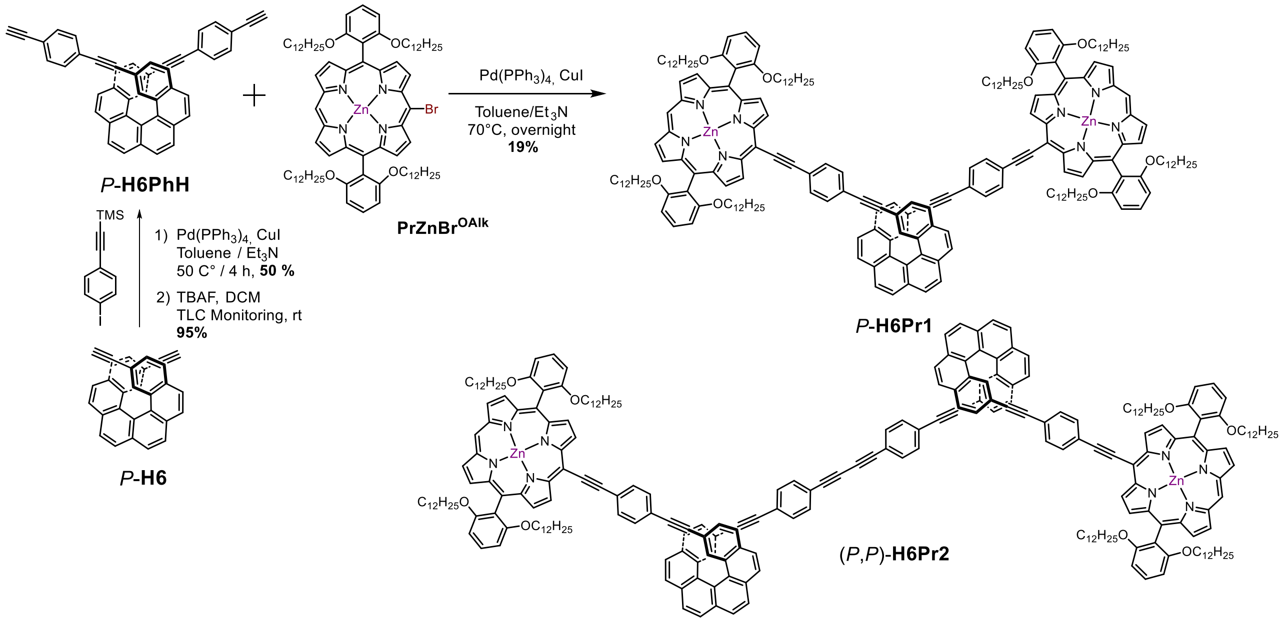

*Scheme 1. Synthetic pathway for the Zn derivatives of the family **H6Pr1** and **H6Pr2**.*

The classical Sonogashira cross-coupling reaction, under these conditions, gave the desired molecule **H6Pr1** with only a 19 % yield, due to the formation of side-products. Among them, the homocoupling of the mono-helicene-porphyrin intermediates was isolated in the two enantiopure forms (*P*,*P)* and (*M*,*M*)-**H6Pr2**. Additionally, the metal-free porphyrin analogue **H6Pr3** was also prepared in quantitative yield by treating **H6Pr1** with trifluoroacetic acid (**Scheme 2**).

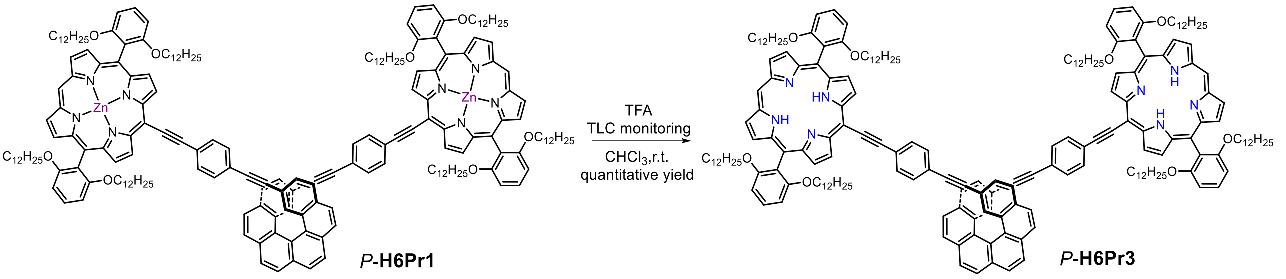

*Scheme 2. Synthesis of the free-base derivative **H6Pr3**.*

Compounds **H6Pr1**, **H6Pr2** and **H6Pr3** were fully characterized by ^1H and ^{13}C NMR spectroscopy, as well as by mass spectrometry.

The **H6Pr1** and **H6Pr3** molecules show limited sets of resonances In their ^1H NMR spectra, thus revealing the highly symmetrical nature of the obtained chiral porphyrin molecules (**Figure 26**). Indeed, only one set of signals is observed, confirming the formation of a C_2-symmetric bis-substituted 2,15-ethynyl-carbo[6]helicene compounds. In addition, for the metal-free porphyrin compound **H6Pr3**, a characteristic signal at -2.4 ppm corresponding to the -NH of the porphyrin moiety [55] was observed, confirming the efficiency of the demetallation reaction (see experimental part).

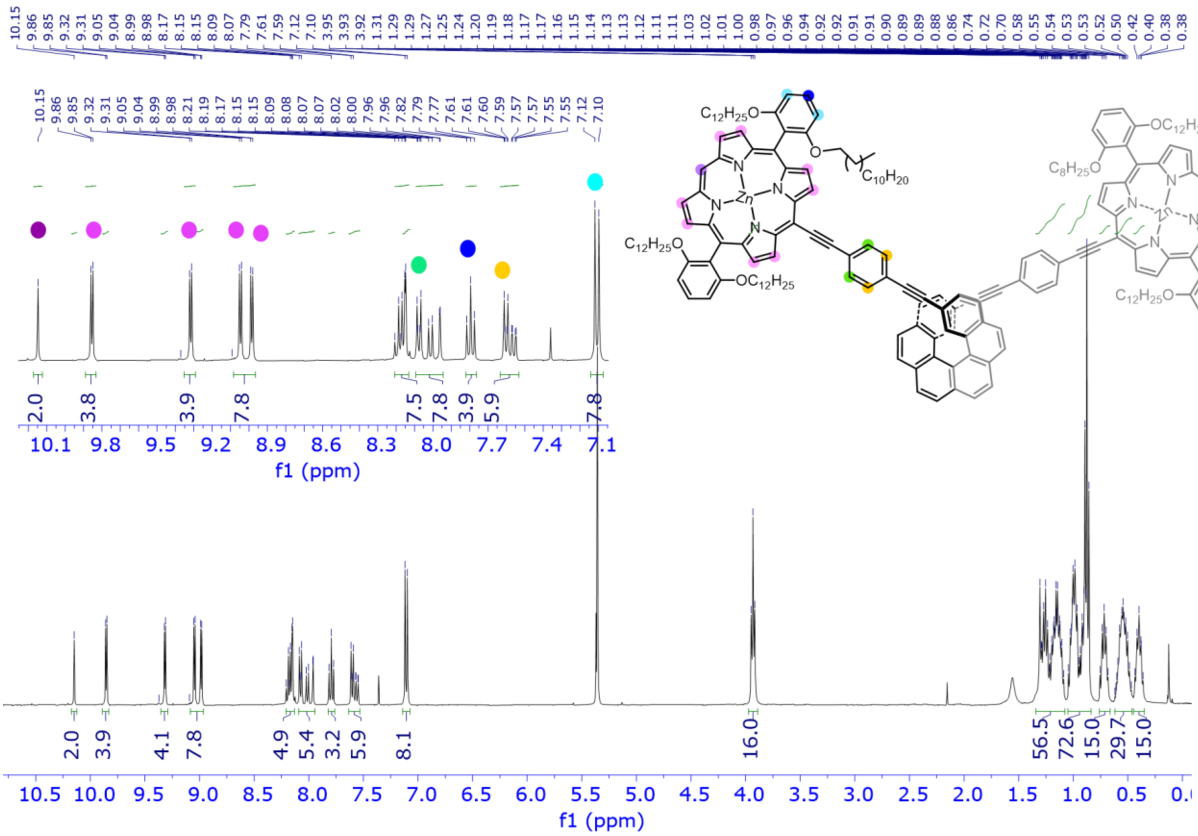

*Figure 26. ^1H-NMR spectrum of **H6Pr1** ($CDCl_3$, 400 MHz, 298 K).*

The ^{1}H-NMR spectra exhibit the characteristic patterns of both the helicene (between 7.5 and 8.4 ppm) and porphyrin (from 8.9 to 10.1 ppm) moieties. 2D NMR experiments allowed us to identify and assign the resonance picks of the β-pyrrolic protons, which fall within the proton at the range of 9.00 to 9.85 ppm, as well as the deshielded proton at 10.15 ppm corresponding to the free *meso* position in the porphyrin core, and the carbon atoms (91 and 89 ppm) of the two ethylenic units.

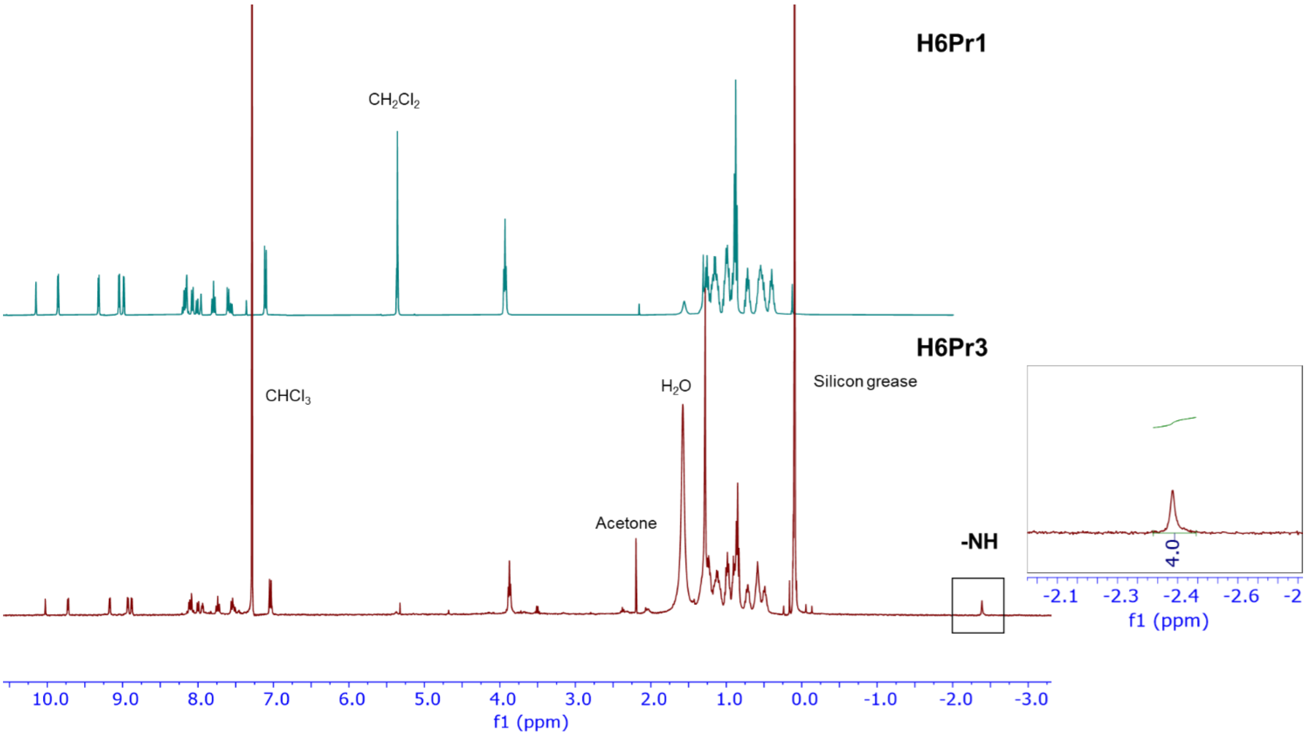

*Figure 27. ^{1}H-NMR spectrum of **H6Pr1** (top) and **H6Pr3** (bottom) in $CDCl_3$ (400 MHz, 298 K).*

The Glaser coupling product **H6Pr2** shows the same ^{1}H-NMR pattern, except for an additional doublet at 7.40 ppm, corresponding to the proton in the ortho position of the phenyl spacer linked to the ethynyl group (see experimental part). Thus, they are no longer chemically equivalent to those of the other spacer.

II.2. Synthetis of ZnPrPhH6

On the basis of these results, we decided to avoid the homocoupling side-products by performing a Suzuki-Miyaura cross coupling reaction. In order to adapt the 2,5-bis-ethynyl carbo[6]helicene precursor for the Suzuki-Miyaura coupling, a reaction with the spacer 1-bromo-4-iodobenzene allowed us to obtain the halogenated species **BrH6** (a) in Scheme 3 in 68% yield. On the other hand, the 5,15-(dimesityl)porphyrin was brominated, metalated and borylated with 4,4,5,5-tetramethyl-1,3,2-dioxaborolane **PrZnBEster** [56] to give the corresponding boronate ester. The so-obtained compounds were subjected to a Suzuki cross-coupling reaction to get the desired molecule **PrZnPhH6** in a 40% yield (b) as shown in **Scheme 3**.

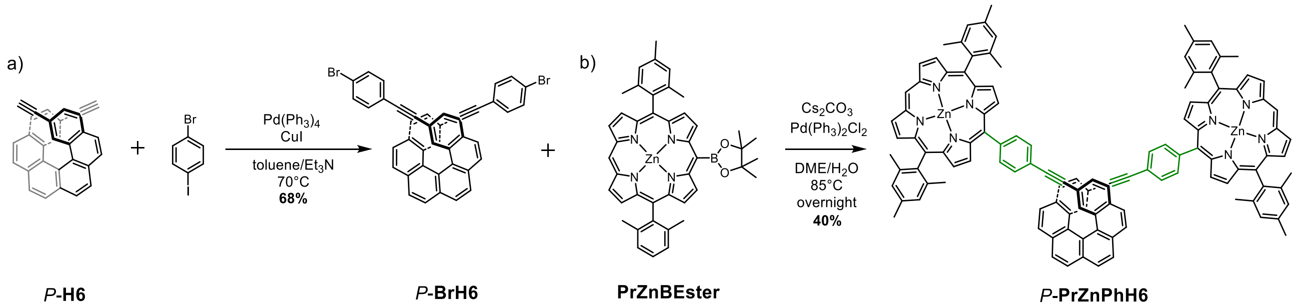

Scheme 3. a) Synthetic route for the helicene derivative ***BrH6****; b) Suzuki coupling between the helicene and the porphyrin to obtain* ***PrZnPhH6****.*

As for the previously described **H6Pr1**, the ^{1}H-NMR illustrates the typical signals for the helicene moiety and the two doublets of the phenyl protons of the spacer at 8.26 and 7.78 ppm, respectively. The porphyrin core presents the same set of peaks as the previous compound **H6Pr-1**, with the proton of the free *meso* position resonating at 10.21 ppm and the β-pirrolic ones represented by the four doublets from 9.38 to 8.88 ppm. Since the porphyrin substitution has been modified, we observed in this case, a singlet at 7.34 ppm corresponding to the aromatic protons of the mesityl unit, as well as two singlets at 1.88 and 2.69 ppm for the -CH$_3$ in ortho- and para- position of the mesityl unit, respectively.

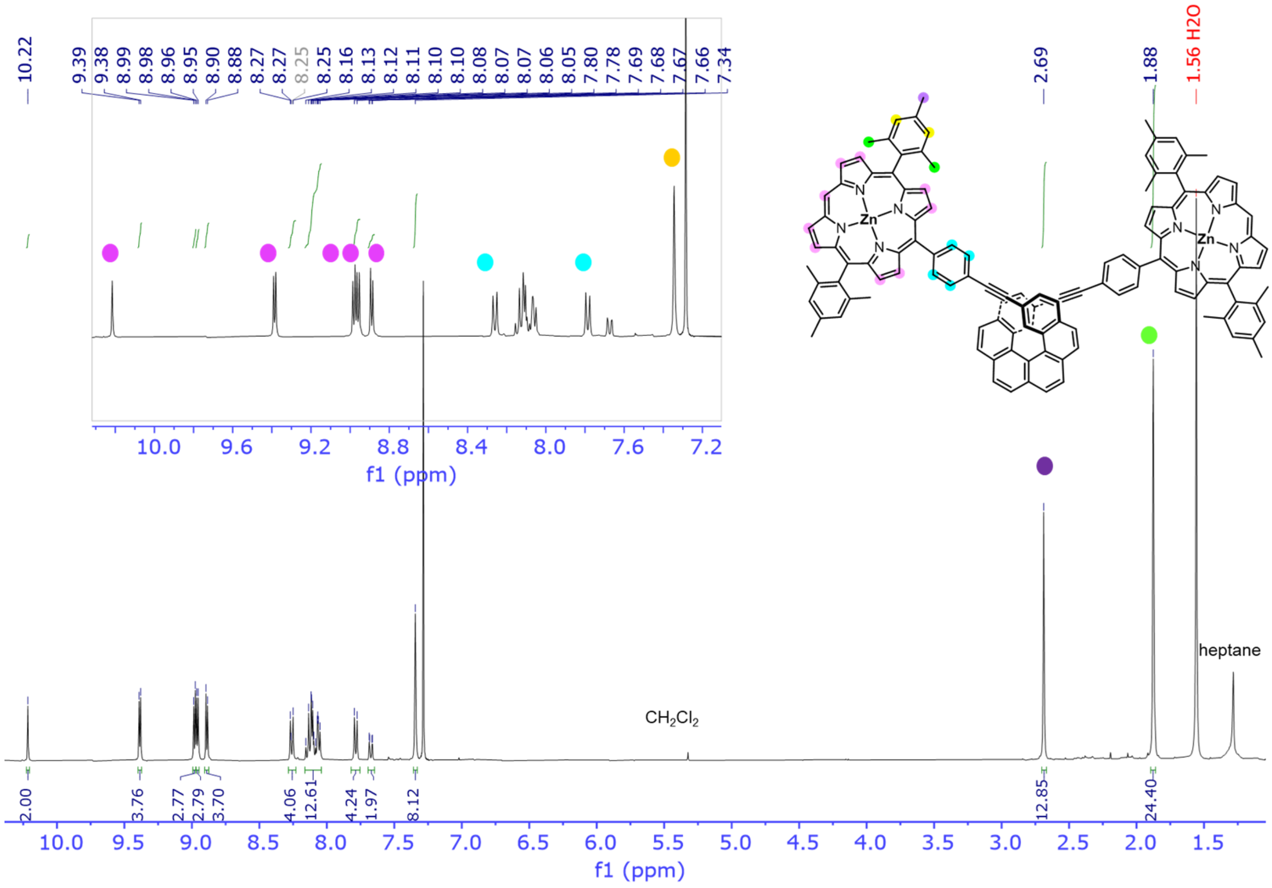

Figure 28. ^{1}H-NMR spectrum of ***PrZnPhH6*** *(CDCl$_3$, 400 MHz, 298 K).*

III. Optical and chiroptical properties of the spacer-bearing derivatives

III.1. UV-vis and ECD spectra of the H6Pr1 series

The UV-visible absorption and electronic circular dichroism (ECD) spectra of **H6Pr1**, **H6Pr2**, and **H6Pr3** are presented in **Figures 29** along with the structures of the three compounds. The measurements were performed in 10^{-5} M dichloromethane solutions.

It is worth saying that, concerning the porphyrin features, a theoretical description for the absorbance spectrum was reported by Gouterman with his four-orbitals model [8]. According to this theory, the absorption bands in porphyrin systems arise from transitions between two HOMOs and two LUMO orbitals, and it is the identities of the metal center and the substituents on the ring that affect the relative energies of these transitions. Mixing splits these two states in energy, creating a higher energy state with greater oscillator strength, giving rise to the Soret band (S2 ← S0 transition), and a lower energy state with less oscillator strength, that corresponds to the Q-bands (S1 ←S0 transitions).

In the high-energy region (below 460 nm), the three compounds exhibit similar characteristic features. Specifically, absorption bands are observed at 298 nm (ε = 68800 M^{-1} cm^{-1}), 345 nm (ε = 49700 M^{-1} cm^{-1}), and 361 nm (ε = 43000 M^{-1} cm^{-1}), which can be assigned to π-π* transitions of the helicene unit. Additionally, a prominent absorption peak at 440 nm (ε = 480000 M^{-1} cm^{-1}) corresponds to the Soret band arising from the two porphyrin units.

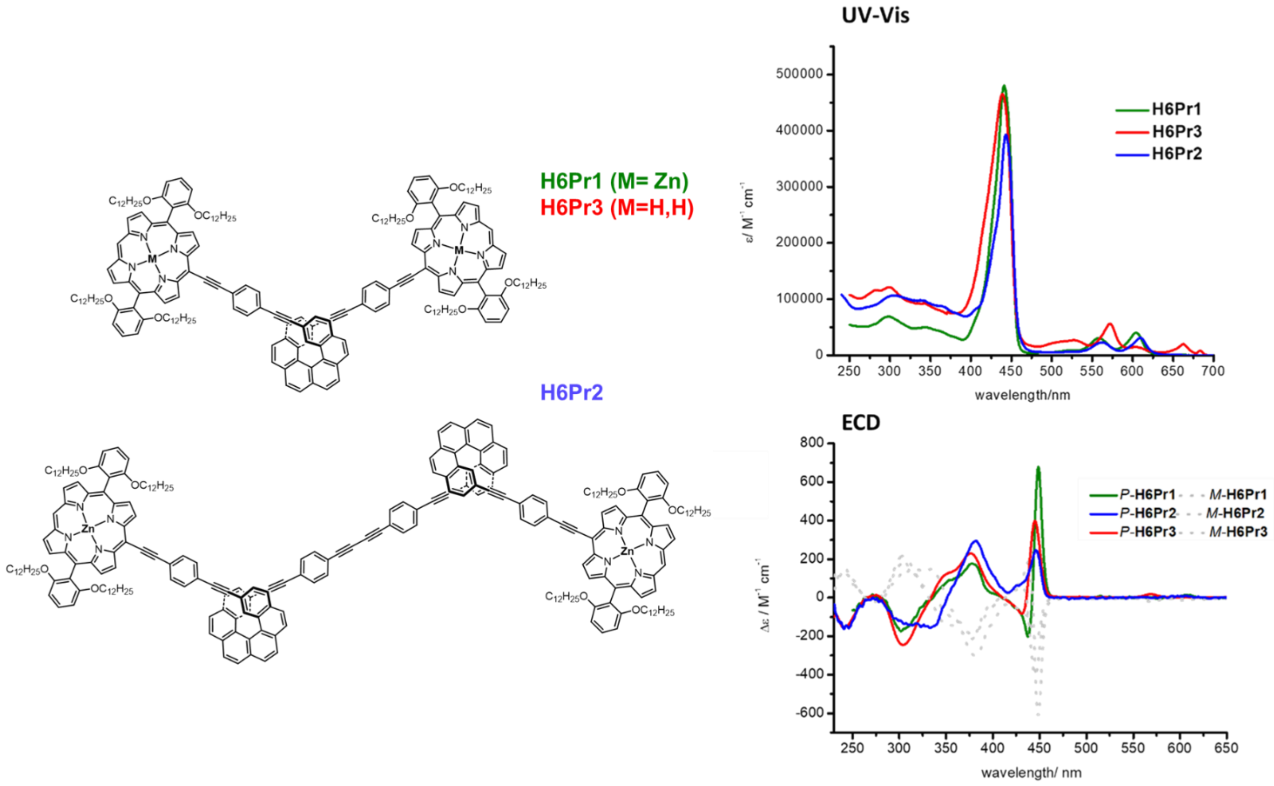

Figure 29. Absorption (top) and ECD (bottom) spectra of the three derivatives ***H6Pr1-3*** *in CH_2Cl_2 solution at 298 K.*

Moving to the low-energy region of the spectrum, distinctive porphyrin Q bands are observed. For the Zn porphyrins (**H6Pr1** and **H6Pr2**), two distinct signals are observed at 558 and 604 nm, whereas for the free-base chromophores (**H6Pr2**), four signals are observed at 525 nm, 575 nm, 662 nm, and 688 nm. All these signals exhibit relatively strong intensities (ε = 30600 - 40000 M^{-1} cm^{-1}), as expected for such chromophores.

Interestingly, each of these bands is active in CD spectroscopy, with the *P*-**H6Pr1** enantiomer displaying the typical negative (Δε -172 M^{-1} cm^{-1} at 302 nm) and positive bands (+89 and +175 M^{-1} cm^{-1} at 352 and 378 nm, respectively) of the helicenic part, and a clear bisignature (-200 at 438 nm and + 671 M^{-1} cm^{-1} at 449 nm) corresponding to EC coupling chirality of the Soret band. Thus, we unambiguously confirm the presence and effectiveness of exciton coupling chirality in helicenes (*vide infra*). It is worth to note that the Q band at 605 nm is also CD-active (Δε +14 M^{-1} cm^{-1}).

P-**H6Pr3** displays a slightly more intense but otherwise similar ECD below 430 nm as *P*-**H6Pr1**, such as a negative band at 304 nm (Δε -245 M^{-1} cm^{-1}) followed by positive ones (+120 and +230 M^{-1} cm^{-1} at 352 and 378 nm, respectively). The excitonic coupling signature was found also for the free porphyrin *P* enantiomer with a positive Cotton effect in the porphyrin Soret band (Δε -82 and +393 M^{-1} cm^{-1} at 430 and 446 nm, respectively) and the Q bands at 570 and 654 nm appeared also CD active (Δε +18 M^{-1} cm^{-1} and 6 M^{-1} cm^{-1}, respectively).

The Glaser product, **H6Pr2**, consisting of two porphyrin-ethynyl-phenyl-ethynyl-hexahelicenyl units connected by two phenyl-ethynyl bridges, obtained as by-product of the Sonogashira coupling, show absence of EC chirality in *P* and *M*-**H6Pr2** since, in this case, the Soret band displays only one CD-active signal at 446 nm (Δε +228 M^{-1} cm^{-1}) and no apparent significant exciton coupling due to the very long distance between the two porphyrin cores. Other CD active bands are found at 334 (-150) and 380 nm (+289), which correspond to the helicenic parts. Note that the negative band originating from the helicene units is strongly red-shifted compared to **H6Pr1** and the **H6PhH** precursor, most probably as a result of strongly extended π-conjugation of the molecule.

These results nicely illustrate how molecular engineering using either extended π-conjugation (**H6Pr2**) or functionalization with strongly polarizable units in close proximity (**H6Pr1** and **H6Pr3**) enables fine tuning of the chiroptical signatures.

III.1.1. Calculated UV-vis spectra

In order to obtain more insights about the electronic transitions responsible for such UV-Vis and CD features, TD-DFT calculations were performed with Gaussian 16 program, LC-PBE0 functional, def2-SV(P) basis and the solvent (dichloromethane) polarizable continuum model (PCM) in collaboration with Dr. Laura Abella and Prof. Jochen Autschbach from University of Buffalo (USA). To simplify the analysis, calculations were carried on a truncated system of **H6Pr1**, where the $Ph(OR)_2$ substituents at the Zn-porphyrin units were replaced by chlorine atoms, denoted here as **H6Pr1**-Cl. In fact, several test calculations showed nearly perfect agreement between the CD spectrum of **H6Pr1**-Cl and that of a larger model for **H6Pr1** including the phenyl rings below 250 nm, owing to the fact that the phenyl rings are perpendicular to the Zn-porphyrin planes and are therefore not part of the π-chromophore. Moreover, the UV transitions of phenyl are weakly intense and do not cause significant exciton coupling in **H6Pr1**. Hence, **H6Pr1**-Cl is a good model for **H6Pr1** for the purpose of this study.

The calculated broadened absorption spectrum of **H6Pr1-Cl** agrees very well with the experimental spectrum for **H6Pr1**. The peaks are systematically blue shifted by 0.3 eV in the calculations (**Figure 30**), which is not uncommon.

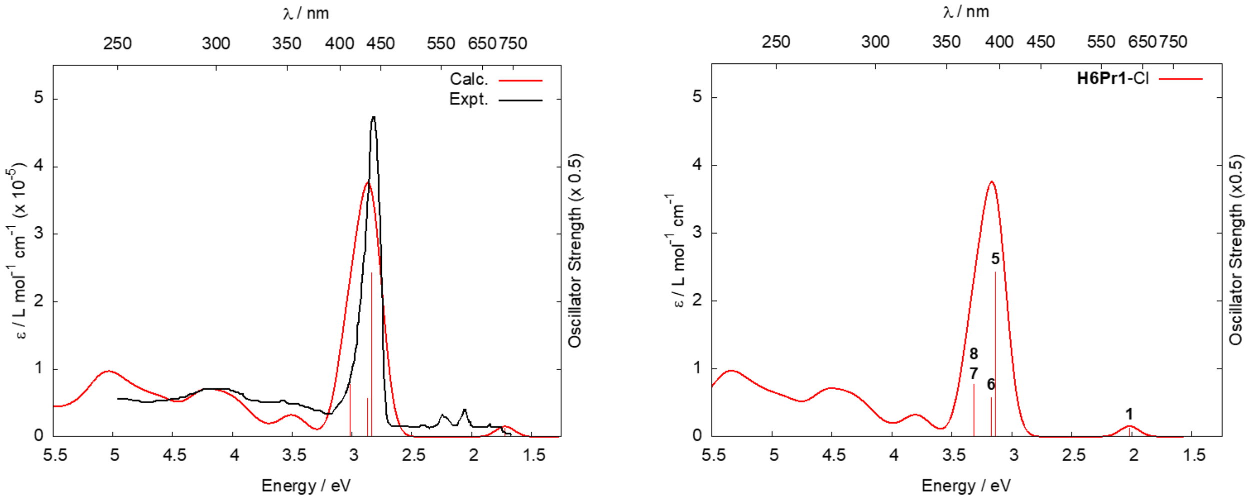

*Figure 30. Left side: Experimental (black) vs. calculated (Calc.) absorption spectra for **H6Pr1**. Right side: Calculated absorption spectrum for **H6Pr1**-Cl. Selected transitions and oscillator strengths indicated as 'stick spectra'. Predominant transitions for **H6Pr1**-Cl are numbered according to Table 1.*

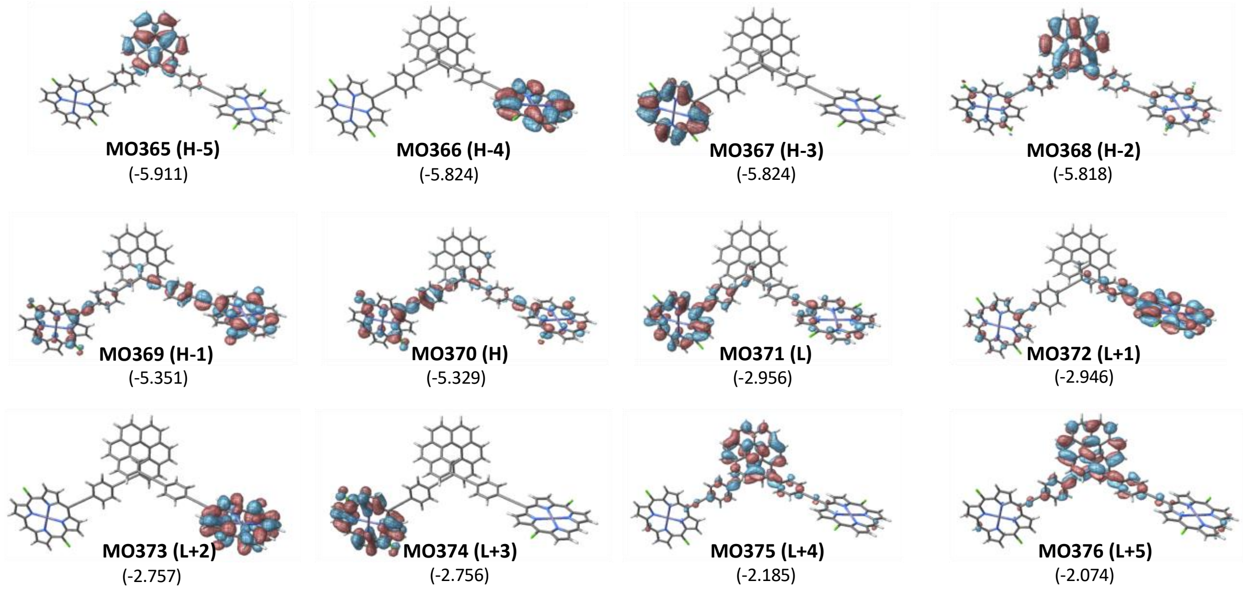

*Figure 31. Isosurfaces (±0.020 au) of Molecular Orbitals (MOs) involved in the selected transitions for P-**H6Pr1**-Cl. Values listed in parentheses are the corresponding orbitals energies in eV. H and L indicate the HOMO and LUMO, respectively.*

*Table 1. Selected excitations and occupied (occ)-unoccupied (unocc) MO pair contributions (greater than 6%) for P-**H6Pr1**-Cl. H and L indicate the HOMO and LUMO, respectively*

Excitation	E [eV]	λ [nm]	*f*	R [10^{-40} cgs]	occ. no.	unocc no.	%
#1	2.018	614	0.264	135.9	370 (H)	371 (L)	23
					367	374	14
#2	2.024	613	0.082	-108.1	369	372	19
					368	373	15
#5	3.136	395	4.882	2998.5	367	374	19
					370	371	10
#6	3.171	391	1.165	-2585.8	368	373	19
					367	374	10
#7	3.313	374	1.271	3980.2	367	371	24
					370	374	20
#8	3.317	374	1.569	-3885.8	368	372	24
					369	373	20
#10	3.772	329	0.182	757.9	365	376	16
#11	3.820	325	0.316	-516.4	366	376	12
					365	375	8
#13	4.172	297	0.311	122.4	365	376	6
					366	375	6
#21	4.329	286	0.143	-268.4	365	377	7
#22	4.351	285	0.422	-217.4	355	372	6
#23	4.505	275	0.279	-446.5	366	376	7

The weak lowest energy/longest wavelength band (614 nm) in the **H6Pr1** spectrum is caused by an effectively degenerate pair of transitions, #1 and #2, which correspond to an exciton coupled set of porphyrin Q band transitions. The Molecular Orbitals (MOs) contributing to these transitions are composed of in-phase and out-of-phase π and π^* porphyrin fragment frontier orbitals (FFOs). The small energetic splitting indicates that the FFOs are only weakly coupled. The frontier MOs (FMOs) in **H6Pr1-Cl** are mostly localized on the porphyrins, but several of the MOs also extended over the π-conjugated systems of the phenyl (Ph) ring and the alkynyl groups in the spacer, and reach into the helicene (**Figure 31**). These MOs are therefore clearly perturbed, relative to isolated Zn-porphyrin. The second set of excitations, #3 and #4, around 2.1 eV, is assigned to coupling of the remaining Q-band porphyrin transitions.

The Soret band has 4 underlying transitions in the calculation, and formally arise from the coupling of the two $\pi \rightarrow \pi^*$ B-band excitations in each porphyrin. Excitation #5, at 395 nm, has by far the largest oscillator strength (4.882), and the leading contributions involve MOs that are mostly, but not entirely, porphyrin centered. Excitations #6 and #8, under the same band, have important contributions from the HOMO-2, which is a helicene π-orbital. The excitations therefore have mixed character of helicene-to-porphyrin charge transfer (CT) and porphyrin $\pi \rightarrow \pi^*$. Bands below 350 nm are of strongly mixed character, varying porphyrin–spacer–helicene contributions.

III.1.2. Calculated circular dichroism (CD)

The calculated CD spectrum of **H6Pr1**-Cl is in very good agreement with experiments, with the same 0.3 eV shift as described for the UV-Vis spectrum, (**Figure 32**) and the assignment of the CD bands are in line with the absorption peaks.

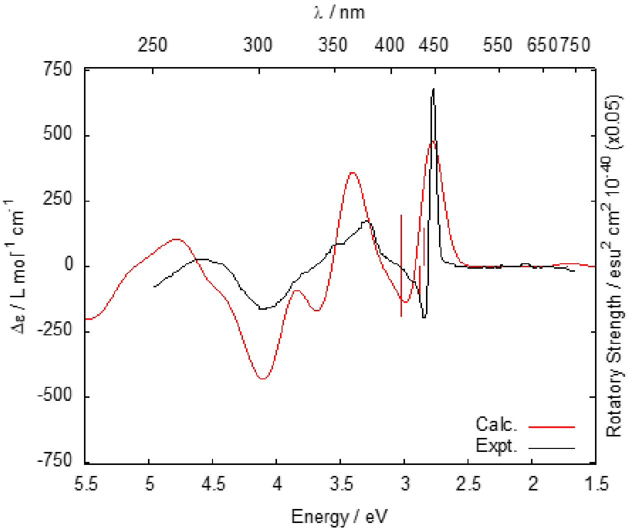

*Figure 32. Experimental (black) vs. calculated (Calc.) electronic circular dichroism (ECD) spectra for P-**H6Pr1**. Selected transitions and rotatory strengths indicated as 'stick spectra'. The computed spectrum is red-shifted by 0.3 eV.*

It is important to highlight that the distance between the two Zn^{2+} ions is evaluated to be around 20 Å, a length consistent with good interactions between the electric transition dipole moments. Therefore, the fundamental point is to determine how much of the intensity of the peak seen in the experimental CD spectrum at around 450 nm of the pure enantiomer of **H6Pr1** is a result of exciton coupling of the Zn-porphyrin B-band transitions. To this end, calculations were performed on different dimers in the same arrangement as in the model for *P*-**H6Pr1**, with increasingly large fragments in the center of the molecule removed, and dangling bonds capped with hydrogen.

The gradual increase of the chromophore extension in the series of models leads to the lowering of energy of the excitations of porphyrin B-band parentage, such that in the largest dimer, **(Pr1-alkynyl-Ph-alkynyl)$_2$**, the intense positive/negative pair of CD bands is almost aligned with those of P-**H6Pr1**-Cl (**Figure 33**).

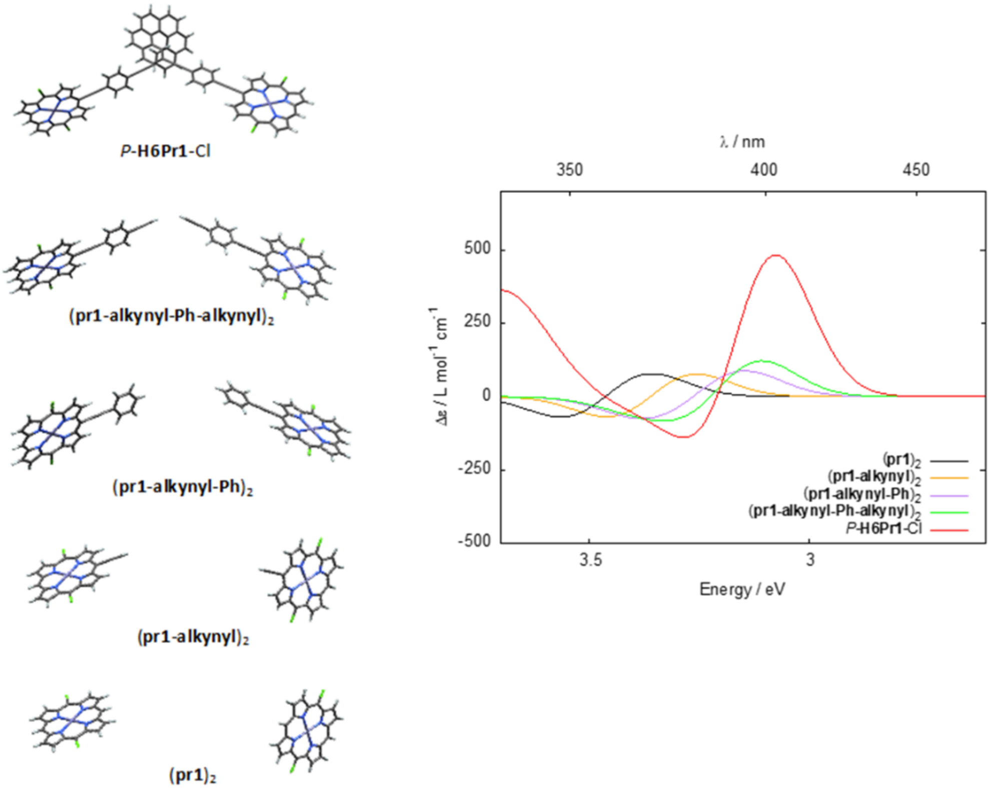

Figure 33. Models of the dimers used for determining the EC intensity.

However, the presence of the helicene evidently plays a crucial role, as the intensity of the exciton CD couplet is much larger in the full system. For further analysis, theoreticians set up a dipole coupling model for the exciton CD, based on the excitations of a truncated version of *P*-**H6Pr1**-Cl (labeled as mono-**H6Pr1**-Cl) in which the [6]helicene is fully intact, but one of the Zn-porphyrins is removed. A visual comparison of the simulated CD spectrum for mono-**H6Pr1**-Cl reflects similar features as the corresponding experimental spectrum of **H6Pr2** (the homocoupling product showing no exciton coupling) and the calculated CD band at 390 nm is much weaker than for **H6Pr1**-Cl.

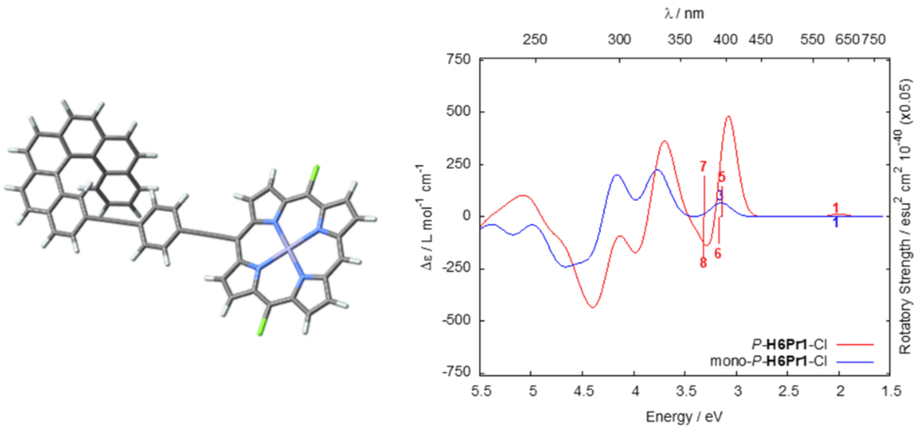

*Figure 34. Truncated version of **P-H6Pr1-Cl** with only one porphyrin and its simulated CD spectrum.*

In conclusion, we can claim that the theoretical calculations confirm that the exciton coupling effect is present in the absorption and CD spectra. It was verified with a truncated model calculation based on the electric transition dipole moments of the mono-substituted *P*-**H6Pr1**-Cl and also with different dimers of *P*-**H6Pr1**-Cl. The models reveal that the long-wavelength band between 360 and 450 nm is originated from exciton coupling between the electric transition dipoles of the porphyrin moieties of **H6Pr1**-Cl with some contributions of the central part of the helicene.

III.2. Total luminescence and CPL of the H6Pr1 series

The total luminescence and CPL of the three compounds were also studied in 10^{-5} M dichloromethane solutions at room temperature, with an excitation wavelength of 440 nm, corresponding to the Soret band in the CD spectra (**Figure 35**).

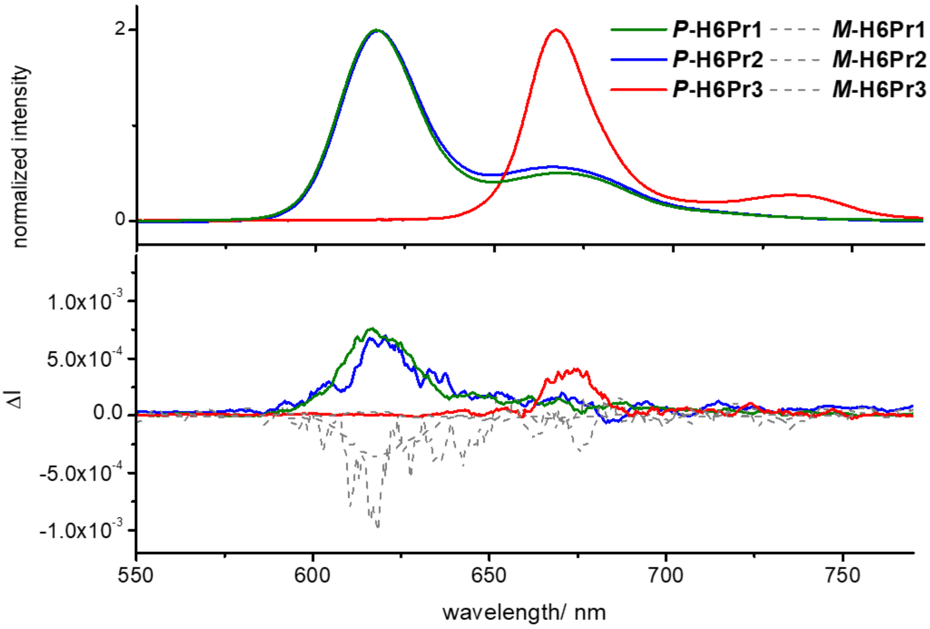

*Figure 35. Total luminescence and CPL spectra in CH_2Cl_2 10^{-5} M solution of **H6Pr1, H6Pr2, H6Pr3**.*

The total luminescence spectrum (on top of **Figure 35**) of the three derivatives illustrates two emission bands: **H6Pr1** and **H6Pr2** show a stronger band at 610 nm and a weaker band at 670 nm, while the free-base compound **H6Pr3** exhibits a red-shifted emission (Δ = 60 nm). These emission peaks arise from the porphyrin transitions. More specifically, since the internal conversion from S2 to S1 is rapid, fluorescence results from the S1 to S0 transitions and they are consistent with the typical luminescence pattern of this chromophore [57].

Moreover, all of the molecules reveal a moderate CPL response, with only one CPL-active emission band (at 610 nm for **H6Pr1** and **H6Pr2**, and 670 nm for **H6Pr3**), and a dissymmetry factor, g_{lum}, around 10^{-4}.

The fluorescence quantum yields were experimentally obtained using tetraphenylporphyrin, TPP, in dichloromethane as reference (ϕ = 0.13) [58]. The different values are depicted in Table 2, along with the dissymmetry factor g_{lum}.

Compound	PLQY^{a}	g_{lum} ^{b} (λ_{ex} = 440 nm)	B_{CPL} ^{c} (M^{-1} cm^{-1})
H6Pr1	0.16	±7.10^{-4}	26
H6Pr2	0.25	±7.10^{-4}	34
H6Pr3	0.22	±2.10^{-4}	10

*Table 2. a) Relative quantum yield of **H6Pr1-3**, TPP in dichloromethane as reference; b) dissymmetry factor, g_{lum}, of each compound; c) CPL brightness calculated from reference [59]:* $B_{CPL} = \varepsilon_{ex} \times \varphi \times {}^{g_{lum}}/_{2}$

Thus, we proved that exciton coupling chirality is a suitable tool to tune helicene response and increase the chiroptical properties of this moiety, obtaining an emissive helicene derivative in the near-infrared region and CPL-active porphyrins, that are quite rare in literature [60, 61].

III.3. UV-vis and ECD spectra of PrZnPhH6

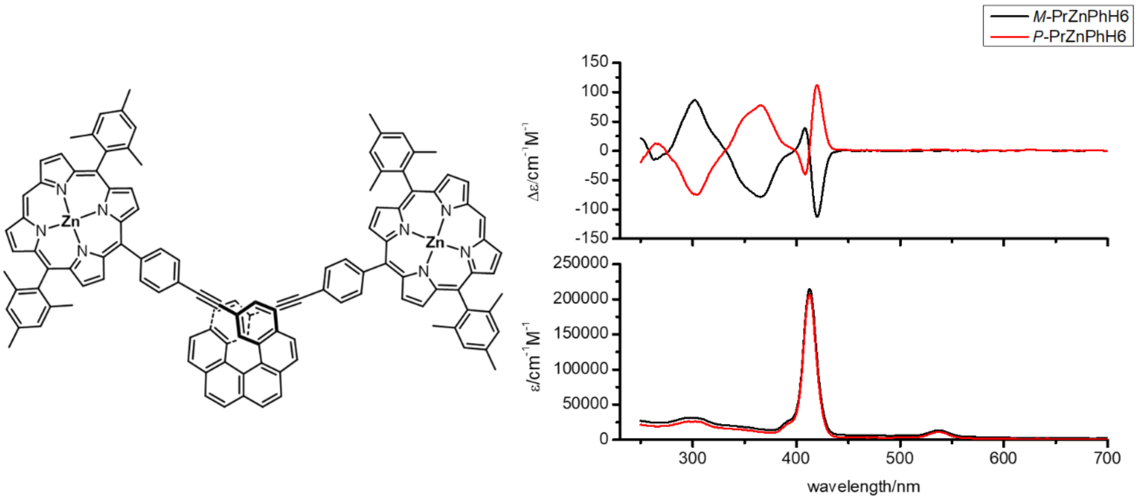

*Figure 36. Absorption (bottom) and ECD (top) spectra of **PrZnPhH6** in CH_2Cl_2 solution at 298 K.*

As depicted in **Figure 36** the absorption spectrum of **PrZnPhH6** shows features very similar to the **H6Pr1** series. In the high-energy region, three absorption bands are observed at 300 nm (ε = 31260 M^{-1} cm^{-1}), 360 nm (ε = 16780 M^{-1} cm^{-1}), and 387 nm (ε = 20000 M^{-1} cm^{-1}), which can be assigned to π-π* transitions of the helicene unit; the Soret band appears at 414 nm (ε = 210755 M^{-1} cm^{-1}) and moving towards the low-energy region of the spectrum one signal for the Q bands of Zn porphyrins is observed at 541 nm (ε = 12860 M^{-1} cm^{-1}).

As expected, due to the variation in the conjugation extent within this system, the signals undergo a blue shift of about 30 nm, and the molar extinction coefficient (ε) values are lower compared to the previously described derivatives. It is also worth to consider that the porphyrin itself bears different para-substituents on the phenyl in *meso* position: it is known that small shifts in the absorption maxima occur as the result of substitution of various polar groups in the para-positions of tetraphenylporphyrins, for example by increasing or decreasing the electron density in the ortho and para in the benzene rings in the *meso* positions [62].

Concerning the CD spectrum, the helicenic part is characterized by the typical negative ($\Delta\varepsilon$ = -73 M^{-1} cm^{-1} at 300 nm) and positive signals ($\Delta\varepsilon$ = + 12 and +75 at 267 and 369 nm, respectively) for the *P* enantiomer (opposite sign values are depicted for *M*-**PrZnPhH6**), as well as the bisignature of the exciton coupling corresponding to the Soret band ($\Delta\varepsilon$ = -38 at 407 nm and +112 at 420 nm). The overall ECD bands intensities are however more than twice as low, revealing the beneficial implication of the triple bonds in the π-conjugated pathway and in the resultant optical activity.

III.4. Total luminescence and circularly polarized luminescence of PrZnPhH6

The total luminescence spectrum of PrZnPhH6, measured by the CPL apparatus, shows two bands, a lower intensity band at 600 nm and a major one at 638 nm, which opposite intensity as for the previously described **H6Pr1** compound series. In addition, **PrZnPhH6** is also CPL active, as illustrated in **Figure 37**, with a g_{lum} value of ± 1×10^{-3} but with a noisy signal. The photoluminescence quantum yield was also calculated in dichloromethane, using again TPP as reference, and a value of 0.08 was obtained. This value is smaller compared to **H6Pr1** series, highlighting the importance of the triple bond present in the spacer to obtain strong emission through a stronger π-conjugation pathway. Note also that the brightness is much lower in **PrZnPhH6** than in the **H6Pr1-3** series (see **Tables 2** and **3**).

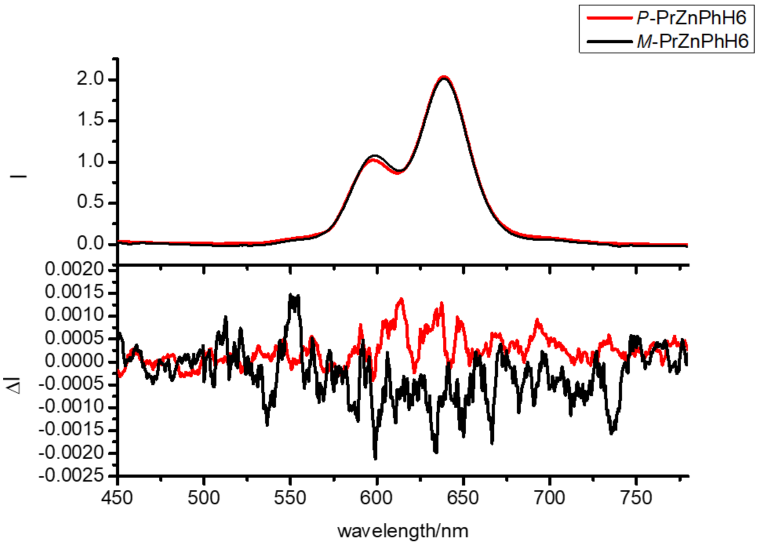

*Figure 37. Total luminescence (top) and CPL (bottom) spectra of **PrZnPhH6** in CH_2Cl_2 solution at 298 K.*

Table 3. a) Relative quantum yield, TPP in dichloromethane as reference; b) dissymmetry factor, g_{lum}, of each compound; c) CPL brightness

Compound	**PLQY[a]**	**g_{lum} [b] (λ_{ex}= 410 nm)**	**B_{CPL} [c] (M^{-1} cm^{-1})**
PrZnPhH6	0.08	$\pm 1\times10^{-3}$	0.8

IV.Conclusions

In this chapter, we illustrated two novel families of helicene-porphyrin conjugates, prepared starting from one common helicenic core and porphyrin units. They were obtained by cross-coupling reactions. The aim was to study the effect of the conjugation and of the interchromophoric distance on the exciton coupling chirality, thus on the chiroptical response of the systems.

The compounds were characterized by ^{1}H and ^{13}C NMR and mass spectrometry and their photophysical and chiroptical properties were investigated experimentally and through theoretical calculations (thanks to the collaboration with the group of Prof. Autschbach at University at Buffalo). The first series of molecules **H6Pr1-3** unambiguously confirmed the presence and effectiveness of EC chirality in helicenes through the very strong bisignate CD response in the Soret band along with slightly ECD-active Q-bands. Interestingly, these systems also revealed CPL activity which is still very rare in chiral porphyrins. This work was published in *Chemical Communications* [63]. The second type of helicene-porphyrin conjugate, namely **PrZnPhH6** bearing one less ethynyl bridge, displayed similar exciton chirality but with overall less intense chiroptical activities (observed both in ECD and in CPL).

These results lead us to further investigations on the exciton coupling of these helicene-porphyrin conjugates. The role of the interchromophoric distance and of the conjugation were explored by changing the spacer between the chiral unit and the chromophores, as well as the metallic centers. These aspects will be detailed in **Chapter 3**.

V. Experimental procedures

^{1}H and ^{13}C{1H} NMR spectra were recorded at room temperature on an *AVANCE III 400 BRUKER* or an *AVANCE I 500 BRUKER* at Center Régional de Mesures Physiques de l'Ouest (CRMPO), Université de Rennes 1. Chemical shifts δ are given in ppm, relative to an internal standard of residual solvent ($CDCl_3$: δ = 7.26 ppm for ^{1}H NMR, δ = 77.16 ppm for ^{13}C NMR; CD_2Cl_2: δ = 5.32 ppm for ^{1}H NMR, δ = 53.84 ppm for ^{13}C NMR), and coupling constants *J* in Hz.

High-resolution mass spectra (HR-MS) determinations were performed at CRMPO on a Bruker MaXis 4G and Ultraflex III by ASAP (+ or -) or ESI techniques with CH_2Cl_2 as solvent. Experimental and calculated masses are given with consideration of the mass of the electron.

UV-Visible (UV-vis, in M^{-1} cm^{-1}) absorption spectra were recorded on a UV-2401PC Shimadzu spectrophotometer.

Specific rotations (in deg cm^2 g^{-1}) were measured in a 1.0 dm thermostated quartz cell on a PerkinElmer Model 341 polarimeter. Electronic circular dichroism spectra (ECD, in M^{-1} cm^{-1}) were recorded on a Jasco J-815 Circular Dichroism Spectrometer (IFR140 facility - Biosit - Université de Rennes 1). Molar rotations are given in deg cm^2 $dmol^{-1}$.

Thin-layer chromatography (TLC) was performed on aluminum sheets precoated with Merck 5735 Kieselgel 60F254. Column chromatography was carried out with Merck 5735 Kieselgel 60F (0.040-0.063 mm mesh).

Chemicals were purchased from Sigma-Aldrich, Alfa Aesar or TCI Europe, and used as received. Porphyrin cores were purchased from PorphyChem and used as received.

PrBr^{Mes,Alk} and the metal complexes **PrMBr ^{Mes,Alk}** were prepared according to the Scheme 4 and following the procedure described in the literature [64].

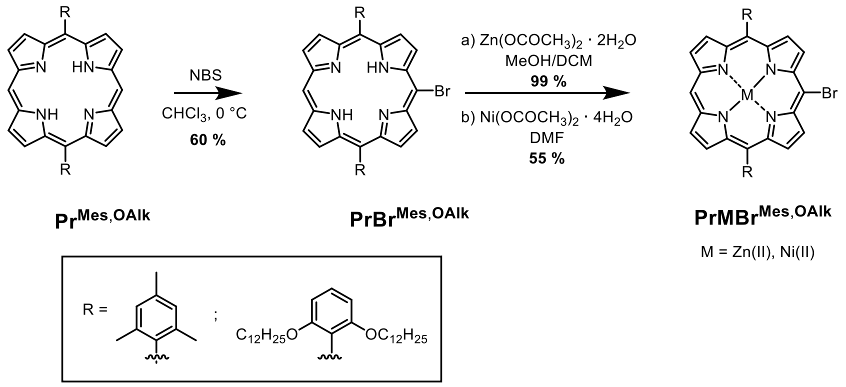

*Scheme 4. Synthetic step for **PrM** ^{Mes,Alk} precursors.*

V.1. Synthetic procedure for H6PrX

- **H6PhH**[63]

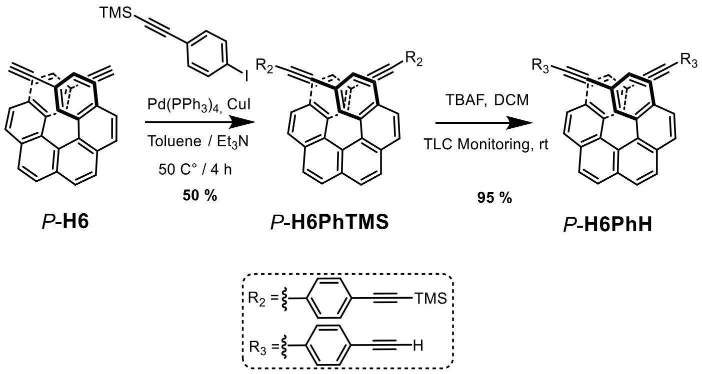

Scheme 5. Synthesis of the helicene moiety starting from 2,15-bis-ethynyl [6]helicene.

Compound **H6** (60 mg, 0,16 mmol), $Pd(PPh_3)_4$ (19 mg, 0.01 mmol), and CuI (6 mg, 0.02 mmol) were dissolved in a triethylamine/ toluene mixture (1/4) (9 mL) which was freed from oxygen by bubbling argon for 1 hour. Then, ((4-iodophenyl)ethynyl)trimethylsilane (191 mg, 0.60 mmol) was added into the solution. The reaction was stirred for 5 h at 50 °C under argon. After the reaction, solvent was stripped off and the residue was purified by a first silica gel column chromatography (100% CH_2Cl_2) followed by a second column (Heptane/Ethyl acetate 8/2) to afford the desired product **H6PhTMS** as a yellow solid (58 mg, 50%).

^{1}H NMR (400 MHz, Methylene Chloride-d2) *δ:* 8.13 – 7.97 (m, 8H, CH_{Ar}), 7.86 (d, J = 8.2 Hz, 2H, CH_{Ar}), 7.82 – 7.78 (m, 2H, CH_{Ar}), 7.49 – 7.44 (m, 4H, CH_{Ar}), 7.40 (dd, J = 8.2, 1.6 Hz, 2H, CH_{Ar}), 7.35 – 7.24 (m, 4H, CH_{Ar}), 0.32 (s, 18H, CH_3-Si).

$^{13}C\{^{1}H\}$ (101 MHz, Methylene Chloride-d2) *δ:* 133.4, 131.9, 131.8, 131.7, 131.2, 129.1, 127.8, 127.7, 127.5, 127.4, 127, 123.8, 123.4, 122.7, 119.1, 104.4, 96.2(s, C≡C), 91.5(s, C≡C), 88.2(s, C≡C), 0.2(s, CH_3-Si).

The obtained **H6PhTMS** (50 mg, 0.07 mmol) was dissolved in DCM (5 mL) for dropwise addition of tetrabutylammonium fluoride (TBAF, 1.0 M solution in THF) until the full conversion to the deprotected **H6PhH** derivative. Then 2 mL of distilled water were added to quench the reaction. After removal of the solvent, the residue was redissolved in 50 mL of CH_2Cl_2. The organic phase was washed four times with water and dried over anhydrous Na_2SO_4. The solvent was removed under vacuum, and the residue was purified by a silica gel column chromatography (100% CH_2Cl_2) to give the final product **H6PhH** as a yellow solid (38 mg, 95%).

^{1}H NMR (400 MHz, Methylene Chloride-d2) *δ* 8.15 – 7.98 (m, 8H, CH_{Ar}), 7.87 (d, J = 8.2 Hz, 2H, CH_{Ar}), 7.82 (d, J = 1.5 Hz, 2H, CH_{Ar}), 7.52 – 7.47 (m, 4H, CH_{Ar}), 7.41 (dd, J = 8.3, 1.6 Hz, 2H, CH_{Ar}), 7.36 – 7.30 (m, 4H, CH_{Ar}), 3.29 (s, 2H, C≡CH).

$^{13}C\{^{1}H\}$ (101 MHz, Methylene Chloride-d2) *δ* 133.4, 132, 131.9, 131.8, 131.8, 131.2, 129.1, 127.8, 127.7, 127.5, 127.4, 127, 123.8, 121.6, 119, 91.6(s, C≡C), 88.1(s, C≡C), 83(s, C≡C), 78.8 (s, C≡C).

- ## H6Pr1 and H6Pr2

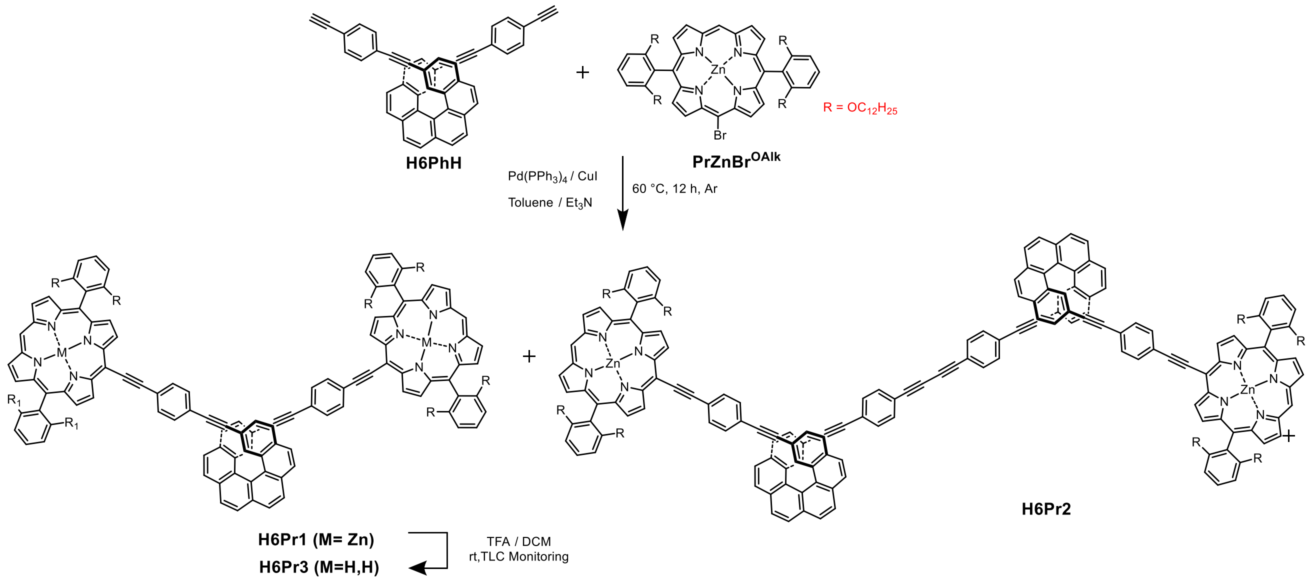

*Scheme 6. Synthetic route for the three derivatives **H6Pr1,2,3**.*

A mixture of compound **H6PhH** (10 mg, 0.017 mmol), **PrZnBr^{OAlk}** (51 mg, 0.038 mmol), CuI (0.6 mg, 0.003 mmol), and Pd (PPh$_3$)$_4$ (2 mg, 0.002 mmol) in toluene (4 mL) and NEt$_3$ (1 mL) was stirred and heated at 60 °C under argon atmosphere for 12 h. After removal of the solvent, the residue was dissolved again in CH$_2$Cl$_2$. The organic phase was washed three times with water and dried over anhydrous Na$_2$SO$_4$. The solvent was removed under vacuum, and the crude product was purified by column chromatography using CH$_2$Cl$_2$ / ethylacetate (8:2) as the eluent to furnish the expected helicene porphyrin derivatives **H6Pr1** (10 mg, 45 %), and **H6Pr2** as green solid (10 mg, 15%).

H6Pr1

^{1}H NMR (400 MHz, Methylene Chloride-d2) *δ* 10.15 (s, 2H, CH$_{meso}$), 9.85 (d, J = 4.6 Hz, 4H, CH$_{Porph}$), 9.32 (d, J = 4.4 Hz, 4H, CH$_{Porph}$), 9.02 (d, J =4.5 Hz, 8H, CH$_{Porph}$), 8.97 (d, 4.5 Hz, 8H, CH$_{Porph}$) 8.21 – 8.13 (m, 8H, CH$_{hel}$), 8.09 (d, J = 8.2 Hz, 4H, CH$_{Phenyl}$ spacer), 8.11 – 7.93 (m, 4H, CH$_{hel}$), 7.79 (t, J = 8.4 Hz, 4H, CH$_{Mes}$ para), 7.60 (d, J = 8.2 Hz, 4H, CH$_{Phenyl}$ spacer), 7.54 (dd, *J* = 12.9, 8.0 Hz, 2H, CH$_{hel}$), 7.11 (d, J = 8.5 Hz, 8H, CH$_{Mes}$ para), 3.93 (t, J = 6.4 Hz, 16H, OCH$_2$), 1.35 – 1.08 (m, 38H, CH$_{2 alkyl\ chain}$), 1.06 – 0.84 (m, 70H, CH$_{2 alkyl\ chain}$), 0.72 (m, 16H, CH$_{2 alkyl\ chain}$), 0.62 – 0.46 (m, 36H, CH$_{2 alkyl\ chain}$), 0.40 (p, J = 7.7 Hz, 24H, CH$_{3 alkyl\ chain}$).

^{13}C{^{1}H} (101 MHz, Methylene Chloride-d2) *δ* 159.9, 151.4, 151, 150.2, 149.3, 132.1, 131.6, 131.3, 130.3, 129.9, 128, 127.5, 127.2, 124.3, 120.6, 119.4, 114.2, 106.6, 105.2, 98.6, 91.5 (s, C≡C), 88.8 (s, C≡C), 68.6 (s, -OCH$_2$), 31.9 (s, CH$_2$), 29.7 (s, CH$_2$), 29.4 (s, CH$_2$), 29.2 (s, CH$_2$), 29.1 (s, CH$_2$), 28.6 (s, CH$_2$), 25.2 (s, CH$_2$), 22.7 (s, CH$_2$), 13.9 (s, CH$_3$)

HR-MS Ultraflex III, MALDI, 370 °C; ion $[M]^{+\cdot}$, $C_{206}H_{252}N_8O_8\,^{64}Zn_2$, m/z calculated 3093.81356, m/z experimental 3093.780 (Δ = 11 ppm).

H6Pr2

^1H NMR (400 MHz, Methylene Chloride-d_2) *δ* 10.14 (s, 2H, CH_{meso}), 9.84 (d, *J* = 4.6 Hz, 4H, CH_{Porph}), 9.31 (d, *J* = 4.5 Hz, 4H, CH_{Porph}), 9.01 (dd, *J* = 23.7, 4.5 Hz, 8H, CH_{Porph}), 8.23 – 8.03 (m, 22H, CH_{hel}), 8.02 – 7.88 (m, 8H, CH_{hel}), 7.79 (t, *J* = 8.4 Hz, 4H, CH_{Mesl} para), 7.58 (d, *J* = 8.2 Hz, 8H, CH_{phenyl} spacer), 7.54 – 7.48 (m, 4H, CHhel), 7.39 (d, *J* = 8.2 Hz, 8H, CH_{phenyl} spacer), 7.10 (d, *J* = 8.5 Hz, 8H, CH_{Mes} ortho), 3.93 (t, *J* = 6.4 Hz, 16H, OCH_3), 1.33 – 1.06 (m, 48H, $CH_{2alkyl\ chain}$), 1.06 – 0.84-0.71 (m, 76H, $CH_{2alkyl\ chain}$), 0.61 – 0.47 (m, 36H, $CH_{2alkyl\ chain}$), 0.46 – 0.35 (m, 24H, $CH_{3alkyl\ chain}$).

$^{13}C\{^1H\}$ (101 MHz, Methylene Chloride-d2) *δ* 167.5, 159.9, 151.4, 151, 150.2, 149.2, 132.4, 132.5, 132.1, 131.9, 131.5, 131.4, 131.3, 130.9, 129.8, 128.7, 127.5, 120.6, 114.2, 105.2, 68.6 (C≡C), 67.9 (C≡C), 53.4, 38.8, 31.9(CH_2), 30.4(CH_2), 29.7(CH_2), 29.5(CH_2), 29.4(CH_2), 29.3(CH_2), 29.2(CH_2), 29.1(CH_2), 28.6(CH_2), 25.2(CH_2), 23.7(CH_2), 22.9 (CH_2), 22.7 (CH_2), 13.8 (CH_3),

HR-MS Ultraflex III, MALDI, 370 °C; ion $[M]^{+\cdot}$, C^{252} H^{274} N_8 O_8 $^{64}Zn_2$, m/z calculated 3667.98571, m/z experimental 3668.010 (Δ = 7 ppm).

H6Pr3

Compound **H6Pr2** (7 mg, 0.002 mmol) was treated with a few drops of TFA in DCM solution until the complete conversion and the obtention of the free porphyrin (the progress of the reaction was carefully monitored by TLC). Then, the reaction was quenched with $NaHCO_3$, washed with water and then extracted with DCM. The organic phase was dried over $MgSO_4$ and the solvent was removed with pressure. The crude was immediately passed through a short plug of silica gel (CH_2Cl_2) to afford the desired product in quantitative yield (6.72 mg) as brownish solid.

^1H NMR (400 MHz, Chloroform-*d*) δ 10.02 (s, 2H, CH_{meso}), 9.72 (d, *J* = 4.7 Hz, 4H, CH_{porph}), 9.17 (d, *J* = 4.6 Hz, 4H, CH_{porph}), 8.93 (d, *J* = 4.7 Hz, 4H, CH_{porph}), 8.88 (d, *J* = 4.5 Hz, 4H, CH_{porph}), 8.14 – 8.05 (m, 8H, CH_{hel}), 8.00 (d, *J* = 7.9 Hz, 4H, CH_{phenyl} spacer), 7.95 (m, 4H, CH_{hel}), 7.74 (t, *J* = 8.4 Hz, 4H, CH_{Mes} para), 7.61 (d, *J* = 7.9 Hz, 4H, CH_{phenyl} spacer), 7.54 (dd, *J* = 12.9, 8.0 Hz, 2H, CH_{hel}), 7.04 (d, *J* = 8.5 Hz, 8H, $CH_{Mes\ ortho}$), 3.87 (t, *J* = 6.5 Hz, 16H, OCH_2), 1.17-1.03 (m, 48H, $CH_{2alkyl\ chain}$), 1.02-0.94 (m, 48H, $CH_{2alkyl\ chain}$), 0.94 – 0.81 (m, 32H, $CH_{2alkyl\ chain}$), 0.73 (m, 32H, $CH_{2alkyl\ chain}$), 0.65 – 0.43 (m, 24H, $CH_{3alkyl\ chain}$).

$^{13}C\{^1H\}$ (101 MHz, Methylene Chloride-d2) *δ* 159.9, 151.4, 151, 150.2, 149.3, 132.1, 131.6, 131.3, 130.3, 129.9, 128, 127.5, 127.2, 124.3, 120.6, 119.4, 114.2, 106.6, 105.2, 98.6, 91.5 (C≡C), 88.8 (C≡C)., 68.6 (CH_2-O), 31.9 (CH_2), 29.7 (CH_2), 29.4 (CH_2), 29.2 (CH_2), 29.1 (CH_2), 28.6 (CH_2), 25.2 (CH_2), 22.7 (CH_2), 13.9 (CH_3)

HR-MS Ultraflex III, MALDI, 370 °C; ion $[M]^{+\cdot}$, C^{252} H^{274} N_8 O_8 $^{64}Zn_2$, m/z calculated 3667.98571, m/z experimental 3668.010 (Δ = 7 ppm).

V.2. Synthetic procedures for PrZnPhH6

The borylation of the bromo-porphyrin was obtained following the procedure described in the literature (**Scheme 8**)[65].

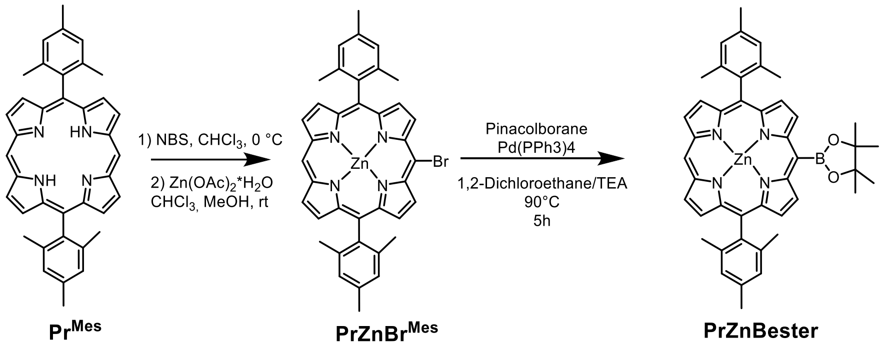

Scheme 8. Synthetic pathway for the porphyrin precursor.

- **BrH6**

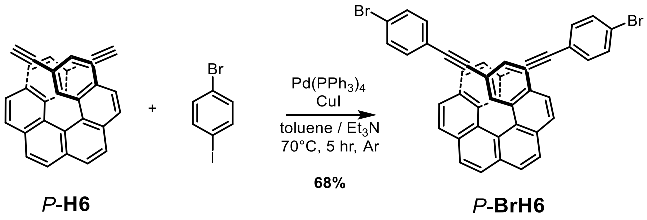

Scheme 9. Synthesis of the helicene precursor.

Compound **H6** (35 mg, 0.09 mmol) and 1-bromo-4-iodobenzene (76 mg, 0.27 mmol) were dissolved in triethylamine and toluene solvent mixture (1/10, 11 mL) which was freed from oxygen by freeze and pump thaw cycles. Then, $Pd(PPh_3)_4$ (5 mg, 0.0045 mmol) and CuI (2 mg, 0.009 mmol) were added to the solution. The reaction was stirred for 5 h at 70 °C under argon. After the reaction, the solvent was removed under vacuum and the residue was purified by a silica gel column chromatography (heptane/ethyl acetate 9/1) followed by size exclusion chromatography in pure chloroform to afford the desired product **BrH6** as a yellowish solid (43 mg, 68%).

^{1}H NMR (300 MHz, Chloroform-*d*) δ 8.08 (d, *J* = 8.2 Hz, 2H, CH_{hel}), 8.05 – 7.99 (m, 5H, CH_{hel}), 7.95 (d, *J* = 8.5 Hz, 2H, CH_{hel}), 7.83 – 7.78 (m, 4H, CH_{hel}), 7.50 – 7.45 (d, *J* = 8.4 Hz ,4H, CH_{phenyl}), 7.38 (dd, *J* = 8.3, 1. 2H, CH_{hel}), 7.22 (d, *J* = 8.2 Hz, 4H, CH_{phenyl}).

^{13}C{^{1}H} NMR (101 MHz, Chloroform-*d*) δ 133.3, 132.8 (CH-Ph), 131.9, 131.8, 131.7 (CH-Ph), 131.5, 129.1, 127.6, 127.47, 127.44, 127.4, 127.1, 122.7, 122.1, 119.1, 90.9 (C≡C), 87.61 (C≡C).

- **PrZnPhH6**

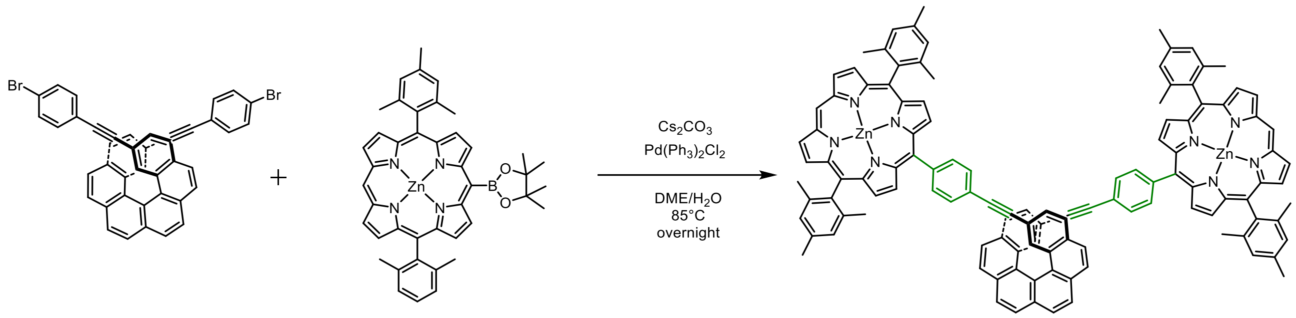

***P*-BrH6** **PrZnBester** ***P*-PrZnPhH6**

*Scheme 10. Synthesis of the bis-porphyrin derivative **PrZnPhH6***

BrH6 (20 mg, 0.03 mmol), Cs_2CO_3 (36 mg, 0.12 mmol) and the porphyrin derivative **PrZnBester** (56 mg, 0.08 mmol) were dissolved in dimethoxyethane and H_2O (10/1, 11 mL) and the solution was degassed by bubbling argon for 30 minutes. Then $Pd(PPh_3)_2Cl_2$ (10% mol) was added and the reaction was left stirring overnight at 85 °C. The mixture was washed with brine, extracted by dichloromethane and the organic phase dried over $MgSO_4$. The solvent was stripped off and the residue was purified by a silica gel column chromatography (heptane/fichloromethane 8/2), to afford the desired product **PrZnPhH6** as a purple solid (19 mg, 38%).

^{1}H NMR (400 MHz, Chloroform-d)) δ 10.22 (s, 2H, CH_{meso}), 9.39 (d, *J* = 4.5 Hz, 4H, CH_{porph}), 8.98 (d, *J* = 4.6 Hz, 4H, CH_{porph}), 8.96 (d, *J* = 4.5 Hz, 4H, CH_{porph}), 8.89 (d, *J* = 4.6 Hz, 4H, CH_{porph}), 8.26 (d, *J* = 8.1 Hz, 4H, CH_{phenyl}), 8.17 – 8.02 (m, 12H, CH_{hel}), 7.79 (d, *J* = 8.0 Hz, 4H, CH_{phenyl}), 7.67 (dd, *J* = 8.2, 1.5 Hz, 2H, CH_{hel}), 7.34 (s, 8H, CH_{arom} Mes), 2.69 (s, 12H, CH_3 Mes), 1.88 (s, 24H, CH_3 Mes).

^{13}C{^{1}H} NMR (101 MHz, Methylene Chloride-d2) δ 150, 149.9, 149.9, 149.4, 142.8, 139.3, 138.9, 137.5, 134.5(CH_{spacer}), 133.4, 132.2(CH_{Poprh}), 132.1 (CH_{porph}), 131.9(CH_{porph}), 131.8(CH_{porph}), 131.4, 130.8(CH_{spacer}), 129.6, 129.4, 128.4, 127.(CH_{Mes}), 127.73, 127.0, 122.6, 119.8, 119.7, 118.9, 105.3 (CH-$_{meso}$), 90.9 (C≡C), 88.9 (C≡C), 66.9, 21.6 (CH_3), 21.5 (CH_3).

HR-MS Ultraflex III, MALDI, 370 °C; ion $[M]^+$, $C_{118}H_{84}N_8\,^{64}Zn_2$, m/z calculated 1740.53964, m/z experimental 1740.544 (Δ = 2 ppm).

References

[1] T. S. Metzger, S. Mishra, B. P. Bloom, N. Goren, A. Neubauer, G. Shmul, J. Wei, S. Yochelis, F. Tassinari, C. Fontanesi, D. H. Waldeck, Y. Paltiel and R. Naaman, *Angew. Chem. Int. Ed.,* no. 59, pp. 1653-1658, 2020.

[2] K. Dhbaibi, L. Favereau, M. Srebro-Hooper, M. Jean, N. Vanthuyne, F. Zinna, B. Jamoussi, L. D. Bari, J. Autschbach and J. Crassous, *Chem. Sci.,* vol. 9, pp. 735-742, 2018.

[3] Y. Lu, Q. Liu, B. W. Jiaxin Luo, T. Feng, X. Zhou, X. Liu and Y. Xie, *ChemSusChem,* pp. 2802-2809, 2019.

[4] M. Jurow, A. E. Schuckman, J. D. Batteas and C. M. Drain, *Coord. Chem. Rev.,* vol. 254, pp. 2297-2310, 2010.

[5] Y. Shi, F. Zhang and R. J. Linhardt, *Dyes and Pigments,* vol. 188, 109136, 2021.

[6] P. K. Poddutoori, Photosynthesis: From Plants to Nanomaterials, Vols. Chapter 10 - Main-group porphyrins in artificial photosynthesis, Academic Press, 2023, pp. 165-195.

[7] K. M. Kadish, K. M. Smith and R. Guilard, Handbook of Porphyns Science, World Scientific, 2012.

[8] M. Goutermann and G. H. Wagniere, *J. Mol. Spectroscopy,* vol. 11, pp. 108-127, 1963.

[9] W. R. Scheidt and Y. J. Lee, *Structure and Bonding,* vol. 64, pp. 1-70, 1987.

[10] A. Stone and E. B. Fleischer, *J. Am. Chem. Soc.,* vol. 90, pp. 2735–2748, 1968.

[11] J. Hoard, *Science,* vol. 174, pp. 295–1302, 1971.

[12] G. Lu, M. Bai, R. Li, X. Zhang, C. Ma, P.-C. Lo, D. K. P. Ng and J. Jiang, *J. Am. Chem. Soc.,* vol. 125, pp. 12257–12267, 2003.

[13] A. Takenaka, Y. Sasada, H. Ogoshi, T. Omura and Z. Yoshida, *Acta Cryst. B,* vol. 31, pp. 1-6, 1975.

[14] P. Brothers, *Chem. Commun,* pp. 2090–2102, 2008.

[15] A. Srinivasan, H. Furuta and A. Osuka, *Chem. Commun.,* pp. 1666–1667, 2001.

[16] M. Byrn, C. Curtis, Y. Hsiou, S. Khan, P. Sawin, S. Tendick, C. Strouse and A. Terzis, *J. Am. Chem. Soc.,* vol. 115, p. 9480–9497, 1993.

[17] Y. Mizuno, T. Aida and K. Yamaguchi, *J. Am. Chem. Soc.,* vol. 122, pp. 5278–5285, 2000.

[18] J. Labuta, S. Ishihara, T. Šikorsky´, Z. Futera, A. Shundo, L. Hanyková, J. Burda, K. Ariga and J. Hill, *Nat. Commun.,* vol. 4, pp. 1-8, 2013.

[19] V. Valderrey, G. Aragay and P. Ballester, *Coord. Chem. Rev.,* vol. 258–259, pp. 137-156, 2014.

[20] N. Berova, P. L. Polavarapu, K. Nakanishi e R. W. Woody, Comprehensive Chiroptical Spectroscopy: Instrumentation, Methodologies, and Theoretical Simulations, Wiley, 2012.

[21] X. Huang, N. Fujioka, G. Pescitelli, F. E. Koehn, R. T. Williamson, K. Nakanishi and N. Berova, *J. Am. Chem. Soc.,* vol. 124, pp. 10320–10335, 2002.

[22] G. Proni, G. Pescitelli, X. Huang, K. Nakanishi and N. Berova, *J. Am. Chem. Soc.,* vol. 125, pp. 12914–12927, 2003.

[23] Q. Yang, C. Olmsted and B. Borhan, *Org. Lett,* vol. 4, pp. 3423−3426, 2002.

[24] M. Tanasova, C. Vasileiou, O. Olumolade and B. Borhan, *Chirality,* vol. 21, pp. 374−382., 2009.

[25] S. Matile, N. Berova, K. Nakanishi, S. Novkova, I. Philipova and B. Blagoev, *J. Am. Chem. Soc.,* vol. 26, pp. 7021–7022, 1995.

[26] G. Pescitelli, S. Gabriel, Y. Wang, J. Fleischhauer, R. W. Woody and N. Berova, *J. Am. Chem. Soc. ,* vol. 125, pp. 7613–7628, 2003.

[27] V. V. Borovkov, J. M. Lintuluoto, M. Fujiki and Y. Inoue, *J. Am. Chem. Soc.,* vol. 122, no. 18, pp. 4403–4407, 2000.

[28] V. V. Borovkov, J. M. Lintuluoto and Y. Inoue, *J. Am. Chem. Soc. ,* vol. 123, pp. 2979–2989, 2001.

[29] V. Borovkov, J. Lintuluoto and Y. Inoue, *Org. Lett.,* vol. 4, pp. 169−171, 2002.

[30] N. Yoshida and A. Osuka, *Tetrahedron Lett.,* vol. 41, p. 9287−9291, 2000.

[31] N. Yoshida, T. Ishizuka, A. Osuka, D. Jeong, H. Cho, D. Kim, Y. Matsuzaki, A. Nogami and K. Tanaka, *Chem. Eur. J.,* vol. 9, pp. 58-75, 2003.

[32] G. Bringmann, D. C. G. Götz, T. A. M. Gulder, T. H. Gehrke, T. Bruhn, T. Kupfer, K. Radacki, H. Braunschweig, A. Heckmann and C. Lambert, *J. Am. Chem. Soc.,* vol. 130, pp. 17812–17825, 2008.

[33] G. Bringmann, S. Rüdenauer, D. Götz, T. Gulder and M. Reichert., *Org. Lett.,* vol. 8, pp. 4743−4746, 2006.

[34] L. Pu, *Chem. Rev.,* vol. 98, pp. 2405-2494, 1998.

[35] M. Kimura, T. Kitamura, M. Sano, T. Muto, K. Hanabusa, H. Shiraia and N. Kobayashi, *New J. Chem.,* vol. 24, pp. 113-114, 2000.

[36] T. Ema, N. Ura, K. Eguchi, Y. Ise and T. Sakai, *Chem. Commun.,* vol. 47, pp. 6090−6092, 2011.

[37] K. Tsubaki, K. Takaishi, H. Tanaka, M. Miura and T. Kawabata, *Org. Lett.,* vol. 8, pp. 2587−2590, 2006.

[38] S. Matile, N. Berova, K. Nakanishi, J. Fleischhauer and R. W. Woody, *J. Am. Chem. Soc.,* vol. 118, pp. 5198–5206, 1996.

[39] F. X. Redl, M. Lutz and J. Daub, *Chem. Eur. J.,* vol. 7, pp. 5350-5358, 2001.

[40] J. B. MacMillan, R. G. Linington, R. J. Andersen and T. Molinski, *Angew. Chem. Int. Ed,* vol. 43, pp. 5946−5951, 2004.

[41] K. Sakakibara, F. Nakatsubo, A. French and T. Rosenau, *Chem. Commun.,* vol. 48, pp. 7672−7674, 2012.

[42] T. Arai, K. Araki, N. Maruo, Y. Sumida, C. Korosue and J. Fukuma, *Chem.,* vol. 28, pp. 1151−1159, 2004.

[43] T. Ema, N. Ouchi, T. Doi, T. Korenaga and T. Sakai, *Org. Lett.,* vol. 7, pp. 3985−3988, 2005.

[44] J. M. Fox, T. J. Katz, S. V. Elshocht, T. Verbiest, M. Kauranen, A. Persoons, T. Thongpanchang, T. Krauss and L. Brus, *J. Am. Chem. Soc.,* vol. 121, pp. 3453–3459, 1999.

[45] B. K. M. T. Sooksimuang, *J. Porphyrins Phthalocyanines,* vol. 6, pp. 66-72, 2002.

[46] F. Zhang, K. Radacki, H. Braunschweig and C. L. P. Ravat, A*ngew. Chem. Int. Ed.,* vol. 60, pp. 23656–23660, 2021.

[47] K. Kato, K. Furukawa, T. Mori and A. Osuka, *Chem. Eur. J. ,* vol. 24, pp. 572-575, 2018.

[48] B. Szyszko, M. Przewoźnik, M. J. Białek, A. Białońska, P. J. Chmielewski, J. Cichos and L. Latos-Grażyński, *Angew. Chem. Int. Ed.,* vol. 57, pp. 4030-4034., 2018.

[49] V. Silber, N. Gruber, M. Jean, N. Vanthuynec and R. Ruppert, *Chem. Commun.,* vol. 58, pp. 6012-6015, 2022.

[50] R.Shediac, M. Gray, H. Uyeda, R. Johnson, J. Hupp, P. Angiolillo and M. Therien, *J. Am. Chem. Soc.,* vol. 122, pp. 7017−7033, 2000.

[51] T. V. Duncan, K. Susumu, L. E. Sinks and M. J. Therien, *J.. Am. Chem. Soc.,* vol. 128, no. 28, pp. 9000-9001, 2006.

[52] J. A. N. Fisher, K. Susumu, M. Therien and A. G. Yodh, *J.Chem. Phys.,* vol. 130, 2009.

[53] G. Bullard, F. Tassinari, C.-H. Ko, A. K. Mondal, R. Wang, S. Mishra, R. Naaman and M. J. Therien, *J. Am. Chem. Soc.,* vol. 141, pp. 14707–14711, 2019.

[54] C.-H. Ko, Q. Zhu, F. Tassinari, G. Bullard, P. Zhang, D. Beratan, R. Naaman and M. Therien, *PNAS ,* vol. 119 (6), 2022.

[55] S. Hiroto, Y. Miyake and H. Shinokubo, *Chem. Rev.,* vol. 117, pp. 2910-3043, 2017.

[56] L. Yu, K. Muthukumaran, I. V. Sazanovich, C. Kirmaier and E. Hindin, *Inorg. Chem.,* vol. 42, pp. 6629-6647, 2003.

[57] M. Uttamlal and A. S. Holmes-Smith, *Chem. Phys. Lett.,* vol. 454, pp. 223-228, 2008.

[58] M. Taniguchi, J. S. Lindsey, D. F. Bocian and D. Holten, *J. Photochem. Photobiol. C: Photochem. Rev.,* vol. 46, 2021.

[59] L. Arrico, L. D. Bari e F. Zinna, *Chem. Eur. J.,* vol. 27, pp. 2920 –2934, 2021.

[60] C. Maeda, K. Ogawa, K. Sadanaga, K. Takaishi and T. Ema, *Chem. Commun.,* vol. 55, pp. 1064-1067, 2019.

[61] J. Crassous, Circularly Polarized Luminescence of Isolated Small Organic Molecules, vol. Chap 4, Springer, pp. 53-97.

[62] D. W. Thomas and A. E. Martell, *J. Am. Chem. Soc.,* vol. 78, pp. 1338–1343, 1956.

[63] K. Dhbaibi, P. Matozzo, L. Abella, M. Jean, N. Vanthuyne, J. Autschbach, L. Favereau and J. Crassous, *Chem. Commun.,* vol. 57, pp. 10743-10746, 2021.

[64] R. Mishra, R. Regar, R. Singhal, P. Panini, G. D. Sharma and J. Sankar, *J. Mater. Chem. A,* vol. 5, pp. 15529-15533, 2017.

[65] A. Ryan, A. Gehrold, R. Perusitti, M. Pintea, M. Fazekas, O. B. Locos, F. Blaikie and M. O. Senge, *Eur. J. Org. Chem.,*vol. 2011 pp. 5817–5844, 2011.

[66] V. V. Borovkov, J. M. Lintuluoto and Y. Inoue, *J. Am. Chem. Soc.,* vol. 123, pp. 2979–2989, 2001.

[67] A. Chiesa, A. Privitera, E. Macaluso, M. Mannini, R. Bittl, R. Naaman, M. R. Wasielewski, R. Sessoli and S. Carretta, *Adv. Mat.*, 2023 **https://doi.org/10.1002/adma.202300472**

[68] C. J. Kingsbury and M. O. Senge, *Coord. Chem. Rev.,* vol. 431, 213760, pp. 1-23, 2021.

Chapter 3

Helicene-porphyrin conjugates: influence of the spacer on EC chirality

I. Context and target molecules

We illustrated within the previous chapter (**Chapter 2**) the first promising results achieved by the functionalization of 2,15-bis-ethynyl-carbo[6]helicene with two porphyrins, using a phenyl moiety as linker. We confirmed the presence and effectiveness of EC chirality in helicenes by the very strong bisignate ECD response in their Soret band (together with slightly ECD-active Q-bands). The porphyrins interact predominantly through space, because the π-conjugation through the helix is partly broken; however the helicene unit leads to a higher intensity of the EC response in comparison to fully non-conjugately assembled dyes, as demonstrated by the computational analysis. Furthermore and interestingly, the strong chiroptical activity also manifests itself in the substantial CPL responses obtained, with CPL being still rarely encountered in chiral porphyrins.

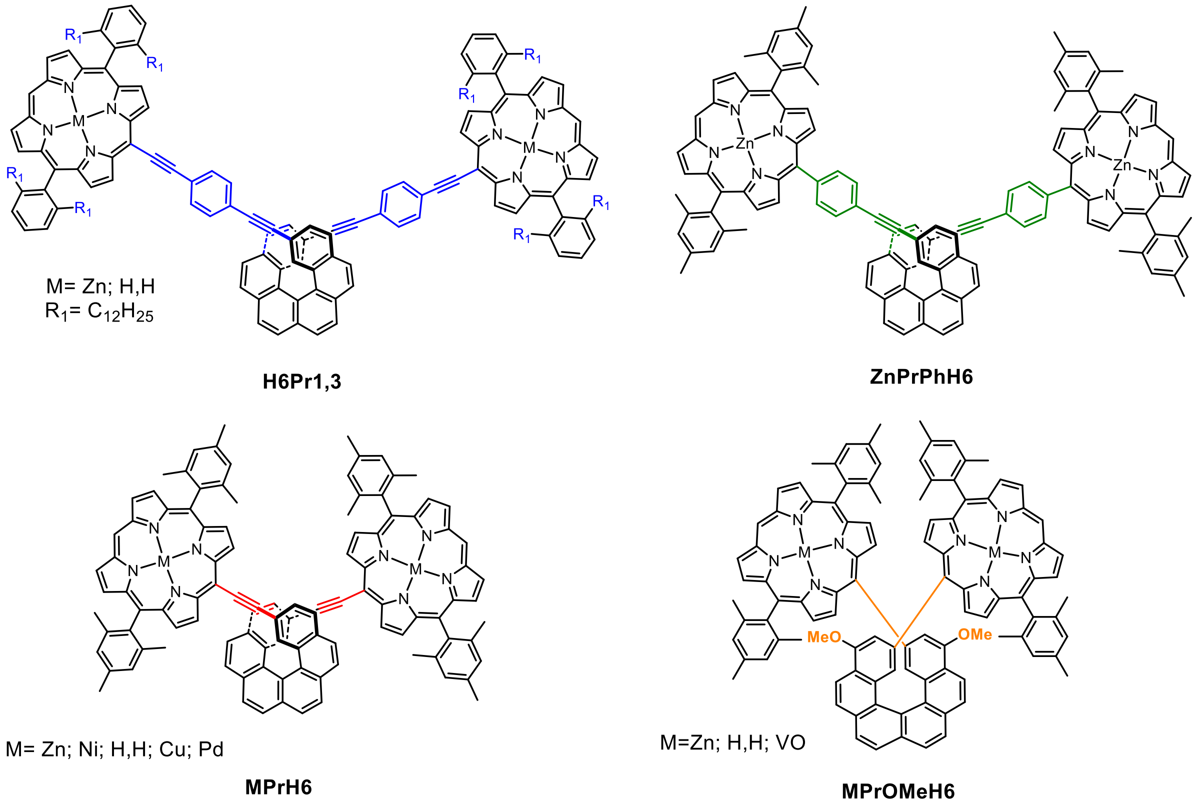

Figure 1. Structure of the four designed systems.

This strategy subsequently allowed us to fine-tune this platform by changing the linker between the helicene and the porphyrin and to achieve higher g_{abs} and g_{lum} values.

This is the case of the **MPrH6** and **MPrOMeH6** series (**Figure 1**) that will be described along this chapter.

For the first group of molecules H6Pr, the bis-ethynyl helicene was maintained as the chiral platform and a noteworthy enhancement of the chiroptical properties was achieved. Hence, the system was selected to be studied by mc-AFM in order to investigate the spin filtering ability. Preliminary results were obtained for the Zn derivative **ZnPrH6**. The effect of a diversity of metallic ions, namely Ni(II), Cu(II) and Pd(II), and their influence on the chiroptical responses was also examined.

The last family of compounds **MPrOMeH6** incorporates a different carbo[6]helicene. The strategy is to obtain a C-C bond between the chiral helical part and the chromophore, in order to further decrease the distance and explore the interaction between the metallic centers in the porphyrin core. More specifically, the vanadyl derivative was synthesized with the perspective to potentially investigate the spin-spin interactions and their correlation to the CISS effect for quantum applications [1].

II. Synthesis for the porphyrin-helicene derivatives with no spacer

II.1. Synthetic procedures for MPrH6 series

As already mentioned, the exciton coupling intensity is strongly dependent on the interchromophoric distance [2], thus we decided to modify this distance, by preparing two novel families of compounds with no spacer between the helicene and the porphyrin units, and investigating the influence on the photophysical and chiroptical properties of the corresponding molecule.

The first derivative was designed starting from the same 2,15-bis-ethynyl-carbo[6]helicene building block. In order to avoid the presence of Glaser by-products, a copper-free Sonogashira reaction between the ethynyl-helicene and the brominated porphyrin was set up (**Scheme 1**), giving the desired compounds **MPrH6** (M = Zn, Ni) in a 45-50 % yield. This reaction has been widely explored in the literature [3], even though the mechanism of the Cu-free Sonogashira cross-coupling is still under debate: while the initial step is accepted to be the oxidative addition reaction of aryl halides palladium(0) complex as for other cross-couplings, diverse mechanisms have been proposed for the other stages of the catalytic cycle [4, 5].

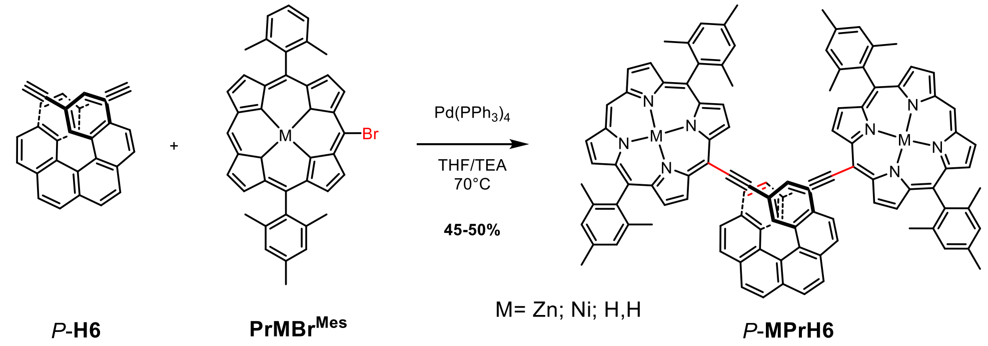

*Scheme 1. Synthetic route for **MPrH6** derivatives.*

In order to study the role of the transition metal within the helicene-porphyrin system, for this specific compound various metals were tested: the free-base, Zn, Ni, Cu and Pd. In the case of the Zn and Ni derivatives, the corresponding coordinated porphyrin was previously prepared, whereas the other compounds were obtained starting from the free-base porphyrin-helicene molecule that was then metalated following a different procedure for each metal (see the experimental part).

All of these derivatives were obtained and fully characterized by ^{1}H and ^{13}C NMR spectroscopy and mass spectrometry, with no significant changes among the various metals. As an example, the ^{1}H-

NMR spectrum of the free base derivative, with the respective assignments for all the protons, is reported in **Figure 2**.

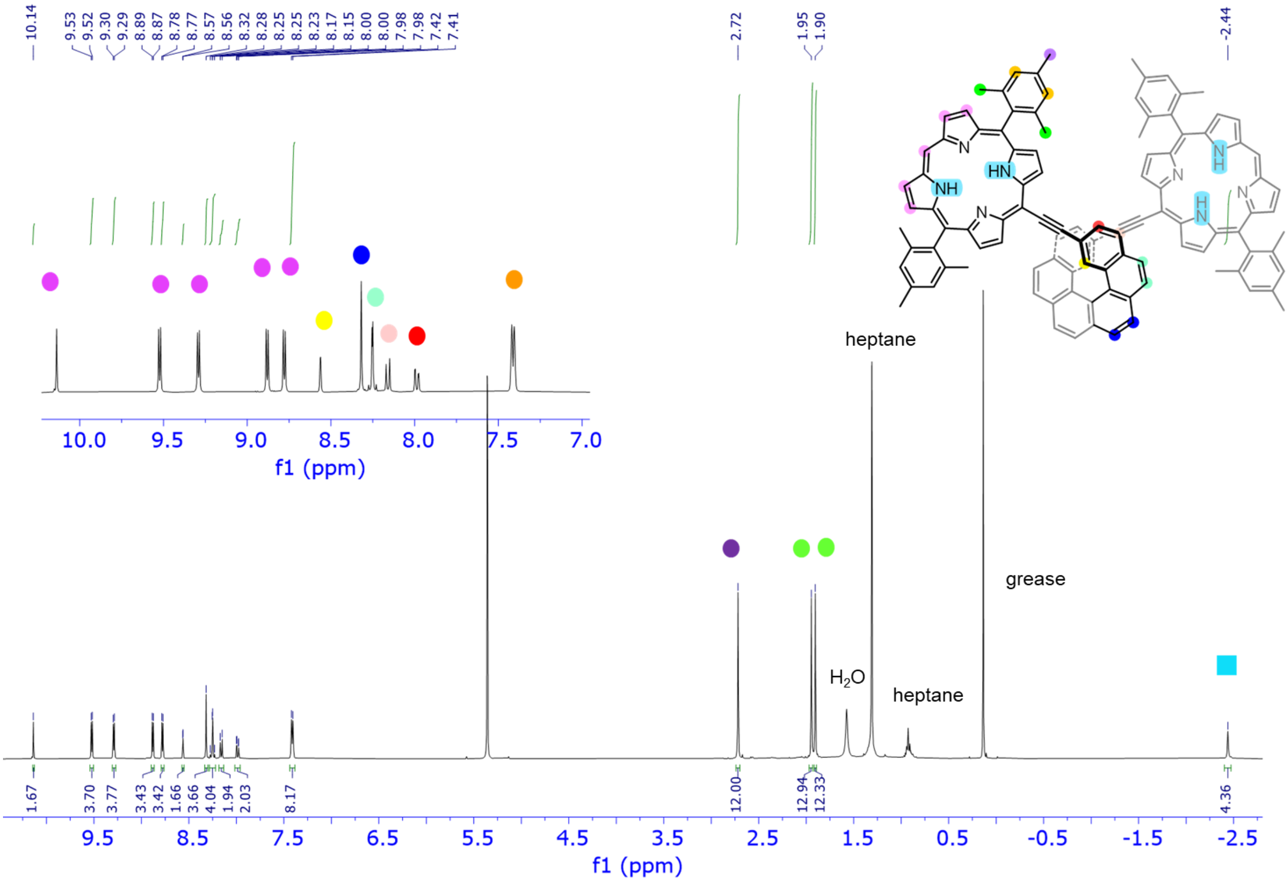

*Figure 2. ^{1}H-NMR of free-base derivative of **MPrH6** in CD_2Cl_2 (400 MHz, 298K).*

Except for the protons on the free porphyrin-helicene derivative, where the NH resonate at -2.44 ppm and that are not present for the coordinated-porphyrin derivatives, the signal pattern of the chromophore in the **MPrH6** family remains unaffected by changing the metal.

In contrast to the previously described **H6Pr1** and **PrZnPhH6**, the helicene unit shows a well-defined set of peaks: the “external” protons resonate as 5 different doublets from 8.31 to 7.98 ppm, while the protons in the ortho position with respect to the triple bond, so at 1,16 inner positions of the helix, resonate as a singlet at 8.57 ppm.

II.2. Synthetic procedures for MPrOMeH6 series

Until this point, we had only prepared porphyrin-helicene derivatives including one or more triple bonds in the spacer unit. With the aim to exploit even shorter interchromophoric distance so the porphyrin and the helicene moieties are bonded by a C-C single bond, we have synthesized another family of compounds with no spacer (**Scheme 2**).

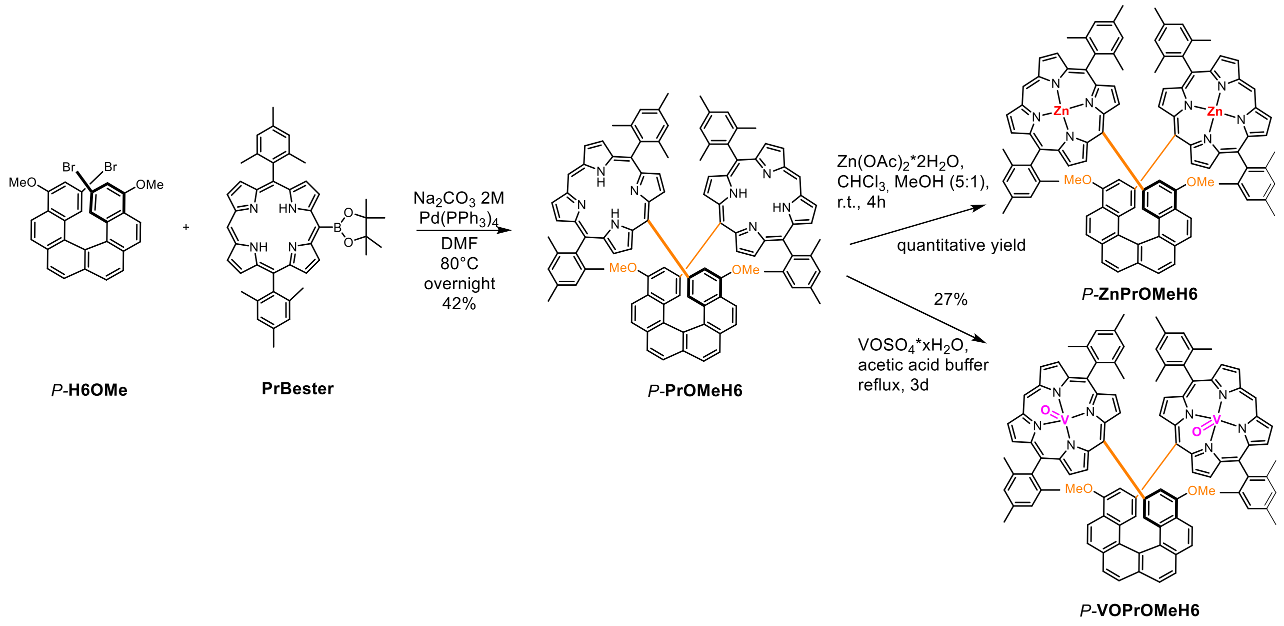

*Scheme 2. Synthetic route to obtain the free-base, Zn and VO derivatives starting from helicene **H6OMe.***

As described in **Scheme 2**, the reaction involves a Suzuki-Miyaura cross coupling with the boronic ester of the porphyrin derivative already used for the preparation of compound **PrZnPhH6**. The reaction conditions, so the solvent, the base and the catalyst, were adapted to the solubility and reactivity of **H6OMe**. This helicene has been developed in collaboration with Stefano Cadeddu, PhD student in our group (**Scheme 3**).

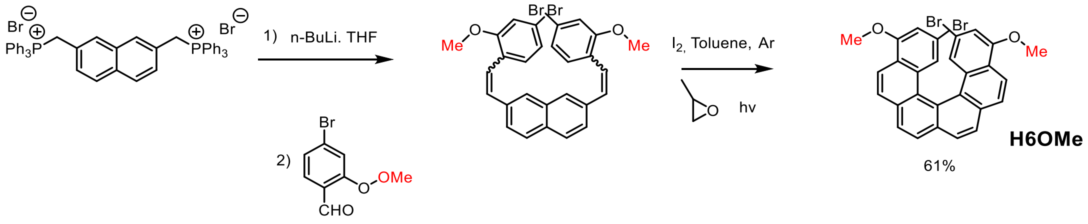

*Scheme 3. Synthetic route for **H6OMe** starting from the bis-phosphonium salt.*

PrOMeH6 was obtained in a 42% yield and it has been fully characterized by ^{1}H and ^{13}C-NMR spectroscopy.

In this context, two different metal complexes were then prepared within **PrOMeH6**: i) the Zn derivative **ZnPrOMeH6** by metalation with $Zn(OAc)_2$ dihydrate in a chloroform/methanol mixture, affording the Zn derivative in quantitative yield for comparison purposes with the previously described Zn complexes; and ii) a VO-complex **VOPrOMeH6** by reaction with vanadyl sulfate in glacial acetic acid, giving the vanadyl-porphyrin compound in a 27% yield. As the VO derivative is paramagnetic, it has been only characterized by mass spectrometry (see experimental part).
This metal was chosen to study the magnetic interactions between the metal ions. Recently transition metal complexes became the subject of studies leading to potential applications in quantum information processing [6]. In this context, the coupling between metals in fused porphyrin dimers was already described in 2005 by the group of Osuka [7] and more recently, the group of Sessoli and then Anderson proposed vanadyl(IV) porphyrin dimers as quantum mediators for

vanadyl qubits [8, 9]. In fact, among the different metals, vanadium(IV) is a suitable candidate for quantum applications thanks to long coherence times, and convenient hyperfine coupling [10].

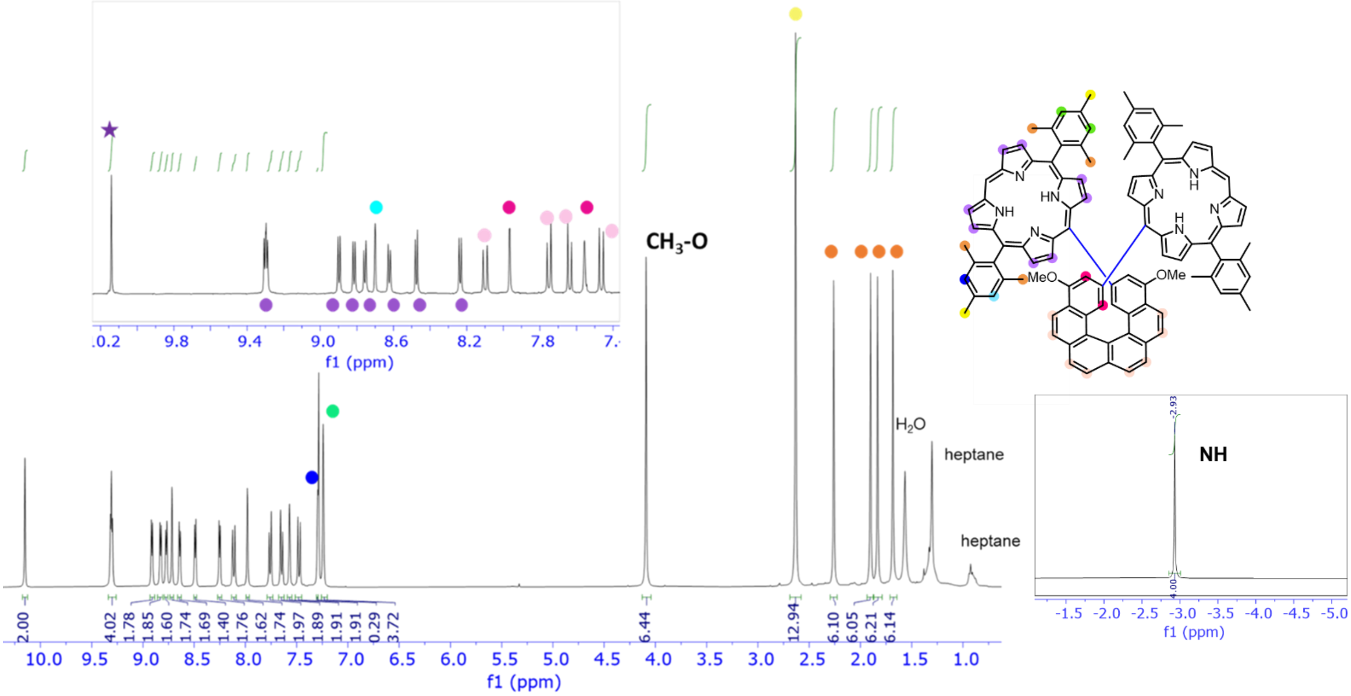

*Figure 3. ^{1}H-NMR (400Hz) in $CDCl_3$ at 298K of **PrOMeH6**.*

In comparison to the other derivatives previously described, the ^{1}H-NMR spectrum of **PrOMeH6** depicted on **Figure 3** displays a different set of signals for the porphyrin part. While the proton in *meso* position remains unchanged, the pyrrolic signals are split into 8 different doublets. Additionally, the CH_3 in ortho position of the mesityl substituents resonate as 4 singlets from 2.25 to 1.67 ppm, which makes us think that the two Mesityl substituents on the porphyrin core are no longer equivalent, probably due to the presence of the -OMe group on the helicene moiety.

Indeed, DFT-B3LYP calculations have been computed by Dr. Pierpaolo Morgante and Prof. Jochen Autschbach at University at Buffalo to obtain further insights on the geometry of the molecules: the optimized geometry (**Figure 4**) confirms the proximity of the methoxy groups to two among the four ortho Mesityl functions.

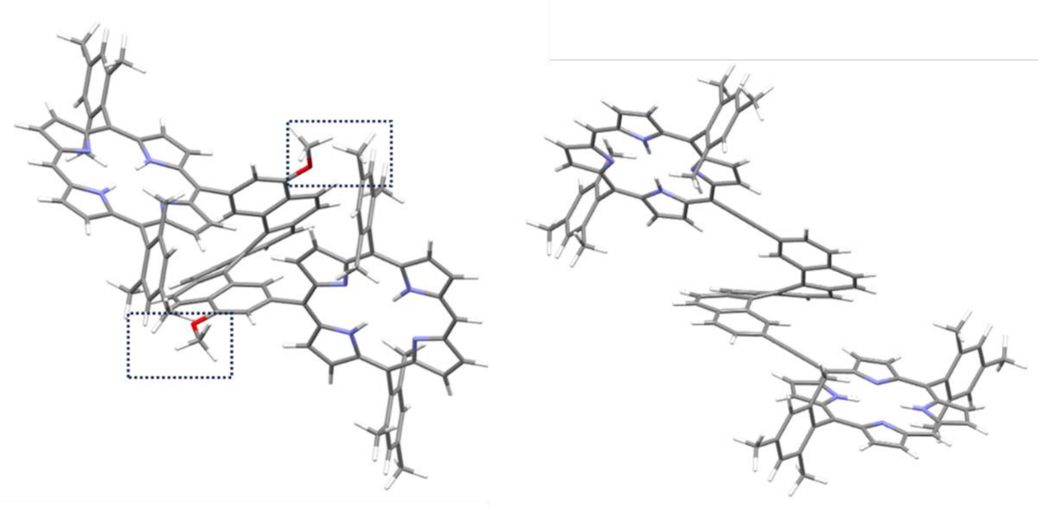

PrOMeH6 H2PrH6

*Figure 4. Optimized computed geometry of **PrOMeH6** (left) and of **H2PrH6** (right), for comparison, obtained by DFT calculations.*

III. Optical and chiroptical properties of the derivatives with no spacer

III.1. UV-vis and ECD spectra of MPrH6

The **MPrH6** series was designed with the aim of changing the extent of the conjugation and the interchromophoric distance: it will modulate the chiroptical response by varying the intensity of the exciton coupling couplet, as explained in the Introduction. The metals contribution is also fundamental for our study.

Thus, the absorption and ECD spectra were recorded in dichloromethane at a concentration of about 10^{-5} M (**Figure 5**).

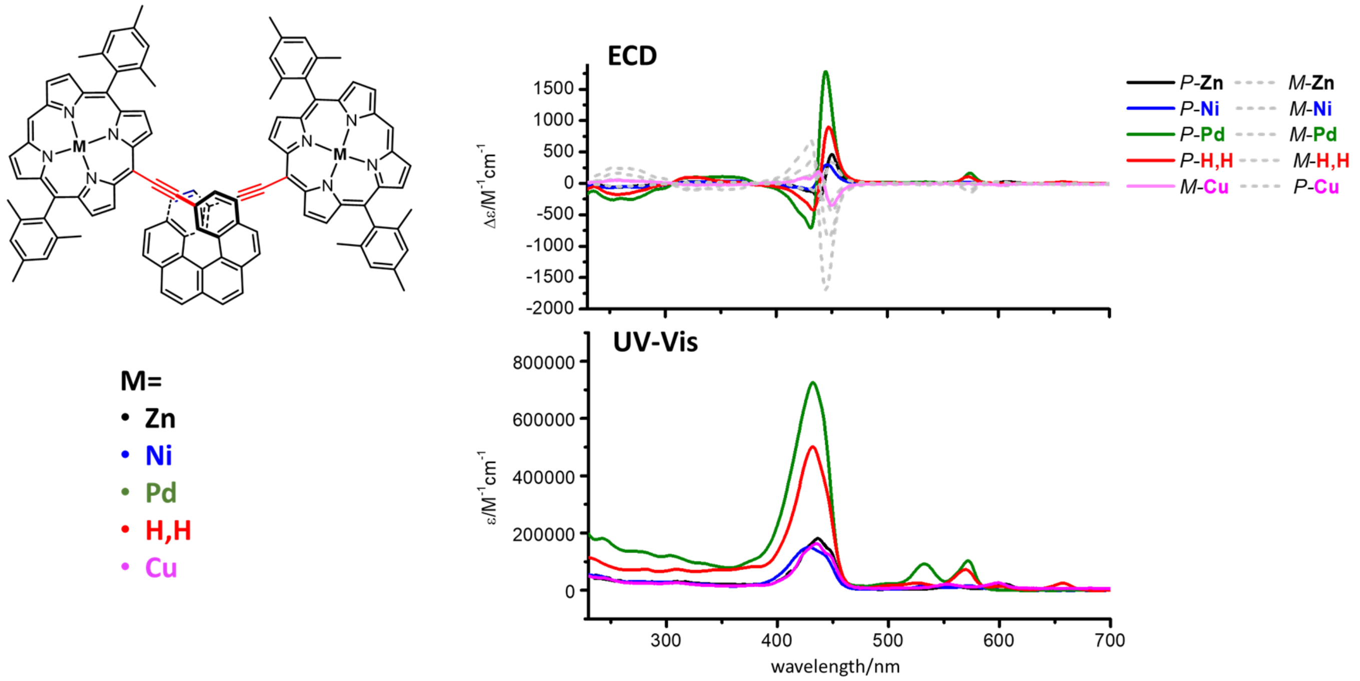

*Figure 5. ECD spectra (top) and absorption spectra (bottom) of the different derivatives of the **MPrH6** series in 10^{-5} CH_2Cl_2 solutions; the Cu(II) derivative labelling is reversed for a better visualization.*

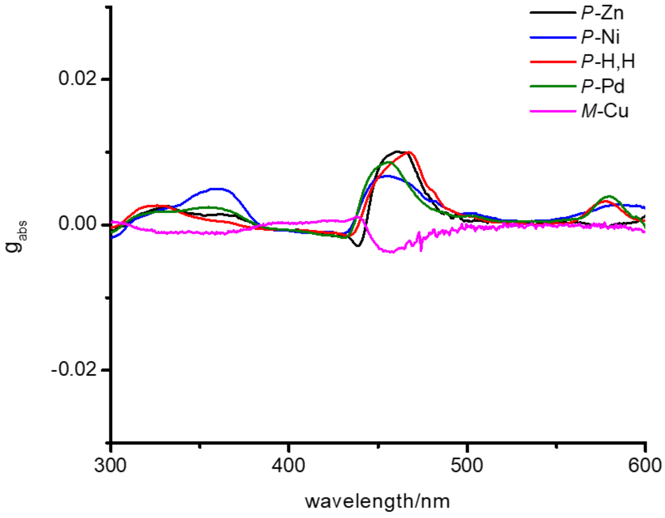

Metal	g_{abs} (Soret band)
***P*-Zn**	$+5*10^{-3}$
***P*-Ni**	$+3.3*10^{-3}$
***P*-Pd**	$+5*10^{-3}$
***M*-Cu**	$-3.7*10^{-3}$
***P*-Free base**	$+4.9*10^{-3}$

*Figure 6. g_{abs} spectra of the P enantiomer for each metal complex **MPrH6**: the Cu(II) derivative labelling is reversed for a better visualization.*

*Table 1. Molar absorption coefficients for the Soret and Q bands of the **MPrH6** derivatives.*

Metal	Soret band (λ, ε)	Q bands (λ, ε)
P-Zn	(436 nm, 180580 M^{-1} cm^{-1})	(557 nm, 14910 M^{-1} cm^{-1}), (604 nm, 20790 M^{-1} cm^{-})
P-Ni	(427 nm, 150000 M^{-1} cm^{-1})	(536, 16760 M^{-1} cm^{-1}), (572 nm, 15660 M^{-1} cm^{-1})
P-Pd	(431 nm, 724080 M^{-1} cm^{-1})	(531 nm, 91440 M^{-1} cm^{-1}), (570 nm, 100460 M^{-1} cm^{1})
P-Cu	(436 nm, 173060 M^{-1} cm^{-1})	(552 nm, 22090 M^{-1} cm^{-1}), (600 nm, 27720 M^{-1} cm^{-1})
P-Free base	(431 nm, 500870 M^{-1} cm^{-1})	(525 nm, 25440 M^{-1} cm^{-1}), (567 nm, 69910 M^{-1} cm^{-1}), (603 nm, 13210 M^{-1} cm^{-1}), (656 nm, 24850 M^{-1} cm^{-1})

As reported in **Table 1**, all the absorption spectra display the same features, such as a predominant band for the Soret band with an intensity variation in relation to the metal, along with different signals for the Q bands. Indeed two absorption bands are depicted for the metalloporphyrin derivatives and four for the free-base compound, in accordance with previous reports [11]: metalloporphyrins typically exhibit a small number of Q bands due to the symmetrisation of the molecule after metal coordination, resulting in a decrease in the number of these signals, while protons on nitrogen split the Q bands into two components x and y [12].

Moreover, in the case of nickel (Ni), the less delocalized π bonds decrease the average electron density of the molecule, thus increasing the energy available for electron transitions. Consequently, a blue shift occurs in the Soret bands (427 nm). On the other hand zinc (Zn(II)) porphyrins possess more delocalized π bonds that increase the average electron density of the porphyrin molecule.

This, in turn, lowers the energy required for electron transitions, leading to a slight red shift in the Soret band (436 nm).

The electronic circular dichroism spectra display similar characteristics as the UV-visible, exhibiting the same intensity changes in the signal at the Soret band. The metalloporphyrins derivatives typically show only one ECD-active Q band, while the free base chromophores exhibit two, as listed in **Table 2** for *P* enantiomers. It is worth mentioning that for the Cu porphyrins the sign is reversed.

*Table 2. Δε values from the ECD spectra for P enantiomers of the **MPrH6** derivatives.*

Metal	Soret band (λ, Δε)	Q bands (λ, Δε)
P-Zn	(450 nm, +460 M^{-1} cm^{-1}) (437 nm, -248 M^{-1} cm^{-1})	(607 nm, +306 M^{-1} cm^{-1})
P-Ni	(446 nm, +300 M^{-1} cm^{-1}) (427 nm, -84 M^{-1} cm^{-1})	(578 nm, +16 M^{-1} cm^{-1})
P-Pd	(444 nm, +1779 M^{-1} cm^{-1}) (430 nm, -693 M^{-1} cm^{-1})	(575 nm, +156 M^{-1} cm^{-1})
P-Cu	(437 nm, +187 M^{-1} cm^{-1}) (450 nm, -380 M^{-1} cm^{-1})	(602 nm, +32 M^{-1} cm^{-1})
P-Free base	(448 nm, +893 M^{-1} cm^{-1}) (434 nm, -416 M^{-1} cm^{-1})	(570 nm, +104 M^{-1} cm^{-1}) (658 nm, +25 M^{-1} cm^{-1})

It is fundamental to highlight how the intensity of the Exciton Coupling couplet increased in this system, where there is an ethynyl spacer between the porphyrin and the helicene core: for instance, for *P*-**ZnPrH6** the Δε value for the couplet at the Soret band is 460 M^{-1} cm^{-1} while comparatively for the positive signal of the helicenic part (330 nm) is only 51 M^{-1} cm^{-1}. This is also nicely seen in the g_{abs} spectra plotted in **Figure 6** which show stronger intensity on the porphyrin centered bands than on the helicenic ones. Note also from **Figure 6** that, except the Cu(II) complex, all derivatives display very similar g_{abs} values.

III.2. Total luminescence and circularly polarized luminescence of MPrH6

The total luminescence of this family of compounds was investigated by measuring the emission of 10^{-6} M solutions in dichloromethane, at room temperature, with an excitation at 440 nm. The spectra are reported in **Figure 7**. Unpolarized luminescence spectra of the **MPrH6** series were measured at room temperature in CH_2Cl_2 solutions for all the derivatives except for the Pd porphyrin. In fact, the phosphorescence of this compound was investigated under inert atmosphere at room temperature.

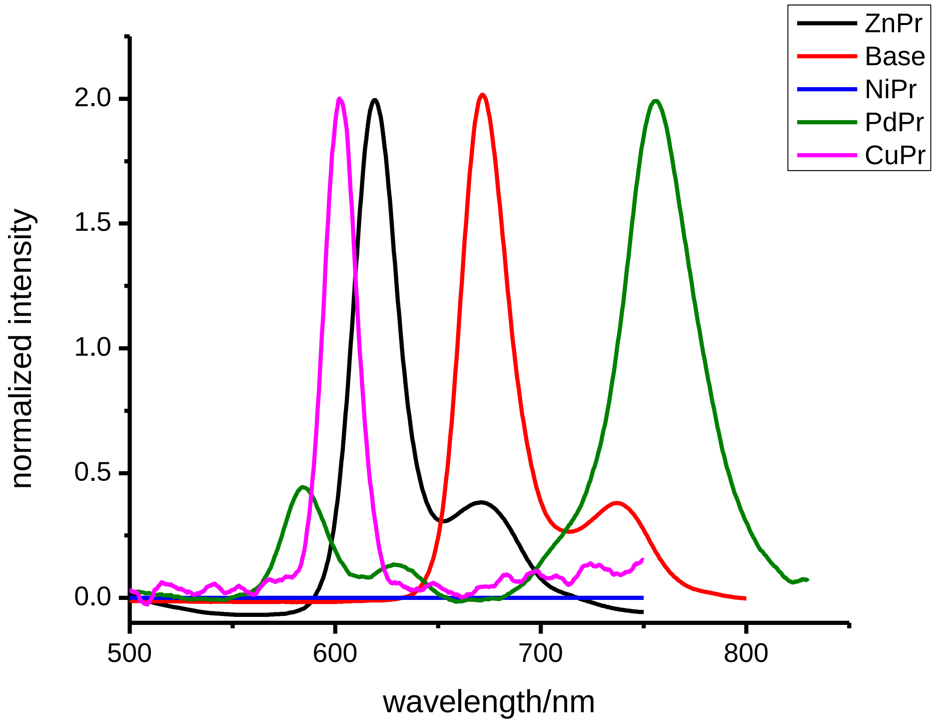

Figure 7. Emission spectra of the MPrH6 series, measured at room temperature in CH_2Cl_2 solutions.

As expected, the Ni derivative shows no emission properties, while the Zn and the free base porphyrins compounds are quite similar to the molecules previously described, and in good agreement with literature [11]: they display two emission peaks, at 620 and 670 nm for **ZnPrH6**, and 670 and 738 nm for the free base, that shows a 50 nm red shift (black and red line in **Figure 7**). Pleasingly, these latter compounds are also CPL-active (**Figure 8**). Overall, the free base and the zinc complex display emission with rather good quantum yields around 30%, substantial g_{lum} values around 10^{-3} and good brightness (**Table 3**).

Table 3. a) Relative quantum yield, TPP in dichloromethane as reference; b) dissymmetry factor, g_{lum}, of each compound; c) CPL brightness

Compound	PLQY[a]	g_{lum} (λ)[b]	B_{CPL}[c]
ZnPrH6	0.28	1.1×10^{-3} (620 nm)	26
H_2PrH6	0.32	1.3×10^{-3} (680 nm)	47

A different consideration should be made for the Pd and Cu derivatives. For the palladium porphyrin, the measurements were performed under inert atmosphere, in order to avoid oxygen quenching, and a predominant peak appeared at 750 nm, as depicted in **Figure 7**. No CPL could be however detected with our instruments.

Regarding the Cu(II) complex, the total luminescence was measured both at room temperature in CH_2Cl_2 and at 77 K in 2-methyl tetrahydrofuran (2-MeTHF), showing one single band at 600 nm but no detection of CPL response. It is well-known in the literature that the photophysics of copper(II) porphyrins is really dependent on the measurement conditions, such as solvent environment, temperature, etc. In our case, and under the previously mentioned conditions, we have not been able to observe any CPL response.

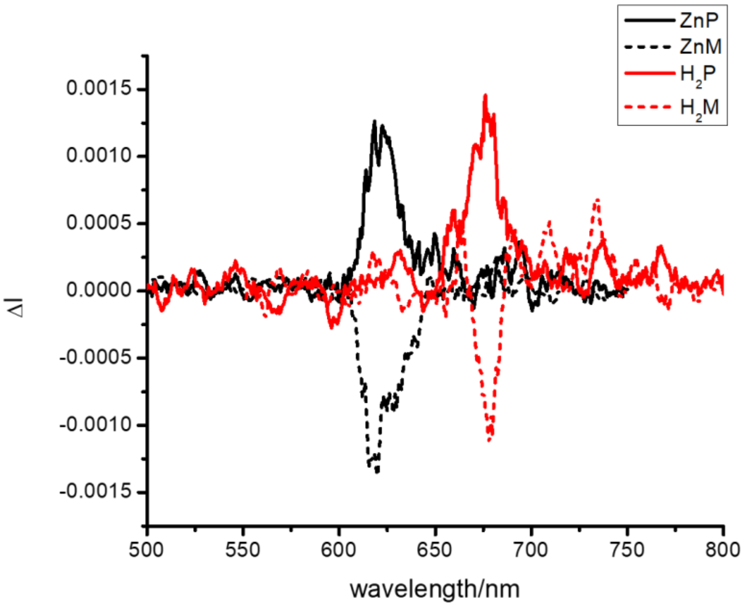

*Figure 8. CPL spectra of **ZnPrH6** (black lines) and **H2PrH6** (red) measured in CH_2Cl_2 at 298K*

III.3. UV-vis and ECD spectra of MPrOMeH6 series

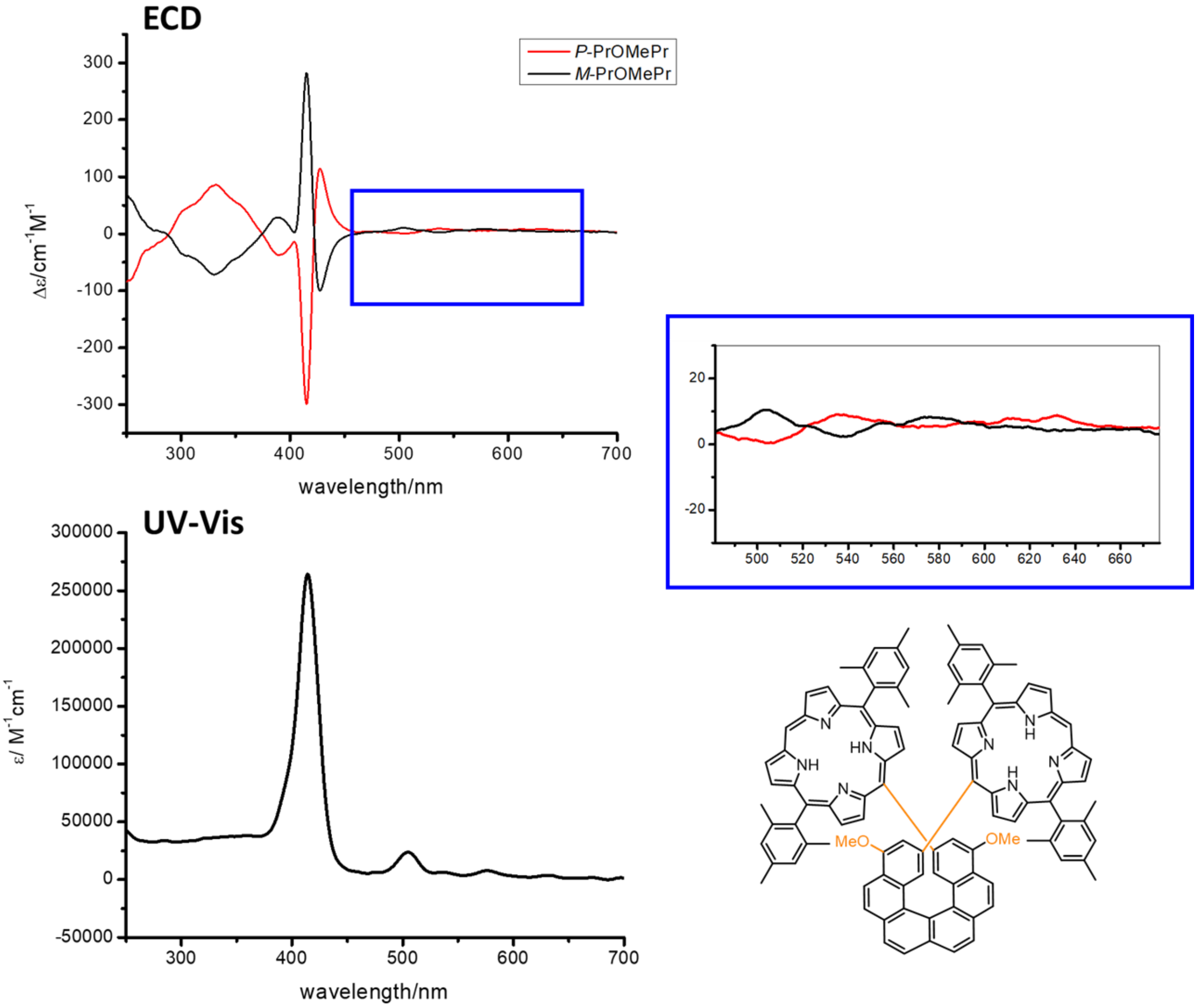

*Figure 9. ECD (top) and UV-Vis (bottom) spectra of the free-base derivative **PrOMeH6** measured in 10^{-5} M solution in CH_2Cl_2*

As depicted in **Figure 9**, in the UV-Vis absorption spectrum of **PrOMeH6** the dominant peak is observed at the Soret band, accompanied by the presence of the four Q bands, while the signal for the helicene covers the region below 400 nm.

All these bands reveal to be active in ECD. For the *P* enantiomer, the helicene π-π* transitions are represented by a positive (330 nm, $\Delta\varepsilon$ = +71 M^{-1} cm^{-1}) and two negative bands (250 and 390 nm, $\Delta\varepsilon$ = -69 and -29 M^{-1} cm^{-1}, respectively). The couplet of the exciton coupling appears at 427 nm ($\Delta\varepsilon$ = +99 M^{-1} cm^{-1}) with a negative peak and 415 nm ($\Delta\varepsilon$ = -482 M^{-1} cm^{-1}) and all the Q bands show a signal in the region between 500 and 700 nm (**Table 4**).

*Table 4. Δε values from ECD spectra for the Soret and Q bands of the free-base P-**PrOMeH6**.*

***P*-PrOMeH6**	**λ, (Δε)**
Soret band	415 nm (-482 M^{-1} cm^{-1}), 427 nm (+99 M^{-1} cm^{-1})
Q bands	504 nm (+10 M^{-1} cm^{-1}), 537 nm (-2 M^{-1} cm^{-1}), 576 nm (+8 M^{-1} cm^{-1}), 663 nm (-4 M^{-1} cm^{-1})

The metalated derivatives (metal = Zn, VO) were as well characterized by UV-Vis absorption and ECD measurements, displaying the same behaviour (**Figures 10** and **11** and **Table 5**). More specifically, in the ECD spectra the three bands for the helicene occur at similar wavelengths as for the free-base compounds (250, 330, 390 nm). Concerning the porphyrin unit, the Soret band is slightly red shifted and the only Q band present in absorption exhibit no ECD signal. Moreover, it is worth noting that for these systems the exciton coupling signature shows a new feature: three separated bands characterize the region of the Soret band and they are usually found in porphyrins giving a π-π stacking or whose rotation is forbidden due to steric hindrance, as shown in paragraph I.3 in **Chapter 2**: the double Cotton effect is often reported as the result of the two components of the Soret band (B_x and B_y). Computational studies are ongoing to further investigate this phenomenon.

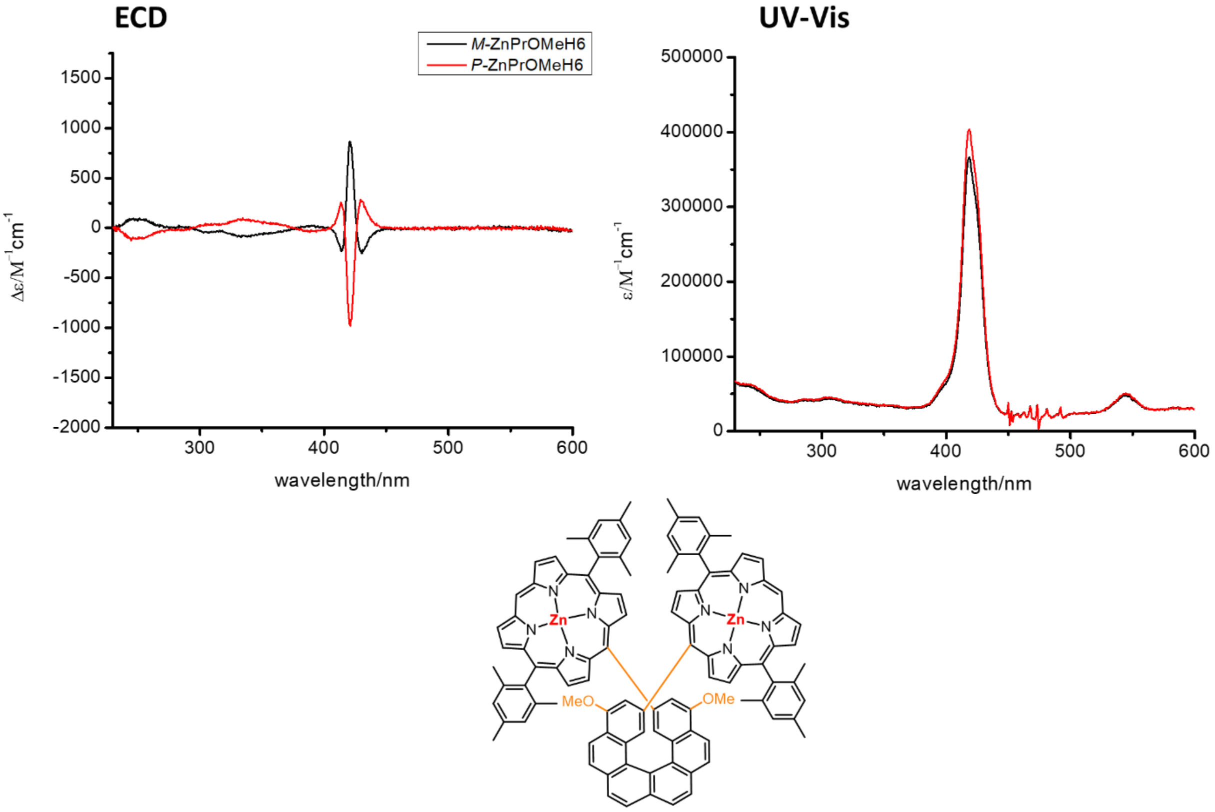

*Figure 10. ECD and absorption spectra of **ZnPrOMeH6** (10^{-5} M solution in CH_2Cl_2).*

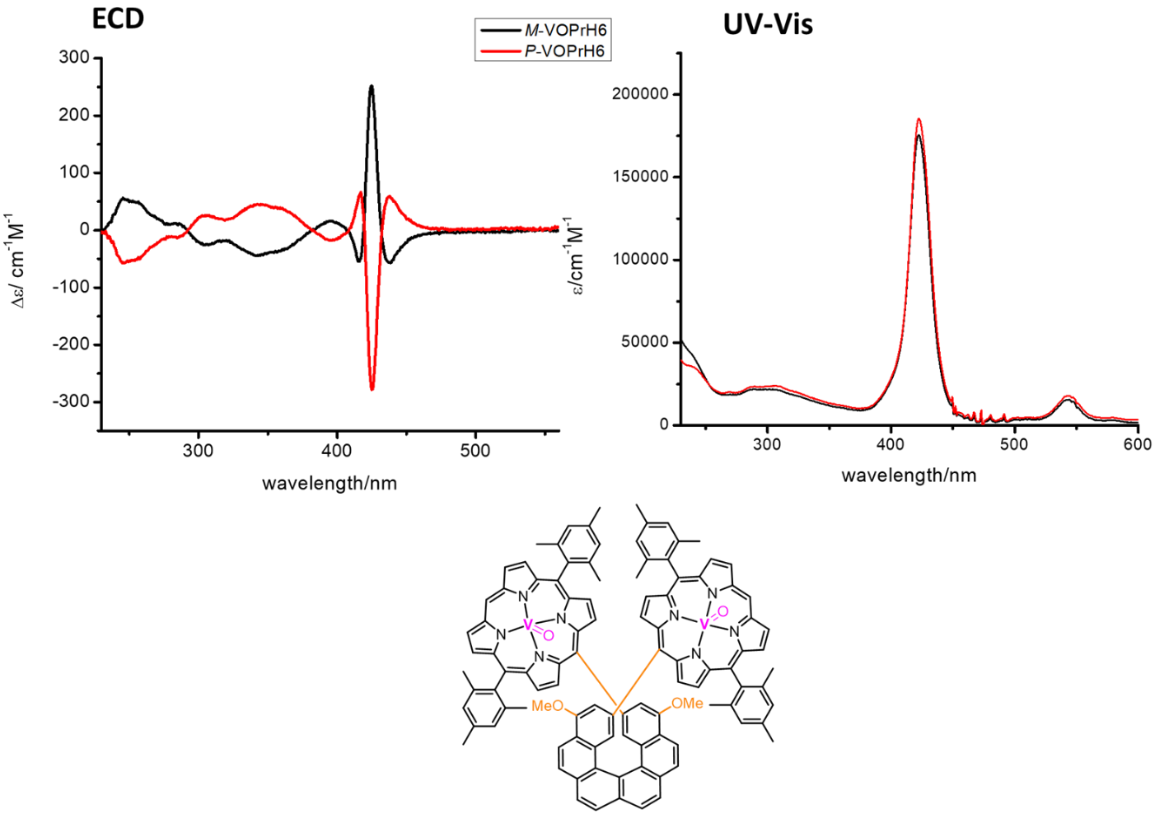

Figure 11. ECD and absorption spectra of the vanadyl derivative VOPrOMeH6 (10^{-5} M solution in CH_2Cl_2).

Table 5. Soret band wavelengths and corresponding Δε values for both metalated compounds.

Compound	Soret band λ (Δε)
P-**ZnPrOMeH6**	438 nm (+251 M^{-1} cm^{-1})
	422 nm (-867 M^{-1} cm^{-1})
	414 nm (+230 M^{-1} cm^{-1})
P-**VOPrOMeH6**	438 nm (+59 M^{-1} cm^{-1})
	425 nm (-278 M^{-1} cm^{-1})
	417 nm (+66 M^{-1} cm^{-1})

The highest values are displayed by the Zn derivative. In a 2009 work on DNA-porphyrins conjugates, Balaz *et al* reported the ECD spectra of different complexes (free base, Zn and Cu) and the respective theoretical investigations. They explained that the Zn-coordinated compound showed the most intense exciton couplet signal thanks to its conformation with a more favorable twist between the interacting chromophores [13]. Conformational studies will confirm this hypothesis for this class of molecules.

III.4. Total luminescence and circularly polarized luminescence of PrOMeH6

The free-base derivative exhibits non-polarized and polarized luminescence in a dichloromethane solution (C ≈ 10^{-6} M) at room temperature, by using an excitation wavelength of 415 nm.

The total luminescence spectrum displays two bands at 645 and 707 nm and both of them show a CPL signal: it is interesting to highlight this sign inversion between the two bands, which have also a different intensity (g_{lum} = 7×10^{-4} and 2×10^{-4} respectively, **Figure 12**).

The photoluminescence quantum yield ϕ is 0.10 with TPP in CH_2Cl_2 as reference.

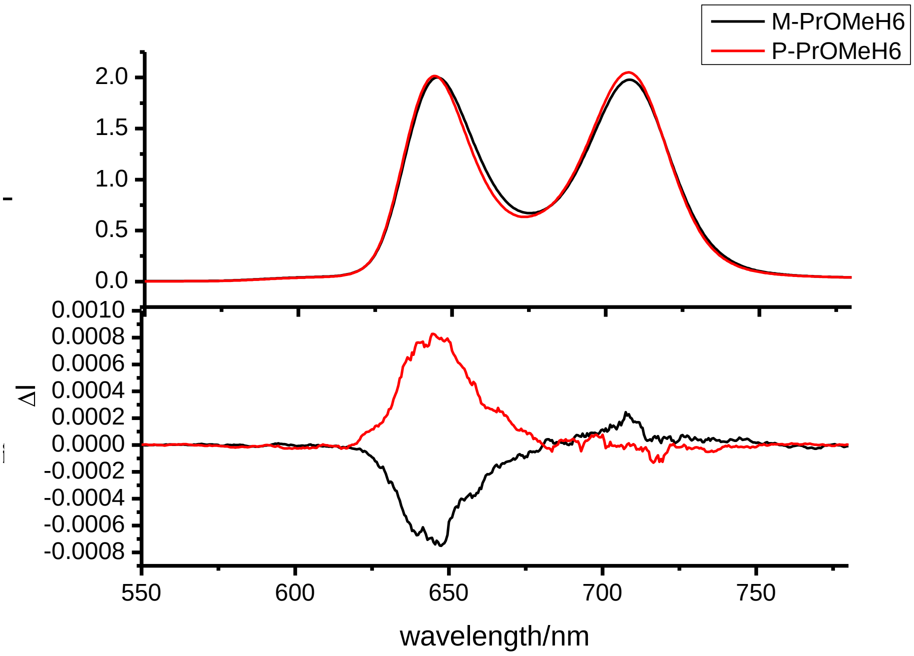

*Figure 12. Total luminescence (top) and CPL (bottom) spectra of the free-base derivative **PrOMeH6** measured in 10^{-6} solution in CH_2Cl_2.*

The luminescence response of **ZnPrOMeH6** was measured and it displays two bands with different intensities: a first peak appears at 600 nm and a stronger one at 640 nm (**Figure 13**).

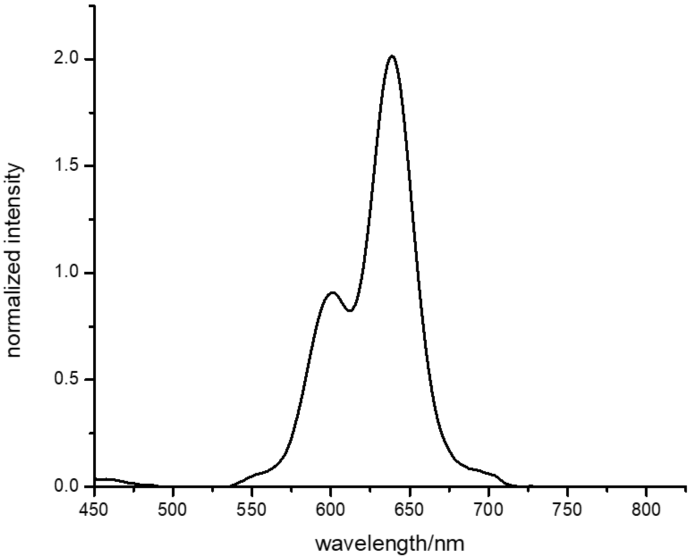

*Figure 13. Unpolarized luminescence spectrum of **ZnPrOMeH6** in dichloromethane solution (10^{-6}M).*

However, none of them display CPL activity. The photoluminescence quantum yield ϕ is 0.07 (TPP in CH_2Cl_2 as reference).

III.5. Comparisons among the different Zn derivatives

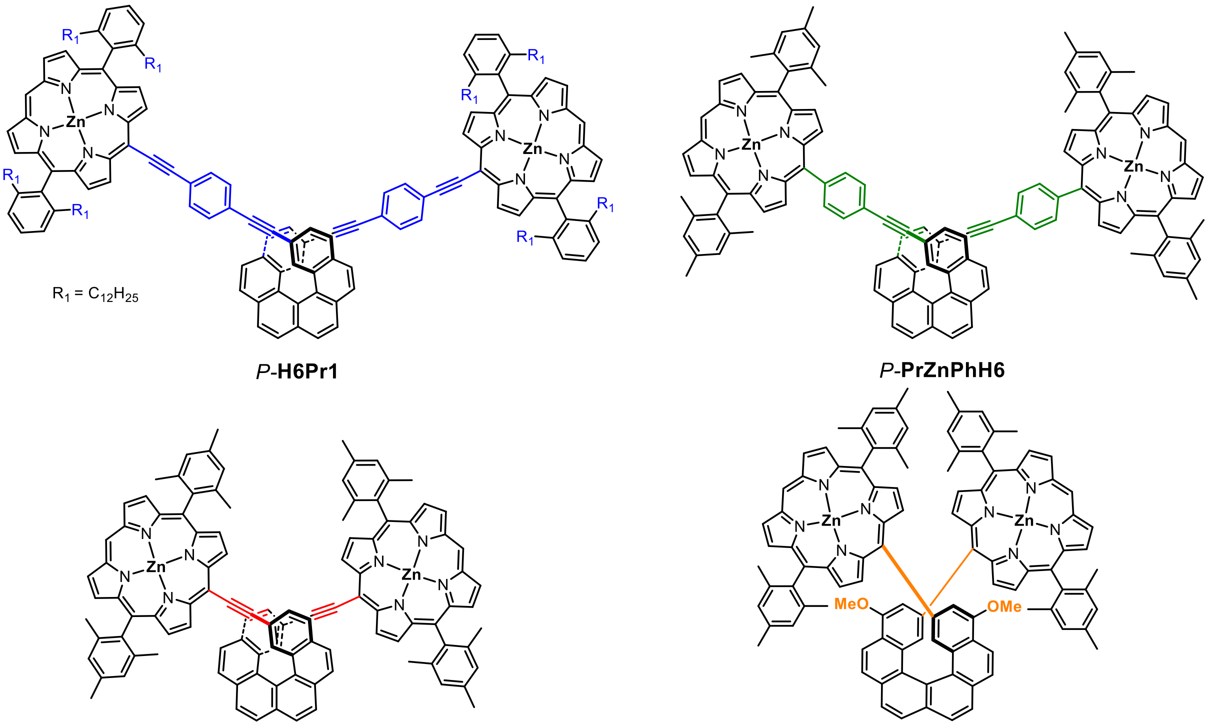

P-**H6Pr1**

P-**PrZnPhH6**

P-**ZnPrH6**

P-**ZnPrOMeH6**

Figure 14. Structures of the Zn complex for each family of porphyrin-helicene conjugate.

The ECD spectra of Zn derivatives of the four different series are compared (**Figure 14**). The higher Δε value corresponding to the Soret band of the porphyrin is displayed by **ZnPrOMeH6**, the compound with the lowest interchromophoric distance (**Table 6**). This result is consistent with the definition of exciton couplet, whose intensity (in terms of Δε values) is inversely proportional to the square of the distance between the chromophore (see Introduction chapter).

H6Pr1 exhibits as well a strong Δε value that can be due to the extent of the conjugation along the spacer, together with a red shift if compared to the other derivative bearing a phenyl spacer **ZnPrPhH6** (green line in **Figure 15**).

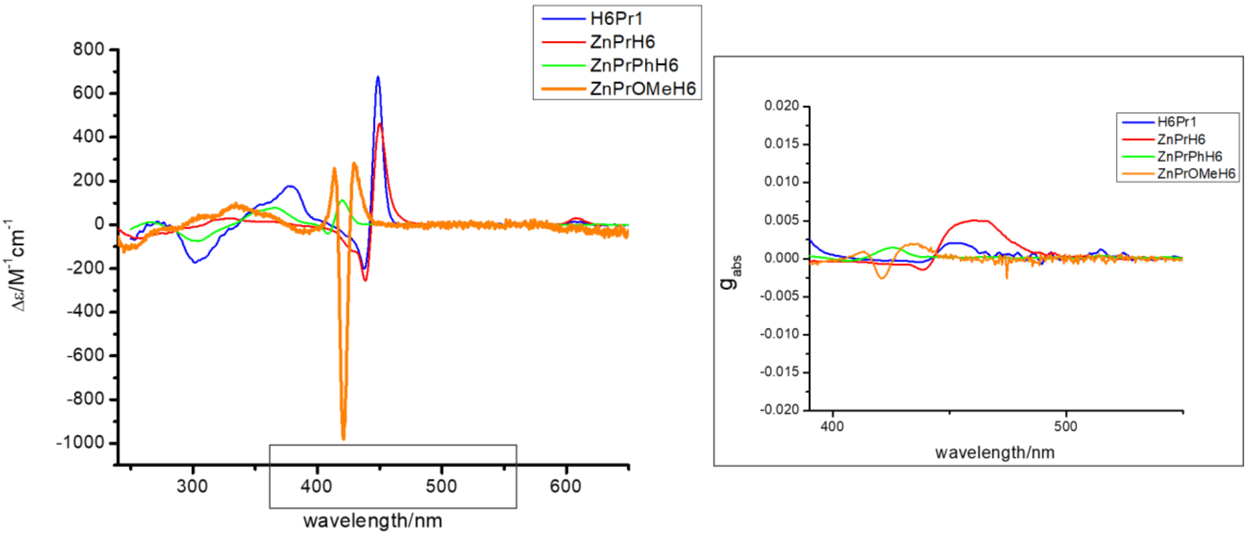

Figure 15. ECD spectra of the Zn derivatives and corresponding g_{abs} spectra for the Soret band range.

Table 6. Δε and ε for the Soret band of all the Zn derivatives.

Compound	Pr-Pr distance (Å)	$\varepsilon_{\text{Soret band}}$ ($M^{-1}cm^{-1}$)	$\Delta\varepsilon_{\text{Soret band}}$ ($M^{-1}cm^{-1}$)
***P*-H6Pr1**	24.3	480000 (440 nm)	-200 (438 nm) +671 (449 nm)
***P*-ZnPrPhH6**	21.5	210755 (414 nm)	-38 (407 nm) +112 (420 nm)
***P*-ZnPrH6**	15.3	180580 (436 nm)	-248 (437 nm) +460 (450 nm)
***P*-ZnPrOMeH6**	12.2	365129 (419 nm)	+251 (438 nm) -867 (422 nm) +230 (414 nm)

As depicted in **Table 7**, the luminescence dissymmetry factor g_{lum} value increases, along with the photoluminescence quantum yield, from **H6Pr1** to **ZnPrH6**: a correlation with the interchromophoric distance or the conjugation of the molecules could not be claimed since the functionalization of the chromophore is different. In fact, after the development of the first series of compound **H6Pr1-3**, the 5,15-(dimesityl) porphyrin was selected as new moiety, in order to avoid the effect of the vibration on the luminescence along with the steric hindrance of the C_{12} alkyl chains.

Table 7. g_{abs} and g_{lum} values for the different compounds.

Compound	Pr-Pr distance (Å)	g_{abs} (Soret band)	g_{lum}	PLQY	B_{CPL}
H6Pr1	24.3	$\pm 2\times10^{-3}$	$\pm 7\times10^{-4}$	0.16	26
ZnPrPhH6	21.5	$\pm 1.1\times10^{-3}$	$\pm 1\times10^{-3}$	0.08	0.8
ZnPrH6	15.3	$\pm 5\times10^{-3}$	$\pm 1.3\times10^{-3}$	0.28	26
ZnPrOMeH6	12.2	$\pm 2.3\times10^{-3}$	-	0.07	-

Concerning the helicene subunit (see **Table 8**), the highest Δε values are presented by the more conjugated compounds **H6Pr1** and **ZnPrPhH6**. This extended conjugation led to a red-shift (40 nm) compared to the other derivatives. Both of them bear two ethynyl groups and two phenyl moieties, which can also enhance the response through another exciton coupling and good alignment of the magnetic and electric transition dipole moments. In fact our group already demonstrated how the simple functionalization with ethynyl moieties first and then with electron donor/acceptor units of the carbo[6]helicene leads to a significant improvement of the chiroptical properties [14].

Table 8. Δε for the helicene moiety

Compound	Pr-Pr distance (Å)	Δε (helicene) (M^{-1} cm^{-1})
H6Pr1	24.3	±176 (378 nm) ±173 (302 nm)
ZnPrPhH6	21.5	±77 (376 nm) ±74 (303 nm)
ZnPrH6	15.3	±51 (330 nm) ±62 (255 nm)
ZnPrOMeH6	12.2	±83 (336 nm) ±97 (247 nm)

IV. CISS effect measurements: mc-AFM

Since mc-AFM measurements involve the deposition of chiral molecules on a gold-coated nickel surface (Au/Ni), the arrangement of these molecules on the surface significantly impacts the efficiency of spin filtering. However, achieving precise molecular orientation is challenging. To address this challenge, researchers have pursued two main approaches: (a) generating self-assembled monolayers (SAMs) using chiral molecules with anchoring groups such as –SH or –OH, as seen in the work by S. Mishra et *al.* [15] and (b) harnessing flat, π-conjugated molecules that can autonomously organize into chiral, columnar arrangements. This approach has been explored by C. Kulkarni et al. [16] and A. K. Mondal et *al*. [17].

In the first approach, the spin selectivity is measured along the primary axis of the molecule, which stands perpendicular to the plane of the substrate. In contrast, the second approach involves polymers arranged on the Au/Ni surface, and the measurement of the CISS effect is taken perpendicular to the molecule's primary axis. However, both methodologies exhibit certain limitations. Approach (a) necessitates intricate modifications either before or after synthesizing the chiral molecule, while approach (b) requires meticulous design and extensive assessment of the supramolecular polymer's properties.

Considering these challenges, finding new spin filters that are suitable compromises between easy processability and high performance is crucial to enable the practical application of the CISS effect in devices.

Due to the compromise between a high g_{abs} value and the significant Δε for the exciton couplet at the Soret band, the **MPrH6** series was selected as suitable candidate for the CISS effect measurements through magnetic conductive AFM. These measurements were performed with the collaboration of Dr. Anil Kumar in Prof. Ron Naaman' group at Weizmann Institute of Science.

More specifically, the first preliminary results were obtained for the two enantiomers of Zn derivative *P* and *M*-**ZnPrH6**.

The substrates for the mc-AFM studies were prepared using the e-beam evaporation deposition technique on Si (100) wafer. A 100 nm layer of Ni layer and a 7 nm layer of Au layer was deposited on a Si wafer. The gold layer has the function to protect Ni from oxidizing. The deposited multilayer surfaces were cleaned by immersing them first in acetone and then in ethanol for 10 minutes. The role of the Ni/Au surfaces is to allow spin polarization of electrons injected from the surface into the chiral molecules induced by a magnetic field.

The chiral molecules were deposited on the Ni/Au surfaces by spin coating a 1 mM solution in dichloromethane with at 3000 rpm for 40 sec.

The mc-AFM images showed an amorphous nanoparticles-like assembly of the molecules onto the substrate (**Figure 16**). The calculation of the roughness of the surfaces will be implemented using an higher resolution AFM.

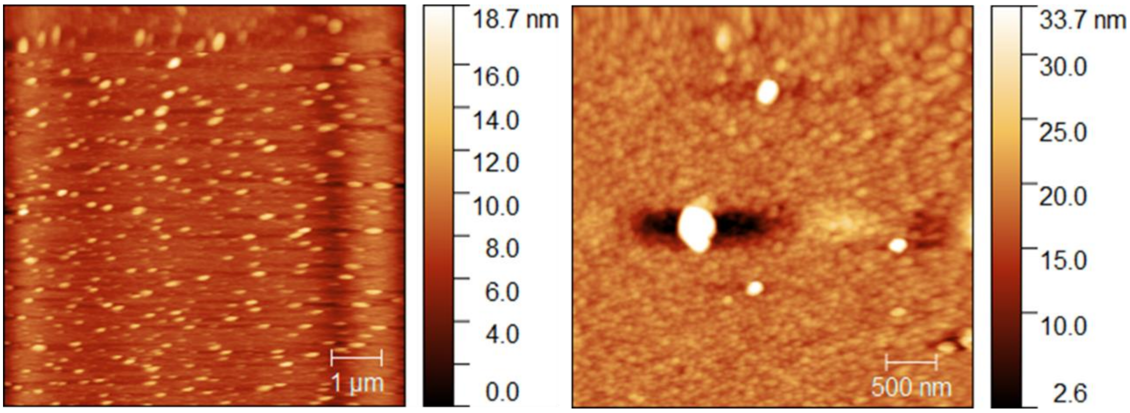

*Figure 16. AFM images of the Ni/Au coated with P-**ZnPrH6**.*

The gold-coated nickel surface (Au/Ni) with the chiral molecules was magnetized perpendicularly to the surface, with the north pole pointing either up (toward the surface) or down. Depending on the direction of the external magnetic field (0.50 T), the spin of the ejected electrons from the nickel substrate to the deposited chiral molecular layer varies. The current displayed by both *M*- and *P*-**ZnPrH6** strongly depends on the direction of the magnetization of the substrate (**Figure 17**): specifically, the *M*-enantiomer exhibits higher currents when the substrate is magnetized with the magnetic field UP. In contrast, in the case of *P*-**ZnPrH6** the current is lower with the same magnetization but higher for magnetization DOWN.

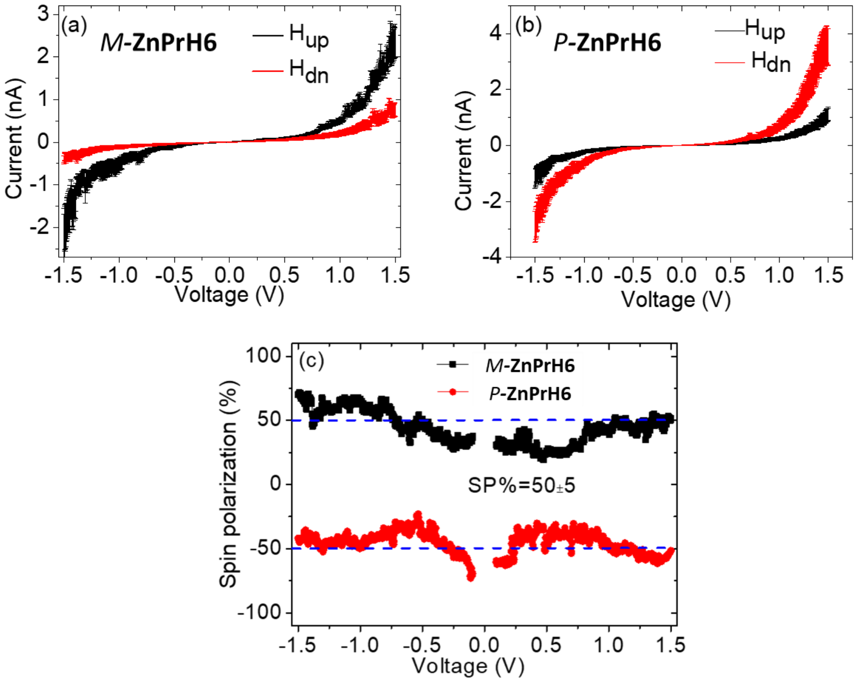

*Figure 17. Current versus voltage (I-V) plots recorded for spin-coated (a) P-, and (b) M-**ZnPrH6** on Ni-Au substrates. In both cases, the Ni substrates were magnetized with the north pole pointing in the up (the black line) and down (the red line) orientations; c) Spin Polarization plot for both compounds.*

Magnetic field-dependent current-voltage (I-V) characteristics of the prepared samples were determined using a multimodal scanning magnetic probe microscopy (SPM) system equipped with a Beetle Ambient AFM and an electromagnet with an R9 electronic controller (RHK Technology). Voltage spectroscopy for the I-V measurements was performed by applying voltage ramps with a non-magnetic Pt tip (DPE-XSC11, µmasch with spring constant 3-5 Nm^{-1}) in contact mode. At least 50 I-V curves were scanned.

In this way, the spin selective electron transport was quantified (spin polarization) as the relative ratio of currents with the two different configurations of the magnet (UP and DOWN), that is:

$$SP = \frac{(I_{UP} - I_{DOWN})}{(I_{UP} \mp I_{DOWN})} \times 100 = 50 \ \pm 5\,\%$$

We can say that this value is quite promising considering that there are no anchoring groups or supramolecular polymerization or organization.

The thin-film organization of these derivatives will be confirmed by solid state ECD measurement.

In the near future, we would like to measure the CISS effects on the other complexes of the series and study the influence of the metal on the final SP values. Indeed, we hope to see some influence of the chiroptical responses (in relation with the exciton coupling chirality) and of the spin-orbit coupling of the heavy metals.

V. Conclusions

This strategy of subsequently allowed us to fine-tune this platform by changing the linker between the helicene and the porphyrin and to achieve higher g_{abs} and g_{lum} values.

A noteworthy enhancement was achieved with the family of molecules **MPrH6. T**he 2,5-bis-ethynyl carbo[6]helicene is linked directly to the porphyrins through an ethynyl moiety, so that the interchromophoric distance was reduced. In the ECD spectrum, the EC bisignature at the Soret band appeared to be the prominent signal compared to the helicene bands, and the value was remarkably improved. Therefore, the investigation of the properties was extended to the influence of the metal and several derivatives were prepared. Thanks to the promising results, these derivatives (Zn(II), Ni(II), Pd(II), Cu(II)) were selected as preliminary candidates for CISS measurements through mc-AFM, in collaboration with Naaman's group at Weizmann Institute of Science: the aim is to try to obtain a good spin polarization value by exploiting the remarkable optical activity, without the need for anchoring groups or supramolecular polymerization. Spin polarization as high as 50% was obtained for the zinc complex.

The last system **MPrOMeH6**, which does not include any spacer but has a direct C-C bond between the chiral unit and the chromophore, was designed to optimize the distance between the metallic centers in the porphyrin core. The aim was to exploit the metal-metal interactions, specifically in magnetically-active centers like the V(IV)O derivative, that will be studied further by EPR spectroscopy. Interestingly, the enantiomeric zinc derivatives *P*- and *M*-**ZnPrOMeH6** exhibited the highest exciton coupling response, thus confirming the impact of proximity. Moreover, the three alternating bands pattern is reminiscent of former examples described in the literature with two interacting perpendicular transition dipole moments (see *meso* bis-porphyrins in **Chapter 2**).
Overall, these results nicely illustrate how molecular engineering using functionalization with strongly polarizable units in close proximity enables the fine-tuning of the chiroptical signatures. This strategy also provides access to CPL active porphyrin derivatives which still remain quite rare, and opens up new opportunities for the design of new suitable candidates for spintronic applications.

V.1. Perspectives

The Suzuki coupling between **PrOMeH6** and the borylated porphyrin gave rise to the mono-substituted derivative as side-product that was used to synthesize a donor-acceptor system with an anthraquinone moiety (**Figure 18**).

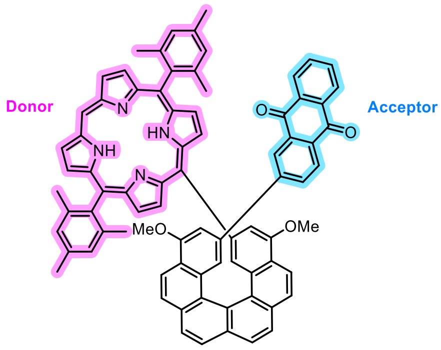

H6PrQ

Figure 18. Schematic structure of the donor-acceptor derivative

The product was synthesized in both enantiomerically pure forms and for now it was only characterized by ^{1}H-NMR. The full characterization will be performed and its chiroptical spectroscopies will be investigated further in the future. The aim is to obtain an electron donor/acceptor pair bearing a chiral bridge and to investigate the influence of the electric dipole direction on the spin filtering ability. Moreover, by coordinating the porphyrin with a magnetically active metal, we could extend the application of CISS effect to quantum technology [1].

VI. Experimental procedures

VI.1. Synthetic procedures for the MPrH6 series

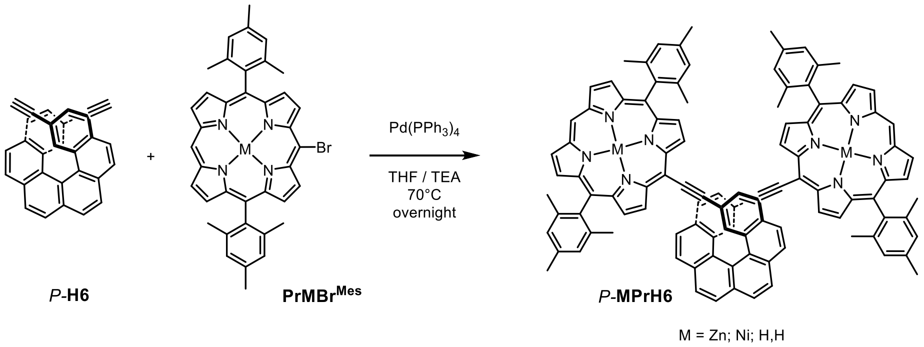

Scheme 49. Sonogashira coupling reaction to obtain MPrH6

Compound **H6** (0.04 mmol, 1 eq) and **PrMBr^{Mes}** (0.10 mmol, 2.5 eq) were dissolved in a triethylamine/THF mixture (1/2) (10 mL) which was freed from oxygen by freeze-pump-thaw cycles. Then, $Pd(PPh_3)_4$ (5% mmol) was added into the solution. The reaction was stirred overnight at 70 °C under argon. After the reaction, solvent was removed under vacuum and the residue was purified by a silica gel column chromatography (heptane/dichloromethane 7/3) followed by size exclusion chromatography in pure chloroform to afford the desired product as a red-purple solid (yield = 45-50%).

- **H2PrH6**

Isolated as purple solid (50%).

^{1}H NMR (400 MHz, Methylene Chloride-d2) *δ* 10.13 (s, 2H, CH_{meso}), 9.53 (d, *J* = 4.6 Hz, 4H, CH_{porph}), 9.29 (d, *J* = 4.6 Hz, 4H, CH_{porph}), 8.89 (d, *J* = 4.7 Hz, 4H, CH_{porph}), 8.78 (d, *J* = 4.6 Hz, 4H, CH_{porph}), 8.56 (s, 2H, CH_{hel}), 8.36 – 8.23 (m, 4H, CH_{hel}), 8.23 (s, *J* = 2.1 Hz, 4H, CH_{hel}), 8.23 – 8.13 (m, 2H, CH_{hel}), 7.99 (dd, *J* = 8.2, 1.6 Hz, 2H, CH_{hel}), 7.41 (s, *4*H, CH_{phenyl}), 7.40 (s, *4*H, CH_{phenyl}), 2.72 (s, 12H, CH_3 Mes), 1.93 (s, 12H, CH_3 Mes), 1.90 (s, 12H, CH_3 Mes), -2.43 (s, 4H, NH).

^{13}C{^{1}H} NMR (101 MHz, Methylene Chloride-d2) *δ* 144.4, 143.0, 142.9, 142.4, 138.8, 138, 136.8, 132.6, 132.2 (CH-Pr), 131.9 (CH-Pr), 131.7 (CH-Pr), 131.3 (CH-Pr), 129.6, 128.4, 128.1, 127.7 (CH-ortho Mes), 127.3, 120.0, 117.9, 105.5 (CH-$_{meso}$ Pr), 99.1, 97.2 (C≡C), 89.6 (C≡C), 66.5, 66.3, 63.50, 50.3, 33.9, 33.7, 33.3, 30.9, , 21.1 (CH_3), 21.0 (CH_3)

HR-MS Ultraflex III, MALDI, 370 °C; ion $[M]^{+\cdot}$, **($C_{106}H_{80}N_8$),** m/z calculated 1464.651, m/z experimental 1464.653 (Δ=2 ppm).

- **ZnPrH6**

Isolated as purple solid (48%).

^{1}H NMR (400 MHz, Cholorform-d) *δ* 10.12 (s, 2H, CH$_{meso}$), 9.57 (d, *J* = 4.6 Hz, 4H, CH$_{porph}$), 9.30 (d, *J* = 4.5 Hz, 4H, CH$_{porph}$), 8.93 (d, *J* = 4.6 Hz, 4H, CH$_{porph}$), 8.85 (d, *J* = 4.5 Hz, 4H, CH$_{porph}$), 8.51(s, 2H, CH$_{hel}$), 8.31 (d, *J* = 8.6 Hz, 2H, CH$_{hel}$), 8.26 (d, *J* = 8.6 Hz, 2H, CH$_{hel}$), 8.20 (s, 4H, CH$_{hel}$), 8.13 (d, *J* = 8.2 Hz, 2H, CH$_{hel}$), 7.94 (dd, *J* = 8.2, 1.5 Hz, 2H, CH$_{hel}$), 7.38 (s, 4H, CH$_{phenyl}$), 7.36 (s, 4H, CH$_{phenyl}$) 2.72 (s, 12H, CH$_3$Mes), 1.92 (s, 12H, CH$_3$Mes), 1.87 (s, 12H, CH$_3$Mes).

^{13}C{^{1}H} NMR (101 MHz, Methylene Chloride-d2) δ 144.4, 143.0, 142.9, 142.4, 138.8, 138.0, 136.8, 132.6, 132.2 (CH-Pr), 131.9 (CH-Pr), 131.7 (CH-Pr), 131.3 (CH-Pr), 129.6, 128.4, 128.2, 127.7 (CH-ortho Mes), 127.3, 120.0, 117.9, 105.5 (CH-$_{meso}$ Pr), 99.1, 97.2 (C≡C),, 89.6 (C≡C), 66.5, 66.3, 63.5, 50.3, 33.9, 33.7, 33.3, 30.9, 21.1 (CH$_3$), 21.0 (CH$_3$).

HR-MS Ultraflex III, MALDI, 370 °C; ion [M]$^{+\cdot}$, **($C_{106}H_{76}N_{8}{}^{64}Zn_{2}$) ,** m/z calculated 1588,47704, m/z experimental 1588.479 (Δ=1 ppm).

- **NiPrH6**

Isolated as reddish solid (45%).

^{1}H NMR (400 MHz, Methylene Chloride-d2) *δ* 9.83 (s, 2H, CH$_{meso}$), 9.39 (d, *J* = 4.8 Hz, 4H, CH$_{porph}$), 9.13 (d, *J* = 4.7 Hz, 4H, CH$_{porph}$), 8.79 (d, *J* = 4.8 Hz, 4H, CH$_{porph}$), 8.69 (d, *J* = 4.7 Hz, 4H, CH$_{porph}$), 8.45 (s, 2H, CH$_{hel}$), 8.29 – 8.18 (m, 8H, CH$_{hel}$), 8.09 (d, *J* = 8.2 Hz, 2H, CH$_{hel}$), 7.88 (dd, *J* = 8.2, 1.6 Hz, 2H, CH$_{hel}$), 7.35 (s, 4H, CH$_{phenyl}$), 7.33 (s, 4H, CH$_{phenyl}$), 2.67 (s, 12H, CH$_3$Mes), 1.92 (s, 12H, CH$_3$Mes), 1.87 (s, 12H, CH$_3$Mes)

^{13}C{^{1}H} NMR (101 MHz, Methylene Chloride-d2) δ 144.4, 143.0, 142.7, 142.4, 138.8, 138.0, 136.8, 132.6, 132.2 (CH-Pr), 131.9 (CH-Pr), 131.7 (CH-Pr), 131.3 (CH-Pr), 129.6, 128.0, 128.1, 127.7 (CH-ortho Mes), 127.3, 120.0, 117.9, 105.5 (CH-$_{meso}$ Pr), 99.1, 97.2 (C≡C), 89.6 (C≡C), 66.5, 66.3, 63.5, , 50.3, 33.9, 33.7, 33.3, 30.9, ,21.1 (CH$_3$), 21.0 (CH$_3$).

HR-MS Ultraflex III, MALDI, 370 °C; ion [M]$^{+\cdot}$, **($C_{106}H_{76}N_{8}{}^{58}Ni_{2}$),** m/z calculated 1576.48944, m/z experimental 1576.483 (Δ=4 ppm).

PdPrH6 and CuPrH6 were prepared by metalation of free base porphyrin-helicene **PrH2H6** derivative according to the following procedure [18]:

PdPrH6

P and *M*-**H2PrH6** (10 mg, 0.007 mmol) and $PdCl_2$ (5 mg, 0.027 mmol) were dissolved in a degassed mixture of benzonitrile/dimethylformamide (3/2, 5mL) and the solution was stirred for 4 h at 150 °C. The mixture was washed twice with water and extracted with dichloromethane. The solvent was removed under vacuum and the crude was purified by silica column chromatography (heptane/dichloromethane 7/3) followed by size exclusion chromatography in pure chloroform to afford the desired product as a reddish solid (11 mg, 94%).

^{1}H NMR (400 MHz, Methylene Chloride-d2) δ 10.16 (s, 2H, CH_{meso}), 9.48 (d, *J* = 4.9 Hz, 4H, CH_{porph}), 9.23 (d, *J* = 4.7 Hz, 4H, CH_{porph}), 8.85 (d, *J* = 4.9 Hz, 4H, CH_{porph}), 8.76 (d, *J* = 4.8 Hz, 4H, CH_{porph}), 8.54 (s, 2H, CH_{hel}), 8.31 (s, 4H, CH_{hel}), 8.26 (d, *J* = 2.4 Hz, 4H, CH_{hel}), 8.16 (d, *J* = 8.2 Hz, 2H, CH_{hel}), 7.97 (dd, *J* = 8.2, 1.6 Hz, 2H, CH_{hel}), 7.40 (s,4H, CH_{phenyl}), 7.39 (s,4H, CH_{phenyl}), 2.71 (s, 12H, CH_3 Mes), 1.92 (s, 12H, CH_3 Mes), 1.87 (s, 12H, CH_3 Mes).

^{13}C{^{1}H} NMR (101 MHz, Methylene Chloride-d2) δ 144.4, 143.0, 142.7, 142.4, 138.8, 138.0, 136.8, 132.6, 132.2(CH-Pr), 131.9 (CH-Pr), 131.7(CH-Pr), 131.3 (CH-Pr), 129.6, 128.0, 128.1, 127.7 (CH-ortho Mes), 127.3, 120.0, 117.9, 105.5 ($CH\text{-}_{meso}$ Pr), 99.1, 97.2(C≡C), 89.6(C≡C), 66.5, 66.3, 63.5, , 50.3, 33.9, 33.7, 33.3, 30.9, 21.1(CH_3), 21.0(CH_3).

HR-MS Ultraflex III, MALDI, 370 °C; ion $[M]^{+\cdot}$, **(C_{106} H_{76} N_8 $^{106}Pd_2$),** 1672.4257 m/z calculated, 1672.426 m/z experimental.

CuPrH6

P and *M*-**H2PrH6** (20 mg, 0.014 mmol) and $Cu(CH_3COO)_2$*H_2O (25 mg, 0.14 mmol) were dissolved in a mixture of chloroform/methanol (5/1, 6 mL) and the solution was stirred for 4 h at room temperature. The mixture was washed twice with water and extracted with dichloromethane. The crude was purified by silica column chromatography (heptane/dichloromethane 7/3) followed by size exclusion chromatography in pure chloroform to afford the desired product as a brownish solid (19 mg, 86%).

HR-MS Ultraflex III, MALDI, 370 °C; ion $[M]^{+\cdot}$, **(C_{106} H_{76} N_8 $^{63}Cu_2$)** m/z calculated 1586.47794, m/z experimental 1586.484 (Δ=4 ppm).

VI.2. Synthetic procedures for the PrOMeH6 series

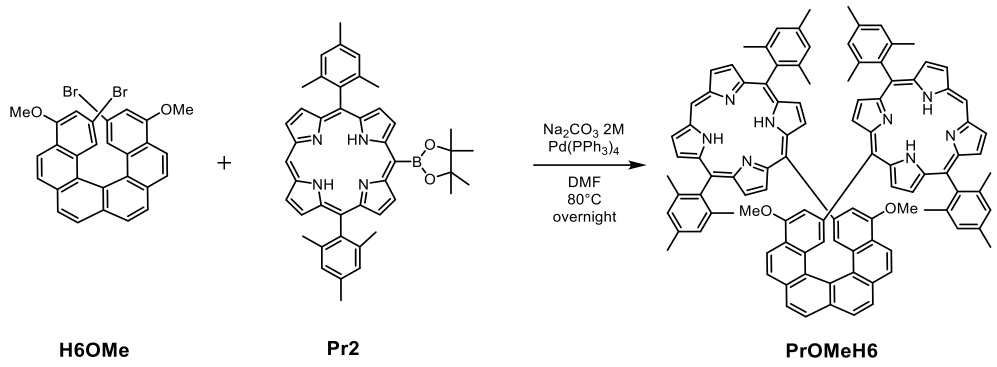

*Scheme 5. Suzuki-Miyaura coupling conditions for **PrOMeH6**.*

Compound **H6OMe** was prepared in collaboration with Stefano Cadeddu, another PhD student in our group. The synthesis is shown in **Scheme 6**.

- ### H6OMe

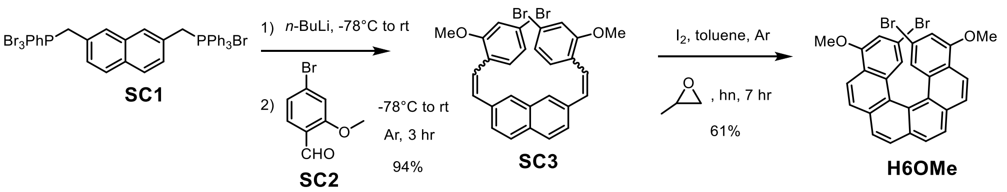

Scheme 6. Synthetic route for H6OMe starting from the bis-phosphonium salt (2,7-naphthalenedimethylene)-bis[triphenylphosphonium-bromide]

The phosphonium salt (2,7-naphthalenedimethylene)-bis[triphenylphosphonium-bromide] **SC1** (1.41 g, 1.68 mmol) was placed in a flame-dried Schlenk under argon atmosphere. Freshly distilled THF (50 mL) was added and the reaction mixture was cooled to -78 °C; *n*-BuLi (1.5 mL, 3.7 mmol) was then added slowly. The cooling bath was removed, and the solution was stirred at room temperature for 30 min. The solution was cooled again to -78°C, then 4-bromo-2-methoxy-benzaldehyde **SC2** (815 mg, 3.79 mmol) dissolved in a minimum amount of dry THF was slowly added to the reaction mixture. The solution was stirred for 3 h. The crude was directly purified by column chromatography over silica gel (heptane/ethyl acetate 8:2) to afford a foamy light-yellow product **SC3** (876mg, 1.58 mmol, 94%) as a mixture of *Z*,*Z*, *Z*,*E* and *E*,*E* isomers.

^{1}H NMR (400 MHz, Chloroform-*d*) δ 9.13 – 5.92 (m, 18H), 4.01 – 3.90 (m, 3H, OCH_3), 3.90 – 3.78 (m, 3H, OCH_3).

^{13}C{^{1}H} NMR (101 MHz, Chloroform-*d*)δ 157.97, 157.44, 137.93, 135.70, 135.49, 135.23, 134.96, 133.81, 133.52, 132.24, 131.78, 131.33, 131.29, 130.78, 130.74, 129.62, 129.16, 128.34, 128.23, 128.17, 128.13, 128.05, 127.47, 127.39, 127.27, 126.92, 126.85, 125.62, 125.43, 125.31, 125.16, 123.95, 123.80, 123.43, 123.39, 122.92, 122.88, 121.97, 121.95, 121.92, 114.56, 114.43, 55.84, 55.80.

The olefin **SC3** (353mg, 0.641 mmol) was placed in a flask (2.2 L) filled with toluene, the solution was bubbled with argon for 40 minutes. Propylene oxide (3.6 mL, 51 mmol) and I_2 (173 mg, 0.682 mmol) were added to the reactor. The solution was irradiated with UV light (mercury lamp, 500 W) for 7 hours. The toluene was evaporated. The crude product was washed with a minimum amount of dichloromethane, and with hot isopropyl alcohol, then dissolved with hot dichloromethane and after slowly addition of methanol, the 2,15-dibromo-4,13-dimethoxy-carbo[6]helicene **H6OMe** crystallized at room temperature as a yellow solid (214 mg, 0.392 mmol, 61%).

^{1}H NMR (400 MHz, Dimethyl sulfoxide-d6) δ 8.30 (d, *J* = 8.8 Hz, 2H, CH), 8.24 – 8.13 (m, 4H, CH), 8.10 (d, *J* = 8.9 Hz, 2H, CH), 7.09 (d, *J* = 0.9 Hz, 2H, CH), 6.99 (s, 2H, CH), 3.99 (s, 6H, OCH_3).

^{13}C{^{1}H} NMR (101 MHz, Methylene Chloride-d2)δ 156.4, 133.6, 132.6, 132.1, 128.0, 127.7, 126.5, 126.3, 124.6, 122.9, 122.8, 121.7, 119.3, 108.9, 56.6.

- **PrOMeH6**

Compound **H6OMe** (18 mg, 0.033 mmol) and **Pr2** (50 mg, 0.07 mmol) were dissolved in DMF (5 mL) and an aqueous solution of 2M Na_2CO_3 (0.5 mL) and the mixture was degassed for 30 minutes by bubbling Argon. Then, $Pd(PPh_3)_4$ (2 mg, 0.002 mmol) was added to the solution and the reaction was stirred overnight at 80 °C. The mixture was washed with brine, extracted with dichloromethane and the organic phase was dried over $MgSO_4$. The solvent was removed under vacuumand the residue was purified by a silica column chromatography (heptane/dichloromethane 7/3) followed by size exclusion chromatography in pure chloroform to afford the desired product **PrOMeH6** as a red solid (15 mg, 42%).

^{1}H NMR (300 MHz, Chloroform-*d*) δ 10.16 (s, 2H, CH_{meso}), 9.31 (d, *J* = 4.7Hz, 2H, CH_{porh}),), 9.30 (d, *J* = 4.7Hz, 2H, CH_{porh}), 8.92 (d, *J* = 4.6 Hz, 2H, CH_{porh}), 8.83 (d, *J* = 4.7 Hz, 2H, CH_{porh}), 8.77 (d, *J* = 4.7 Hz, 2H, CH_{porh}), 8.71 (s, 2H, CH_{phenyl}), 8.64 (d, *J* = 4.8 Hz, 2H, CH_{porh}), 8.49 (d, *J* = 4.7 Hz, 2H, CH_{porh}), 8.26 (d, *J* = 4.7 Hz, 2H, CH_{porh}), 8.11 (d, *J* = 9.0 Hz, 2H, CH_{hel}), 7.98 (s, 2H, CH_{hel}), 7.76 (d, *J* = 8.3 Hz, 2H, CH_{hel}), 7.65 (d, *J* = 8.2 Hz, 2H, CH_{hel}), 7.57 (s, 2H, CH_{hel}), 7.48 (d, *J* = 9.0 Hz, 2H, CH_{hel}), 7.29 (s, 2H, CH_{Phenyl}), 7.24 (s, 4H, CH_{Phenyl}), 4.09 (s, 6H,OCH_3), 2.63 (s, 12H, CH_3 Mes), 2.26 (s,6H CH_3 Mes), 1.90 (s, 6H, CH_3 Mes), 1.83 (s, 6H, CH_3 Mes), 1.68 (s, 6H, CH_3 Mes), -2.94 (s, 4H, NH).

^{13}C{^{1}H} NMR (101 MHz, Chloroform-*d*) δ 153.6, 140.13, 140. 11, 139.31, 139.34, 138.4, 138.0, 137.6, 137.5, 132.9, 131.5 (CH-Pr), 130.3 (CH-Pr), 128.9 (CH), 127.9 (CH_3-ortho Mes), 127.76, 127.72, 127.6, 127.0 (CH), 126.4 (CH), 126.3, 125.6 (CH), 124.4, 123.6, 121.5 (CH), 120.0, 117.7, 117.6, 112.8 (CH), 104 ($CH\text{-}_{meso}$), 55.8 (O-CH_3), 22 (CH_3-Mes), 21.0 (CH_3-Mes), 21.6 (CH_3-Mes), 21.41 (CH_3-Mes), 21.43 (CH_3-Mes).

HR-MS Ultraflex III, MALDI, 370 °C; ion $[M]^+$, **($C_{104}H_{84}N_8O_2$)**, m/z calculated 1476.67117, m/z experimental 1476.677 (Δ = 4 ppm).

- **ZnPrOMeH6**

Compound **PrOMeH6** (10 mg, 0.007 mmol) was dissolved in a mixture of $CHCl_3$/MeOH (5/1, 10 mL) and $Zn(OAc)_2$ dihydrate (44.5 mg, 0.2 mmol) was added. The solution was stirred at room temperature for 4 h. The mixture was washed with water, extracted by chloroform and the organic phase dried over $MgSO_4$, affording the desired product as a pinkish solid in quantitative yield (11 mg).

^{1}H NMR (400 MHz, Chloroform-*d*) δ 10.16 (s, 2H, CH_{meso}), 9.37 (d, *J* = 4.5 Hz, 2H, CH_{porph}), 9.33 (d, *J* = 4.5 Hz, 2H, CH_{porph}), 8.97 (d, *J* = 4.4 Hz, 2H $^?$ CH_{porph}), 8.87 (d, *J* = 4.5 Hz, 2H $^?$ CH_{porph}), 8.78 (d, *J* = 3.9 Hz, 4H, CH_{phenyl}), 8.69 (d, *J* = 4.6 Hz, 2H, CH_{porph}), 8.57 (d, *J* = 4.6 Hz, 2H, CH_{porph}), 8.36 (d, *J* = 4.6 Hz, 2H, CH_{porph}), 8.15 (d, *J* = 9.0 Hz, 2H), 7.97 (s, 2H, CH_{he}), 7.75 (d, *J* = 8.2 Hz, 2H, CH_{he}), 7.64 (d, *J* = 8.2 Hz, 2H, CH_{he}), 7.53 (s, 2H, CH_{hel}) 7.48 (d, *J* = 9.1 Hz, 2H, CH_{he}), 7.21 (d, *J* = 12.9 Hz, 4H, CH_{phenyl}), 4.07 (s, 6H, OCH_3), 2.61 (d, *J* = 7.7 Hz, 12H, $CH_{3\,\mathrm{Ortho}}$ Mes), 2.20 (s, 6H, CH_3 Mes), 1.89 (s, 6H, CH_3 Mes), 1.78 (s, 6H, CH_3 Mes), 1.65 (s, 6H, CH_3 Mes).

^{13}C{^{1}H} NMR (101 MHz, Chloroform-*d*) δ 153.6, 140.1, 140.3, 139.3, 139.34, 138.4, 138.0, 137.6, 137.5, 132.9, 131.5(CH-Pr), 130.3(CH-Pr), 128.9(CH), 127.9 (CH_3- ortho Mes), 127.76, 127.72, 127.6, 127.0(CH), 126.4(CH), 126.3, 125.6(CH), 124.4, 123.6, 121.5(CH), 120.01, 117.7, 117.6, 112.8(CH), 104($CH\text{-}_{meso}$), 55.8(O-CH_3), 22.0(CH_3-Mes), 21.0 (CH_3-Mes), 21.6 (CH_3-Mes), 21.41 (CH_3-Mes), 21.43 (CH_3-Mes).

HR-MS Ultraflex III, MALDI, 370 °C; ion $[M]^+$, **C_{104} H_{80} N_8 O_2 $^{64}Zn_2$)**, m/z calculated 1600.49817, m/z experimental 1600.502 (Δ = 2 ppm).

VI.3. Synthetic procedure for VOPrOMeH6

The VO derivative was prepared by modifying a literature procedure [19].

Vanadyl sulfate (9 mg, 0.06 mmol) and the free-base porphyrin **PrOMeH6** (10 mg, 0.007 mmol) were heated to reflux in an acetic acid buffer (glacial acetic acid (5 mL) and sodium acetate (30 mg) for 3 days. The residue was diluted in dichloromethane and washed with water. Then the crude was purified by silica gel column chromatography (Heptane/ Petroleum ether 6/4) (3 mg, 27 %).

HR-MS Ultraflex III, MALDI, 370 °C; ion $[M]^+$ **(C_{104} H_{80} N_8 O_4 $^{51}V_2$)**$^{\cdot}$, 1606.51763 m/z calculated, 1606.522 m/z experimental (Δ=3 ppm).

References

[1] A. Chiesa, A. Privitera, E. Macaluso, M. Mannini, R. Bittl, R. Naaman, M. R. Wasielewski, R. Sessoli and S. Carretta, *Adv. Mat.*, 2023.

[2] N. Berova, P. L. Polavarapu, K. Nakanishi and R. W. Woody, Comprehensive Chiroptical Spectroscopy: Instrumentation, Methodologies, and Theoretical Simulations, Wiley, 2011.

[3] F. Mohajer, M. M. Heravi, V. Zadsirjana and N. Poormohammad, *RSC Adv.,* vol. 11, pp. 6885-6925, 2021.

[4] A. Soheili, J. Albaneze-Walker, J. A. Murry, P. G. Dormer and D. L. Hughes, *Org. Lett. ,* vol. 5, pp. 4191–4194, 2003.

[5] M. Gazvoda, M. Virant, B. Pinter and J. Košmrlj, *Nat. Commun.,* vol. 9, 2018.

[6] E. Coronado, *Nat. Rev. Mater.,* vol. 5, pp. 87−104, 2020.

[7] T. Ikeue, K. Furukawa, H. Hata, N. Aratani, H. Shinokubo, T. Kato and A. Osuka, *Angew. Chem. Int. Ed. ,* vol. 44, pp. 6899−6901, 2005.

[8] I. Pozo, F. Lombardi, D. Alexandropoulos, F. Kong, J.-R. Deng, P. Horton, S. Coles, W. Myers, L. Bogani and H. Anderson, *ChemRxiv,* 2023.

[9] D. Ranieri, F. Santanni, A. Privitera, A. Albino, E. Salvadori, M. Chiesa, F. Totti, L. Sorace and R. Sessoli, *Chem. Sci.,* vol. 14, pp. 61-69, 2023.

[10] J. M. Zadrozny, J. Niklas, O. G. Poluektov and D. E. Freedman, *J. Am. Chem. Soc.,* vol. 136, pp. 15841–15844, 2014.

[11] W. Zheng, N. Shan, L. Yu and X. Wang, *Dyes and Pigments,* vol. 77 , pp. 153-157, 2008.

[12] M. Gouterman, *J. Chem. Phys.,* vol. 30, pp. 1139–1161, 1959.

[13] A. Mammana, G. Pescitelli, T. Asakawa, S. Jockusch, A. Petrovic, R. Monaco, R. Purrello, N. Turro, K. Nakanishi, G. Ellestad, M. Balaz and N. Berova, *Chem. Eur. J. 2009, 15,* vol. 15, pp. 11853–11866, 2009.

[14] K. Dhbaibi, L. Abella, S. Meunier-Della-Gatta, T. Roisnel, N. Vanthuyne, B. Jamoussi, G. Pieters, B. Racine, E. Quesnel, J. Autschbach and J. Crassous, *Chem. Sci.,* vol. 12, pp. 5522-5533, 2021.

[15] u. Mishra, A. K. Mondal, E. Z. B. Smolinsky, R. Naaman, K. Maeda, T. Nishimura, T. Taniguchi, T. Yoshida, K. Takayama and E. Yashima, *Angew. Chem., Int. Ed.,* vol. 59, pp. 14671–14676, 2020.

[16] C. Kulkarni, A. K. Mondal, T. K. Das, G. Grinbom, F. Tassinari, M. F. J. Mabesoone and E. W. M. R. Naaman, *Adv. Mater.,* vol. 32, 2020.

[17] A. K. Mondal, M. D. Preuss, M. L. Ślęczkowski, T. K. Das, G. Vantomme, E. W. Meijer and R. Naaman, *J. Am. Chem. Soc.,* vol. 143, pp. 7189–7195, 2021.

[18] R. Mishra, R. Regar, R. Singhal, P. Panini, G. D. Sharma and J. Sankar, *J. Mater. Chem. A,* vol. 5, pp. 15529-15533, 2017.

[19] J. L. Appleton, N. L. Breton, M.-A. Carvalho, J. Weiss, A. K. Boudalis, C. Gourlaouen, S. Choua and R. Ruppert, *Cryst. Growth De.s,* vol. 23, pp. 1689–1696, 2023.

Chapter 4

Synthesis of helicene derivatives for surface grafting and Spin Dependent Electrochemistry

I. Context and target molecules

I.1. The principle of spin-dependent electrochemistry

The idea behind spin-dependent electrochemistry (SDE) is to observe the chiral induced spin selectivity (CISS) effect by using electrochemical techniques, more specifically by modifying the classical cyclic voltammetry (CV) cell (**Figure 1**) and observing differences between left-handed and right-handed systems upon applying a magnetic field in up or down direction.

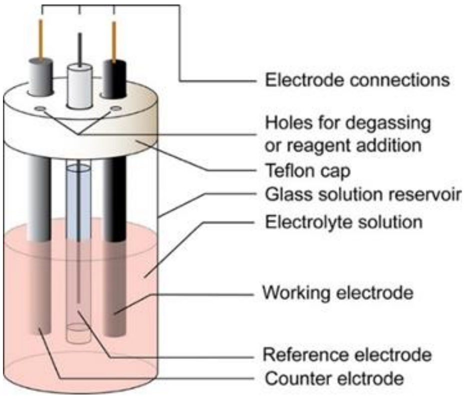

Figure 1. Schematic representation of an electrochemical cell for CV experiments. Reproduced from [23]

The typical spin-dependent cyclic voltammetry setup consists in the same three-electrode system with a reference electrode (RE), a counter electrode (CE) but the working electrode (WE) is represented by a ferromagnetic substrate where a very thin film (or a self-assembled monolayer, SAM) of chiral molecules is deposited. A redox probe is normally used as the standard reference (typically a ferrocene derivative, see below) which can be either grafted onto the working electrode, i.e. covalently bonded with the adsorbate, or be present in the bulk solution. A permanent magnet is then placed underneath the substrate to apply an external magnetic field to the system. This experimental implementation was described for the very first time in 2013 by Naaman, Fontanesi, Zacharias and co-workers [1], where, after photoelectron transmission experiments on different substrates, an electrochemical study was conducted on the purple membrane of a protein, the bacteriorhodopsin, deposited onto a nickel substrate. In this investigation, CV curves were recorded as a function of the magnetization of a Ni substrate supporting the purple membrane. The chosen redox couple was 1 mM $K_4[Fe(CN)_6]/K_3[Fe(CN)_6]$, and the experiments were conducted in an aqueous solution. Initially, CVs were recorded on the bare Ni surface, which had a thin layer of NiO of approximately 2 nm width. Subsequently, CVs were recorded after covering the Ni substrate with the purple membrane containing the chiral compound, while varying the external magnetic field direction.

The CV curves showed distinct characteristics and displayed a "quasi-reversible" behaviour that differed significantly from the CVs obtained on the bare Ni surface. The sharp current peaks observed on the bare Ni surface were replaced by broader oxidation and reduction shoulders, resulting in a larger separation in potential values. This change in the CV curves, from a reversible state (**Figure 2**), to a quasi-reversible state, was attributed to the low electrical conduction of the purple membrane.

Furthermore, the CVs recorded with different magnetic field directions exhibited a systematic difference in the current. This observation suggests that electron transfer through the chiral membrane is dependent on the spin orientation [1].

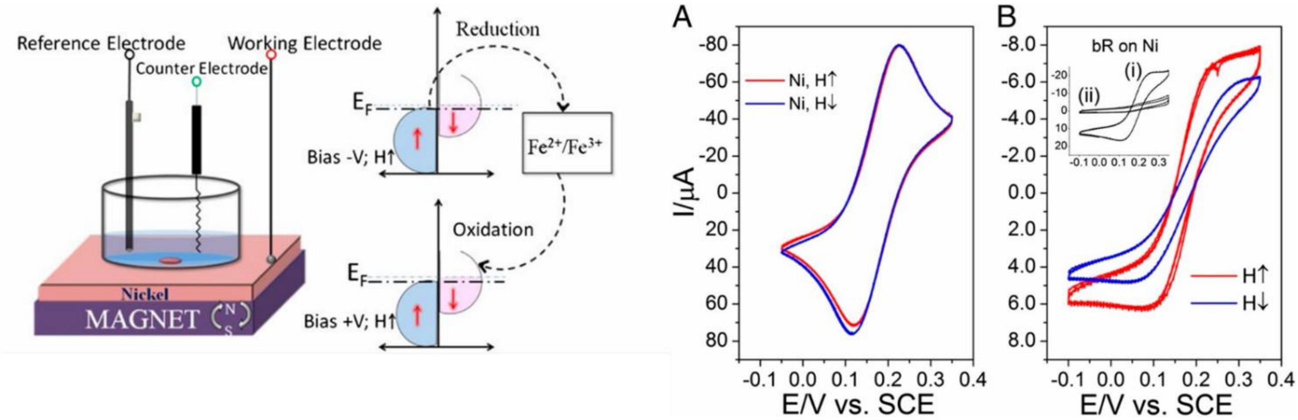

Figure 2. Left: schematic representation of a SDE setup: the permanent magnet is placed underneath the ferromagnetic substrate. Right: experimental CVs obtained in the case of the purple membrane of bacteriorhodopsin deposited onto a nickel surface electrode. Reproduced from ref [1].

The theoretical principle of this technique is based on the fact that when a ferromagnetic material is magnetized with a specific direction of the magnetic field, the “majority” spins (per definition, the spins parallel to the magnetization direction) of the charge carrier are stabilized with respect to the “minority” spin; this results in a difference in population of the spins (“UP” vs. “DOWN” or α vs. β) of the ferromagnetic electrode. Thus, most of the spins ejected from the electrode have the spin orientation leading to a spin polarized current which flows through the chiral film adsorbed on the ferromagnetic electrode surface [2].

The current through the adsorbate is observed as a function of the applied voltage for two different magnetizations of the supporting substrate. The current is measured when the substrate is magnetized so that its magnetic moment is pointing toward the adsorbed film (j_U) or away from it (j_D). In this experimental design, the difference in the transmitted current indicates the spin-selective electron transmission. In principle, the spin polarization, P, can be obtained from the asymmetry in the current,

$$P = \frac{(j_U - j_D)}{(j_U + j_D)}$$

Where j_U and j_D are the currents for the two different magnetizations, UP or DOWN, applied on the substrate.

I.2. Chiral helical polymers

Most of the SDE results are obtained using ferromagnetic materials, such as nickel or cobalt, as working electrode (WE) in close contact with a permanent magnet. Thus, the spin polarization of the conducting electrons in the ferromagnetic electrode can be manipulated by flipping the orientation, north/south, of the permanent magnet. Nevertheless, electrochemical setups involving a non-ferromagnetic working electrode (WE), have been also described in the literature. This is the case of the work of Mussini and co-workers, where the working electrode was modified by an electroactive chiral film. The charge carriers entirely originated and moved along a twisted chiral pathway with no need of a magnetic electrode as spin injector; indeed, an indium tin oxide (ITO) glass was coated by electrodeposition with (*R*) or (*S*)-2,2′-bis(2,2′-bithiophene-5-yl)-3,3′-bibenzothiophene (**BT_2T_4**) to yield oligo(*R*/*S*)-**BT2T4** as described in **Figure 3**.

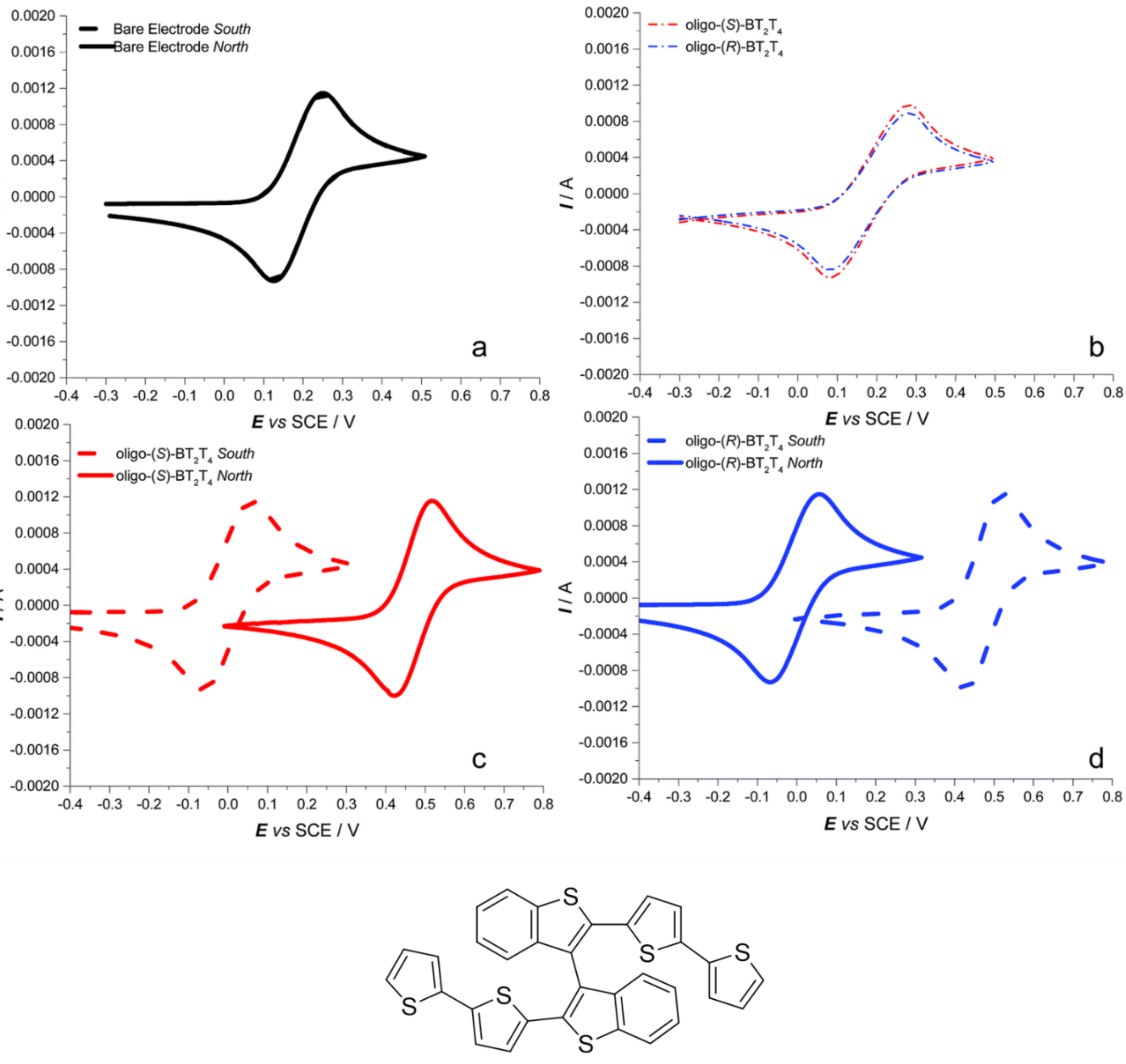

BT_2T_4

*Figure 3. Structure of **BT2T4** and CV patterns recorded in the paper for: (a) the bare ITO electrode, as a function of the magnetic field orientation (solid line for the north pole towards the electrode, dashed line for the south pole); (b) on hybrid ITO|oligo-**BT2T4** electrodes (blue line for the (R)-configuration, red for (S)-) without an external magnet; (c) and (d) at the hybrid ITO|oligo-**BT2T4** interface, as a function of the applied magnetic field orientation. Adapted from ref [21].*

The cyclic voltammetry (CV) measurements were carried out in acetonitrile with 0.1 M tetrabutylammonium hexafluorophosphate, $^{t}Bu_4NPF_6$, as the supporting electrolyte and a magnetic field was applied, perpendicular to the electrode surface by placing a permanent magnet. Despite the absence of a magnetic electrode acting as a spin injector, they observed that, when flipping the magnet’s orientation, the CV peaks of two chiral *R* or *S* films underwent impressive potential shifts. This discovery yields fascinating evidence of the spin selectivity characteristics of chiral oligomeric thin films and the condensed electrochemical system, which can be easily prepared, holds great potential for applications in spintronic devices as redox spin injectors.

In these setups, the redox probe is mainly represented by the classical ferrocene/ferrocenium couple, which is widely described in the literature [3]. Indeed, since 1951, ferrocene has been widely used as an important redox probe to study electrochemical charge-transfer processes in various experimental platforms, including solution-based systems, molecular thin films, solid-state molecular electronics and spintronic devices. This is due to different reasons: i) the Fc/Fc^+ self-exchange reaction is kinetically fast and the rate is not influenced by the solvent; ii) the oxidation to reduction current density is near to unity ($I_{pa}/I_{pc} = 1$); iii) the peak-to-peak difference (ΔEp) is very close to ideal value (57 mV for a one-electron transfer redox-process); and iv) it has a similar diffusion coefficient for both oxidized and reduced species.

Therefore, chiral and achiral ferrocenes represent a suitable redox probe for the Spin Dependent Electrochemistry to study the magnetic-field effect on electrochemical charge-transfer phenomena. One straightforward example is represented by the work on a chiral polymer poly{[methyl-*N*-(tertbutoxycarbonyl)-*S*-3-thienyl-L-cysteinate]-cothiophene} (**PCT-L**) and its enantiomer **PCT-D** by Naaman and collaborators [4]. The chiral polymer was grafted on a ferromagnetic Ni substrate, coated with gold, used as working electrode and magnetized by an underneath magnet of 0.5 T in UP or DOWN magnetization direction. First an achiral ferrocene was employed as solution probe for the CV measurements in methanol. For the UP magnetization, current changes its sign from oxidation to reduction. However, for the opposite direction of magnetization (DOWN), it does not vary its direction, suggesting a high barrier for charge transfer from **PCT-L** to Fc^+ ion due to the effect of spin filtering. Then, they used a chiral ferrocene probe, *R* or *S* chiral *N*,*N*-dimethyl1-ferrocenyl-ethylamine (**Figure 4**), to investigate the enantioselective interaction between the adsorbed polymer and the chiral redox probes in the solution. The adsorbed **PCT-D** interacts strongly with S-ferrocene, whereas **PCT-L** interacts more strongly with R ferrocene, as shown in the CV curves in **Figure 4.**

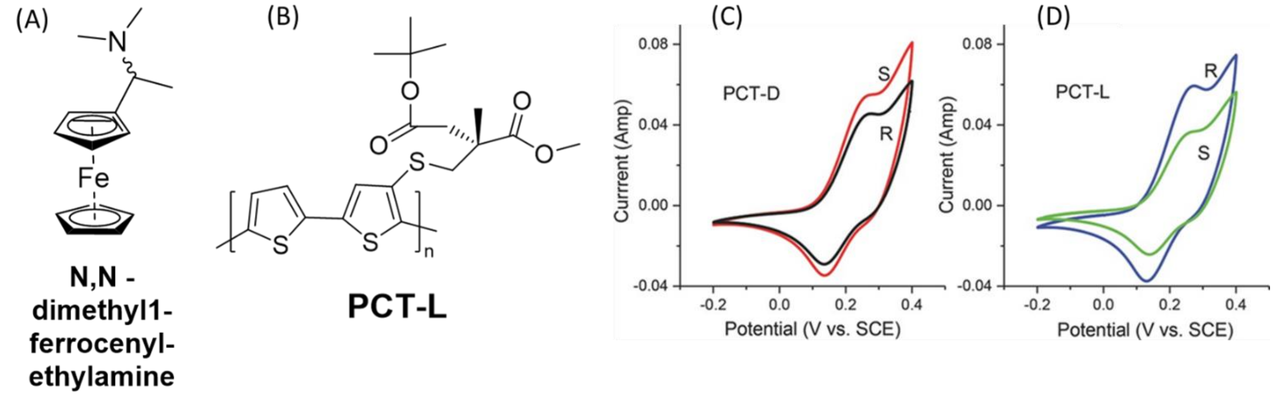

Figure 13. A) Structure of racemic ferrocene probe; B) L-cysteine derivative; C) CV curves obtained with **PCT-D** *when the redox couple is either S-ferrocene (red) or R-ferrocene (black). For comparison D) CV curves obtained when* **PCT-L** *is used with S-ferrocene (green) and R-ferrocene (blue). The working electrode in this case is gold. Reproduced from ref [4].*

I.3. Self-assembled monolayers

As already mentioned, the essential requirement for the SDE is the presence of a chiral layer deposited on the working electrode (WE), acting as spin filter. It is fundamental to have a proper orientation and thickness on the surface in order to maximize the current through the chiral molecules and self-assembled monolayers (SAMs) are an appealing tool to achieve these results. When the monomolecular layer is formed upon chemical reaction (chemisorption), a better stability and a stronger interaction with the surface are ensured.

The formation process of SAMs involves surface-specific interactions that result in the development of a densely packed and highly organized monolayer. These interactions include surface-adsorbate interactions, electrostatic interactions between adsorbates, and van der Waals interactions. Additionally, surface reorganization plays a role in achieving the equilibrium structure of the assembly. Thus, to form an ordered monolayer on the surface of interest, SAM molecules need to possess the following two characteristics. They must contain functional groups that strongly react with the surface (grafting unit) and they should assemble themselves in a high density and uniform manner on the surface via intermolecular interactions.

Concerning the first point, thiol-based layers are by far the most conventional and most popular SAMs used in electrochemistry, and take advantage of the –SH group which strongly interacts with many metals [5].

Among the different reports on chiral SAMs based on thiols studied by electrochemistry, we focused on those on gold surfaces: in the process of alkanethiol reaction on a Au surface, the chemisorption of sulfur containing molecules occurs and Au-S bond is formed by oxidative addition of S-H bond to the Au surface followed by reductive elimination of the hydrogen. More specifically, in the context of chiral thiol-based layers, cysteine and homocysteine monolayers were deeply investigated: an exhaustive example is provided by the work of Naaman, Fontanesi and Waldeck [6], where a gold-coated-nickel working electrode was chemically modified by a self-assembled monolayer of L and D-cysteine covalently attached to the redox active dye toluidine blue O (TBO), working as probe for the SDE measurements, as shown in **Figure 5**.

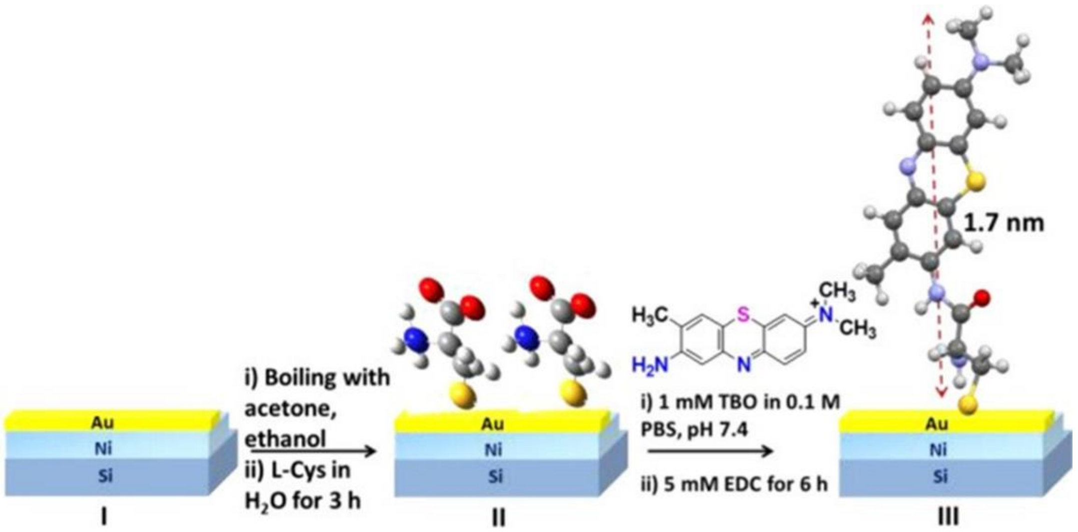

Figure 5. Schematic illustration of the step for covalently binding TBO to the working electrode via a cysteine linker. Reproduced from ref [6].

An external magnetic field was applied with a permanent magnet below the working electrode and its field direction was changed by physically rotating the magnet. The CV curves showed that for D-cysteine, the faradaic current is higher when the magnetic field is oriented away from the monolayer/solution interface (“DOWN”); while for L-cysteine, the higher value is for the opposite configuration (**Figure 6**). Therefore, they claim that the electrochemical current depends on both, the chirality of the cysteine linker and the direction of the magnetic field, as explained by the principle of the CISS effect.

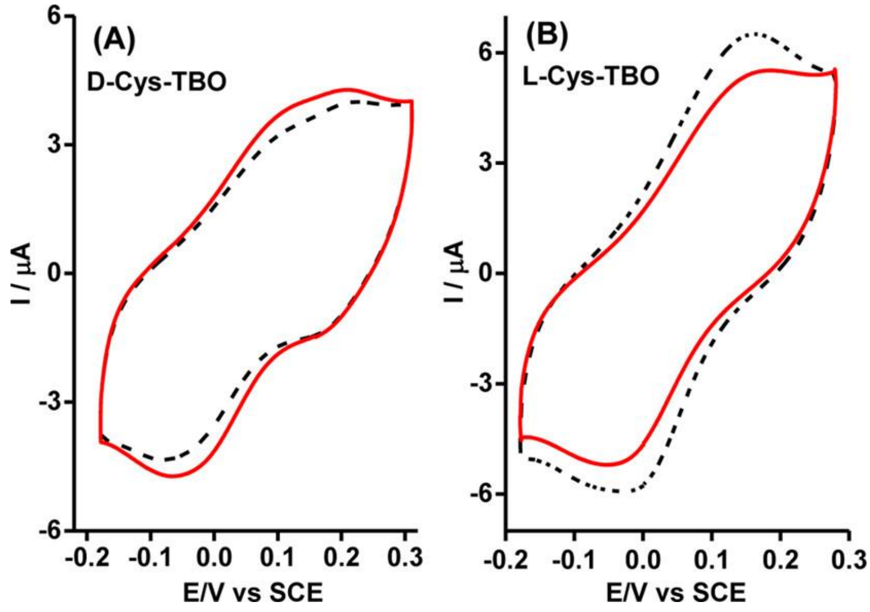

*Figure 6. Cyclic voltammograms for **D-cysteine-TBO** (panel A) and **L-cysteine-TBO** (panel B). When the nickel is magnetized, it is either with its magnetic moment pointing UP, toward the monolayer (dashed black curve), or DOWN, away from the monolayer (solid red curve*)

In 2020, Cardona-Serra and collaborators prepared SAMs of Lanthanide Binding Tags (LBTs)- short peptide sequences comprising 15-20 naturally occurring amino acids that bind lanthanide with high affinity [7] to clarify the effect of the paramagnetic nuclei through SDE measurements. They functionalized the different metalloLBT with cysteine in order to graft the compounds onto a Ni/Au substrate used as working electrode WE in a classical spin-dependent electrochemistry setup. The results showed that the current density in the case of the bare Ni/Au WE was quasi-independent of the orientation of the magnet placed underneath while, when the MetalloLBT cysteine-modified WE was used, the current density decreased dramatically due to the presence of the insulating SAM in the WE. Additionally, a clear dependency of the current density with the magnetic field was recorded. Higher values of current density were displayed with the magnetic field pointing “down” for the right-handed helical molecule along with a shift in the oxidation and reduction potentials of systems was observed by changing the orientation of the magnet. Interestingly, when the diamagnetic Y^{3+} center replaces the paramagnetic Tb^{3+}, the SP effect was slightly decreased [8].

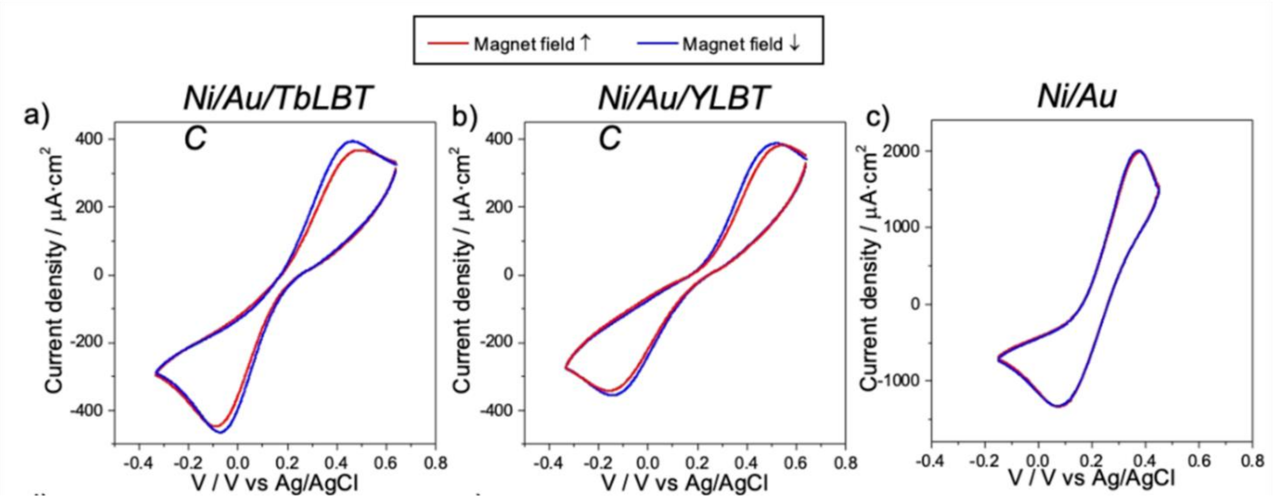

Figure 7. CV curves using a Fe^{2+}/Fe^{3+} solution as probe: (a) SAM of the Tb^{3+} derivative on Ni/Au; (b) Y^{3+} derivative SAM on Ni/Au, and a bare Ni/Au (c); reproduced from ref [8].

I.4. Targeted molecules

Hence, by following these results, we decided to explore the spin selectivity of helicenes through the formation of self-assembled monolayers (SAMs) bearing a ferrocene group, in order to measure Spin Dependent Electrochemistry. More specifically, the 2,15-bis-ethynyl-carbo[6]helicene **H6** was selected as building block thanks to the possibility to easily functionalize the two terminal alkynyl units via cross-coupling reactions: one extremity was dedicated to the redox probe and, in order to obtain a monolayer on surface, the other terminal unit of the hexahelicene was functionalised with two different types of anchoring unit, namely, thiol- (**H6FeSAc**) and carboxylic-acid-terminated molecules (**H6FeCOOH**) (**Scheme 1**). This led us to study the effect of the anchoring-group on the grafting efficiencies of helicene active molecules in gold and ITO surfaces.

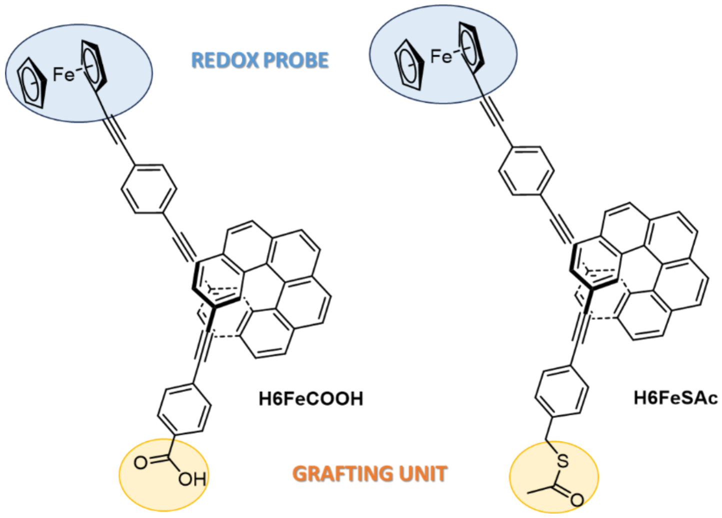

Scheme 1. Structure of the target molecule with the grafting unit and the ferrocene as electrochemical probe.

As previously mentioned (see Introduction chapter), thiol-based SAMs have been widely investigated and the CISS effect in helicenes bearing this anchoring group has been already measured by mc-AFM and magnetoresistance [9] but not through SDE. The second grafting group we have selected is a carboxylic acid. With this unit, we have been able to explore another type of surface such as indium tin oxide (ITO) glass, which is widely used as hole injector for OLED or OPV devices along with the possibility of obtaining helicene- based SAM for other substrates, such as less costly noble metal surfaces [10].

II. Synthesis of helicenic ligands

The helicenic building block 2,15-bis-ethynyl-carbo[6]helicene **(H6)** was prepared by following the classical procedure used by our group, as described in **Chapter 1**. The first step involves the Wittig reaction between the previously synthesized bis-bromo phosphonium salt and the commercially available 4-[(trimethylsilyl)ethynyl]benzaldehyde, obtaining the di-stilbene derivative in a 90% yield. The double oxidative catalytic photocyclization reaction was performed in toluene using a 500 W Hg lamp and 5% iodine as oxidizing agent (52% yield). The racemic ***rac*-H6(TMS)$_2$** was separated by chiral HPLC into the two pure enantiomers (*P* and *M*) thanks to the collaboration with the group of Dr. Vanthuyne at Chirosciences, University of Aix-Marseille. The enantiopure molecules were deprotected by using K_2CO_3 in a chloroform/methanol 1 to 1 mixture, to give, quantitatively, *P* and *M*-**H6**.

The target enantioenriched helicene derivatives **H6FeCOOH** and **H6FeSAc** were prepared via a statistical Sonogashira coupling reaction, following classical conditions, between the 2,15-bis-ethynyl-carbo[6]helicene **H6** as a starting material and two corresponding halogenated moieties, as depicted in **Scheme 2**. This was confirmed by the disappearance of the alkynyl proton signal (δ 2.7 ppm) of the starting material in ^{1}H-NMR as well as by ^{13}C NMR with a chemical shift of a few ppm for the substituted alkynyl carbon atom (from 81 to 88 ppm for **H6FeCOOH**, and from 81 to 85 ppm in the case of **H6FeSAc**).

Concerning the helicene bearing the carboxylic acid, we prepared first the *P* and *M* configured enantiomers of the corresponding methyl ester **H6FeCOOMe** using a slight excess of iodomethyl benzoate **2** and a stochiometric amount of the previously synthesized 4-iodo-phenylethynylferrocene **3** (see experimental part), in a 23% yield. Afterwards, both enantiomers, *P* and *M*-**H6FeCOOMe**, were saponified using LiOH to yield quantitatively *M* and *P*-**H6FeCOOH**.

The reason for the low yield of the Sonogashira coupling between the helicene and the two halogenated reagents is related to the formation of the symmetrical di-substituted side products, namely, **H6(Fe)$_2$** and **H6(COOMe)$_2$**, that were isolated along with the desired molecule in 35 and 40% yields, respectively.

Adopting the same synthetic approach, we successfully obtained **H6FeSAc** in 30% yield, starting this time from compound **3** and 4-iodophenyl-methylene-methylthioacetate **4**. Again, C_2-symmetrical side products were generated: **H6(Fe)$_2$** (in 34% yield) and **H6(SAc)$_2$** (in 20% yield).

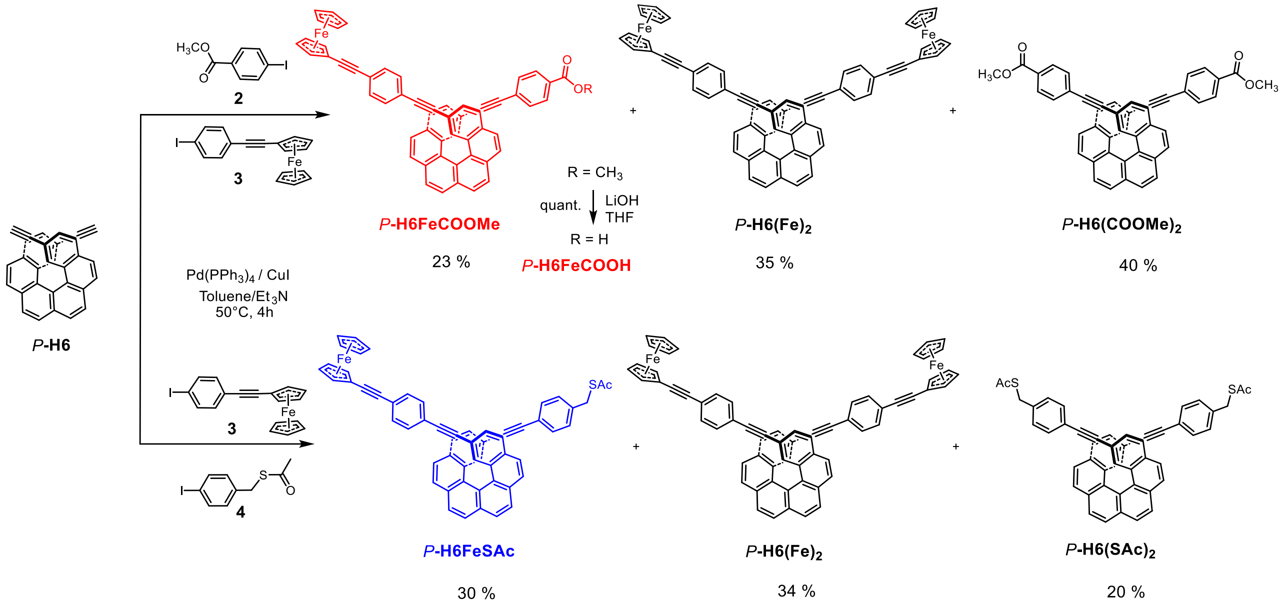

*Scheme 2. Preparation of enantiopure dissymmetrical helicenic compounds P-**H6FeCOOH** bearing a carboxylic acid grafting unit and of P-**H6FeSAc** with a thioacetate moiety, together with symmetrical side products.*

The two desired final products were fully characterized by ^{1}H and ^{13}C NMR and by High Resolution mass spectrometry. Both of the ^{1}H NMR spectra shown in **Figures 8** and **9** display the absence of the **H6** terminal ethynyl proton at 2.7 ppm, confirming the accomplishment of the coupling reaction and full consumption of the starting helicene. The protons corresponding to the ferrocene moiety, appears as two triplets at 4.56 and 4.33 ppm and a singlet at 4.30 ppm for the two compounds.

Moreover, for **H6FeSAc**, two additional singlets, corresponding to the methyl of the thioacetate (δ 2.40 ppm) and the benzylic protons (δ 4.15 ppm), were observed. On the other hand, the ^{13}C-NMR confirms the presence of the two quaternary carbons, the carboxylic acid for **H6FeCOOH** (δ 170 ppm), and that of the thioacetate unit in the case of **H6FeSAc** (δ 194 ppm).

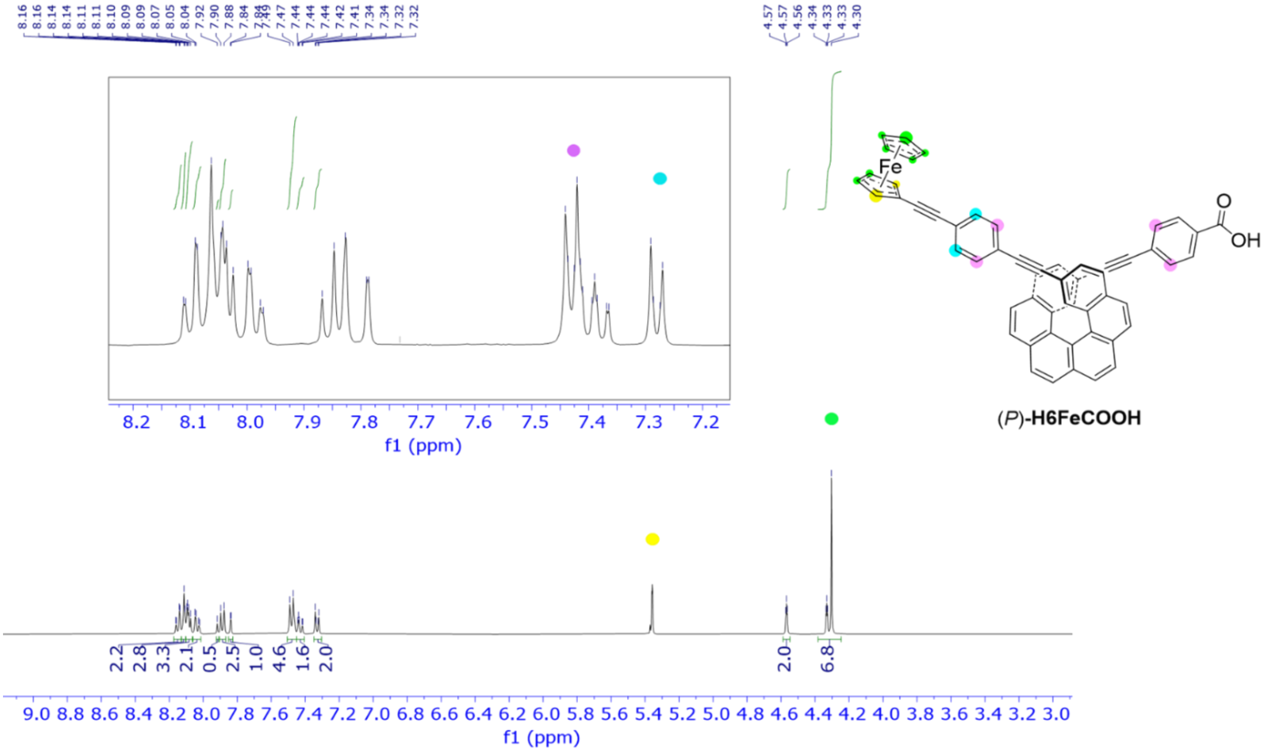

Figure 814. Proton NMR (400 Hz) of **H6FeCOOH** in CD_2Cl_2 at room temperature.

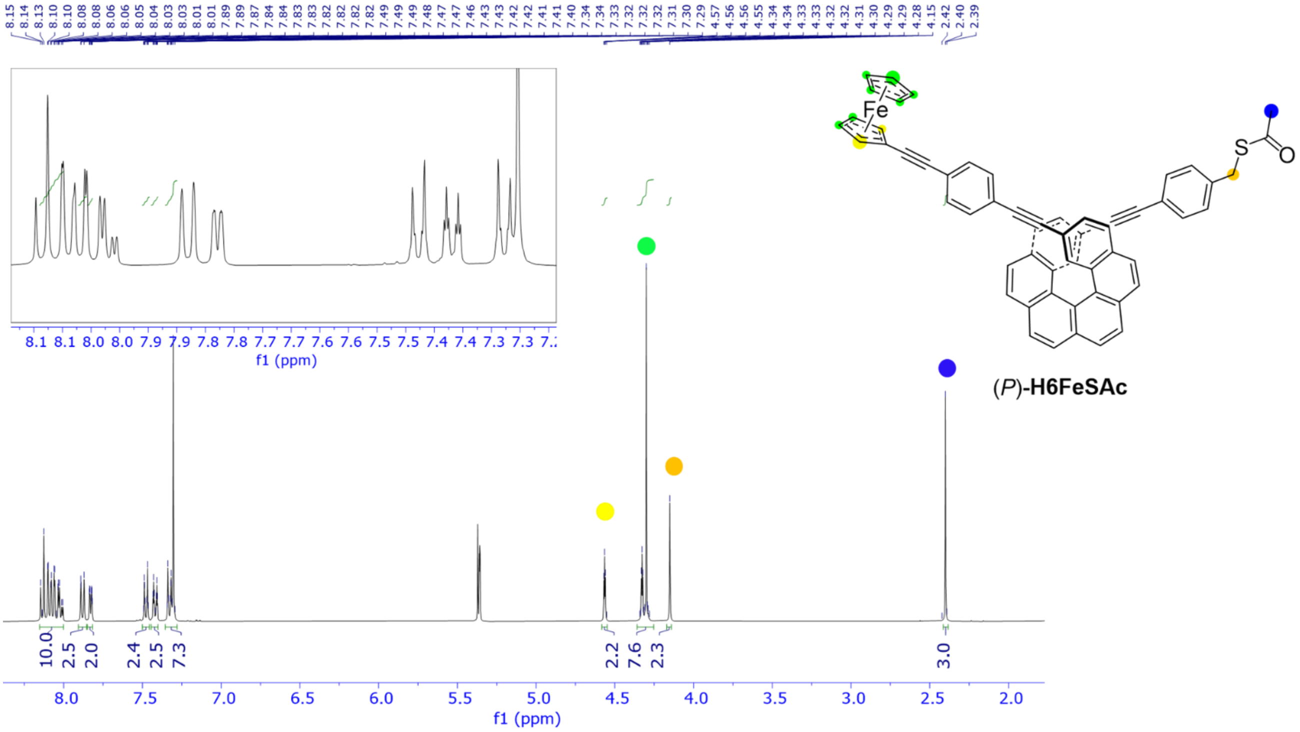

Figure 9. Proton NMR (400 Hz) of **H6FeSAc** in CD_2Cl_2 at room temperature.

III. Optical and chiroptical characterizations

It is already known that the spin polarization is in close relation with the chiroptical activities of chiral molecules, precisely, their electronic circular dichroism responses (**Chapter 1** and **3**).

Our group already reported several experimental and theoretical investigations revealing that by optimizing the mutual orientation of the electric and magnetic dipoles it is possible to improve the chiroptical response by an intense helicene-mediated exciton coupling. This result is already evident in the comparison between the carbo[6]helicene and the correspondent ethynyl derivative, which shows a weak exciton coupling between each π-conjugated arm[11] (see **Chapter 1**). Thus, before studying the spin filtering ability of our systems, we first investigated their polarized and unpolarized light absorption.

As depicted in **Figure 10**, both compounds, **H6FeCOOH** and **H6FeSAc**, showed UV-vis absorption between 250 and 440 nm with a maximum at 300 nm ($\Delta\varepsilon$ = 51100 M^{-1} cm^{-1}) and 311 nm (ε = 62530 M^{-1} cm^{-1}) for **H6FeSAc** and **H6FeCOOH**, respectively. Regarding the electronic circular dichroism spectra, the two studied helical molecules showed very similar absorption profiles with mirror-imaged spectra for their respective *P* and *M* enantiomers. However, a small bathochromic shift ($\approx$10 nm) and more intense dichroic response for **H6FeCOOH** in comparison with **H6FeSAc** could be detected. The *P* enantiomer of **H6FeSAc** reveals two strong Cotton effects with a first negative band centered at 308 nm ($\Delta\varepsilon$ = -173 M^{-1} cm^{-1}) followed by a positive one with a maximum at 373 nm ($\Delta\varepsilon$ = 254 M^{-1} cm^{-1}). Those bands are red shifted in the case of *P*-**H6FeCOOH** and located at 323 nm ($\Delta\varepsilon$ = - 200 M^{-1} cm^{-1}) and 378 nm ($\Delta\varepsilon$ = 293 M^{-1} cm^{-1}). At longer wavelengths (424 nm), the ECD spectra show quasi-identical bands with almost the same molar circular dichroism coefficients ($\Delta\varepsilon$= 23 M^{-1} cm^{-1}), thus, revealing that both studied enantioenriched helicene molecules may give similar spin polarization answers.

The optical rotations values were also determined to be + 5563 and + 5160 for *P*-**H6FeSAc** and *P*-**H6FeCOOH,** respectively, in 10^{-4} M dichloromethane solutions at room temperature, revealing once again the close similarity of the chiroptical properties for these helical chiral structures.

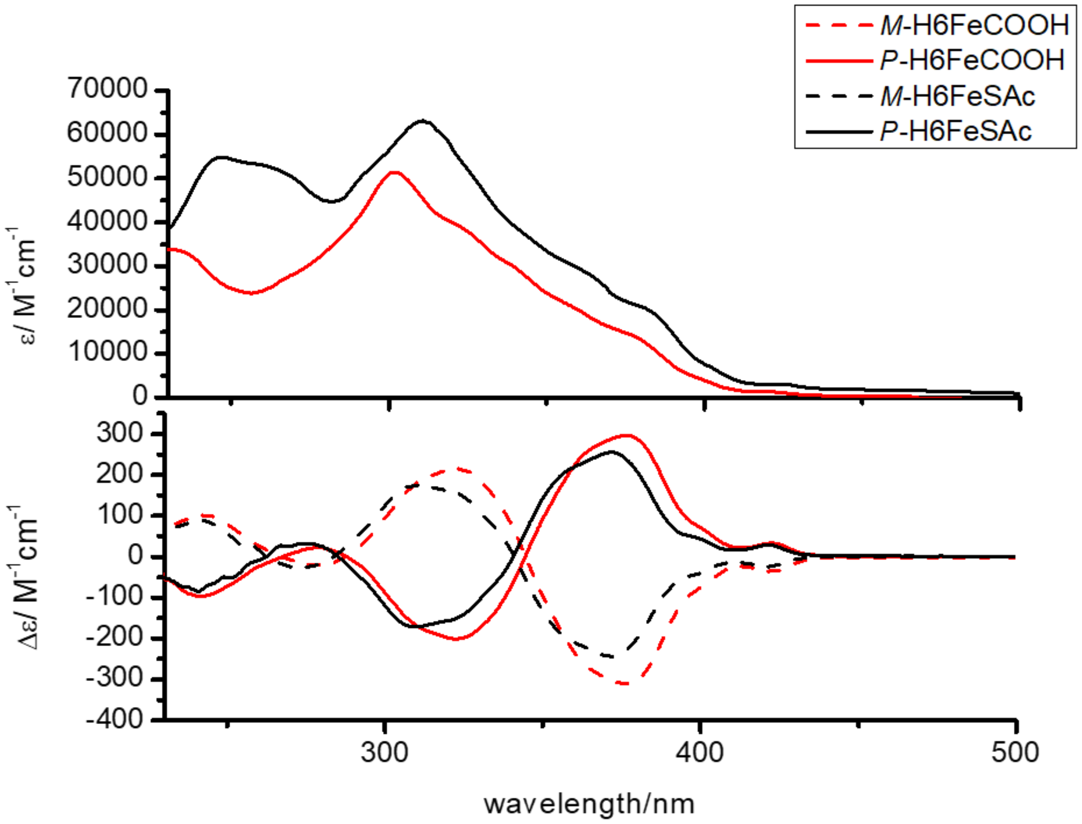

Figure 10. Absorption and ECD spectra of ***H6FeCOOH*** *(red) and* ***H6FeSAc*** *(black) in a 10^{-6} M CH_2Cl_2 solutions at 298 K.*

Note that no emission properties were detected for these compounds. This is probably due to the presence of the redox-active ferrocene moiety[12].

The UV-Vis and ECD spectra were also obtained for the by-products of both reactions. Very similar patterns in the molar extinction coefficients were observed (see experimental part).

IV. Cyclic voltammetry

IV.1. Electrochemistry in solution

Before grafting the molecules onto the surfaces for the SDE measurements, their electrochemical behavior was studied by cyclic voltammetry (CV) in solution. We used the same single-compartment three-electrode cell setup for both compounds: a Saturated Calomel Electrode (SCE) as reference and two platinum wire as working and counter electrodes, respectively. The chosen electrolyte was tetrabutylammonium hexafluorophosphate NBu_4PF_6 at a concentration of 0.1 M in dry dichloromethane that was purged with argon for 15 min before the measurements, and the scan rate was 200 mV/s.

As shown in **Figure 11**, the two voltammograms reproduce the distinctive signature of the couple ferrocene/ferrocenium. This is the typical duck-shape pattern for a one-electron reversible process.

The two compounds show the same oxidation and reduction potentials, respectively at 0.62 V and 0.49 V vs SCE, for both derivatives, confirming their similarity that was already illustrated by the ECD spectra. In comparison to the unsubstituted ferrocene redox potential in CH_2Cl_2 with 0.1 M tetrabutylammonium hexafluorophosphate as supporting electrolyte (0.46 V) [13], the voltammograms illustrate positively shifted values for both helicene derivatives: it can be attributed to an electron-withdrawing effect of the conjugated substituents [14].

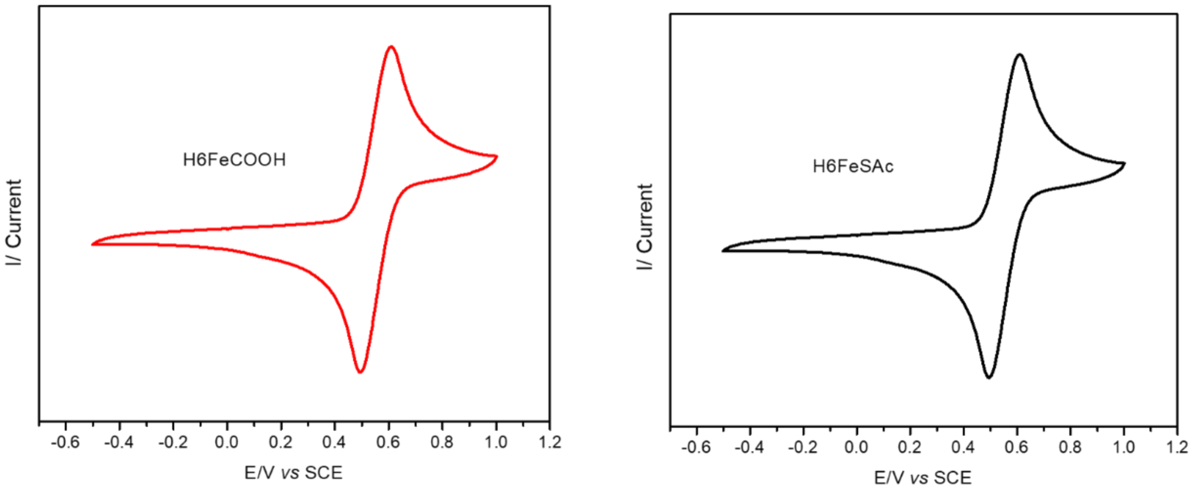

Figure 11. Cyclic Voltammetry in CH_2Cl_2 solution for the two derivatives.

IV.2. Spin Dependent Electrochemistry

The spin-dependent electrochemistry measurements were performed in collaboration with Dr. Kakali Santra in the group of Prof. Ron Naaman at Weizmann Institute of Science. As previously said, we aimed investigate how the electron transfer though a chiral SAM of helicene is spin-dependent. The two SAMs of **H6FeCOOH** and **H6FeSAc** were formed onto two different substrates that served as working electrodes for the Spin Dependent Electrochemistry measurements.

The type of solvent, concentration of the compound, temperature and the presence of moisture affect the formation of SAM on the surface, thus suitable experimental conditions should be applied during the growth process. For instance, concentration of solution and immersion time are related to each other. It has been suggested that solutions with low concentration requires longer immersion time, while shorter immersion time may be required if highly concentrated solutions are used. Sometimes, when high concentrations of SAM are used, cross-linking of end groups can happen or, in the case of free thiols reacting with a Au surface, the H_2 released by the reaction can damage the surface itself. Thus, the experimental procedure we followed is the result of several tests and of an optimization of different parameters, such as concentration, immersion time and specifically for the carboxylic acid, surface activation methods.

The thiol terminated helicenes obtained from deprotected **H6FeSAc**, were grafted onto a gold coated ferromagnetic layer (Ti/Ni/Au) prepared using e-beam evaporation on a p-doped Si (100) wafer (the surface preparation is described in the experimental section). The gold layer has a dual purpose: it functions as a protective layer to prevent oxidation of the Ni, while also providing a surface that can covalently bind with thiol groups present in the helicene molecules. The immobilization of **H6FeSAc** onto surfaces was achieved following a previously reported procedure [15]. The surface was immersed in a 2mM THF solution of the enantiopure compound with hydrazine monohydrate as a deprotecting reagent and left to incubate for 12 h at room temperature (**Figure 12b** and **c**).

For the carboxylic acid derivative, **H6FeCOOH**, we selected a ITO glass as surface and this substrate underwent a particular pre-treatment. It was first activated by hydroxylation and then a first SAM of 2-aminoethylphosphonic acid was grown onto it (**Figure 12a**). In fact, in order to achieve a more efficient SAM formation through a stronger bond, it is common to previously modify the ITO substrate. Among the different methods, self-assembly of the phosphonic acids monolayer was demonstrated to be the most effective approach due to binding strength when compared to siloxanes and carboxylic acids, with high stability under ambient conditions [16]. Thus, while the phosphonic acid group reacts through a condensation with the -OH group of the surface, forming a first layer on the surface, the terminal free amine units are available for the interaction with the -COOH of the helicene.

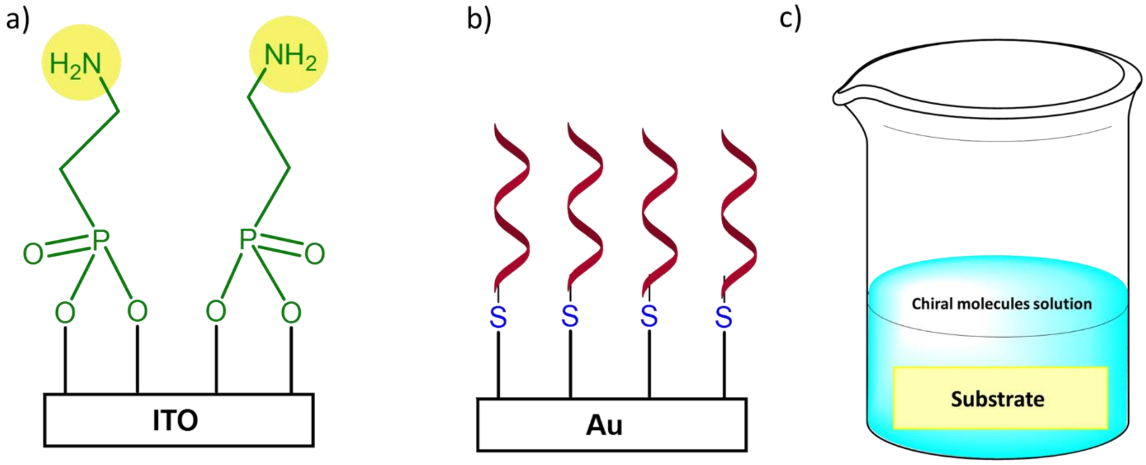

Figure 12. Schematic representation of: a) the ITO surface activated with 2-aminoethylphosphonic acid: the free amine groups will interact with the carboxylic acid; b) helicene with thioacetate after deprotection; c) grafting of the molecules onto surfaces by incubation method.

The electrochemical measurements were performed using a three-electrode electrochemical cell, equipped with a SCE reference electrode and a platinum wire as the counter electrode, while the working electrode was the helicene molecule grafted substrates (ITO or Si-Ni-Au). The electrolyte used for the measurements was 0.1 M phosphate buffer PBS (pH = 7) and the solution was purged with Ar for 30 min before starting the analysis. The scan was cycled from 0.0 V to 0.65 V vs. SCE, with a scan rate of 100 mV/s.

By following the basic principle of the SDE, the unpaired electrons in the Ni layer were polarized by placing a permanent Nd magnet beneath the substrate facing the North (or South) magnetic pole facing upwards, in order to allow a spin polarized current to flow through the chiral film adsorbed on the electrode surface. The CV curves are shown in **Figures 13** and **14**.

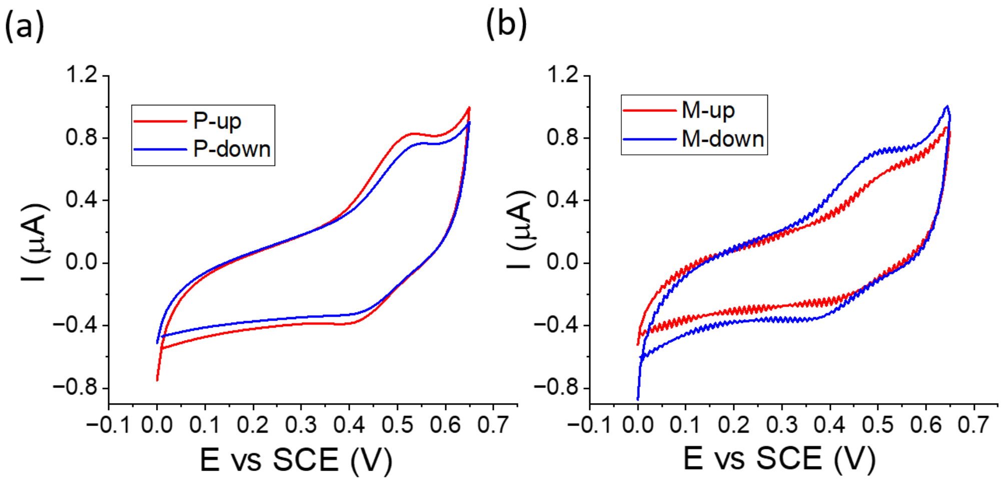

*Figure 13. Cyclic voltammetry plots for the SAM of (a) P- and (b) M-**H6FeSAc** helicene on Ni-Au surface. The up and down indicate that the direction of magnetic north pole facing the solution and it is away from it, respectively.*

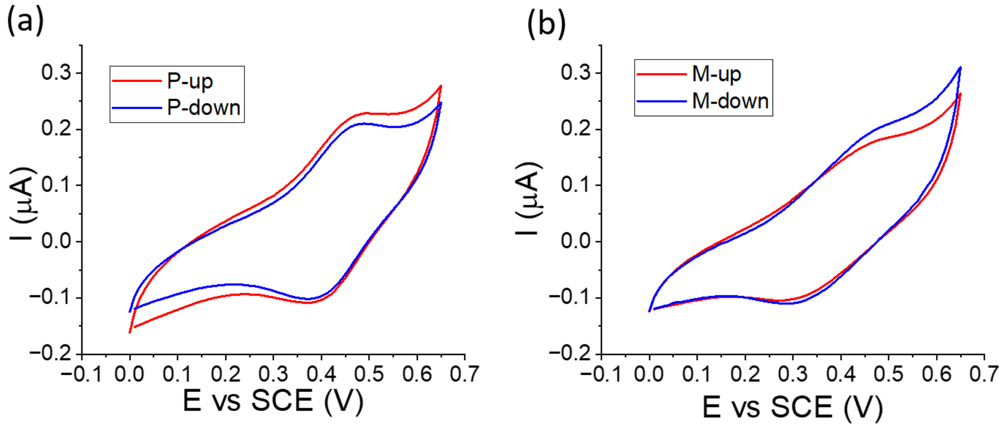

*Figure 14. Cyclic voltammetry plots for the SAM of (a) P- and (b) M-**H6COOH** helicene on ITO surface. The up and down indicate that the direction of magnetic north pole facing the solution and it is away from it, respectively.*

The voltammograms showed a dependence of the faradaic current on the direction of the substrate magnetization for both compounds: the *P* enantiomer of **H6FeSAc** and **H6FeCOOH** produces a higher faradaic current (both cathodic and anodic) when the magnetization of the modified working electrode was “UP” than when it was “DOWN”, while the *M* enantiomer has the opposite behaviour. Note that it is not possible to compare the absolute signal levels between the data for the two derivatives because the coverage and the working electrode preparation can vary.

Nevertheless, the main result of these measurements is that the electrochemical current depends on both the chirality of the helicene film and the direction of the magnetic field for both surfaces and the results are consistent between the two samples.

V. Conclusions

The aim of this work was to investigate the spin filtering properties of hexahelicene through a different technique that was not applied for helicenic systems so far, such as the Spin Dependent Electrochemistry. Thus, two substrates were selected, a ferromagnetic Ni coated with gold and a non-magnetic indium tin oxide (ITO) glass.

In order to obtain a self-assembled monolayer on these surfaces, the 2,15-bis-ethynyl-hexahelicene H6 was functionalized with an anchoring group, namely a benzoic ester that was hydrolyzed as carboxylic acid for the ITO substrate (**H6FeCOOH**), and a thioacetate to be deprotected for the gold surface (**H6FeSAc**). Both compounds present also a ferrocene unit as the electrochemical probe. The two compounds were characterized by NMR and their chiroptical activity was investigated through ECD measurements before studying the electrochemical response, both in solution and on surface. The results of the SDE measurements showed that, after application of a magnetic field, there is a consistent dependence of the current on the direction of the magnetization for the two enantiomers. Higher values were obtained for the P enantiomer when the direction of the magnet was facing the surface (UP), while the M enantiomer showed the opposite behaviour. Hence, we present the first example of helicene derivative investigated by Spin Dependent Electrochemistry on surface, confirming the spin filter ability of this moiety.

In order to add further insights on the grafting of the molecules onto the two substrates, other analyses should be performed. The difference in the roughness from the bare surface and the functionalized one can be ascertained through ellipsometry measurements along with AFM, while X-ray Photoelectron Spectroscopy (XPS) will confirm the chemical adsorption by showing the presence of S-Au bond.

VI. Perspectives

On the basis of these results and in collaboration with Dr Bruno Fabre at University of Rennes, we were able to graft the same bis-ethynyl-hexahelicene onto a new type of substrate, an oxide-free silicon surface, by exploiting a different functionalization. A hydrosilylation reaction was used to form a strong covalent bond between the alkynyl moiety and Si-H unit of the substrate. In fact Si−H is a particularly attractive substrate for electrical applications due to the ease and reproducibility of its preparation, its well-defined structure, its very low density of electrically active surface defects and its propensity to be chemically modified with organic monolayers through robust interfacial Si−C bond[17], and ethynyl helicene are a suitable candidate for this purpose.

Thus, 2,15- bis(4-ethynyl-phenyl-ethynyl)-carbo[6]helicene **H6PhH**, whose synthesis is described in **Chapter 2**, was selected to functionalize this substrate, following a multistep approach (**Scheme 3**). Herein we will show some preliminary results concerning the grafting of the racemic species.

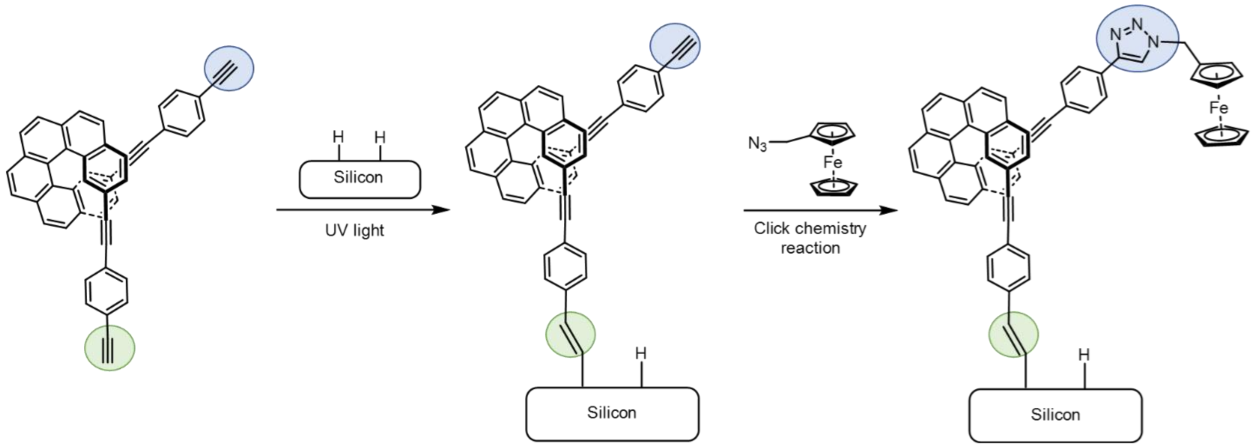

Scheme 3. Schematic representation of the multistep grafting of the helicene onto the silicon surface

The first step involves the hydrosilylation reaction between one of the alkynyl terminal units of the helicene and the free hydrogen on the substrate. The reaction is performed under irradiation of a UV lamp. To ensure the grafting of the molecule, XPS and ellipsometry measurements were performed. For the racemic derivative a thickness of 18.3 ± 1 Å was found and in XPS spectra a major component in the C1s spectrum at 285 eV is attributed to C-C, C=C, and C≡C bonds of the grafted molecule (**Figure 15**).

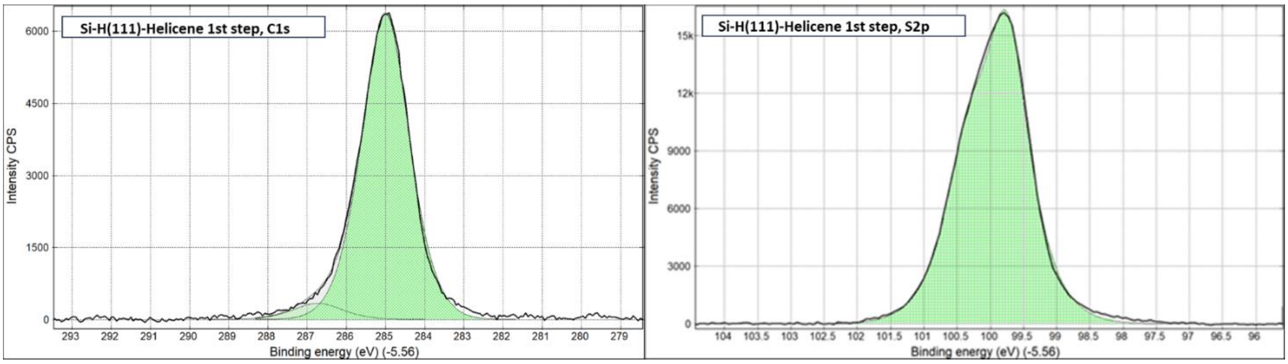

Figure 15. XPS of the helicene-grafted surface after the first step: C spectrum on the left and Si on the right side.

The second step requires a post-grafting functionalization with the redox probe, which will be used for the electrochemistry measurements. Hence, the free alkynyl unit of the helicene was involved in a click reaction under classical conditions with the ferrocenyl azide. The thickness of the new surface is detected to be 27.7 ± 1 Å and the XPS exhibit different peculiar features, illustrated in **Figure 16**. The component on the C1s spectrum at 285 eV (C-C, C=C, and C≡C of the grafted molecule) is still observed. N and Fe are also detected but at very low concentrations and it is consistent with a low coverage rate due to the steric hindrance of the molecule. Silicon is now oxidized (component at 103-104 eV), which is logical considering the significant number of remaining free Si-H groups in the first step and the experimental conditions used for click chemistry. The grafting was then confirmed through classical electrochemical measurements in acetonitrile using 0.1M Bu_4NClO_4 as electrolyte and using the helicene-grafted silicon surface as working electrode.

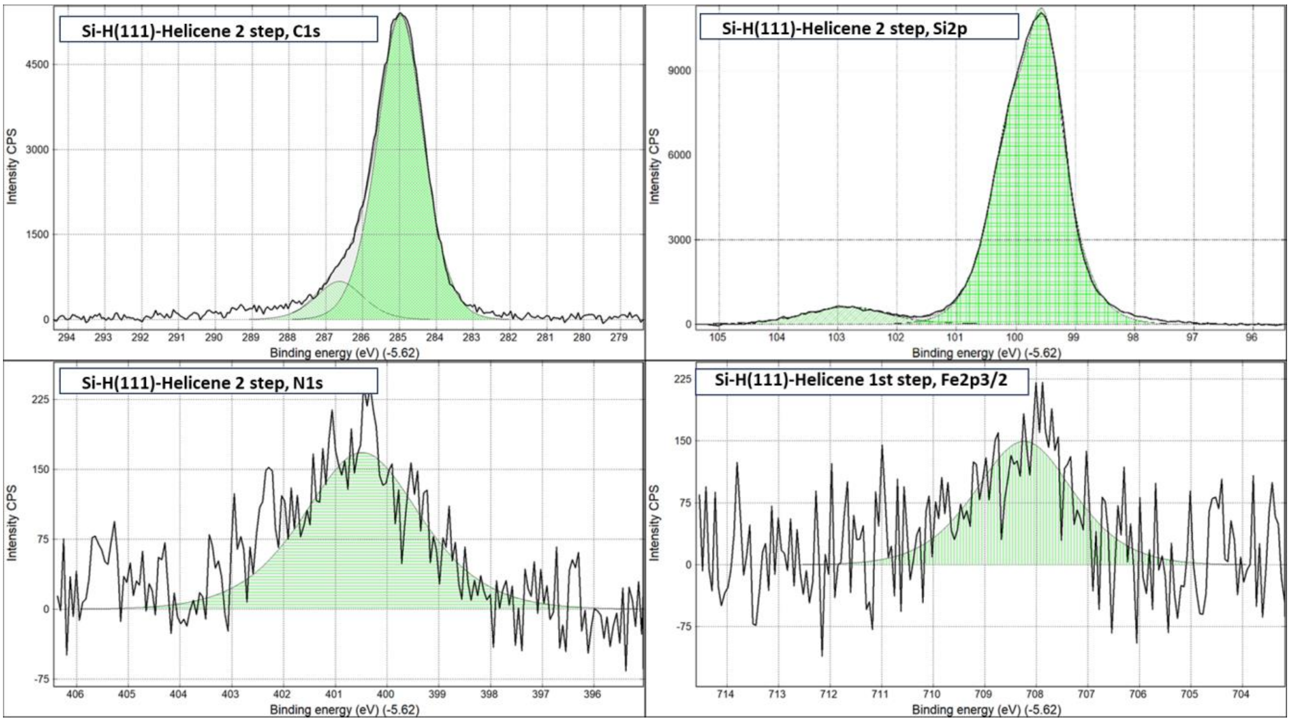

Figure 16. XPS of the helicene-grafted surface after the click chemistry reaction; TOP: C spectrum on the left and Si on the right side; BOTTOM: N and Fe at left and right side respectively.

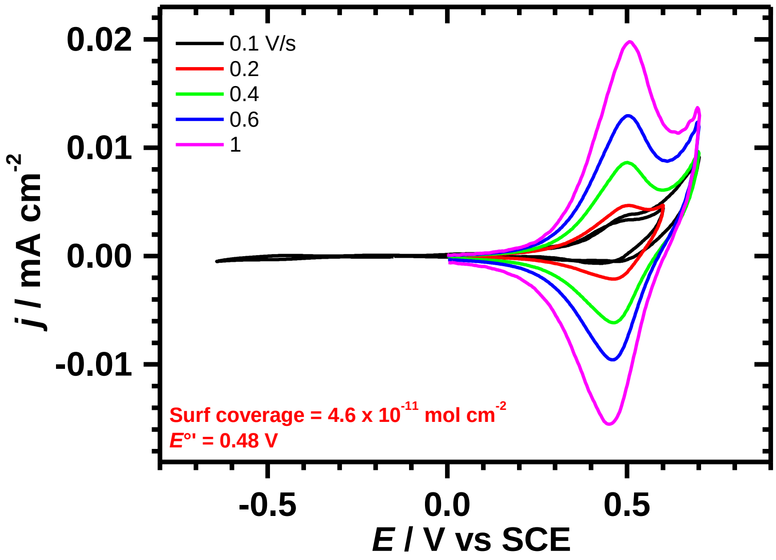

Figure 17. Cyclic voltammograms at different scan rates for the surface after click chemistry with ferrocene.

The voltammograms reproduce the distinctive signature of the couple ferrocene/ferrocenium, demonstrating that the helicene with the redox probe are properly grafted onto the substrate.

To proceed with further measurements of the CISS effect, such as Spin Dependent Electrochemistry and mc-AFM analysis, and obtain the spin polarization value for this derivative, it is crucial to include an intermediate step prior to the click chemistry reaction. This step involves saturating all the Si-H free sites, aiming to prevent surface oxidation, which significantly affects the current measurements in both techniques. This will be conducted in future works.

VII. Experimental part

^{1}H and ^{13}C{1H} NMR spectra were recorded at room temperature on an *AVANCE III 400 BRUKER* or an *AVANCE I 500 BRUKER* at Center Régional de Mesures Physiques de l'Ouest (CRMPO), Université de Rennes 1. Chemical shifts δ are given in ppm, relative to an internal standard of residual deuterated solvent ($CDCl_3$: δ = 7.26 ppm for ^{1}H NMR, δ = 77.16 ppm for ^{13}C NMR; CD_2Cl_2: δ = 5.32 ppm for ^{1}H NMR, δ = 53.84 ppm for ^{13}C NMR), and coupling constants *J* in Hz.

High-resolution mass spectra (HR-MS) determinations were performed at CRMPO on a Bruker MaXis 4G and Ultraflex III by ASAP (+ or -) or ESI techniques with CH_2Cl_2 as solvent. Experimental and calculated masses are given with consideration of the mass of the electron.

UV-Visible (UV-vis, in M^{-1} cm^{-1}) absorption spectra were recorded on a UV-2401PC Shimadzu spectrophotometer.

Specific rotations (in deg cm^2 g^{-1}) were measured in a 1.0 dm thermostated quartz cell on a PerkinElmer Model 341 polarimeter. Electronic circular dichroism spectra (ECD, in M^{-1} cm^{-1}) were recorded on a Jasco J-815 Circular Dichroism Spectrometer (IFR140 facility - Biosit - Université de Rennes 1). Molar rotations are given in deg cm^2 $dmol^{-1}$.

Thin-layer chromatography (TLC) was performed on aluminum sheets precoated with Merck 5735 Kieselgel 60F254. Column chromatography was carried out with Merck 5735 Kieselgel 60F (0.040-0.063 mm mesh).

Chemicals were purchased from Sigma-Aldrich, Alfa Aesar or TCI Europe, and used as received.

Electrochemical measurements in solution were performed with a potentiostat-galvanostat AutoLab PGSTAT 302N controlled by resident General Purpose Electrochemical System (GPES 4.9) software using a conventional single-compartment three-electrode cell. The working and auxiliary electrodes were platinum electrodes and the reference electrode was the saturated potassium chloride calomel electrode (SCE). The supporting electrolyte was 0.1 M Bu_4NPF_6 in CH_2Cl_2 and solutions were purged with argon before the measurements. The scan rate was 200 mV/s. All potentials are quoted relative to SCE.

Electrochemical measurements on surface (**Spin-dependent Electrochemistry**) were performed using a three-electrode electrochemical cell, equipped with an SCE reference electrode and a platinum wire as the counter electrode. The working electrode was helicene molecule grafted substrates (ITO or Si-Ni-Au). Electrochemical data were recorded at room temperature on a PalmSens4 electrochemical workstation. The working electrode was static during all the measurements. The unpaired electrons in the Ni layer were polarized by placing a permanent Nd magnet beneath the substrate facing the North (or South) magnetic pole facing upwards. The electrolyte used for the measurements was 0.1 M phosphate buffer PBS (pH = 7). Before measurements, the electrolyte was purged with Ar for 30 min. The scan was cycled from 0.0 V to 0.65 V vs. SCE with a scan rate of 100 mV/s.

VII.1. Synthetic procedures

Compounds **2** and **3** were prepared according to the scheme 4 via procedures already described in the literature. *P* and *M*-**H6** enantiomers were obtained following a strategy previously reported by our group [18].

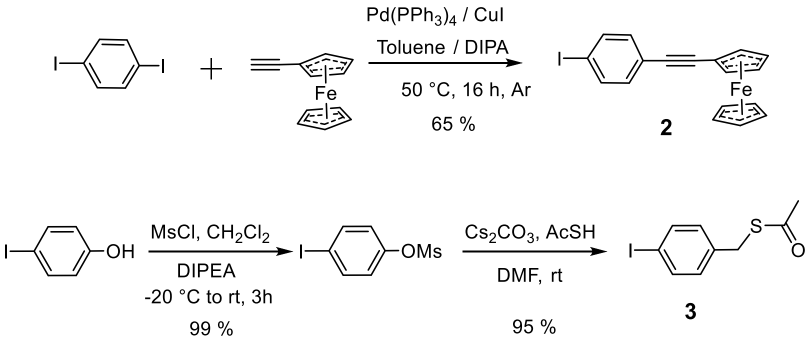

*Scheme 4. Preparation of compounds **2** and **3.***

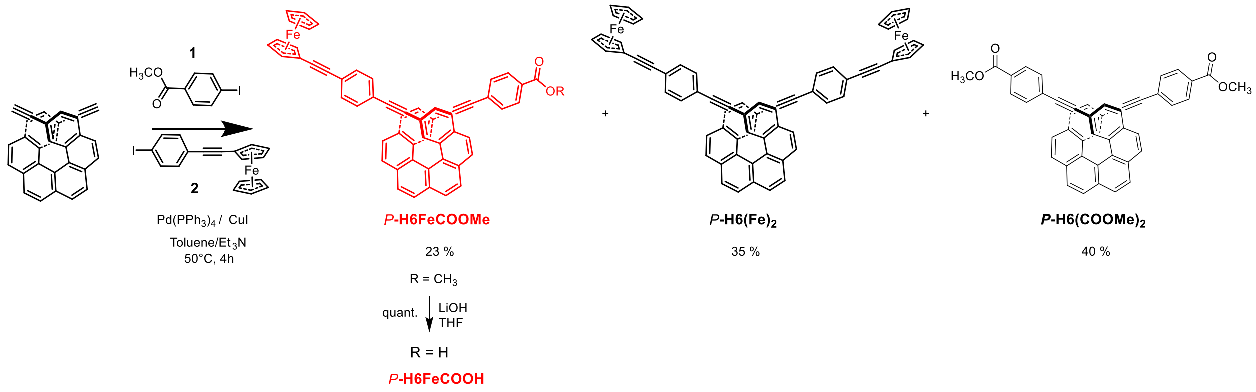

*Scheme 5. Preparation of enantioenriched compounds P-**H6FeCOCH3**, P-**H6(COCH3)$_2$** and P-**H6(Fe)$_2$***

- ***P*-H6FeCOCH3 , *P*-H6(COCH3)$_2$ and *P*-H6(Fe)$_2$**

P-2,15-Diethynylhexahelicene **H6** (26 mg, 0.07 mmol, 1.0 eq), methyl 4-iodobenzoate (23 mg, 0.08 mmol, 1.2 eq), and compound **2** (26 mg, 0.06 mmol, 1.0 eq) were dissolved in toluene (4 mL) and Et$_3$N (1 mL) under argon. Then Pd(PPh$_3$)$_4$ (8 mg, 10% mmol) and CuI (6 mg, 10% mmol) were added. After stirring at 50 °C for 4 h, the starting material was fully consumed. Thus, the solvent was removed under reduced pressure and the residue was purified by a silica gel column chromatography first by using 100% of heptane and then by increasing the polarity until 10 % of ethyl acetate to give the target compound **H6FeCOCH$_3$** (14 mg, yield 23%). **H6Fe$_2$** and **H6(COCH$_3$)$_2$** were isolated as side products of the reaction. Same procedure for enantiomer ***M.***

H6FeCOCH$_3$

^{1}H NMR (400 MHz, Chloroform-*d*) δ: 8.12 – 7.94 (m, 8H, CH$_{hel}$)), 7.83 (dd, *J* = 8.2, 6.6 Hz, 4H), 7.48 – 7.44 (m, 2H, CH$_{phenyl}$), 7.43 – 7.37 (m, 2H, CH$_{hel}$), 7.31 (m, 2H, CH$_{phenyl}$), 4.54 (t, *J* = 1.9 Hz, 2H, CH$_{Fe}$), 4.29 (d, *J* = 2.3 Hz, 7H, CH$_{Fe}$), 3.96 (s, 3H,OCH$_3$).

^{13}C{^{1}H} NMR (101 MHz, Chloroform-*d*) δ: 166.6 (C=O), 133.4, 132.2, 131.9, 131.8, 131.7, 131.3, 131.2, 129.4, 129.2, 128.3, 128.0, 127.7, 127.6, 127.6, 127.5, 127.4, 127.4, 127.2, 124.0, 123.6, 122.6, 119.4, 118.9, 92.9 (C≡C), 91.4(C≡C), 90.5(C≡C), 88.7(C≡C), 88.0 (C≡C), 85.6(C≡C), 77.3, 77.2, 76.7, 71.5 (CH-ferrocene), 70.0(CH-ferrocene), 69.0 (CH-ferrocene), 65.0, 52.2 (-OCH$_3$).

H6(Fe)$_2$

^{1}H NMR (400 MHz, Chloroform-*d*) δ: 8.12 – 7.93 (m, 8H, CH$_{hel}$)), 7.85 – 7.80 (m, 4H, CH$_{hel}$)), 7.49 – 7.47 (d, J = 8.2 Hz, 4H, CH$_{phenyl}$), 7.43 – 7.38 (dd, *J* = 8.2, 1.5 Hz, 2H, CH$_{hel}$), 7.33 – 7.30 (d, J = 8.2 Hz, 2H, CH$_{phenyl}$), 4.56 – 4.53 (t, J = 1.8 Hz, 4H, CH$_{hel}$)), 4.31 – 4.27 (d, J = 2.1 Hz, 14H, CH$_{Fe}$).

^{13}C{^{1}H} NMR (101 MHz, Methylene Chloride-*d$_2$*) δ: 133.4, 131.9, 131.7, 131.6, 131.2, 131.1, 129.2, 127.8, 127.7, 127.48, 127.44, 127.42, 127.4, 127.0, 123.8, 123.7, 122.4, 119.2, 91.2 (C≡C), 90.6 (C≡C), 88.5 (C≡C), 85.3 (C≡C), 71.4 (CH-ferrocene), 70.0 (CH-ferrocene), 69.1 (CH-ferrocene), 64.8.

HR-MS Ultraflex III., MALDI, 370 °C; ion [M]$^{+\cdot}$, $C_{66}H_{40}{}^{56}Fe_2$, m/z calculated: 944.18233, m/z experimental: 944.181 (Δ=1 ppm).

H6(COCH$_3$)$_2$

^{1}H NMR (400 MHz, Chloroform-*d*) δ: 8.11 – 8.00 (m, 8H, CH$_{hel}$), 7.96 (d, *J* = 8.5 Hz, 2H, CH$_{hel}$), 7.85 – 7.83 (m, 3H, CH$_{hel}$), 7.81 (s, 1H, CH$_{hel}$), 7.40 (d, *J* = 8.3 Hz, 8H, CH$_{phenyl}$), 3.96 (s, 6H).

^{13}C{^{1}H} NMR (101 MHz, Chloroform-*d*) δ: 166.6 (C=O), 133.4, 132.2, 131.9, 131.3, 129.4, 129.2, 128.2, 128.0, 127.8 – 127.3 , 127.2, 123.9, 118.9, 92.9(C≡C), 88.0(C≡C), 52.2 (O-CH$_3$).

- ***P*-H6FeCOOH**

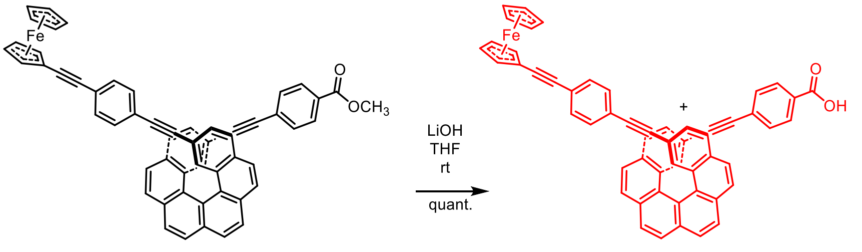

P-**H6FeCOOMe**

P-**H6FeCOOH**

H6FeCOCH$_3$ (14 mg, 0.02 mmol, 1.0 eq) was dissolved in THF (8 mL) and a solution of LiOH (6 mg, 0.03 mmol, 1.5 eq) in MeOH (0.8 mL) was added. The mixture was left stirring at room temperature for 2 days and then washed with water, extracted from CH_2Cl_2 and dried over $MgSO_4$ affording the desired product in quantitative yield (13 mg).

^{1}H (400 MHz, Methylene Chloride-*d₂*) δ: 8.17 – 8.13 (dd, J = 8.2, 1.5 Hz, 2H, CH_{hel}), 8.12 – 8.10 (m, 2H, CH_{phenyl} ortho), 8.10 – 8.07 (m, 2H, CH_{hel}), 8.06 – 8.02 (dd, J = 8.6, 2.2 Hz, 2H, CH_{hel}), 7.92 (s, 1H, , CH_{hel}), 7.91 – 7.87 (d, J = 8.0 Hz, 2H, CH_{hel}), , 7.85 – 7.82 (d, J = 1.4 Hz, 1H, CH_{hel}), 7.50 – 7.45 (d, J = 8.2 Hz, 4H, CH_{phenyl} meta), 7.45 – 7.41 (m, 2H, CH_{hel}), 7.36 – 7.30 (m, 2H, CH_{phenyl} ortho), 4.59 – 4.54 (t, J = 1.9 Hz, 2H, CH_{Fe}), 4.35 – 4.28 (d, J = 10.9 Hz, 7H, CH_{Fe}).

^{13}C{^{1}H} NMR (126 MHz, Methylene Chloride-*d₂*) δ 170.4 (C=O), 133.4, 132.1, 132, 131.9, 131.91, 131.7, 131.6, 131.3, 131.2, 131.1, 129.9, 129.2, 129.1, 128.9, 128.3, 127.8, 127.8, 127.7, 127.6, 127.5, 127.4, 127.04, 127.02, 123.8, 123.7, 122.3, 119.2, 118.6, 93.1(C≡C) , 91.1(C≡C), 90.6(C≡C), 88.5(C≡C), 87.8(C≡C), 85.32(C≡C), 71.4 (CH-ferrocene), 70.0 (CH-ferrocene), 69.1(CH-ferrocene), 64.8, 29.4.

HR-MS Ultraflex III., MALDI, 370 °C; ion $[M]^{+\cdot}$, $C_{55}H_{32}O_2{}^{56}Fe$, m/z calculated: 780.17462, m/z experimental: 780.174 (Δ=1 ppm).

Experimental optical rotation values

(*P*)-(+)-**H6FeCOOH**: $[\alpha]_D^{25} = + 5563$ (± 5 %) (c = 2.10^{-4} mol. L^{-1} in CH_2Cl_2)

(*M*)-(-)-**H6FeCOOH**: $[\alpha]_D^{25} = - 6403$ (± 5 %) (c = 2.10^{-4} mol. L^{-1} in CH_2Cl_2)

- *P*-H6FeSAc and *P*-H6(SAc)$_2$

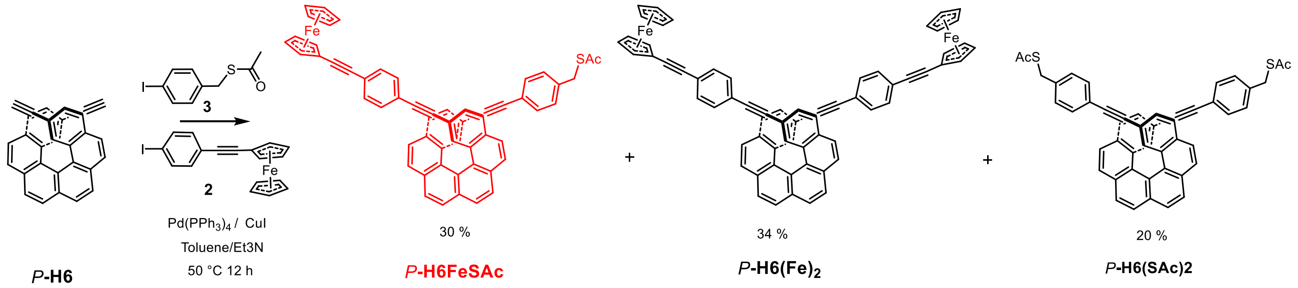

*Scheme 7. Preparation of enantioenriched compounds (P)-**H6FeSAc** and (P)-**H6(SAc)₂***

In an oven-dried 50 mL Schlenk tube, *P*-**H6** (30 mg, 0.08 mmol, 1.0 eq), compound **3** (30 mg, 0,10 mmol, 1.3 eq.) and compound **2** (42 mg, 0.10 mmol, 1.3 eq) were mixed in toluene (4 mL) and Et_3N (1 mL) under argon. Then $Pd(PPh_3)_4$ (9 mg, 10% mmol) and CuI (3 mg, 0.0016 mmol) was added. After stirring at 50 ° C for 12 h, the solvent was removed under reduced pressure, and the residue was purified on a silica gel column first by using 100% of heptane to get the compound ***P*-H6(Fe)₂** (red color) (26 mg, 34 %), then dichloromethane to give the target compound ***P*-H6FeSAc** (20 mg, 30 %) and *P*-**H6(SAc)₂** (15 mg, 20%). Same procedure for enantiomer *M.*

H6FeSAc

^{1}H NMR (400 MHz, Methylene Chloride-*d₂*) δ: 8.22 – 7.95 (m, 8H, CH_{hel}), 7.88 (d, J = 8.4 Hz, 2H, CH_{hel}), 7.84 – 7.82 (m, 2H, CH_{hel}), 7.50 – 7.46 (m, 4H, CH_{Phenyl}), 7.42 (dt, J = 8.2, 1.6 Hz, 2H, CH_{hel}), 7.32 (d, J = 13.8 Hz, 4H, CH_{phenyl}), 4.56 (t, J = 1.9 Hz, 2H, CH_{Fe}), 4.31 (d, J = 10.8 Hz, 7H, CH_{Fe}), 4.15 (s, 2H, S-CH_2), 2.40 (s, 3H, CH_3).

^{13}C{^{1}H} NMR (101 MHz, Methylene Chloride-*d₂*) δ: 194.7 (S-C=O), 138.2, 133.4, 131.9, 131.9, 131.7, 131.6, 131.62, 131.5, 131.3, 131.1, 129.2, 128.8, 127.9, 127.8, 127.76, 127.73, 127.45, 127.39, 127.34 , 127.03 , 123.8, 123.7, 122.4, 119.3, 119.2, 91.2 (C≡C), 90.6 (C≡C), 89.7 (C≡C), 88.4 (C≡C), 85.3 (C≡C), 71.5 (CH-ferrocene), 70.0 (CH-ferrocene), 69.1 (CH-ferrocene), 64.8, 33.1 (CH_2-S), 31.5 (CH_3).

HR-MS: Q-Exactive, ESI, 370 °C; ion $[M]^{+\cdot}$, $C_{57}H_{36}OS^{56}Fe$, m/z calculated: 824.18308, m/z experimental: 824.178 (Δ= 6 ppm).

(*P*)-(+)-**H6FeSAc**: $[\alpha]_D^{25} = + 5160$ (± 5 %) (c = 2.10^{-4} mol. L^{-1} in CH_2Cl_2)

(*M*)-(-)-**H6FeSAc**: $[\alpha]_D^{25} = - 5500$ (± 5 %) (c = 2.10^{-4} mol. L^{-1} in CH_2Cl_2)

H6(SAc)₂

^{1}H NMR (400 MHz, CD2Cl2) δ: 8.17 – 7.96 (m, 8H, CH_{hel}), 7.91 – 7.78 (m, 4H, CH_{hel}), 7.44 – 7.35 (m, 2H, CH_{hel}), 7.30 (d, J = 1.0 Hz, 8H, CH_{phenyl}), 4.15 (s, 4H, S-CH_2), 2.40 (s, 6H, CH_3).

^{13}C{^{1}H} NMR (101 MHz, CD_2Cl_2) δ: 194.7 (S-C=O), 138.2, 133.4, 131.9, 131.7, 131.6, 131.5, 131.3, 131.1, 129.2, 128.8, 127.9, 127.7, 127.4, 127.4, 127.3, 127.1, 123.9, 122.1, 119.3, 89.7, 88.3, 77.5, 71.5, 70, 69.1, 33.1 (CH_2-S), 30.2 (CH_3).

VII.2. Chiroptical characterization: Electronic Circular Dichroism ECD

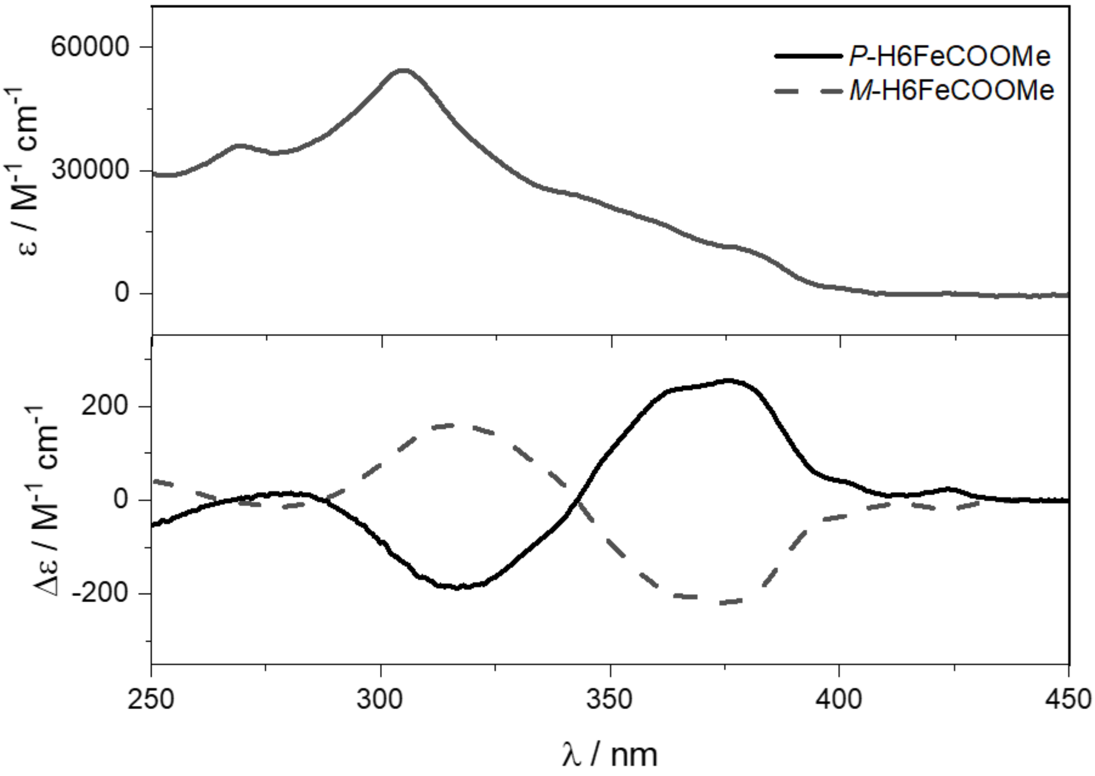

Figure 18. UV-Vis (top) and ECD (bottom) spectra of ***H6FeCOOMe*** *at 298 K in CH_2Cl_2 10^{-6}M solutions.*

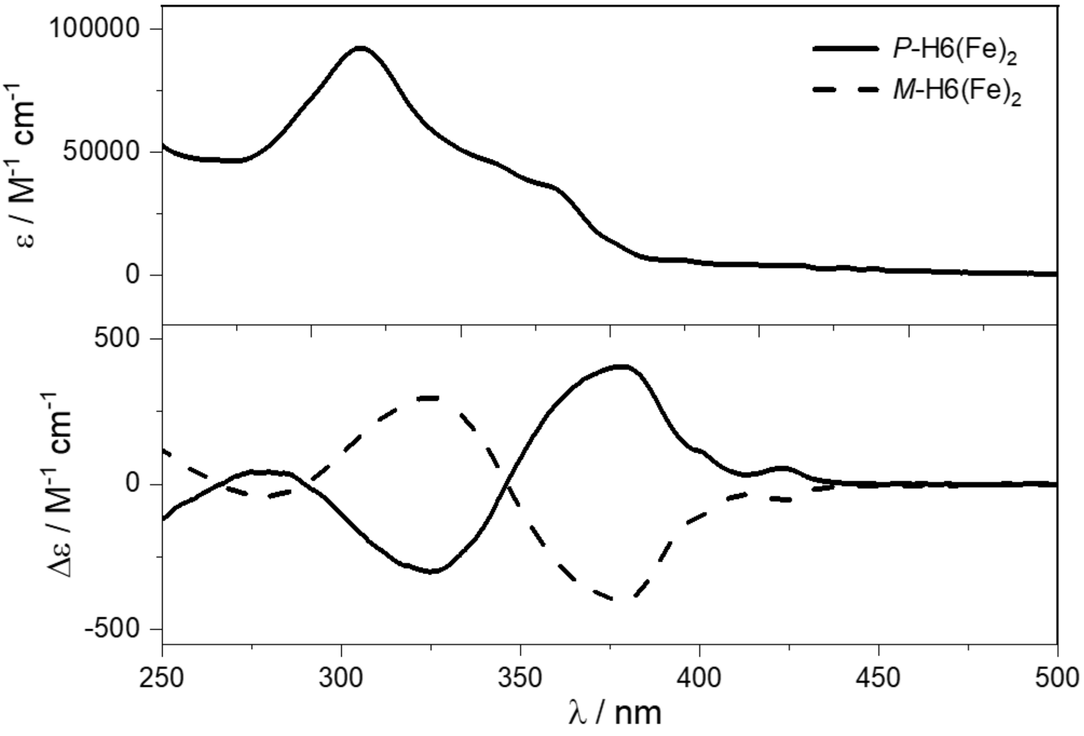

Figure 19. UV-Vis (top) and ECD (bottom) spectra of ***$H6(Fe)_2$*** *at 298 K in CH_2Cl_2 10^{-6} M solutions.*

VII.3. Surface preparation

- **Preparation of the substrate and formation of SAM on the ITO glass:**

ITO glasses (10 Oh/sqcm) were cut into 2 cm x 1.2 cm pieces, sonicated for 15 mins in soapy water, then washed three times in deionized water, boiled in acetone followed by ethanol for 10 minutes each and dried with a stream of N_2 gas. Next, the hydroxylation was performed on the ITO glasses by immersing them into a basic piranha solution (H_2O: NH_3: H_2O_2 = 5:1:1) for 30 minutes and then rinsing copiously with DI water (3 times), drying under a stream of N_2 gas before surface modification. Then the ITO glasses were immersed in a 2 mM aqueous solution of 2-aminoethylphosphonic acid for 24 h. Thereafter, the substrates were cleaned with deionized water for 3 times with sonication for 10 s every time and immediately dried with N2 gun. 2 mM THF containing carboxyl functional group helicene molecule was prepared. The THF was purged for 30 minutes before preparing the solution. The pretreated ITO glasses were immersed in this solution at RT for 24 h [19]. The slides were removed, washed with THF and methanol, dried under a stream of nitrogen. The SAMs prepared this way were used for the AFM and electrochemical studies.

- **Preparation of the substrate and formation of SAM on the gold surface:**

Gold coated ferromagnetic film was prepared using e-beam evaporation on a p-doped Si <100> wafer. The substrate configuration is: Ti (8)/ Ni (100)/ Au (10) nm. The top gold layer acts as a capping layer to protect Ni from oxidation and as a surface that covalently bind with thiol tags in the helicene molecules. As prepared substrates were cut into 1.2 cm x 2 cm for the electrochemical measurements. The substrates were washed with acetone, ethanol for 10 minutes each, dried with a N_2 gun, immersed immediately to the helicene solution. For the SAc-helicenes, a 2 mL 2mM argon saturated THF solution was prepared and 1uL of hydrazine monohydrate was added. The substrates were incubated for 12 h at room temperature [20]. Then they were washed with THF, methanol, water, and dried under a stream of argon. The SAMs prepared this way were used for the AFM and electrochemical studies.

References

[1] D. Mishra, T. Z. Markus, R. Naaman, M. Kettner, B. Göhler, H. Zacharias, N. Friedman, M. Sheves and C. Fontanesi, *PNAS,* vol. 110, 37, pp. 14872–14876, 2013.

[2] C. Fontanesi, *Curr. Opin. Electrochem.,* vol. 7, pp. 36–41, 2018.

[3] L. Fabbrizzi, *ChemTexts,* vol. 22, 2020.

[4] P. C. Mondal, N. Kantor-Uriel, S. P. Mathew, F. Tassinari, C. Fontanesi and R. Naaman, *Adv.Mater.,* vol. 27, pp. 1924–1927, 2015.

[5] J. C. Love, L. A. Estroff, J. K. Kriebel, R. G. Nuzzo and G. M. Whitesides, *Chem. Rev.,* vol. 105, pp. 1103–1170, 2005.

[6] P. C. Mondal, C. Fontanesi, D. H. Waldeck and R. Naaman., *ACS Nano,* vol. 9, pp. 3377–3384, 2015.

[7] B. R. Sculimbrene and B. Imperiali, *J. Am. Chem. Soc.,* vol. 128, pp. 7346–7352, 2006.

[8] R. Torres-Cavanillas, G. Escorcia-Ariza, I. Brotons-Alcázar, R. Sanchis-Gual, P. C. Mondal, L. E. Rosaleny, S. Giménez-Santamarina, M. Sessolo, M. Galbiati, S. Tatay, A. Gaita-Ariño and A. Forment-Aliaga, *J. Am. Chem. Soc.,* vol. 142, pp. 17572–17580, 2020.

[9] V. Kiran, S. P. Mathew, S. R. Cohen, I. H. Delgado, J. Lacour and R. Naaman, *Adv. Mater.,* vol. 28, pp. 1957–1962, 2016.

[10] S. Jadhav, *Cent. Eur. J. Chem.,* vol. 9, pp. 369–378, 2011.

[11] K. Dhbaibi, L. Abella, S. Meunier-Della-Gatta, T. Roisnel, N. Vanthuyne, B. Jamoussi, G. Pieters, B. Racine, E. Quesnel, J. Autschbach and J. Crassous, *Chem. Sci.,* vol. 12, pp. 5522–5533, 2021.

[12] S. Fery-Forgues and B. Delavaux-Nicot, *J. Photochem. Photobiol., A,* vol. 132, pp. 137–159, 2000.

[13] N. G. Connelly and W. E. Geiger, *Chem. Rev.,* vol. 96, pp. 877–910, 1996.

[14] G. Roy, R. Gupta, S. R. Sahoo, S. Saha, D. Asthana and P. C. Mondal, *Coord. Chem. Rev.,* vol. 473, pp. 214816, 2022.

[15] J. C. M. Kistemaker, G. London, W. R. Browne, P. Rudolf and B. L. Feringa., *J. Am. Chem. Soc.,* vol. 136, pp. 3219–3224, 2014.

[16] X. Hou, X. Xiao, Q.-H. Zhou, X.-F. Cheng, J.-H. He, Q.-F. Xu, N.-J. L. Hua Li, D.-Y. Chen and J.-M. Lu, *Chem. Sci.,* vol. 8, pp. 2344–2351, 2017.

[17] B. Fabre, *Chem. Rev.,* vol. 116, pp. 4808–4849, 2016.

[18] E. Anger, M. Srebro, N. Vanthuyne, L. Toupet, S. Rigaut, C. Roussel, J. Autschbach, J. Crassous and R. Réau, *J. Am. Chem. Soc. ,* vol. 134, pp. 15628–15631., 2012.

[19] X. Hou, X. Xiao, Q.-H. Zhou, X.-F. Cheng, J.-H. He, Q.-F. Xu, H. Li, N.-J. Li, D.-Y. Chen and J.-M. Lu, *Chem. Sci.,* vol. 8, pp. 2344–2351, 2017.

[20] K.-Y. Chen, O. Ivashenko, G. T. Carroll, J. Robertus, J. C. M. Kistemaker, G. London, W. R. Browne, P. Rudolf and B. L. Feringa, *J. Am. Chem. Soc.,* vol. 136, pp. 3219–3224, 2014.

[21] T. Benincori, S. Arnaboldi, M. Magni, S. Grecchi, R. Cirill, C. Fontanesi and P. R. Mussin, *Chem. Sci.,* vol. 10, pp. 2750–2757, 2019.

[22] P. C. Mondal, C. Fontanesi, D. H. Waldeck and R. Naaman, *ACS Nano,* vol. 9, pp. 3377–3384, 2015.

[23] N. Elgrishi, K. J. Rountree, B. D. McCarthy, E. S. Rountree, T. T. Eisenhart and J. L. Dempsey, *J. Chem. Educ.,* vol. 95, pp. 197–206, 2018.

Conclusions and perspectives

General conclusion

During this thesis work, new helical molecular structures with an extended π-conjugated system were prepared, their chiroptical responses, in particular the Exciton Coupling phenomenon, were studied and an intriguing recently discovered property, namely the Chiral-Induced Spin Selectivity, was investigated by different techniques.

First, we illustrated two novel families of helicene-porphyrin conjugates, **H6Pr1-3** and **PrZnPhH6** prepared starting from one common helicenic core and porphyrin units. The first systems **H6Pr1-3** were fully characterized and their photophysical and chiroptical properties were investigated experimentally and by theoretical calculations (in collaboration with the group of Prof. Autschbach at University at Buffalo), unambiguously confirming the presence and effectiveness of EC chirality in helicenes through the very strong bisignate CD response in the Soret band along with slightly ECD-active Q-bands. Interestingly, these systems also revealed CPL activity which is still very rare in chiral porphyrins. This work was published in *Chemical Communications*[1]. The second type of helicene-porphyrin conjugate, namely **PrZnPhH6** bearing one less ethynyl bridge displayed similar exciton chirality but with overall less intense chiroptical activities (observed both in ECD and in CPL).

These results led us to further investigations on the exciton coupling of these helicene-porphyrin conjugates: the role of the interchromophoric distance and of the conjugation were explored by changing the spacer between the chiral unit and the chromophores, as well as the metallic centers. This strategy subsequently allowed us to fine-tune this platform by changing the linker between the helicene and the porphyrin and to achieve higher g_{abs} and g_{lum} values.

A noteworthy enhancement was achieved with the **MPrH6** family of molecules in which the 2,5-bis-ethynyl carbo[6]helicene is directly linked to the porphyrins to avoid a spacer and reduce the interchromophoric distance.

In the ECD spectrum, the EC bisignature at the Soret band appeared to be the prominent signal compared to the helicene bands, and the value was remarkably improved. Therefore, the investigation of the properties was extended to the influence of the metal and several derivatives were prepared. Thanks to the promising results, these derivatives (Zn(II), Ni(II), Pd(II), Cu(II)) derivatives were selected as preliminary candidates for CISS measurements through mc-AFM, in collaboration with Naaman's group at Weizmann Institute of Science. The aim is to try to obtain a good spin polarization value by exploiting the remarkable optical activity, without the need for anchoring groups or supramolecular polymerization. Spin polarization as high as 50% was obtained for the zinc complex.

The last system **MPrOMeH6**, which does not include a spacer but has a direct C-C bond between the chiral unit and the chromophore, was designed to optimize the distance between the metallic centers in the porphyrin core. The aim is to exploit the metal-metal interactions, specifically in magnetically-active centers like the V(IV)O derivative, that will be studied further through EPR spectroscopy. Interestingly, the enantiomeric zinc derivatives *P*- and *M*-**ZnPrOMeH6** exhibited the highest exciton coupling response, thus confirming the impact of proximity.

Overall, these results nicely illustrate how molecular engineering using functionalization with strongly polarizable units in close proximity enables the fine-tuning of the chiroptical signatures. This strategy also allows access to CPL active porphyrin derivatives, which still remain quite rare and opens up new opportunities for the design of new suitable candidates for spintronic applications.

In the last chapter we described the investigation of the spin filtering ability of helicene- based Self-Assembled Monolayer through the formation of a chemical bond with the surface. The helicenic unit was decorated with a redox moiety and a grafting unit to achieve a proper orientation on the surface and explore how the electron transfer reaction depends on the chirality and affects the electrochemical current by Spin Dependent Electrochemistry. More specifically, the bis-ethynyl hexahelicene has been functionalized with a conjugated ferrocene unit as an electrochemical probe on one side and i) a carboxylic acid (anchoring group for TiO_2) for **H6FeCOOH** ; ii) a thioacetate moiety (for Au surface) for **H6FeSAc** and iii) with a terminal alkyne (for grafting onto Si-H surface).
Promising preliminary results have been obtained for the **H6FeCOOH** and **H6FeSAc** derivatives but further characterizations such as XPS and CD on thin films are needed to explore the organization of the compounds on the surface and mc-AFM measurements are ongoing in collaboration with Naaman's group.
By combining the carbohelicene helical center with chromophores and different grafting functions we are able to obtain promising materials with intriguing chiroptical properties and spin filtering ability.

Moreover, other studies related to the CISS effect in helicene-based assemblies were carried out [2,3].
By decorating the bis-ethynyl-carbo[6]helicene with aggregating amide units, we obtained different supramolecular organizations depending on the position of the functionalization. The 2,15-substituted [6]helicene assembled in a head-to-tail manner and the 4,13- substituted [6]helicene in a head-to-head fashion, with some differences for the two amide units we utilized.
The chiroptical responses and spin filtering were investigated and displayed interesting modifications related to the supramolecular assembly and spin polarization values from 50% to 80%.

[1] K. Dhbaibi, P. Matozzo, L. Abella, M. Jean, N. Vanthuyne, J. Autschbach, L. Favereau and J. Crassous, *Chem. Commun.,* vol. 57, pp. 10743–10746, 2021.]

[2] R. Rodríguez, C. Naranjo, A. Kumar, P. Matozzo, T. K. Das, Q. Zhu, N. Vanthuyne, R. Gómez, R. Naaman, L. Sánchez and J. Crassous, *J. Am. Chem. Soc,* vol. 144, pp. 7709–7719, 2022.

[3] R. Rodríguez, C. Naranjo, A. Kumar, K. Dhbaibi, P. Matozzo, F. Camerel, N. Vanthuyne, R. Gómez, R. Naaman, L. Sánchez and J. Crassous, *Chem. Eur. J.*, 2023, accepted https://doi.org/10.1002/chem.202302254

Résumé en français

Les hélicènes sont les archétypes des molécules hélicoïdales : ces molécules sont composées de n anneaux aromatiques ou hétéroaromatiques orthofusionnés dont la structure hélicoïdale entraîne une chiralité inhérente et des propriétés intrigantes. En effet ces molécules interagissent fortement avec la lumière polarisée circulairement, ce qui donne lieu à des réponses chiroptiques remarquables telles que des valeurs de rotation optique élevées, un dichroïsme circulaire électronique (CD) intense et une luminescence polarisée circulairement (CPL).

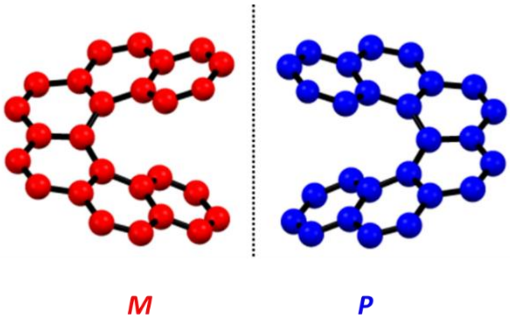

Figure 15. Représentation des deux énantiomères du carbo[6]hélicène.

Les hélicènes ont donc été étudiés, entre autres, comme capteurs et commutateurs chiraux, ligands chiraux dans la catalyse asymétrique et émetteurs à polarisation circulaire dans des dispositifs ou des assemblages supramoléculaires [1].

Au cours des dernières décennies, une nouvelle propriété fascinante liée aux molécules chirales a été révélée : il a été démontré que la transmission des électrons à travers les molécules chirales dépendait du spin. Selon ce concept, les électrons injectés à travers un matériau chiral doivent avoir leur spin sélectionné dans une direction préférentielle. C'est ce qu'on appelle l'effet de sélectivité de spin induit par la chiralité (CISS), qui ouvre la voie à de nouvelles applications en spintroniques pour ce type de composés grâce à la polarisation de spin [2].

Après le premier exemple décrit en 2016 par Lacouret Naaman démontrant un effet CISS dans les hélicènes, notre groupe a contribué au domaine en observant des effets CISS dans des auto-assemblages supramoléculaires d'hélicènes obtenus à partir de carbo[6]hélicène portant différentes unités d'agrégation [3, 4].

Dans ce contexte, nous avons conçu de nouveaux dérivés d'hélicène dans le but d'explorer la capacité de filtrage de spin de cette plateforme chirale à l'aide de différentes techniques, telles que la microscopie à force atomique magnétiquement conductrice (mc-AFM) et l'électrochimie dépendante du spin (SDE). Les travaux ont été réalisés en collaboration avec le groupe du Professeur Ron Naaman du Weizmann Institute of Science en Israël dans le cadre du projet ITN HEL4CHIROLED (programme de recherche et d'innovation Horizon 2020 de l'Union européenne dans le cadre de la convention de subvention Marie Sklodowska-Curie n° 859752).

Après une introduction à la chiralité et au motif hélicoïdal, le premier chapitre est consacré à diverses méthodes de synthèse des hélicènes et à l'illustration de leur comportement chiroptique. Un accent particulier est mis sur le phénomène du Couplage Excitonique (EC) [5] et sur la définition de l'effet CISS, ses techniques de mesure et quelques exemples simples de la littérature.

Le deuxième chapitre décrit la synthèse et les propriétés chiroptiques des premiers systèmes hélicène-bis-porphyrines conjugués. Nous illustrons deux nouvelles familles d'hélicène-porphyrines conjuguées, **H6Pr1,3** et **PrZnPhH6** (Figure 2), préparés à partir d'un noyau carbo[6]hélicène commun et d'unités porphyriniques. Les premiers systèmes **H6Pr1,3** ont été entièrement caractérisés et leurs propriétés photophysiques et chiroptiques ont été étudiées expérimentalement et par des calculs théoriques (grâce à la collaboration avec le groupe du Professeur Autschbach de l'université de Buffalo), confirmant sans ambiguïté la présence et l'efficacité du Couplage Excitonique dans les hélicènes grâce à la très forte réponse en dichroïsme circulaire dans la bande de Soret ainsi qu'à des bandes Q légèrement actives. Il est intéressant de noter que ces systèmes ont également révélé une activité en CPL, ce qui est encore très rare dans les porphyrines chirales. Ces résultats ont été publiés dans la revue *Chemical Communication* [6]. Le deuxième type de d'hélicène-porphyrines conjuguées **PrZnPhH6** portant un pont éthynyle en moins, présente une chiralité similaire mais avec des activités chiroptiques globalement moins intenses (observées à la fois dans le CD et dans la CPL).

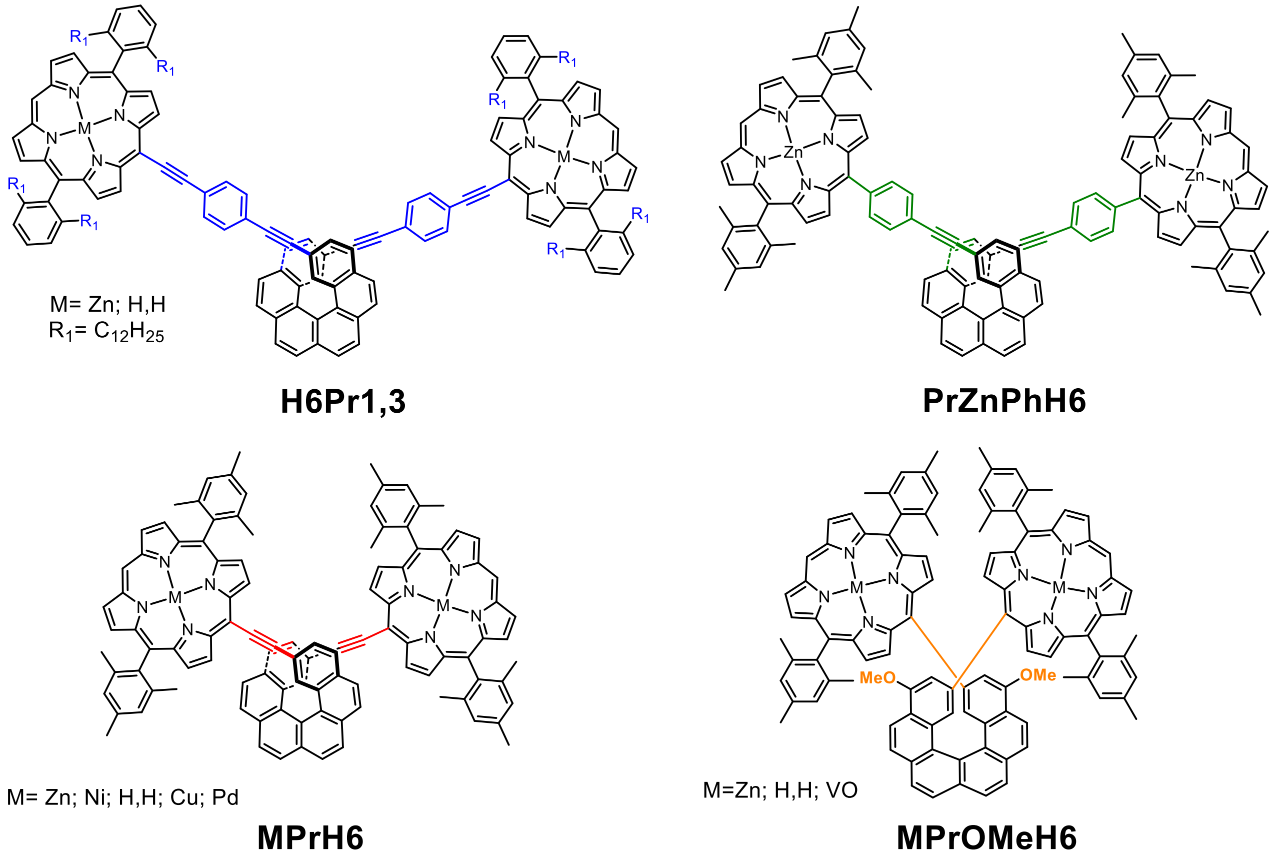

Figure 16. Structures des dérivés hélicène-bis-porphyrines.

Le phénomène du Couplage Excitonique peut être utilisé dans les hélicènes pour obtenir des molécules chirales dotées de fortes propriétés chiroptiques, telles qu'une forte réponse de dichroïsme circulaire et une forte émission de luminescence polarisée circulairement, grâce au placement de groupes achiraux fortement polaires dans un environnement hélicoïdal. En outre, il peut avoir une influence dans les effets CISS car il permet l'ingénierie des moments de transition dipolaires magnétique et électrique. Il est démontré que la conjugaison et la distance entre les chromophores ont un impact sur les réponses chiroptiques : une étude du rôle de la distance entre les porphyrines et de la conjugaison est donc poursuivie dans le troisième chapitre, où différentes familles de dérivés de l'hélicène et de la porphyrine sont explorées (**MPrH6** et **MPrOMeH6**). Les méthodes de synthèse utilisées sont basées sur des couplages de Suzuki et de Sonogoshira, en fonction du dérivé hélicénique de départ considéré.

Une amélioration notable a été obtenue avec la famille de molécules **MPrH6** : le 2,5-bis-éthynyl carbo[6]hélicène est directement lié aux porphyrines en évitant l'espacement, de sorte que la distance interchromophorique est réduite. Dans le spectre CD (Figure 3), la bisignature EC de la bande de Soret semble être le signal le plus important par rapport aux bandes de l'hélicène, et la valeur a été remarquablement améliorée. Par conséquent, l'étude des propriétés a été étendue à l'influence du métal et plusieurs dérivés ont été préparés.

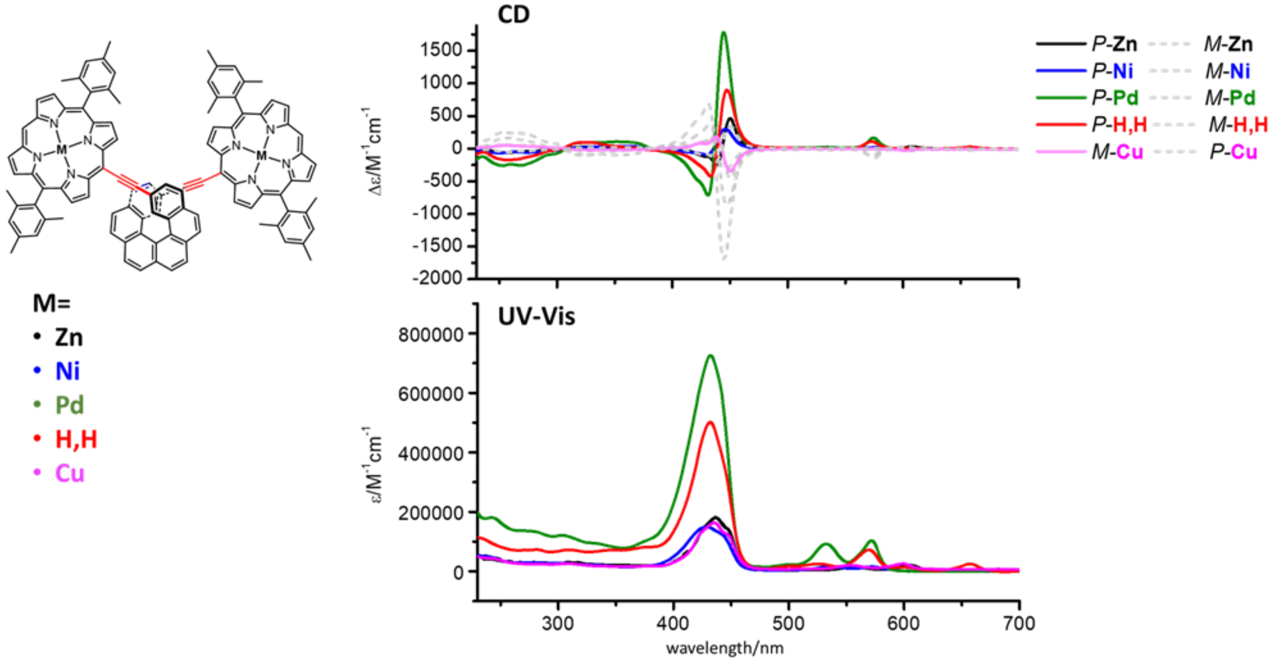

Figure 17. Spectres CD et spectres d'absorption pour la série MPrH6 : la légende pour le dérivé de Cu(II) est inversée pour une meilleure visualisation de la courbe.

Grâce à ces résultats prometteurs, ces dérivés (Zn(II), Ni(II), Pd(II), Cu(II)) ont été sélectionnés comme candidats préliminaires pour les mesures CISS par mc-AFM, en collaboration avec le groupe du Professeur Ron Naaman au Weizmann Institute of Science : l'objectif est d'essayer d'obtenir une bonne valeur de polarisation des spins en exploitant l'activité chiroptique remarquable, sans avoir besoin de groupements d'ancrage ou de polymérisation supramoléculaire. Une polarisation de spin de 50 % a ainsi été obtenue pour le complexe de zinc **ZnPrH6** (Figure 4).

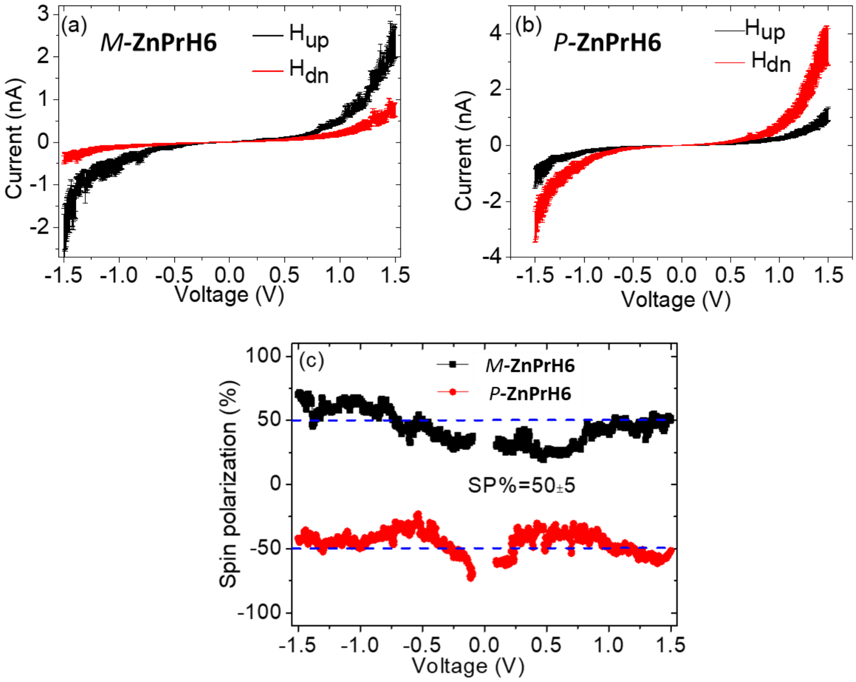

*Figure 18. Courant en fonction de la tension (I-V) enregistré pour (a) P-, et (b) M-**ZnPrH6** déposés sur des substrats Ni-Au. Dans les deux cas, les Ni ont été magnétisés avec le pôle nord orienté vers le haut (ligne noire) et vers le bas (ligne rouge) ; c) tracé de polarisation de spin pour les deux composés.*

Le dernier système **MPrOMeH6**, qui ne comprend pas d'espaceur mais une liaison C-C directe entre l'unité chiral et le chromophore, a été conçu pour optimiser la distance entre les deux centres métalliques dans le noyau de la porphyrine. L'objectif est d'exploiter les interactions métal-métal, en particulier dans le cas des centres magnétiquement actifs comme le dérivé V(IV)O, qui sera dans l'avenir étudié plus en détail par spectroscopie RPE.

Dans le dernier chapitre, nous explorons une autre technique pour mesurer la capacité de filtrage de spin de l'hélicène : l'électrochimie dépendante du spin. Dans ce but, l'unité hélicénique a été décorée avec une unité rédox et une fonction de greffage afin d'obtenir une orientation correcte sur la surface de l'électrode et d'explorer comment la réaction de transfert d'électrons dépend de la chiralité et affecte le courant électrochimique. Plus précisément, le bis-éthynyl hexahélicène a été fonctionnalisé avec comme sonde électrochimique une unité de ferrocène conjuguée d'un côté et i) un acide carboxylique (groupe d'ancrage pour l'ITO) dans le cas de **H6FeCOOH**, ou ii) un groupement thioacétate (pour la surface Ni-Au) dans **H6FeSAc**.

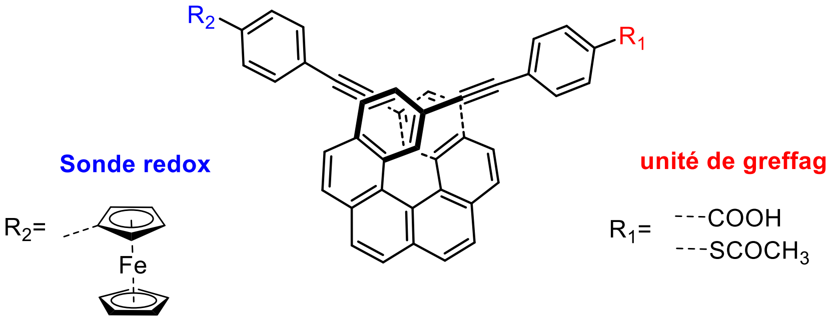

Figure 19. Structure hélicèniques avec les deux fonctionnalisations (unité rédox et fonction de greffage).

Des résultats préliminaires prometteurs ont été obtenus pour les dérivés **H6FeCOOH** et **H6FeSAc** mais des caractérisations supplémentaires sur des films minces sont nécessaires afin d'explorer l'organisation des composés sur la surface et des mesures mc-AFM sont en cours en collaboration avec le groupe de Ron Naaman.

Grâce à la combinaison du centre hélicoïdal du carbohélicène avec des chromophores et différentes fonctions de greffage, nous sommes en mesure d'obtenir des matériaux prometteurs avec des propriétés chiroptiques intrigantes et une capacité de filtrage de spin.

Références

[1] J. Crassous, I. G. Stara and I. Stary (Eds), Helicenes: Synthesis, Properties and Applications, Wiley, 2022.

[2] R. Naaman and D. H. Waldeck, *J. . Phys. Chem. Lett.,* vol. 3, p. 2178–2187, 2012.

[3] R. Rodríguez, C. Naranjo, A. Kumar, K. Dhbaibi, P. Matozzo, F. Camerel, N. Vanthuyne, R. Gómez, R. Naaman, L. Sánchez and J. Crassous, *Chem. Eur. J.,* vol. 29, e202302254, 2023.

[4] R. Rodríguez, C. Naranjo, A. Kumar, P. Matozzo, T. K. Das, Q. Zhu, N. Vanthuyne, R. Gómez, R. Naaman, L. Sánchez and J. Crassous, *J. Am. Chem. Soc.,* vol. 144, pp. 7709–7719, 2022.

[5] N. Berova, L. D. Bari et G. Pescitelli, *Chem. Soc. Rev.,* vol. 36, pp. 914–931, 2007.

[6] a) K. Dhbaibi, L. Favereau, M. Srebro-Hooper, M. Jean, N. Vanthuyne, F. Zinna, B. Jamoussi, L. D. Bari, J. Autschbach and J. Crassous, *Chem. Sci.,* vol. 9, pp. 735-742, 2018. b) K. Dhbaibi, P. Matozzo, L. Abella, M. Jean, N. Vanthuyne, J. Autschbach, L. Favereau and J. Crassous, *Chem. Commun.,* vol. 57, pp. 10743–10746, 2021.

COLLEGE SCIENCES DE LA MATIERE
DOCTORAL DES MOLECULES
BRETAGNE ET MATERIAUX

Université
de Rennes

Titre : Dérivés Hélicènes-Porphyrines : Couplage Excitonique et Sélectivité de Spin Induite par la Chiralité

Mots clés : Hélicènes, porphyrines, couplage excitonique, polarisation du spin

Résumé : De nouveaux dérivés hélicéniques ont été synthétisés dans le but d'investiguer leur réponse photophysique et chiroptique ainsi que leur capacité à filtrer le spin à travers différentes techniques.

La première partie de cette thèse offre une introduction de la chiralité et des hélicènes par les méthodes de synthèse et leur comportement chiroptique. Une attention particulière est accordée à la définition de couplage excitonique et à l'effet CISS. Des techniques de mesure et des exemples illustratifs de la littérature sont présentés.

Le deuxième chapitre illustre la synthèse et la caractérisation des premiers derivés hélicène-porphyrine, en mettant l'accent sur le rôle de l'hélicène dans le couplage excitonique.

Ce phénomène est ensuite approfondi dans le troisième chapitre au travers de la description de différents systèmes hélicène-porphyrine, ainsi que les résultats préliminaires sur les propriétés de filtrage du spin de l’électron.

Dans le dernier chapitre, nous explorons une deuxième technique pour évaluer la capacité de filtrage du spin dans les hélicènes décorés par des unités redox et greffés sur différentes surfaces.

Title : Helicene-porphyrin conjugates : Exciton Coupling and Chiral-Induced Spin Selectivity effect

Keywords : Helicenes, porphyrins, Exciton Coupling Chirality, spin polarization

Abstract : Novel helicene-porphyrin derivatives were synthesized with the aim to investigate their photophysical and chiroptical responses and their spin filtering ability, through different techniques.

The first chapter provides an introduction of chirality and helicenes across various methods of synthesis and their chiroptical behavior. Particular attention is given to Exciton Coupling chirality and the definition of the CISS effect. Measurement techniques and illustrative examples from the literature are also presented.

The second chapter illustrates the synthesis and characterization of the first helicene-porphyrin conjugates, with a focus on the role of helicene in the Exciton Coupling chirality. This phenomenon is further investigated in the third chapter through the description of different helicene-porphyrin derivatives along with the preliminary results on the spin filtering properties.

In the final chapter, we explore an alternative technique based on electrochemistry to assess the spin filtering capacity of helicenes decorated by redox unit and grafted onto diverse surfaces.